CRANFIELD UNIVERSITY

D BRUNO

GEOSYNCHRONOUS SYNTHETIC APERTURE RADAR:

DESIGN AND APPLICATIONS

SCHOOL OF ENGINEERING

PhD THESIS

CRANFIELD UNIVERSITY

School of Engineering

Space Research Centre

PhD THESIS

Academic Year 2009

DAVIDE BRUNO

Geosynchronous Synthetic Aperture Radar: design and applications

Supervisor: Dr. S. E. Hobbs

Presented: October 2009

Abstract

Synthetic Aperture Radar (SAR) imaging from geosynchronous orbit has significant potential advantages over conventional low-Earth orbit (LEO) radars, but also challenges to overcome.

This thesis investigates both active and passive geosynchronous SAR configurations, presenting their different features and advantages.

Following a system design trade-off that involved phase uncertainties, link budget, frequency and integration time, an L band bi-static configuration with 8-hour integration time that reuses the signal from a non-cooperative transmitter has been presented as a suitable solution.

Cranfield Space Research Centre looked into this configuration and proposed the GeoSAR concept, an L band bi-static SAR based on the concept by Prati *et al.* (1998). It flies along a circular ground track orbit, reuses the signal coming from a non-cooperative transmitter in GEO and achieves a spatial resolution of about 100 m.

The present research contributes to the GeoSAR concept exploring the implications due to the 8-hour integration time and providing insights about its performance and its possible fields of application.

Targets such as canopies change their backscattered phase on timescales of seconds due to their motion. On longer time scales, changes in dielectric properties of targets, Earth tides and perturbations in the structure of the atmosphere contribute to generate phase fluctuations in the collected signals. These phenomena bring temporal decorrelation and cause a reduction in SAR coherent integration gain. They have to be compensated for if useful images are to be provided.

A SAR azimuth simulator has been developed to study the influence of temporal decorrelation on GeoSAR point spread function. The analysis shows that ionospheric delay is the major source of decorrelation; other effects, such as tropospheric delay and Earth tides, have to be dealt with but appear to be easier to handle.

Two different options for GeoSAR interferometry have been discussed. The system is well suited to differential interferometry, due to the short perpendicular baseline induced by the geometry. A GeoSAR has advantages over a Low Earth Orbit (LEO) SAR system to monitor processes with significant variability over daily or shorter timescales (e.g. soil moisture variation). This potential justifies further study of the concept.

Acknowledgments

My first thought is for my parents Enrico and Franca. They sustained me in all the steps of my life and even this achievement would have been much more difficult without their constant support.

I want to express my sincere gratitude to my PhD supervisor, Dr. Steve Hobbs, Director of the Cranfield Space Research Centre. He guided me throughout this experience with his precious and constructive advices. I have been in touch with him since 2002; during this long period I had the opportunity to appreciate his professional qualities and his genuine personality.

I would like also to thank all the people that contributed with their expertise and work to the realization of this research:

- Dr. Les Oswald from the Cranfield University Computer Centre;
- all the Cranfield University Library staff and in particular the “student off-site service” led by Ms. Anita Beal; without her precious help, running a project off-campus would have been really difficult;
- all the Cranfield Space Research Centre Staff.

I would like to acknowledge the Remote Sensing and Photogrammetry Society that partially supported the attendance to two IAC conferences in Fukuoka and Glasgow.

In these years I have met in Cranfield many good friends and I have shared with them both fun and hard work. I wish to thank all of them for their friendship. Ad maiora!!!

The last of my thought is for my beloved Irene. Her constant love and support have been essential in these years. I have to thank her enduring comprehension for the time we were not spending together during holidays and weekends.

Contents

List of Acronyms

1D	One-Dimensional
2D	Two-Dimensional
3D	Three-Dimensional
CNES	Centre National Etudies Spatiales
DEM	Digital Elevation Model
DFT	Discreet Fourier Transform
DTEC	Differential Total Electron Content
DTM	Digital Terrain Model
ECF	Earth Centred Fixed
EO	Earth Observation
ERS	European Remote Sensing Satellite
ESA	European Space Agency
FFT	Fast Fourier Transform
FM	Frequency Modulation
GEO	Geostationary
GESS	Global Earthquake Satellite System
GNSS	Global Navigation Satellite System
GPS	Global Positioning System
InSAR	SAR Interferometry
IRF	Impulse Response Function
ITU	International Telecommunication Union
JPL	Jet Propulsion Laboratory
LAAS	Local Area Augmentation System
LEO	Low Earth Orbit
LSTID	Large Scale Travelling Ionospheric Disturbances
MSTID	Medium Scale Travelling Ionospheric Disturbances
NASA	National Aeronautics and Space Administration
PDF	Probability Density Function
PGA	Phase Gradient Autofocus
PRF	Pulse Repetition Frequency
PRI	Pulse Repetition Interval
PS	Permanent Scatterer
PSF	Point Spread Function
PWV	Precipitable Water Vapour
RADAR	RAdio Detection And Ranging
RAR	Real Aperture Radar
RF	Radio Frequency
RCS	Radar Cross Section
RR	Radio Regulation
rms	Root Mean Square
RX	Receiver
SAR	Synthetic Aperture Radar
SHD	Slant Hydrostatic Delay

SLC	Single Look Complex
SNR	Signal to Noise Ratio
SRTM	Shuttle Radar Topography Mission
SSTID	Small Scale Travelling Ionospheric Disturbances
STAP	Space Time Adaptive Processing
STD	Slant Total Delay
STEC	Slant Total Electron Content
SWD	Slant Wet Delay
STK	Satellite Tool Kit
TEC	Total Electron Content
TECU	Total Electron Content Unit
TID	Travelling Ionospheric Disturbances
TX	Transmitter
UM	Unified Model
VLBI	Very Large Baseline Interferometry
VMF	Vienna Mapping Function
VTEC	Vertical Total Electron Content
WVR	Water Vapour Radiometer
ZHD	Zenith Hydrostatic Delay
ZND	Zenith Neutral Delay
ZWD	Zenith Wet Delay

Notation

A_e	Effective antenna area
A_i	Illuminated Area
A_{rs}	Effective aperture of the receiving antenna
B	Geometrical baseline
	Signal bandwidth
$B_{\parallel}$	Parallel component geometrical baseline
$B_{\perp}$	Perpendicular component geometrical baseline
B_D	Doppler bandwidth
B_h	Horizontal component geometrical baseline
B_R	Range bandwidth
B_v	Vertical component geometrical baseline
B_w	Bandwidth
c	Speed of light
c_0	Speed of light in vacuum
	Radar calibration factor
C_φ	Variance-covariance matrix
δS_{NEU}	Total/neutral slant path delay from receiver antenna to satellite
D	Length of the antenna
	Distance between TX and RX satellites
E	Electric field
e	Partial water vapour pressure
	Orbit eccentricity
e_l	Electron charge
f_a	Fraction of power absorbed by the scatterer
F	Noise figure
f_D	Doppler frequency
G_t	Antenna Gain
G_{ts}	Gain of the scatterer in the direction of the receiver
h	Satellite altitude
H	Topographic altitude
H_{sat}	Satellite altitude
$h_{2\pi}$	Height ambiguity
i	Orbit inclination
k	Wavenumber
	Boltzmann's constant
L	Antenna height
	Number of looks
	System losses
L_A	Length of the synthetic antenna
m	electron charge
$m_h(\vartheta)$	Hydrostatic delay mapping function
$m_{wv}(\vartheta)$	wet delay mapping function
n	Refractivity index

N	Scaled refractivity index
n_{sat}	Number of satellites (multi-static SAR)
p	Static pressure
P_{avg}	Average transmitted power
P_T	Transmitted power
P_R	Received power
R	Radar range
$\dot{R}$	Slant range velocity
$\ddot{R}$	One-half of the slant range acceleration
R_1	Slant range master image
R_2	Slant range slave image
R_{GEO}	altitude of GEO orbit
R_e	Earth's radius (6378 km)
R_T	Transmitter-target slant range
R_R	Target-Receiver slant range
t_D	Round-trip time
T	Noise temperature
	Static Temperature
T_{int}	Integration time
v_{sc}	Spacecraft ground-track velocity
v_{ss}	Spacecraft orbital velocity
W	Liquid water content
$Z_{d/w}$	Compressibility factors for dry and wet air
β	Power law index
	Bi-static angle
γ	Complex coherence
γ_{geom}	Geometric Correlation
$\gamma_{temporal}$	Temporal Correlation
$\gamma_{thermal}$	Thermal Correlation
γ_{vol}	Volumetric Correlation
δ	Atmospheric slant delay
$\Delta\varphi$	Variation in interferometric phase
Δf_D	Doppler frequency resolution
$\Delta R_{azimuth}$	Radar resolution in azimuth
ΔR_{range}	Radar resolution in range
Δz	Height difference between the scatterers in the same resolution cell
ε	Grazing angle
	Phase error
ε_0	Dielectric permissivity of vacuum
φ	Interferometric phase
λ	Radar wavelength
μ	Refractive index of the atmosphere
ρ	Radar slant range
ρ_l	Density of liquid water
ρ_v	Density of water vapour
ρ_x	correlation

θ	Look angle (degrees)
θ_r	Pulse beam-width in range
θ_a	Pulse beam-width in azimuth
σ	Radar cross section standard deviation
σ^0	Differential scattering coefficient
σ_h	Standard deviation topographical height
σ_φ	Standard deviation interferometric phase
τ	Radar pulse duration
τ_0	Compressed pulse duration
τ_c	Correlation time
τ_{gr}	Group delay
τ_p	Radar pulse duration
τ_{ph}	Phase delay
ω	Width of the tube containing the trajectories of the n_{sat} SARs
ω_T	Earth's angular velocity

List of Figures

List of Tables

1 Introduction

This report presents research undertaken at the Cranfield University Space Research Centre (SRC) from October 2003 to September 2009. The work focuses on the analysis and the development of the concept for a geosynchronous Synthetic Aperture Radar (SAR). This concept has been already demonstrated in literature (Tomiyasu, 1978; Tomiyasu and Pacelli, 1983; Madsen *et al.*, 2001; Prati *et al.*, 1998), but its main technical challenges have not been discussed in any piece of work.

This first chapter describes the background and rationale of the research. It then presents a literature review on SAR satellites in a geosynchronous orbit that leads to the problem formulation and the definition of the research objectives. The final section states briefly the methodology and outlines the content of the report.

1.1 Background and rationale

Before presenting the specific objectives of the research, it is important to introduce its background and rationale, covering aspects related to both Earth observation and Synthetic Aperture Radar. A literature review of the publications about geosynchronous SARs will provide the necessary background to understand the research aim and its objectives.

1.1.1 Earth observation

Remote sensing is proved to be a unique source of information on the Earth and is often a precious source of data for the understanding of both environmental and anthropogenic processes.

Surface imaging space-borne sensors operate in specific regions of the electromagnetic spectrum where constituents of the atmosphere (e.g. water vapour and carbon dioxide) do not absorb radiation. Such sensors can be primarily divided into passive and active types. The former group measures radiation naturally reflected or emitted from the ground, atmosphere and clouds (e.g. optical sensors in the visible or thermal infrared spectrum). The latter instead employs an artificial source of radiation as a probe and measures the resulting signal that is scattered back (e.g. SAR platforms operating in the microwave spectral region). The main subject of the present research is Synthetic Aperture Radar therefore only SAR satellites will be considered further in the discussion.

A precise definition of temporal and spatial resolution, two of the main parameters that are used in EO system classification, can be useful to understand geosynchronous SAR peculiarities. Temporal resolution is defined in terms of the frequency at which images of the same location on Earth can be captured. Spatial resolution identifies the minimum separation between two objects at which the resulting images of the objects appear distinct and separate.

Typically, EO satellites are placed in Low Earth Orbit (LEO), to take advantage of the shorter slant range. The key limitation of LEO for remote sensing is the difficulty of providing frequent timely images of an area. A single satellite typically images a swath 100-200 km wide steerable within a field of view 500 km across. LEO orbit periods are approximately 100 minutes, and in this time, the Earth has turned almost 3000 km at the equator: it thus takes ~3000/500=6 days to obtain complete access. Envisat actually uses a 35-day repeat orbit, which means a repeat period of 5 weeks for interferometry, and 1-2 weeks (at mid-latitudes) for imaging. Processes with timescales shorter than these periods are difficult to measure usefully. Satellites in geosynchronous orbit, on the other hand, have a permanent view of 1/3 of Earth's surface so that, as soon as one image is complete, the next can be started. Allowing for the time required to acquire the image this means that a geosynchronous satellite could provide in principle several images each day of any location in the field of view.

An inconvenience caused by the geosynchronous orbit is its fixed longitude. This implies that only a constellation of at least three satellites can guarantee a nearly global coverage. Even so, polar zones cannot be imaged with nominal resolution. However, global coverage is not always an essential requisite for a space system. The problem that many satellite service providers have to tackle is that the request for satellite products is concentrated in the most industrialised regions of the globe therefore a system that is able to provide nearly continuous imaging of a certain region may prove to be advantageous for certain customers.

A typical example of a regional market for satellite data is agriculture monitoring. In 2004, 50% of the global cereal production was concentrated in only four countries (Figure 1-1) according to FAO data that has been reported in Bruno *et al.* (2006).

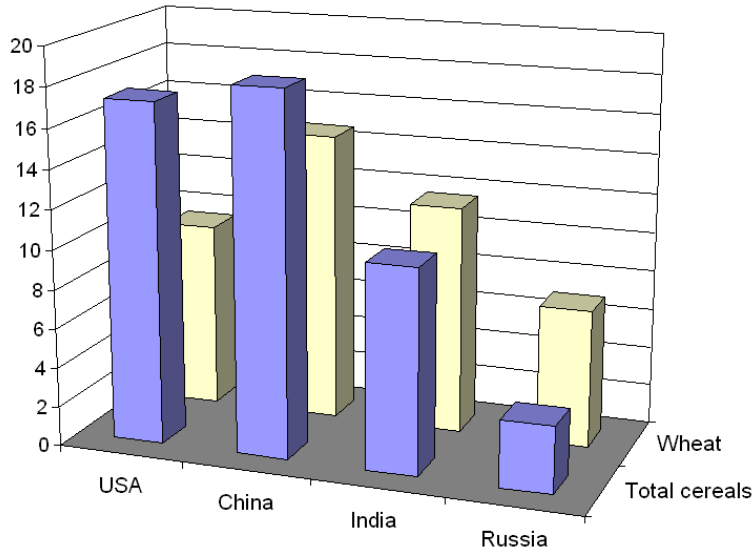

Figure 1-1. 2004 cereals production data, percentage of the global production in the four most productive countries. © FAO, 2005 (Bruno *et al.*, 2006).

Spatial resolution achievable from a geosynchronous orbit is quite poor compared to LEO satellites. For that reason, a SAR in a geosynchronous orbit cannot replace LEO satellites as it is not able to provide the same services. However, GeoSAR could be profitably employed in all those applications that require measurements with a short revisit time.

1.1.2 Literature review on Geosynchronous SAR

A geosynchronous orbit has a period of 23h and 56.08 min, equivalent to a sidereal day as measured with respect to the stars. This configuration can guarantee a very short revisit time. Within the area covered in every orbit, several mappings of the same region can be obtained allowing a very good temporal resolution. A single geosynchronous spacecraft cannot provide global coverage, this feature could be provided only by a constellation of satellites (at least 3).

The 24-hour period is extremely useful to understand transient phenomena that characterize the Earth. This orbit has not been used so far for radar remote sensing because of the complexities related to the large slant range. It requires a large antenna and a long integration time to focus a radar image (up to several hours for the passive bi-static configuration). The latter fact causes a quite strong influence of the atmosphere on the radar signal that cannot be neglected and that has to be taken into account in the design of such a system.

To obtain a synthetic aperture there should be a relative motion between the satellite and the terrain imaged. A geostationary orbit (a geosynchronous orbit with zero

eccentricity and zero inclination) is not acceptable for imaging purposes, as the satellite is stationary with respect to an observer on the Earth. On the contrary, an eccentric or inclined geosynchronous orbit can provide the required relative motion between radar and target. The orbit inclination has an important influence even on the coverage of the system. During the orbit, the most northern/southern latitude of the sub-satellite point is equal to the inclination of the orbit itself.

This section presents the relevant papers in literature that present concept and ideas directly related to a SAR system in a geo-synchronous orbit. A complete literature review that covers all aspects discussed in the present research has been included in Chapter 2.

Tomiyasu (1978) is the first who mentions the potential applications of SAR imaging from a geosynchronous orbit. The proposed orbit has an eccentricity of 0.009, 1° inclination angle and 90° argument of perigee.

Tomiyasu and Pacelli (1983) carried on the analysis performed by Tomiyasu himself some years before. They realised that a geosynchronous orbit with high inclination (about 50°) could provide a large coverage. The main consequence is that the relative velocity between the satellite and the imaged scene is greater and the integration time is smaller.

Tomiyasu and Pacelli (1983) highlight some important operational and design constraints of a SAR system:

- Areas cannot be imaged near the nadir point.
- Imaging at broadside (azimuth angle 90°) is more favourable than other oblique angles since the dwell time is shorter and the complexity of the range cell migration problem during data processing is smaller.
- The antenna size depends from ambiguity constraints.

Prati *et al.* (1998) is the first paper that describes a passive bi-static geosynchronous SAR. The system reuses the signal transmitted by an L band GEO Digital Audio Broadcasting system. The receiving antenna is placed in a slightly inclined orbit that generates a north-south wander (velocity 2 m/s) to create a synthetic aperture. The system is ambiguous in Doppler as the synthetic aperture is limited in length by the actual motion of the satellite. The paper provides some insights about the signal processing issues and provides a link budget to demonstrate the technical feasibility of this concept. Some key SAR parameters from this concept are included in Table 1-1, they are typical values for a bi-static geo-synchronous configuration.

Table 1-1. SAR parameters in the concept described by Prati *et al.* (1998).

Frequency	1.25 GHz
Synthetic Aperture Length	80 km
Interferometric Repeat Period	12 hours
Azimuth resolution	120 m
Signal Bandwidth	4 MHz
Integration time	8.3 hours
Antenna size	4.8 m
Pulse Repetition Interval	20 seconds
SNR	9.2 dB

Prati *et al.* (1998) provides some useful considerations that will be further investigated in this thesis:

- The link budget requires a very long integration time (i.e. about 8 hours).
- A passive bi-static SAR in a geosynchronous orbit has to be designed ambiguous in Doppler in order to achieve the longest possible integration time.
- Only objects that are stable during the integration time can be imaged. Sea, foliage screens and all moving objects will be virtually invisible to the system.
- Atmosphere monitoring on land is a promising field of application.

Madsen *et al.* (2001) gave the most important analysis up to date of an active geosynchronous SAR system as they focused on possible applications, the main performance parameters and system design considerations.

The three main advantages that a geosynchronous system can provide are: fine temporal resolution, very short revisit time and approximately daily global coverage. They specify that there is a wide range of possible applications for such a system:

- Fine temporal sampling can be exploited for disaster management with monitoring being conducted in near real time and data collected before and after events.
- Observations taken every few hours, correlated interferometrically, could provide near-real-time mapping of crustal processes and main surface changes caused by earthquakes or volcanoes.
- Monitoring vegetation and soil moisture could be important to understand the global carbon and hydrological cycles.

The concept presented in the next section has been widely derived by the work carried out by Madsen *et al.* (2001).

1.1.2.1 GESS (Global Earthquake Satellite System)

The concept GESS (Global Earthquake Satellite System), developed by NASA JPL, is the only concept described in detail in literature (NASA JPL, 2003). The main technical specifications are described in Table 1-2, SAR parameters provided are representative of the technical requirements for an active geo-synchronous SAR configuration.

Table 1-2. GESS satellite parameters (NASA JPL, 2003).

ORBIT	
Altitude	35788 km
Inclination	60°
Interferometric Repeat Period	1 day
Look angle	1.6° – 8°
Ground Incidence Angle	10.6 - 66.4°
Ground range From Nadir	1000-6500 km
Footprint Area	79 x 10^6 km^2
Sub-swath Width	400 km
INSTRUMENT	
Antenna Diameter	30 m
Electronic Steering	8° in azimuth and elevation
Wavelength	24 cm
Peak Transmit Power	60 kW
Pulse duration	1 ms
Bandwidth	10-80 MHz
Pulse Repetition Frequency	125-250 Hz
PERFORMANCE	
Ground range resolution	20 m
Nominal SNR	10 dB
Stripmap Azimuth resolution	2-20 m

NASA JPL has planned to develop a geosynchronous radar constellation to monitor earthquakes on a global scale. The ten satellites will be launched in five different 60° inclined orbits in order to achieve global coverage. Each one will carry an L band SAR. The main advantage of this configuration is that it can achieve global coverage and a very short revisit time nearly on the entire globe. Figure 1-2 shows that there is a constant coverage on the 23% of the globe (bright green) and only polar zones and some locations on the equator have a revisit time larger than two hours (red).

This is only a concept and it requires some new technologies to be developed especially in the field of large area antennas.

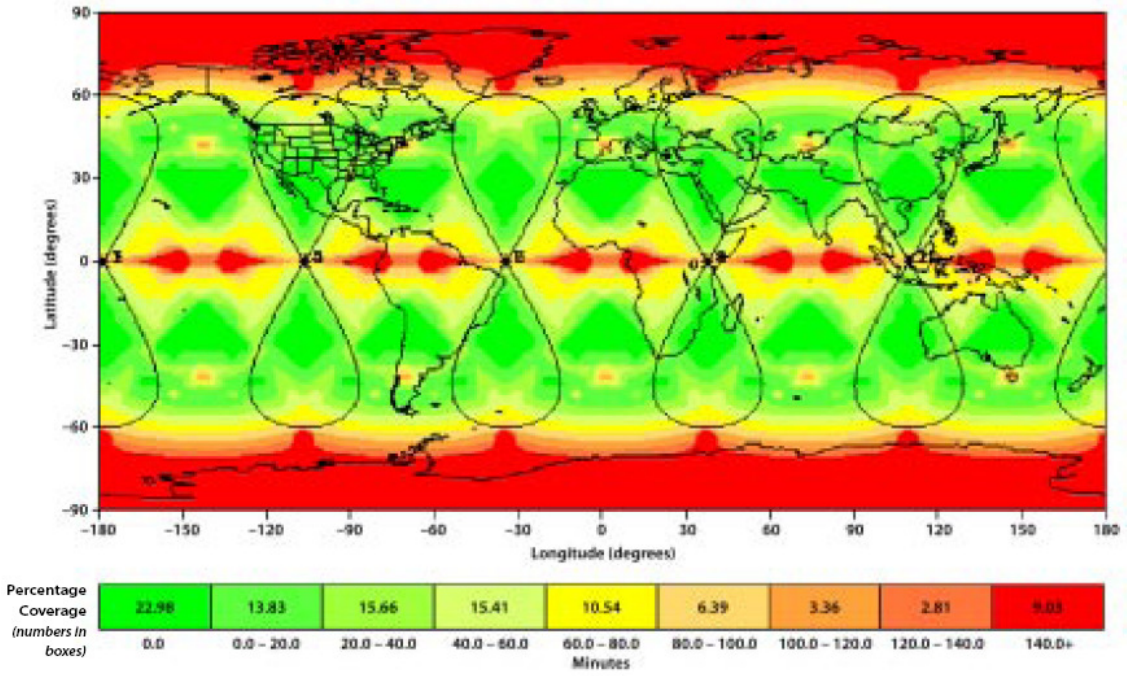

Figure 1-2. The maximum revisit time for a constellation of ten GEO satellites, five ground tracks, 12-hour phasing, at an inclination of 60° (NASA JPL, 2003).

NASA JPL (2003) stresses that the exact knowledge of atmospheric effects on SAR signal is a crucial issue to obtain significant results and achieve an accuracy in measuring crustal deformations as small as 1 mm/year.

1.2 Research aim

The foundation of this research builds on the background of this introductory overview; it is therefore possible to state the overall aim of the research:

> *The research aim is to make an innovative contribution to the analysis of the potential and the challenges related to a geosynchronous SAR satellite.*

1.3 Problem Formulation and Research Objectives

The literature review proposed has established the potential of geosynchronous SAR configurations and highlighted that in literature its technical challenges and its fields of application have not been analysed in detail. Therefore building on the literature review provided, the general problem formulation addressed in this study is:

> *Propose a geosynchronous SAR configuration, analyse quantitatively its performance and its limitations focussing on possible fields of application.*

This research presents a high degree of novelty as it addresses some problems that have been only marginally tackled in previous literature. To clarify the roadmap followed by this study three different objectives have been identified. For each of them a brief explanation has been included.

1. *Investigate both active and passive geosynchronous SAR configurations to choose a suitable system design.*

In particular, the choice of the system configuration has been justified through a quantitative and qualitative trade-off analysis.

2. *Analyse technical challenges and predict quantitatively system performances.*

Image formation has been identified as the main technical challenge of this configuration. The present research focuses on the analysis of factors such as Earth tides usually neglected in literature that however play a significant role in a geosynchronous SAR configuration.

3. *Emphasize possible field of applications.*

SAR interferometry and other applications that benefit from the short revisit time (such as soil moisture monitoring) are areas of possible scientific and industrial interest.

A brief introduction of the methodology used in this research is presented in the following section.

1.4 Overall Research Methodology

Starting from the problem formulation and the objectives defined, the block diagram in Figure 1-3 presents the overall research methodology that has been applied in the present research.

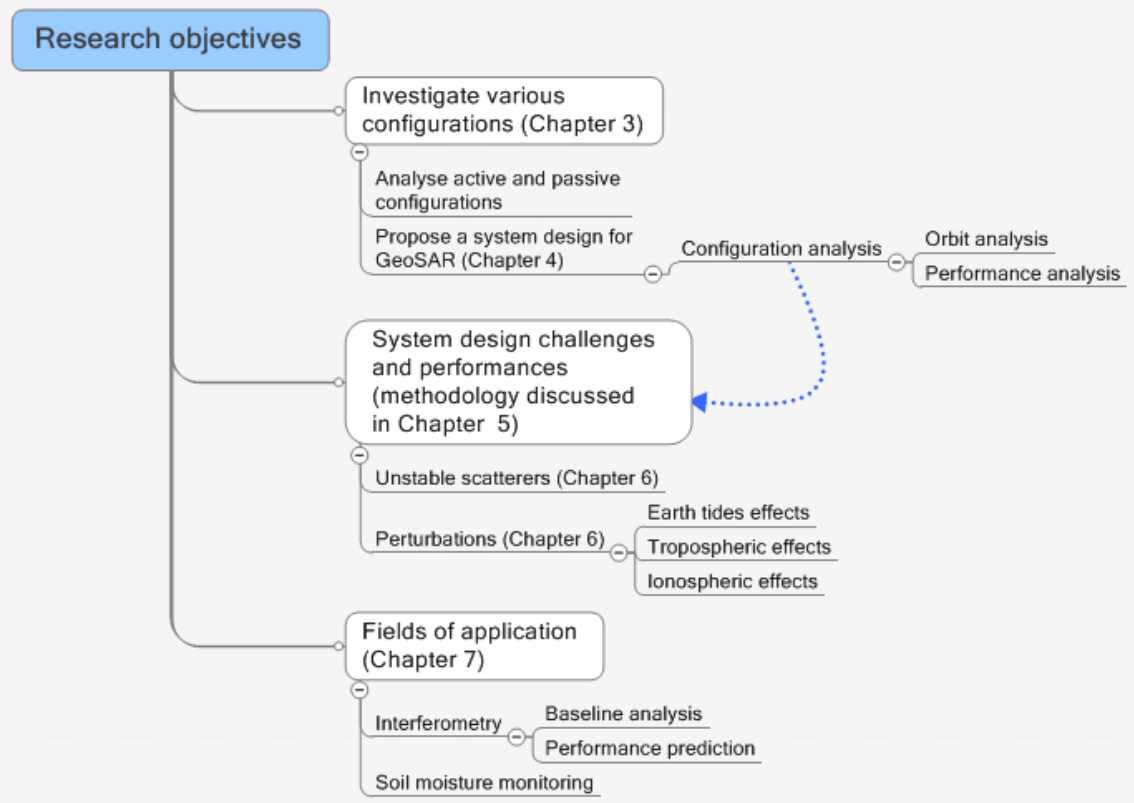

Figure 1-3. Overall research procedure.

1.5 Report Outline

Chapter 1, *Introduction*, outlines the background of the research and provides the reader with the geosynchronous SAR concept. It presents a literature review on geosynchronous SAR leading to the rationale of the research. This is followed by the definition of the research objectives. The chapter then clarifies the overall research procedure.

Chapter 2, *Background and objectives*, is mainly dedicated to space-borne SAR remote sensing. It first presents the imaging principles and then focuses on bi-static SAR configuration. The chapter introduces the main issues related to SAR processing and provides a background on signal atmospheric propagations and other perturbations such as Earth tides, tropospheric and ionospheric effects that affect GeoSAR focussing.

Chapter 3, *GeoSAR active and passive configuration*, is dedicated to the analysis of the two options for the system design of this concept. Both active and passive configurations have been investigated. A system trade-off has been carried out to choose the most suitable frequency. The outcome of this analysis is the proposal of a passive bi-static configuration as the most appropriate configuration.

Chapter 4, *GeoSAR concept*, provides further details and a basic performance analysis for GeoSAR, a concept for a bi-static passive geosynchronous SAR that has been developed at Cranfield Space Research Centre. A geo-location budget has been carried out to evaluate the accuracy of GeoSAR products.

Chapter 5, *SAR Azimuth Focussing Simulation,* outlines the methodology applied in the present research to study the effects of the long integration time on GeoSAR imaging. An azimuth SAR processor has been implemented in order to assess the effect of Gaussian white or correlated noise on GeoSAR azimuth Point Spread Function.

Chapter 6, *Presentation of results*, is dedicated to the analysis of the disturbances caused by fluctuating targets and an evaluation of the effects induced by Earth tides, tropospheric and ionospheric heterogeneities.

Chapter 7, *Applications*, focuses on GeoSAR's main fields of application. A quantitative analysis of InSAR performances has been carried out.

Chapter 8, *Conclusions and Further Work*, summarises the key points of the data analysis and discussions and presents areas of further development of the research.

2 Background

Having defined the rationale and the objectives of the research, this chapter will present the background relevant to the project. Section 2.1 is dedicated to a brief introduction to SAR remote sensing. Subsequent sections are dedicated to monostatic SAR (Section 2.2) and bi-static SAR (section 2.3). The physics related to SAR imaging are presented in section 2.4 (SAR image interpretation). Section 2.5 presents SAR interferometry describing the basic principles and introducing all the key concepts that provide the essential background to the analysis carried out in the chapter dealing with possible fields of applications. The notion of signal coherence is analysed in section 2.6 while the following section is dedicated to the principle of SAR image processing. Multi-static SAR configurations are discussed in section 2.8 while section 2.9 and the remaining part of the chapter present a literature review on Earth tides, tropospheric and ionospheric effects on SAR imaging.

These are all the key topics for the understanding of the research; however, a reader who already has a strong background in any of the areas might want to skip relative sections accordingly.

More specialist literature related to the methodology applied in the research will be presented in the relevant chapters.

2.1 Introduction to radars

Radar is an acronym that stands for RAdio Detection And Ranging. As an instrument, it has been developed as a means of using radio waves to detect the presence and the distance of objects. A specific class of radar systems is the imaging radar. It is commonly used in remote sensing. Radar imagery systems differ from optical ones as they provide their own means of illumination.

Referring to a general classification of imaging systems as that provided by Rees (2001), radar sensors are included among active systems, those "*who emit radiation and analyse what is sent back to them*".

Radar systems work in the microwave region of the electromagnetic spectrum, the one with frequencies in the range between 30 MHz and 300 GHz. The key concept in radar systems is that they emit a microwave pulse and detect its backscattered echo. The distance between the sensor and the target is obtained by measuring the time elapsed between the pulse transmission and the reception of the backscattered echo. Additional information about the target imaged can be inferred from the backscatter intensity and from the use of signals with different polarisations.

Imaging radar systems may be classified in two different categories: Real Aperture Radars (RAR) and Synthetic Aperture Radars (SAR). The former are even known as non-coherent radars. As RAR are not commonly used in space application, in this chapter only SAR systems will be described as they provide an indispensable background to understanding geosynchronous SAR.

Radar can be classified as monostatic or bi-static. In the former, the signal backscattered is collected by the transmitting antenna; in the latter, there is a separate antenna that collects the reflected signal. Monostatic SARs are discussed in section 2.2 while bi-static SAR peculiarities are presented in section 2.3.

2.2 Monostatic SAR

Monostatic SAR is the most common configuration. Figure 2-1 describes the typical space-borne monostatic SAR geometry; the direction of the emitted radiation is side looking with respect to the satellite's direction of travel, also known as along-track or azimuth. The antenna is flying with a velocity v_{sat}, looking at an incidence angle θ, and it repeatedly radiates radio pulses of duration τ_p at a rate defined by the Pulse Repetition Frequency (PRF). The antenna is of length L and height D and mounted on a platform at an altitude H_{sat}. θ_r and θ_a are the pulse beam-width respectively in range and in azimuth.

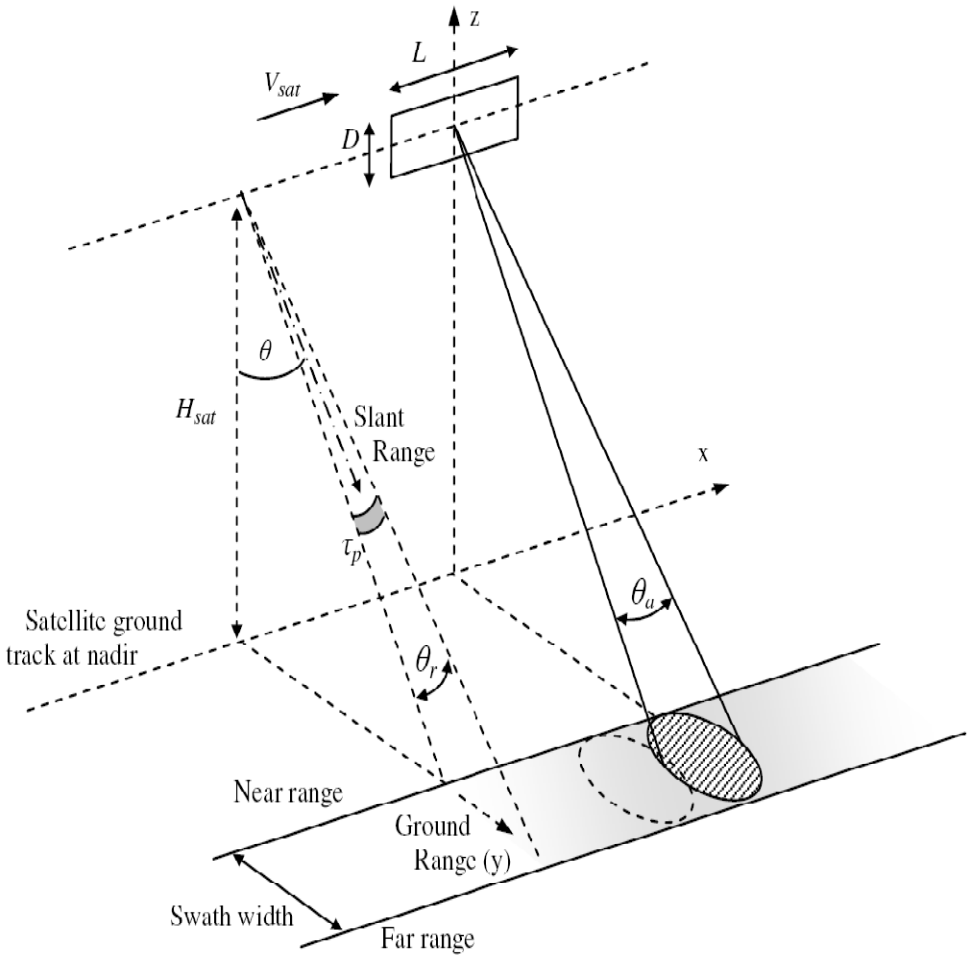

Figure 2-1. SAR geometry and system parameters. (Ottavianelli, 2007).

2.2.1 Range resolution

In all radar systems, both RAR and SAR, range resolution is directly related to the pulse length of the transmitted signal and is independent of the satellite height. The slant range resolution is fixed by the pulse duration τ. Two individual scatterers can be distinguished if their backscatters are received at different range gates of duration τ. The expression for range resolution ΔR_{range} is presented in Equation 2-1 (Hanssen, 2001).

$$\Delta R_{range} = \frac{c}{2B_R} \qquad \text{Equation 2-1}$$

In Equation 2-1, c is the speed of light;
B_R is the radar pulse bandwidth.

A larger bandwidth pulse will result in a higher resolution in range direction. A significant improvement can be achieved using a pulse or chirp compression technique. The frequency of the pulse is varied linearly (FM, Frequency Modulation) to increase the bandwidth of the signal.

The pulse sinusoidal waveform can be written in its complex form as in Equation 2-2 (Hanssen, 2001).

$$s(t) = g(t)e^{j2\pi f_0 t} \quad \text{Equation 2-2}$$

In Equation 2-2, $s(t)$ is the pulse waveform;
$g(t)$ is the initial signal, a square wave of duration τ, repeated at a given PRF;
f_0 is the carrier frequency.

If the frequency of the pulse is linearly increased (FM modulation) with slope s as in Equation 2-3 and the carrier frequency is f_0:

$$f(t) = f_0 + st \quad \text{Equation 2-3}$$

Then the pulse wave equation (Equation 2-2) can be written in the form:

$$s(t) = g(t)e^{j2\pi f(t)} = g(t)e^{j2\pi f_0 t}e^{j2\pi st^2} \quad \text{Equation 2-4}$$

The bandwidth of the range signal is expressed by Equation 2-5 (Hanssen, 2001).

$$B_R = s\tau \quad \text{Equation 2-5}$$

2.2.2 Resolution in azimuth

The physical dimensions of the antenna determine resolution in azimuth for real aperture radar. The diffraction limit will normally mean that the ground resolution of the antenna is ΔR_{az} for far-field approximation (Equation 2-6; Rees, 2001).

$$\Delta R_{az} = \frac{\lambda R}{D} \quad \text{Equation 2-6}$$

In Equation 2-6, λ is the wavelength of the pulse;
D is the length of the antenna aperture;

R is the slant range from the antenna to the target.

The azimuth (i.e. along-track) ground resolution ΔR_{az} is inversely proportional to the physical length of the antenna D and proportional to the slant range R. To obtain a reasonable ground azimuth resolution using a space-borne RAR the antenna needs unfeasible physical dimensions; hence, those systems are not currently used in space applications. This problem has been overcome in SAR systems developing the so-called "*synthetic aperture*".

2.2.3 The synthetic aperture

Synthetic aperture systems can generate a very small effective beam width by detecting Doppler frequency shifts. A Doppler shift is a change in the wave frequency caused by the relative velocity between the source of the signal and the receiver.

Within the antenna azimuth beam, it is possible to discriminate between areas behind the nadir point of the satellite that will experience a downshift in frequency and regions ahead of the satellite whose frequencies will result up shifted (Figure 2-2). Only a very small area at the centre of the beam width will not experience any frequency shifts. This is called region of zero Doppler shift (Lillesand and Kiefer, 2000).

Carl Wiley of the Hughes Aircraft Company (Wiley, 1954) first explained how the motion of the platform with advanced signal processing could be used to synthesise a much longer antenna.

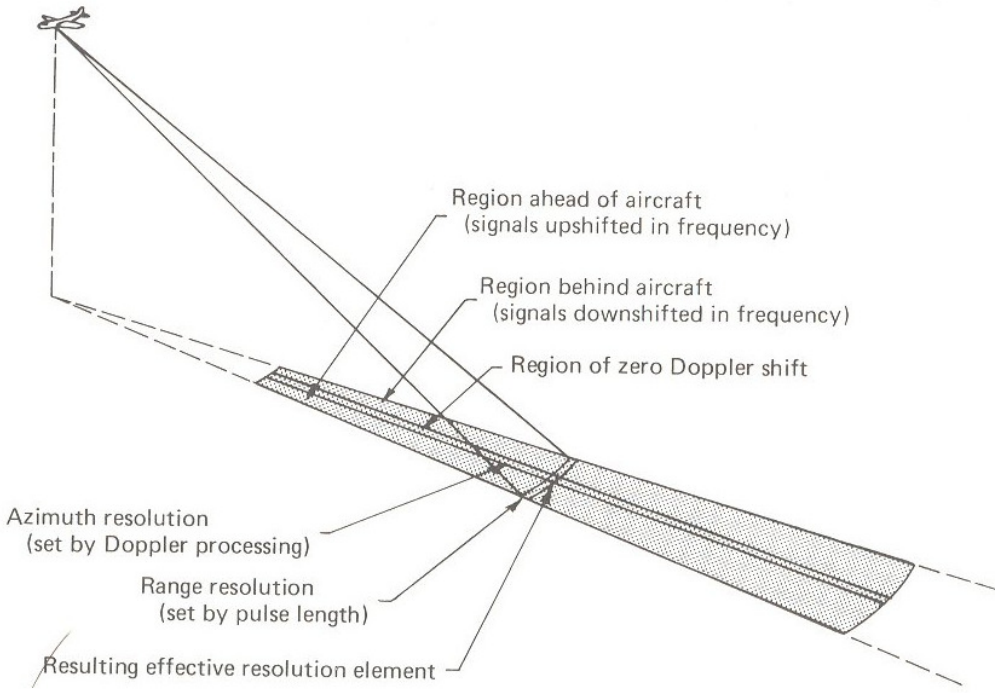

Figure 2-2. Different areas of Doppler shift in the azimuth beam of a side-looking SAR antenna. (Lillesand and Kiefer, 2000).

The Doppler frequency f_D in the SAR case is illustrated in Equation 2-7 (Hanssen, 2001).

$$f_D = \frac{2v_{sc}}{\lambda}\sin\theta \qquad \text{Equation 2-7}$$

In Equation 2-7, v_{sc} is the flight velocity of the spacecraft;
θ is the look angle (it is required because only the velocity component along the slant range direction produces a Doppler shift).

The angle θ can be referred to a specific y coordinate along the azimuth direction using Equation 2-8, thus Doppler frequency f_D is expressed by Equation 2-9 (Hanssen, 2001).

$$\sin\theta = \frac{y}{R} \qquad \text{Equation 2-8}$$

$$f_D = \frac{2v_{sc}\,y}{\lambda R} \qquad \text{Equation 2-9}$$

Differentiating Equation 2-9, azimuth resolution ΔR_{az} can be calculated as a function of the Doppler frequency resolution Δf_D (Equation 2-10).

$$\Delta R_{az} = \left[\frac{\lambda R}{2 v_{sc}} \right] \Delta f_D \qquad \text{Equation 2-10}$$

Δf_D is the inverse of the radar integration time (T_{int}), i.e. the time for which the target is within the beam of the radar (Hanssen, 2001).

$$\Delta f_D = \frac{1}{T_{\text{int}}} \qquad \text{Equation 2-11}$$

$$T_{obs} = \frac{R\lambda}{D v_{sc}} \qquad \text{Equation 2-12}$$

The synthetic aperture is defined as the distance flown by the antenna with the target inside its main lobe. Its value corresponds to the projection on the Earth's surface of the main lobe as in Equation 2-13.

$$L_A = \frac{R\lambda}{D} = T_{obs} v_{sc} \qquad \text{Equation 2-13}$$

Substituting Equation 2-11 and Equation 2-12 in Equation 2-10 the new expression for ΔR_{az} is:

$$\Delta R_{az} = \frac{\lambda R}{2 v_{sc}} \times \frac{D v_{sc}}{\lambda R} = \frac{D}{2} \qquad \text{Equation 2-14}$$

The variation of the Doppler frequency during the passage of the scatterer through the beam is expressed by the Doppler bandwidth B_D (Hanssen, 2001).

$$B_D = \frac{2\theta_a v_{sc}}{\lambda} \qquad \text{Equation 2-15}$$

Therefore, considering Equation 2-10, azimuth resolution can also be expressed using Equation 2-16 (Hanssen, 2001).

$$\Delta R_{az} = \frac{v_{sc}}{B_D} = \frac{v_{sc}\lambda}{2\theta_a v_{sc}} = \frac{D}{2} \qquad \text{Equation 2-16}$$

It is important to notice that the system Pulse Repetition Frequency (PRF) has to be able to sample the Doppler bandwidth. This implies that an improvement in the azimuth

resolution requires a faster sampling and a consequent larger amount of data to be processed on board.

The equations discussed in this section are based on the assumption that the velocity of the transmitter is constant and is along a straight path. If the radar antenna is moving with variable velocity (or following a curved path), pulse-to-pulse phase compensation should be applied.

To achieve the best azimuth resolution the full Doppler spectrum available should be used to process signal entering from the whole SAR antenna beam width. However, a shorter synthetic antenna (i.e. a shorter integration time) could be used if a coarser resolution (with more frequent images) is wanted.

In this case the bandwidth of the Doppler signal, given Equation 2-11, is reduced according to the chosen value of the integration time T_{int}. Azimuth resolution is degraded proportionally to the ratio between the maximum achievable synthetic aperture (i.e. Doppler bandwidth) and the actual one.

2.2.4 Monostatic radar equation

The power density at a slant range *R* away from the radar (assuming a lossless medium) is presented in Equation 2-17:

$$P_R = \frac{P_T G}{4\pi R^2} \qquad \text{Equation 2-17}$$

In Equation 2-17, P_T is the transmitted power (W);
P_R is the received power at the slant range *R* (Wm^{-2});

The power received at the antenna P_{DR}(monostatic case) is:

$$P_{DR} = \frac{P_T G \sigma}{\left(4\pi R^2\right)^2} A_e = \frac{P_T G^2 \lambda^2 \sigma}{\left(4\pi\right)^3 R^4} \qquad \text{Equation 2-18}$$

In Equation 2-18, A_e is the effective antenna area;
σ is the radar cross section.

Thermal noise that enters an antenna is proportional to the system bandwidth.

$$N_i = kTB \qquad \text{Equation 2-19}$$

In Equation 2-19, k is the Boltzmann constant (JK^{-1});
T is the noise temperature (K);
B is the system bandwidth (Hz).

Considering other system losses including multipath, *L* and the noise figure *F*, the system Signal to Noise Ratio (SNR) may be expressed as (Skolnik, 1990):

$$SNR = \frac{P_T G^2 \lambda^2 \sigma}{(4\pi)^3 kT\ B\ F\ L\ R^4} \qquad \text{Equation 2-20}$$

The radar cross section is a function of the size of the radar ground resolution cell, the terrain reflectivity σ^0 and the radar incidence angle θ.

$$\sigma = \sigma^0 \Delta R_{range} \Delta R_{az} \sin\theta \qquad \text{Equation 2-21}$$

Following Equation 2-21, the expression of the SNR_1 for a single pulse is:

$$SNR_1 = \frac{P_t G^2 \lambda^2 \sigma^0 \Delta R_{az} \Delta R_{range} \sin\theta}{(4\pi)^3 R^4 kT\ B\ F}; \qquad \text{Equation 2-22}$$

Following the math provided by Skolnik (1990), in pulse compression radar, SNR improvement can be obtained increasing the ratio between the uncompressed pulse length τ_i and the compressed pulse length τ_0 as presented in section 2.2.1.

In a SAR there is an integration gain due to the generation of a synthetic antenna, this is due to the coherent integration of a number of pulses. The number of pulses integrated is equal to the product of the pulse repetition frequency (PRF) and the integration time (i.e. the time lapse necessary to generate the synthetic antenna).

$$\text{Improvement factor} = \left[\frac{\tau_i}{\tau_0}\right] \frac{PRF\ L}{v} = \left[\frac{\tau_i}{\tau_0}\right] \frac{PRF\ R\lambda}{2\Delta R_{az} v} \qquad \text{Equation 2-23}$$

$$SNR_{Ns} = \frac{P_t G^2 \lambda^3 \sigma_0 \Delta R_{range} T_{\text{int}} \sin\theta}{2(4\pi)^3 R^3\ kTB\ F} \frac{\tau_i}{\tau_0} \frac{PRF}{L} \qquad \text{Equation 2-24}$$

In Equation 2-24, T_{int} is the integration time;
L is the synthetic aperture;
θ is the ground incidence angle.

Equation 2-24 implies that SNR is independent of the along-track resolution. However, the power budget is driven by the range resolution ΔR_{range}.

The average power P_{avg} is a parameter much more interesting than peak power in order to size the system. The relation between peak and average power is presented in Equation 2-25 where τ_p is the radar pulse length.

$$P_t = \frac{P_{avg}}{\tau_p PRF}$$ Equation 2-25

The bandwidth of the signal B is related to pulse duration. However, pulse compression is usually implemented in SAR systems to achieve a shorter theoretic pulse length.

$$B = \frac{1}{\tau_p}$$ Equation 2-26

Skolnik (1990) provides the final expression for integrated SNR:

$$SNR_{Ns} = \frac{P_{av}}{8\pi} \frac{A_e^2 \sigma_0 \Delta R_{range}}{kT_0 F R^3 \lambda} \frac{\sin\theta}{v}$$ Equation 2-27

Substituting the effective area of the receiver antenna (A_e) to the expression of the gain and solving with respect to P_{avg}:

$$P_{avg} = \frac{SNR_{Ns} 8\pi R^3 kTF \lambda v}{A_e{}^2 \sigma_0 \Delta R_{range} \sin\theta}$$ Equation 2-28

The relations obtained in this section will be used in the preliminary design of a geosynchronous SAR system.

2.3 Bi-static SAR

Willis (1991) and Cherniakov (2008) in their textbooks regarding bi-static radar provide a thorough review of bi-static radar equations. This section highlights the main peculiarities of bi-static SARs that will be relevant in the present research.

2.3.1 Range resolution

Conventional radars are able to discriminate echoes at the receiver that are separated by a distance $c\tau/2$. In bi-static radars, iso-range lines are spaced by the distance $c\tau/[2\cos(\beta/2)]$ (Willis, 1991) where β is the bi-static angle. This implies that slant range resolution is affected by the bi-static angle.

$$\Delta R_{range} = \frac{c\tau}{2\cos\left(\beta/2\right)}$$ Equation 2-29

In bi-static radars slant range resolution varies with the location of the satellites as it is a function of the bi-static angle.

The bi-static angle significantly affects radar backscatter that could differ significantly from the mono-static radar backscatter in presence of a large bi-static angle (Willis, 1991). Configurations where the radar slant range is comparable with the distance between transmitter and receiver are also known as quasi-monostatic.

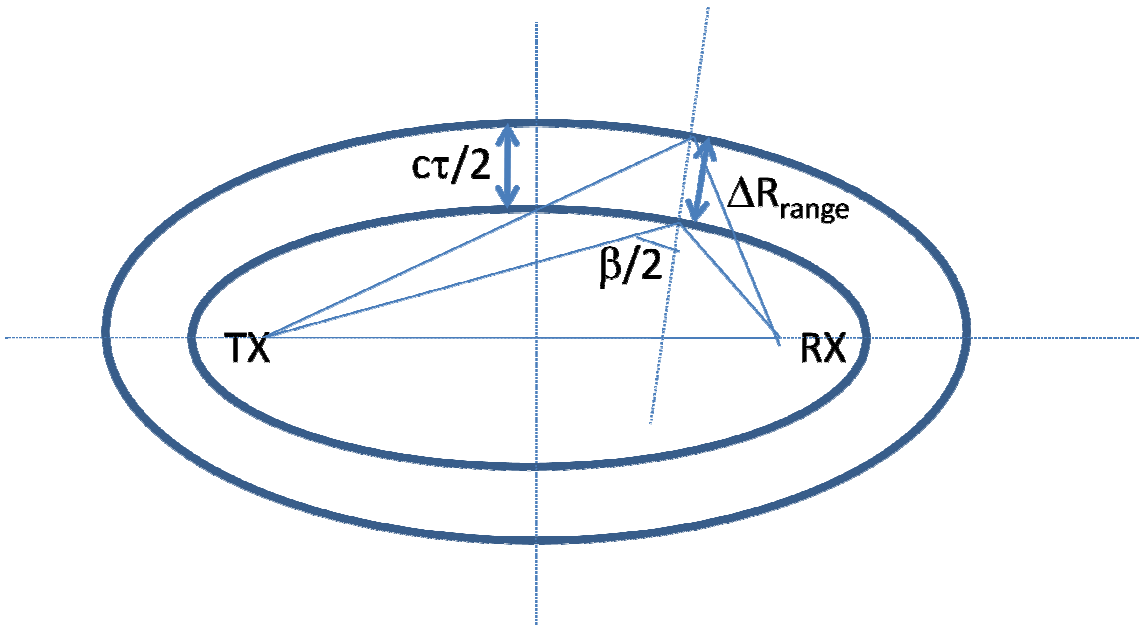

Figure 2-3. Two iso-range ovals with the indication of the position of the transmitter (TX), the receiver (RX) and the half bi-static angle β/2 and range resolution ΔR_{range}.

2.3.2 Doppler relationships

Bi-static Doppler shift is the time rate of change of the total path length of the scattered signal (Equation 2-30):

$$B_D = \frac{1}{\lambda}\left(\frac{dR_T}{dt} + \frac{dR_R}{dt}\right) \qquad \text{Equation 2-30}$$

In Equation 2-30, R_T is the slant range from the target to the transmitter;
R_R is the slant range from the target to the receiver.

When the transmitter is stationary, as in the ideal cases considered by Tomiyasu (1978), Tomiyasu and Pacelli (1983) and Prati *et al.* (1998), the effective Doppler

bandwidth is half the value that can be achieved with monostatic SAR. This case has further implications such as doubling azimuth resolution ΔR_{az}.

Doppler bandwidth B_D for a satellite moving at a velocity v_{sc} collecting the signal of a static transmitter is given in Equation 2-31. As expected, it is half the value achievable for monostatic radar (Equation 2-9).

$$B_D = \frac{v_{sc}}{\lambda} \qquad \text{Equation 2-31}$$

In bi-static radars, both transmitter and receiver contribute to generate a Doppler bandwidth.

In a bi-static SAR, azimuth resolution (Willis, 1991) can be expressed as:

$$\Delta R_{az} = \frac{\lambda R}{v_{sc}} \frac{1}{T_{obs} \cos \beta/2} = \frac{\lambda R}{L_A} \frac{1}{\cos \beta/2} = \frac{v_{sc}}{B_D} \frac{1}{\cos \beta/2} \qquad \text{Equation 2-32}$$

In a bi-static SAR, the synthetic aperture is unchanged, but a given length only achieves twice the spatial resolution (in metres) of the monostatic case.

2.3.3 Bi-static radar equation

For bi-static radar, the link budget can be derived in a manner completely analogous to that presented for monostatic radar (Equation 2-17 and those following). The range term R^4 becomes $R_T^2 R_R^2$ to take into account that the distance from the target to the transmitter R_T might be different from the range from the target to the receiver R_R.

$$SNR \propto \frac{1}{R_T^2 R_R^2} \qquad \text{Equation 2-33}$$

According to Equation 2-33 (Willis, 1991) iso-SNR lines describe a family of curves called ovals of Cassini, that is the locus of the vertex of a triangle when the product of the sides adjacent to the vertex is constant and the length of the opposite side is fixed.

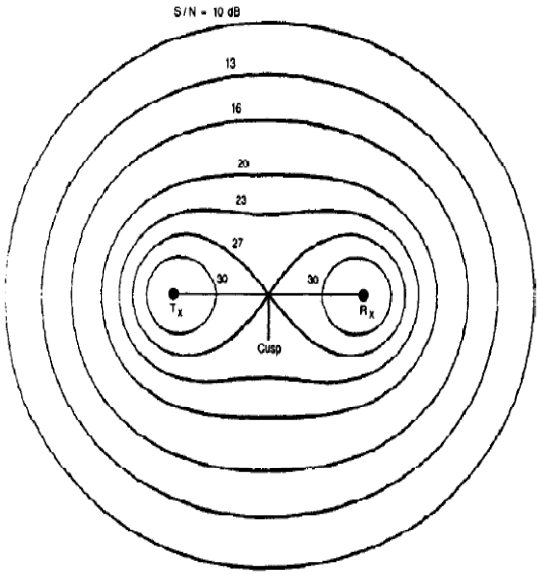

Figure 2-4. Contours of constant SNR – ovals of Cassini (Willis, 1999)

2.4 SAR image interpretation

Figure 2-5 shows an example of a SAR amplitude image (Ottavianelli, 2007). These measured values represent the effects of the target on the transmitted wave. Through an absolute radiometric calibration, they can be translated into the geophysical properties of the scene. The calibration procedure also allows data from different SAR sensors to be compared.

2.4.1 Geometric Distortion

A radar image is composed of pixels that represent the backscatter of radar pulses. Each pixel is discriminated by considering the time when its backscatter reaches the receiver. For a vertical structure such as a mountain, the pulse return from the top of the structure may reach the antenna earlier than the backscatter from the base. This will cause an effect very evident in radar images; the vertical feature imaged "layovers" and appears to lean towards the satellite nadir (feature A and B in Figure 2-6). "*This effect occurs when the terrain slope is steeper than a line perpendicular to the direction of the radar pulse, expressed by the look angle*" (Lillesand and Kiefer, 2000). The amount of layover is obviously greater at near range where the look angle is smaller.

"*The phenomenon of radar shadow is even influenced by the look angle and by the slope of the terrain. Slopes facing away from the radar antenna will return weak signals*

or no signal at all" (Lillesand and Kiefer, 2000). The first case (represented in feature A) occurs when the surface is facing away but its slope is less steep than the pulse direction. If the slope is steeper than the pulse direction than there is no backscatter at all and the area will be completely dark in the image (features B, C, D). It is easy to observe that shadow length increases with range as the look angle increases too.

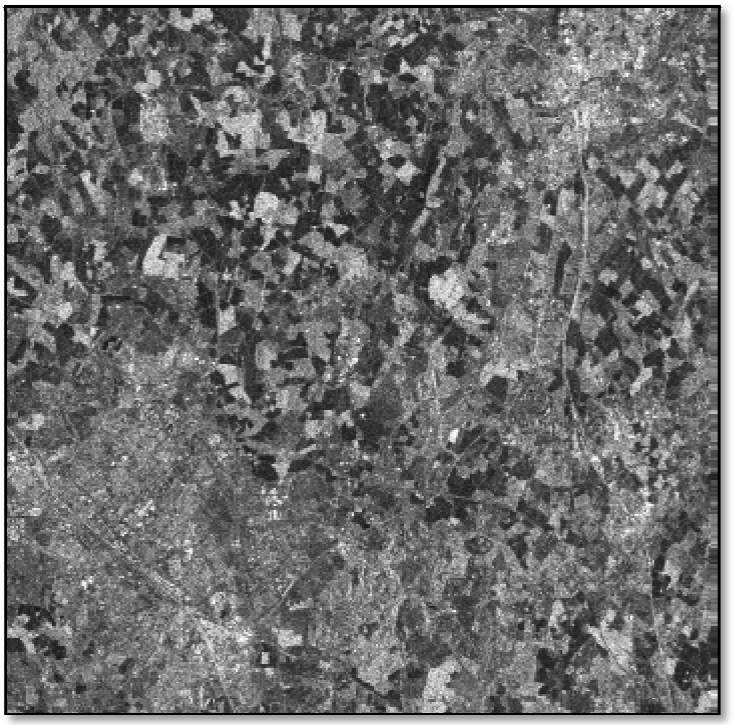

Figure 2-5. ESA ERS-1 SAR backscattered amplitude values. The scene was acquired on 25th June 1995 (descending orbit: 20623; track: 94; frame: 2547). The SAR look angle is from right to left. The image shows a 30 by 30 km area centred on Cranfield University. It is possible to identify the University runways as three crossing dark lines. The cities of Milton Keynes and Bedford are identifiable by the brighter backscatter return. They are located respectively in the bottom left and the top right of the image. The original scene has been flipped horizontally and spatially averaged by five pixels in the azimuth direction to eliminate the ground resolution distortion. (Ottavianelli, 2007).

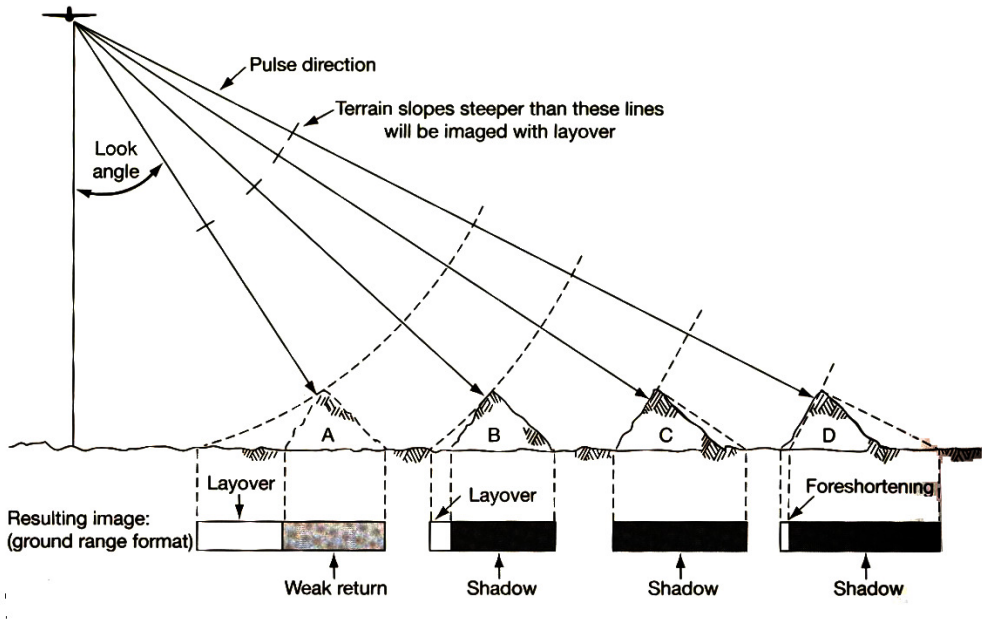

Figure 2-6. Effects of terrain relief on side-looking radar images. Feature (A) illustrates layover effect; features (B), (C) and (D) describe the shadow effect; feature (D) describes the foreshortening effect. (Lillesand and Kiefer, 2000).

When the slope facing the antenna is less steep than the line perpendicular to the look angle, layover does not occur (feature D in Figure 2-6) as the response of the base arrives to the antenna earlier than that of the top of the structure. In this case, many areas of the slope appear to have the same distance from the spacecraft. The receiver collects all the backscattered echoes at the same time and interprets them as a small area with a very high backscatter instead of detecting a large area with a smaller backscatter. This effect is called foreshortening. In feature C the front slope is perpendicular to the look angle and it has been foreshortened to zero length.

2.4.2 SAR image backscatter

For introducing the concept of radar backscatter, the radar equation, the relation between radar characteristics, the target and the signal, have to be discussed. Ulaby *et al.* (1986) provide a thorough description of image backscatter and of its properties. The monostatic radar equation has already been discussed in section 2.2.4. This section will recall the expression of the power received by the antenna in order to focus on the influence of target backscatter.

If the antenna of a radar transmits a power P_t with gain G_t the power per unit area incident on a scatterer at a distance R_T is:

$$P_R = P_t G_t \frac{1}{4\pi R_T{}^2} \qquad \text{Equation 2-34}$$

The power effectively intercepted is a function of the effective area of the scatterer (A_{rs}).

$$P_{Rs} = P_R A_{rs} \qquad \text{Equation 2-35}$$

In Equation 2-35, A_{rs} is the effective receiving area of the scatterer (m^2);
P_R is the incident power per unit area (W/m^2).

A scatterer absorbs or transmits a fraction f_a of the impinging power and reflects a portion (1- f_a) of it. Moreover, the signal reflected from the scatterer is characterised by a gain factor G_{ts} in direction of the receiver. The receiver is at a distance R_R from the target and its antenna area is *Ar*.

$$P_{Rs} = \left[\frac{P_t G_t A_r}{(4\pi)^2 R_T^2 R_R^2} \right] \left[A_{rs} (1 - f_a) G_{ts} \right] \qquad \text{Equation 2-36}$$

In Equation 2-36, f_a is the fraction of power absorbed or transmitted by the scatterer;
G_{ts} is the gain of the scatterer in the direction of the receiver;
A_{rs} is the effective aperture of the receiving antenna.

The factors associated with the scatterer could be combined into a single factor, the radar scattering cross-section σ:

$$\sigma = A_{rs} (1 - f_a) G_{rs} \qquad \text{Equation 2-37}$$

The basic scattering model for an area on the ground is based on the assumption that it consists of many scattering targets. Taking into account the amount of power retransmitted from every single scatterer, Equation 2-36 can be generalised in the form:

$$P_r = \frac{\lambda^2}{(4\pi)^3} \sum_{i=1}^{N} \frac{P_{ti} G_i{}^2 \sigma_i}{R_{Ti}^2 R_{Ri}^2} \qquad \text{Equation 2-38}$$

In Equation 2-38, R_{Ti} is the slant range from the transmitter to the i^{th} target;
R_{Ri} is the slant range from the i^{th} target to the receiver;
σ_i is the radar cross section for the i^{th} scatterer.

Defining the differential scattering coefficient σ^0 as the average value of the scattering cross-section per unit area (Equation 2-39):

$$\sigma^0 = \left\langle \frac{\sigma_i}{\Delta A_i} \right\rangle \qquad \text{Equation 2-39}$$

Using the value σ^0 and substituting the summation with an integral over the illuminated area A_I:

$$P_r = \frac{\lambda^2}{(4\pi)^3} \int_{A_I} \frac{P_t G^2 \sigma^0}{R_T^2 R_R^2} dA \qquad \text{Equation 2-40}$$

Equation 2-40 applies under the following assumptions:

- Many point scatterers exist in a region over which the parameters P_t, G and R could be considered constant.
- Many more scatterers exist in the total illuminated area at any instant.

Equation 2-40 is used to estimate the backscattering coefficient σ.

With a full knowledge of the antenna pattern, it is possible to determine the weighted area A_w that takes into account the gain variation inside the beam.

$$G_0^2 A_w = \int_{Beam} G^2 dA \qquad \text{Equation 2-41}$$

Hence, the expression for σ^0 is approximated as:

$$\sigma^0 \approx \frac{(4\pi)^3 R_T^2 R_R^2}{G_0{}^2 \lambda^2 A_w} \left(\frac{P_r}{P_t} \right) \qquad \text{Equation 2-42}$$

If the illuminated area is replaced by the area perpendicular to the slant range direction (i.e. $A\cos\theta$), a different scattering coefficient γ is usually considered.

$$\sigma^0 = \gamma \cos\theta \qquad \text{Equation 2-43}$$

2.4.3 Nature of surface scattering

The amplitude of the signal received by the receiving antenna is a measure of the backscatter of the target area. Generally, the backscatter increases with the roughness of the surface. The Rayleigh criterion is used to determine if a surface could be considered smooth.

"*They act as a specular reflector (i.e. flat landscapes or calm water surfaces) when their rms height variation is less than approximately λ/8 (λ is the wavelength of the radar wave) divided by the cosine of the local incident angle; such surfaces reflect most of the energy away from the sensor, resulting in a very low return signal"* (Lillesand and Kiefer, 2000).

The backscattering properties of a surface are a function of the incident wavelength. In Figure 2-7 the properties of four sample surfaces at two different frequencies are described.

Urban areas have a very typical aspect in radar images due to the geometric shapes present in their landscape. Buildings usually have an angular construction that, if surrounded by smooth surfaces, causes a double reflection of the radar wave. The main effect is a very high backscatter that usually appears as a bright spot on the image. In some experiments, corner reflectors have been used in order to generate correlation with existing maps to obtain a precise geo-location of the radar scene. It is important to point out that they cannot provide an accurate reference as the high backscattering zone in the scene is usually larger than the real physical dimensions of the object.

A simplified sketch with the reflections of three sample landscapes is presented in *Figure 2-8*. A rough surface shows usually diffuse reflection; specular reflection is obtained when water surfaces are imaged; an isolated building is a common sample for a corner reflector.

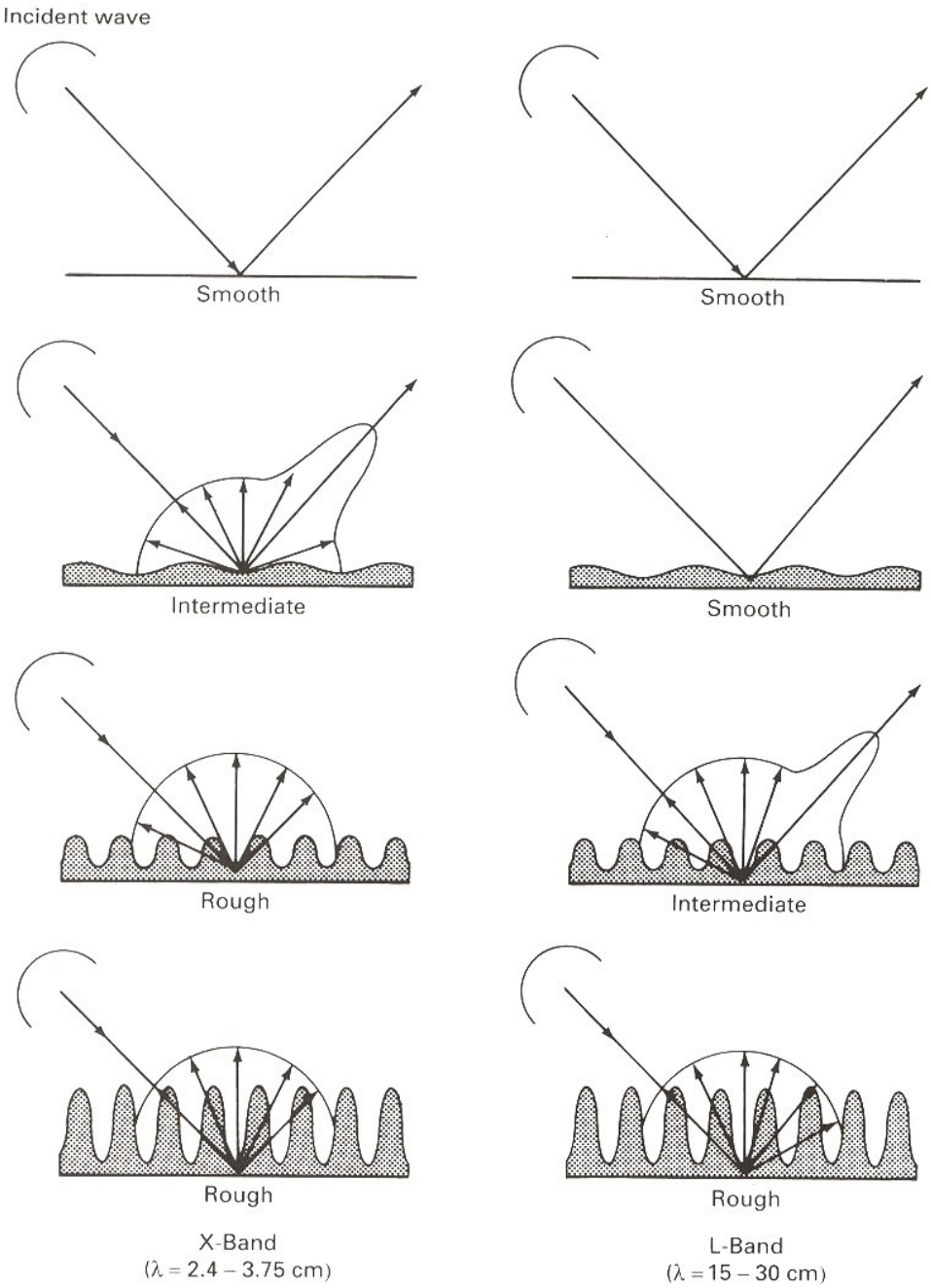

Figure 2-7. Radar reflections from various surfaces with different roughness at two frequencies, X band and L band. (Lillesand and Kiefer, 2000).

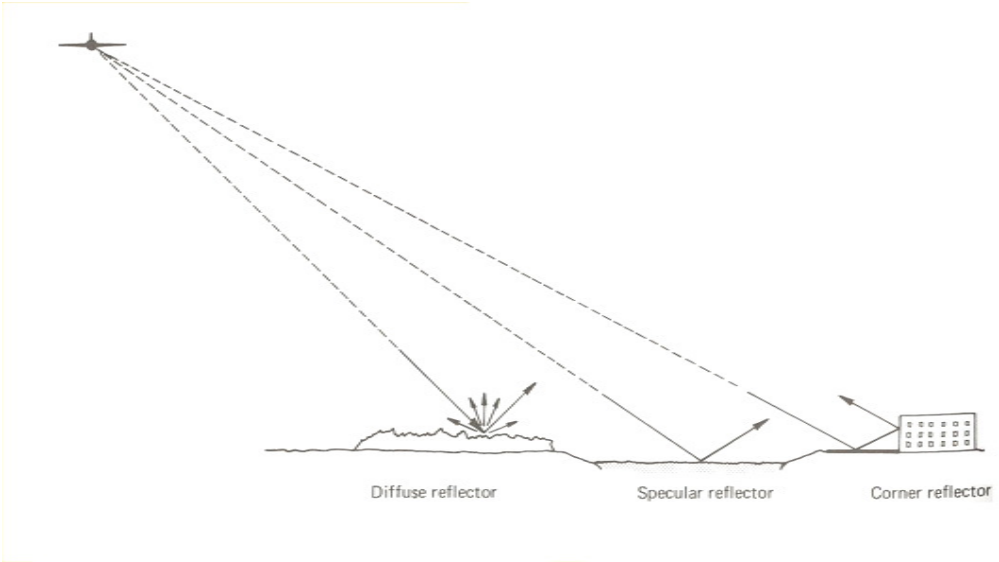

Figure 2-8. Backscatter properties of three different landscapes imaged. (Lillesand and Kiefer, 2000).

Surface scattering is connected to the roughness of the surface. The angular radiation pattern of a generic surface is made of two different components: a reflected component (or coherent scattering component) and a diffuse scattering component (or non-coherent). For an ideal specular surface (at the operational wavelength), all the energy is coherently scattered and the backscattered coefficient is virtually zero. For a slightly rough surface there is a major fraction of the energy that is reflected coherently while a minor part is diffused incoherently in all the directions; this implies a backscattering coefficient greater than zero. Finally, a very rough surface is characterised by a radiation pattern that is approximately Lambertian and for which the backscattering coefficient (Ulaby *et al.* 1986) varies as the factor $cos\theta^2$.

The two fundamental parameters that are generally used to characterise the roughness of a surface are: the standard deviation of the height variation and the surface correlation length.

Given a rectangular surface with geometric dimensions L_x and L_y, the mean height of the surface is defined in Equation 2-44.

$$\overline{z} = \frac{1}{L_x L_y} \int_{-L_x/2}^{L_x/2} \int_{-L_y/2}^{L_y/2} z(x,y)\,dxdy \qquad \text{Equation 2-44}$$

The second moment is given in Equation 2-45 (Ulaby *et al.* 1986).

$$mean(z^2) = \frac{1}{L_x L_y} \int_{-L_x/2}^{L_x/2} \int_{-L_y/2}^{L_y/2} z^2(x,y)\,dxdy \qquad \text{Equation 2-45}$$

The standard deviation of the surface height is defined in Equation 2-46.

$$\sigma = \left[mean\left(z^2\right) - \overline{z}^2 \right]^{1/2} \qquad \text{Equation 2-46}$$

The deviation from the mean is given by Equation 2-47.

$$z' = z - \overline{z} \qquad \text{Equation 2-47}$$

The normalised autocorrelation length is the second parameter involved in the definition of the degree of roughness of a given surface. It provides a reference for estimating the statistical independence of two points on the surface. For a 1D profile the correlation function is defined in Equation 2-48.

$$\rho\left(x'\right) = \frac{\int_{-L_x/2}^{L_x/2} z'(x)\, z'(x+x')\, dx}{\int_{-L_x/2}^{L_x/2} z'(x)^2\, dx} \qquad \text{Equation 2-48}$$

The correlation length is the displacement *x'* for which the correlation function has the value *1/e*.

2.4.4 Criteria for smoothness

A surface may appear rough or smooth depending on the wavelength of the incident electromagnetic energy. The criteria that define smoothness are a function of the wavelength.

The Rayleigh criterion may be expressed as:

$$\sigma < \frac{\lambda}{8\cos\theta} \qquad \text{Equation 2-49}$$

In Equation 2-49, σ is the standard deviation of the terrain defined in Equation 2-46;
θ is the incidence angle of the electromagnetic wave.

Ulaby *et al.* (1986) in the microwave region (where the wavelength is usually of the order of σ) suggest a more stringent criterion, which is called Fraunhofer criterion (Equation 2-50).

$$\sigma < \frac{\lambda}{32\cos\theta}$$ Equation 2-50

2.4.5 Simple physical models for point scatterers

There are three main simple physical models that are presented in literature and that describe the relationship between the backscattering coefficient and the incidence angle of the electromagnetic wave (Ulaby *et al.*, 1986).

$$\sigma^0(\theta) = \sigma^0(0)$$ Equation 2-51

$$\sigma^0(\theta) = \sigma^0(0)\cos\theta$$ Equation 2-52

$$\sigma^0(\theta) = \sigma^0(0)\cos^2\theta$$ Equation 2-53

Ulaby *et al.* (1986) specifies that many authors describe the scattering coefficient referring to the projected area rather than to the surface area. In these cases, the backscattering coefficient is expressed using the coefficient γ as in Equation 2-43.

2.4.6 Electrical characteristics

Backscattered power intensity is influenced even by electrical properties of the terrain. Water has a dielectric constant about 10 times bigger than most natural materials and so the content of moisture can increase radar reflectivity. Plants, with their high moisture content, are usually good reflectors of the radar signal.

It is important to notice that the moisture content of the landscape is also influenced by atmospheric conditions. "*In particular, clouds decrease or stop vegetation transpiration, which in turn changes the water potential, dielectric constant, and radar backscatter of vegetation*" (Lillesand and Kiefer, 2000).

2.4.7 Speckle

For SAR systems, the size of a resolution cell is many times larger than the radar wavelength. Thus, a pixel does not correspond to a single reflection but it describes an area where there are many scatterers. The brightness of the pixel is the sum of the interactions of the radar wave with all the targets within the same resolution cell of the

image. This result is highly unpredictable and its aspect is typical of radar images. This phenomenon is called speckle (Figure 2-9).

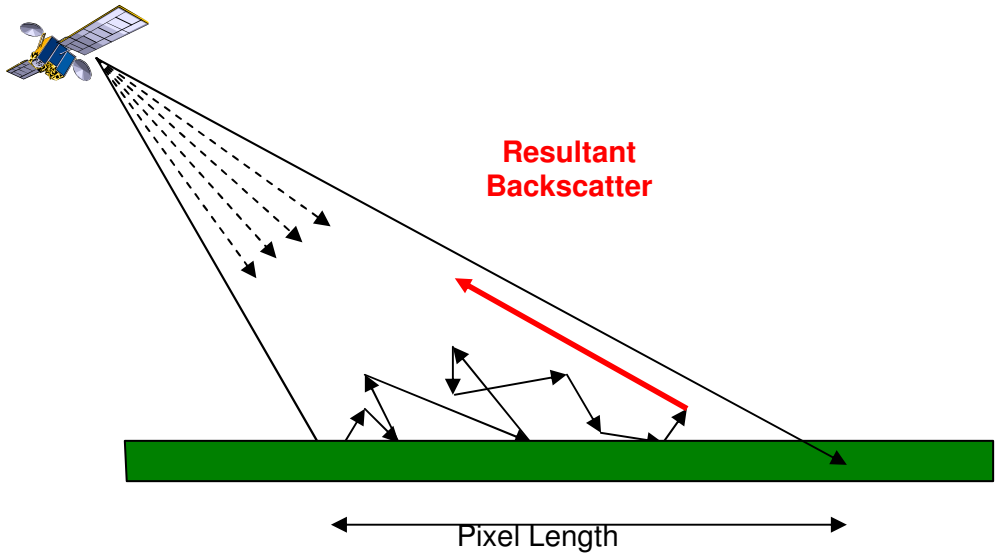

Figure 2-9. Resultant backscatter of all the individual scatterers that are within the same resolution cell of a SAR image (Elder, 2002).

In a mathematical form, the total backscatter amplitude is expressed as (Seynat, 2000):

$$V = |V| e^{j\phi} = \sum_{k=1}^{n} |V_k| e^{j\phi_k} \qquad \text{Equation 2-54}$$

In Equation 2-54, $|V|$ is the radar backscatter;
$|V_k|$ and ϕ_k are the individual amplitude and phase contributions from each scatterer.

Individual scatterers have a phase uniformly distributed between $-\pi$ and $+\pi$. With such a phase distribution, the summation in Equation 2-54 is equivalent to a random walk in two dimensions. The resulting backscatter amplitude has a Rayleigh distribution.

2.5 SAR interferometry

Synthetic Aperture Radars retain phase information for each pulse. The principle that led the way to SAR interferometry is to exploit this piece of information enclosed in radar data to obtain distances and angle measurements. SAR interferometry (InSAR) takes multiple coherent images of the same area at different times with slightly different orbit geometries. If the positions of the imaging satellites are known, the differences in the phase content of the images are used to obtain information about topographical heights of the surface being imaged. If both orbit geometries and topography are

known, phase differences observed can be related to local subsidences occurred in the time elapsed between the two acquisitions.

InSAR technique are traced back to the 1960s when the US Army used an airborne radar to map a province in Panama. Graham (1974) was the first to publish results of this method using two antennas and coherent additive interferometry. A more effective way of generating interferograms using multiplicative interferometry started in the 1980s. Zebker and Goldstein (1986) at JPL published the first interferogram obtained in this way using a dual-antenna (single pass) airborne radar. Li and Goldstein (1987) first demonstrated the possible application of interferometry to satellite data (using historic SEASAT data).

SAR interferometry exploits the phase measurements to infer differential range and range change in two or more SAR images of the same target area. From space, there are two ways to achieve this. The first option is to have two SAR antennas orbiting at the same time. This can be achieved by having them on the same platform, as implemented in the Shuttle Radar Topography Mission (SRTM), or by having a satellite constellation as suggested by Massonet (2001). The second option is to acquire the same scene with the same SAR antenna at two different times. This latter solution is mostly used with space-borne SAR systems and it is called repeat-pass interferometry. For this interferometric technique to be applicable, data sets must be obtained when the scene is viewed from almost the same look angle for each of the passes. Figure 2-10 illustrates a simplified interferometric imaging geometry,

Interferometry can be along-track or across-track (Schwäbisch and Siegmund, 2002). In the present research, only across-track interferometry has been investigated, traditionally used for differential interferometry or topographic applications.

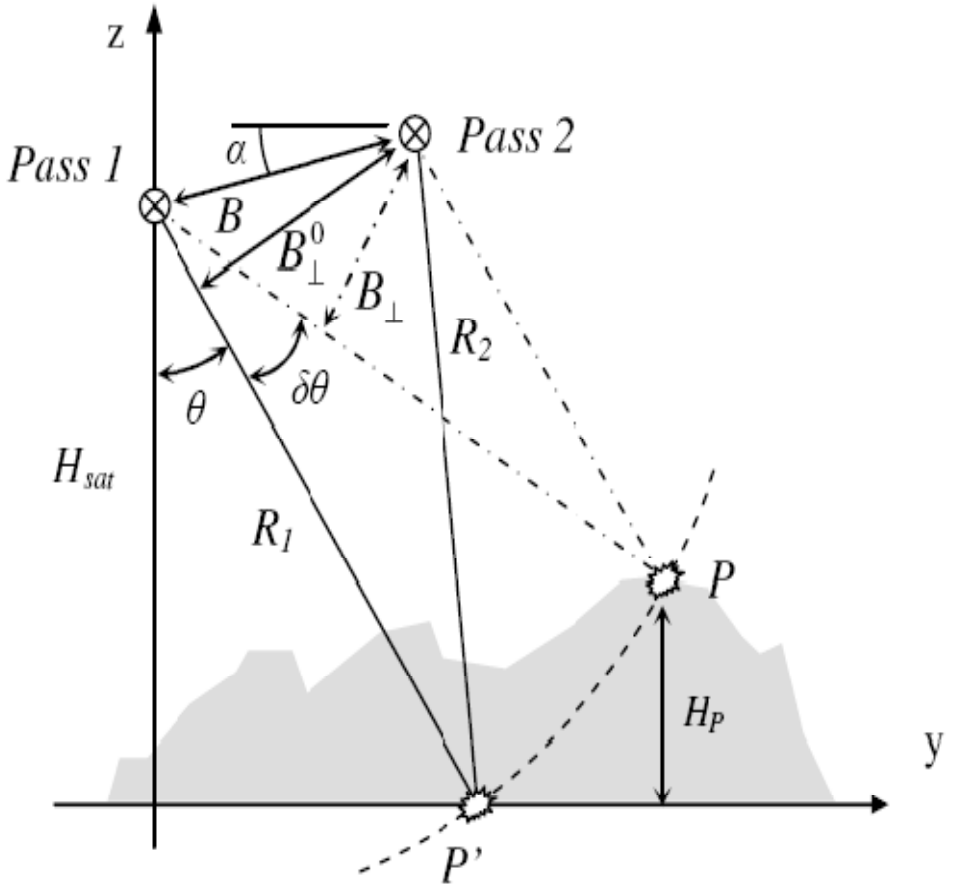

Figure 2-10. Geometry for SAR repeat-pass interferometry (Hanssen, 2001).

The two concepts of temporal and geometrical baseline are necessary to understand fully repeat-pass interferometry.

2.5.1 Temporal baseline

Temporal baseline is the time lapse between the acquisitions of the two images involved in the interferometric processing. In repeat-pass interferometry, it is usually the repeat-pass time of the satellite. For topographical applications the temporal baseline should be the shortest possible to avoid any possible changes in the scattering properties of the landscape imaged (Hanssen, 2001). For tandem ERS 1-2 pairs the temporal baseline is 1 day. It is quite short thus ERS tandem images are extremely valuable for topographical applications.

For other applications such as deformation monitoring, the best value for the temporal baseline is strongly dependent on the phenomenon that has to be monitored.

2.5.2 Geometrical baseline

Geometrical baseline is defined as the effective distance between the two imaging sensors. The perpendicular or effective baseline, the projection of the geometrical baseline on a direction perpendicular to the look direction, has a strong influence on the quality of the interferogram.

An analytical analysis of the geometry involved in repeat-pass interferometry is best given by Hobbs (2002) below. The geometry of a repeat-pass acquisition is illustrated in Figure 2-11.

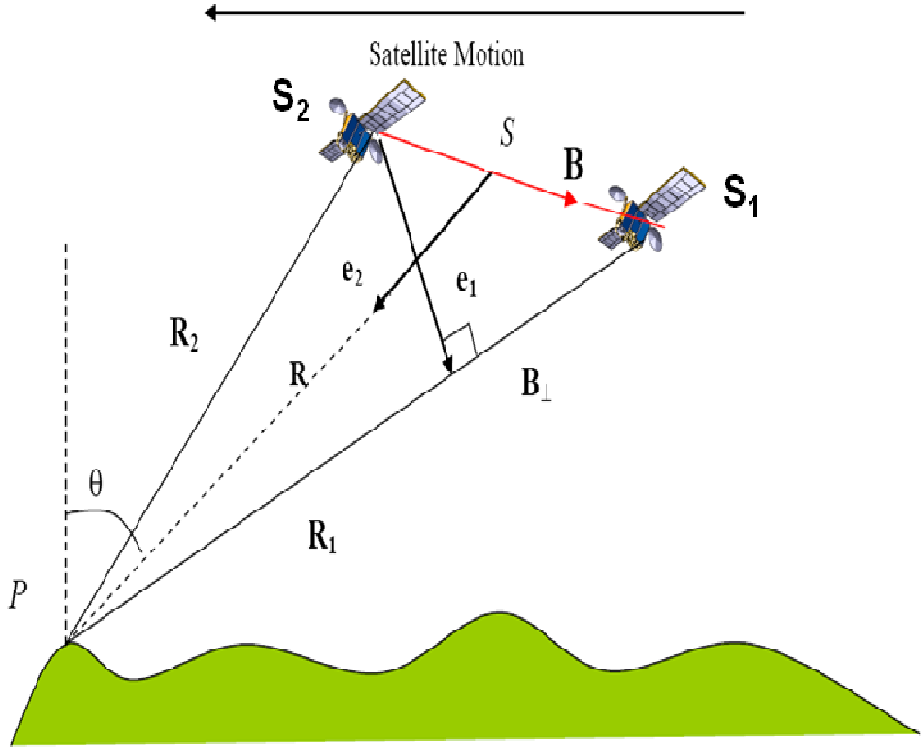

Figure 2-11. Baseline geometry for a repeat-pass SAR interferometry acquisition. (Modified from Elder, 2002).

The origin of the reference frame is assumed in the point *P*, target of the two observations. Two vectors $\boldsymbol{R_1}$ and $\boldsymbol{R_2}$ can define the positions of the two satellites. In the same frame, the baseline vector $\boldsymbol{B}$ is given by Equation 2-55. In the following equations, vectors are in bold.

$$\mathbf{B} = \mathbf{S}_1 - \mathbf{S}_2 \qquad \text{Equation 2-55}$$

At this point, it is possible to define a new reference frame with its origin in the point *S*, mid-point of the vector ***B***.

The first axis of this new frame is along the direction from the point S to the target. The unit vector along this axis is:

$$\mathbf{e}_1 = \frac{\mathbf{P} - \mathbf{S}}{|\mathbf{P} - \mathbf{S}|} \qquad \text{Equation 2-56}$$

A second axis is the one perpendicular to the radial vector $\boldsymbol{e_1}$. Along this axis, it is possible to measure the perpendicular baseline. In vector form it is:

$$\mathbf{B}_\perp = \mathbf{B} - \mathbf{e}_1(\mathbf{B} \bullet \mathbf{e}_1) \qquad \text{Equation 2-57}$$

The unit vector along this direction is:

$$\mathbf{e}_2 = \frac{\mathbf{B}_\perp}{|\mathbf{B}_\perp|} \qquad \text{Equation 2-58}$$

The third axis of the new frame (unit vector $\boldsymbol{e_3}$) is perpendicular to both $\boldsymbol{e_1}$ and $\boldsymbol{e_2}$:

$$\mathbf{e}_3 = \mathbf{e}_1 \times \mathbf{e}_2 \qquad \text{Equation 2-59}$$

The unit vector $\mathbf{e_3}$ is typically parallel to satellite's velocity, i.e. the along-track direction.

2.5.3 Interferogram construction

The master and the slave images have to be co-registered on the same spatial grid. Information is stored in the form of complex values, or phasors, for each pixel. They are presented in complex form as suggested by some authors (Ghiglia and Pritt, 1998; Hanssen, 2001).

$$y_1 = |y_1| e^{j\sigma_1}$$
$$y_2 = |y_2| e^{j\sigma_2} \qquad \text{Equation 2-60}$$

In Equation 2-60, $|y_1|, |y_2|$ are the magnitudes of the complex signals;

$\sigma_{1,}\sigma_2$ are the pixel phases.

An interferogram can be generated by conjugate multiplication (Equation 2-61). This kind of interference is called multiplicative to make a difference with the additive interferometry that is obtained simply by adding amplitudes of the signals (Hanssen, 2001).

$$v = |y_1||y_2|e^{j(\sigma_1-\sigma_2)} \qquad \text{Equation 2-61}$$

If it is assumed (Hanssen, 2001) that the scattering properties of the target are the same in both the images the interferometric phase can be written as:

$$\varphi = -\frac{4\pi(R_1 - R_2)}{\lambda} \qquad \text{Equation 2-62}$$

In Equation 2-62, φ is the wrapped interferometric phase;
R_1 and R_2 are the slant ranges from the target to the satellite for master and slave image.

Referring to the baseline geometry defined in section 2.5.2, it is possible to determine the relationship between interferometric phase difference and topographical height. This is usually demonstrated using a monochromatic approach, the assumption that the RF bandwidth is so small to be negligible. This is true for many satellites including ERS 1-2 or ENVISAT.

The distance from the satellites (i=1.2) to the target can be defined using the reference system presented in Figure 2-11.

$$|\mathbf{R}_i| = |\mathbf{R} \pm \delta\mathbf{R}| = \left|\mathbf{R} \pm \frac{1}{2}\mathbf{B}_\perp\right| \approx R\left(1 \pm \frac{1}{R}\mathbf{e_1} \bullet \mathbf{B}\right) \qquad \text{Equation 2-63}$$

In Equation 2-63, $\boldsymbol{R}$ is the vector from the imaged point and the midpoint of the baseline (Figure 2-11).
$\boldsymbol{e_1}$ is the unit vector along the direction of the vector $\boldsymbol{R}$;
$\boldsymbol{B}$ is the geometrical baseline vector.

The former equation is valid assuming the slant range approximation, which considers parallel the vectors from the two satellites to the target (Zebker and Goldstein, 1986). This simplification is acceptable as the altitude of the satellite is usually at least three orders of magnitude larger than the geometrical baseline.

Interferometric phase can now be easily calculated as described by Hobbs (2002) moving from Equation 2-62 and using Equation 2-63 for the vectors R_i.

$$\Delta\varphi = -\frac{4\pi}{\lambda}\Delta R = -\frac{4\pi R}{\lambda}\left(\frac{1}{R}\mathbf{e_1} \bullet \mathbf{B}\right) = -\frac{4\pi}{\lambda}\left(\mathbf{e_1} \bullet \mathbf{B}\right) \quad \text{Equation 2-64}$$

In Equation 2-64, ΔR is the path length difference from the point P to the two satellites.

The phase difference or interferometric phase $\Delta\varphi$, is sensible to the third dimension (Hobbs, 2002).

Differentiating Equation 2-64, a variation in the interferometric phase is related to a difference δR in the height of neighbouring pixels:

$$\delta\varphi = -\frac{4\pi}{\lambda}\mathbf{B} \bullet \left(\mathbf{e}_1' - \mathbf{e_1}\right) \quad \text{Equation 2-65}$$

$$\left(\mathbf{e}_1' - \mathbf{e_1}\right) = \mathbf{e}_2\delta\theta \quad \text{Equation 2-66}$$

In Equation 2-66, e_1' and e_1 are the unit vectors that correspond to two neighbouring pixels.

$$\delta\theta = \frac{\delta R}{R} \quad \text{Equation 2-67}$$

In Equation 2-67, $\delta\theta$ is the difference in look angle caused by the difference δR in topographical height.

The perpendicular baseline is expressed as in Equation 2-68:

$$\mathbf{B}_\perp = \mathbf{B} \bullet \mathbf{e_2} \quad \text{Equation 2-68}$$

The final expression that relates the height difference δR and the interferometric phase $\delta\varphi$ is:

$$\delta R = -\frac{R\lambda\delta\varphi}{4\pi B_\perp} \quad \text{Equation 2-69}$$

From Equation 2-69 it is quite clear that the perpendicular baseline is a key parameter in the valuation of topographical heights as already mentioned in section 2.5.2.

The length of the baseline determines the suitability of the data set for a particular application as outlined by Solaas (1994) and summarized in Table 2-1. As expressed by Equation 2-69, the accuracy of topographical details detected increases with the length of the perpendicular baseline. The table show that there are values of the

perpendicular baseline that are not suitable for interferometric application. This value, known as critical baseline, will be discussed in section 2.6.4 in the discussion about geometrical correlation.

Table 2-1. Potential applications for SAR interferometry for the ERS satellites (Solaas, 1994).

Applications	Baseline
Practical SAR limit	$B_\perp$ >600 m
Digital Elevation Models	150 m < $B_\perp$ < 300 m
Surface Change Detection	30 m < $B_\perp$ < 70 m
Surface Feature Movement	0 < $B_\perp$ < 5 m

For a perfectly flat Earth, a phase contribution due to the displacement in the e_2 direction (Figure 2-11) has to be taken into account. This has to be evaluated and removed. Given a horizontal displacement x, if the local incidence angle is θ, the component of the displacement in the e_2 direction is given in Equation 2-70.

$$p = x \sin\theta \qquad \text{Equation 2-70}$$

This corresponds to a change in phase that has to be removed (Hobbs, 2002).

$$\Delta\varphi = \frac{4\pi B_\perp x \sin\theta}{\lambda R} \qquad \text{Equation 2-71}$$

This process, called flat Earth removal, should produce an ideally constant phase for a horizontal plane. To be calculated it requires a very precise knowledge of the position of the two imaging sensors. An error in the knowledge of the exact position of the satellites will cause some residual fringes that are not connected with the topography of the landscape. Closa (1998) gives a description of the flat Earth removal process.

Usually the flat Earth approximation is not sufficient to achieve a good quality interferogram. The phase corresponding to a reference body such as an ellipsoid is commonly subtracted in software packages.

2.6 Coherence

The concept of complex coherence in literature is usually related to SAR interferometry as current LEO SAR systems have a short integration therefore the scene is not subject to changes happening during the integration time.

A geosynchronous SAR poses different problems as the integration time is very long and the scene or the propagation medium are going to change their properties with time scales comparable with image formation time. This implies that coherence can be referred to interferometry (i.e. coherence between the two images of the interferometric couple) or to pulse-to-pulse coherence (i.e. coherence in the backscatter received from a single scatterer).

Interferometry is an inherently coherent process, thus a measurement of the correlation between the two SAR images is a key quality factor. Complex coherence plays a major role both in the unwrapping methods and in the stochastical model for interferometric phase.

Under the hypotheses described by Hanssen (2001), a SAR observation may be considered as a complex Gaussian random variable. This approach is reasonable as it takes into account the nature of the image itself. It requires, among the other assumptions, that the resultant pixel backscatter is the sum of many individual uncorrelated scatterers in the same resolution cell.

The complex coherence γ for two zero-mean circular Gaussian variables is defined as (Hanssen, 2001):

$$\gamma = \frac{E\{y_1 y_2\}}{\sqrt{E\{|y_1|^2\} E\{|y_2|^2\}}} \qquad \text{Equation 2-72}$$

In Equation 2-72, y_1, y_2 are the local complex values of the SAR images;
$E\{\ \}$ is the statistical expectation operator.

The absolute value of complex coherence $|\gamma|$ has a value in the range between zero and one, where a null coherence means a total loss of correlation between the two images.

Equation 2-72 can be applied to estimate the change between the backscatter collected during the integration time. In this case, y_1 and y_2 refer to the radar backscatter from a target on the ground at two different epochs during the integration time.

Complex correlation γ_{total} may be split into four contributions (Hensley *et al.* 2003).

$$\gamma_{total} = \gamma_{temporal} \cdot \gamma_{spatial} \cdot \gamma_{thermal} \cdot \gamma_{vol}$$ Equation 2-73

In Equation 2-73, γ_{total} is the total correlation and it includes four different terms:

- $\gamma_{thermal}$ is due to thermal noise.
- $\gamma_{temporal}$ includes the effects of the scattering changes occurring during the time lapse between the two observations.
- γ_{vol} includes the effects of volumetric decorrelation.
- $\gamma_{spatial}$ is the term induced by the perpendicular baseline, caused by the difference in the incidence angles between different observations.

2.6.1 Thermal decorrelation

Thermal decorrelation $(1-\gamma_{thermal})$ is associated with the noise introduced in SAR processing. It is related to SNR from the following relation (Zebker and Villasenor, 1992):

$$\gamma_{thermal} = \frac{1}{1+SNR^{-1}}$$ Equation 2-74

In Equation 2-74, SNR is expressed in absolute values.

For a SNR of 10 dB $\gamma_{thermal}$ is equal to 0.9.

2.6.2 Temporal decorrelation

The concept of temporal decorrelation $(1-\gamma_{temporal})$ is specific to different observations of the same target that happen at different epochs. It occurs because of a change of the scattering properties of individual scatterers on the surface or because of a change in the propagation medium. Different time scales are considered to account for the change of scattering properties:

- At short time scales (seconds), the wind can move the canopies. Troposphere is affected by turbulence that modifies its induced phase delay.
- At medium time scales (hours) the dielectric properties of the scatterers are affected by rain and temperature transitions. Troposphere and ionosphere can change significantly. Earth tides can change the apparent location of the scatterers.
- At long time scales (weeks, months) the changes in scattering properties are caused by physical changes in the terrain being imaged that modify their

scattering properties. "*Weathering, vegetation, or anthropogenic activities are common causes of temporal decorrelation*" (Hanssen, 2001).

2.6.3 Volumetric decorrelation

The contribution of volumetric decorrelation $(1-\gamma_{vol})$ depends on imaging geometry too. When backscattering comes from targets with a different elevation within the resolution cell, volumetric decorrelation is neglected if Equation 2-75 is satisfied (Gatelli *et al.*, 1994).

$$|\Delta z| << \left| \frac{\lambda H_{sat} \tan\theta}{2B_{\perp}} \right| \qquad \text{Equation 2-75}$$

In Equation 2-75, Δz is the height difference between the scatterers in the same resolution cell;
H_{sat} is the satellite altitude;
θ is the look angle (referring to a Cartesian geometry).

This condition is easily achieved for a geosynchronous orbit therefore volumetric decorrelation can be neglected.

2.6.4 Geometric decorrelation

Geometric decorrelation $(1-\gamma_{spatial})$ is due to the different look angles between subsequent observations. According to Zebker and Villasenor (1992), it is a function of the perpendicular baseline $B_{\perp}$.

$$\gamma_{spatial} = \frac{2|B_{\perp}|\Delta R_r \cos\theta}{\lambda R} \qquad \text{Equation 2-76}$$

In Equation 2-76, θ is the radar angle of incidence,
$B_{\perp}$ is the perpendicular baseline,
ΔR_r is the range resolution,
R is the slant range.

The estimate proposed by Zebker and Villasenor (1992) requires that angles and distances are measured in an equivalent flat-Earth Cartesian geometry.

Geometric decorrelation is closely related to the concept of critical baseline $B_{\perp crit}$, the value of the perpendicular baseline that causes a complete signal decorrelation. The expression for $B_{\perp crit}$ (for a monostatic configuration) is given in Equation 2-77 (with the notation presented by Hanssen, 2001).

$$B_{\perp crit} = \frac{\lambda B_w R \tan\theta}{c}$$ Equation 2-77

In Equation 2-77, B_w is the radar signal bandwidth;
c is the speed of light.

An analytical derivation of the expression of the critical baseline is provided in Chapter 7.

2.7 SAR processing

In the present research, temporal decorrelation aspects related to geosynchronous SAR will be investigated. An azimuth SAR processor has been implemented and will be further described in the chapter that presents the methodology. A brief introduction about SAR processing is required to discuss the relevant issues related to SAR image focussing.

The fundamental technical advance that led the way to SAR processing is the use of pulse compression algorithm or matched filter. The matched filter is the mathematical basis of SAR imaging. Picardi (2000) is a thorough reference for the analytical derivation of the algorithm.

A description of the main steps in SAR imaging both in time and in frequency domain is described by Barber (1985) and Curlander and McDonough (1991). The following sections describe the SAR imaging algorithm for an airborne or space borne radar that uses pulse compression and is flying at constant velocity during the aperture synthesis period. A SAR in a geosynchronous orbit will not use the same processing as some other factors have to be taken into account. However, the principles that lay behind standard SAR processing will be used to simulate part of the system. The following sections present the basic procedure for SAR processing that has been applied in the present research.

2.7.1 Range compression

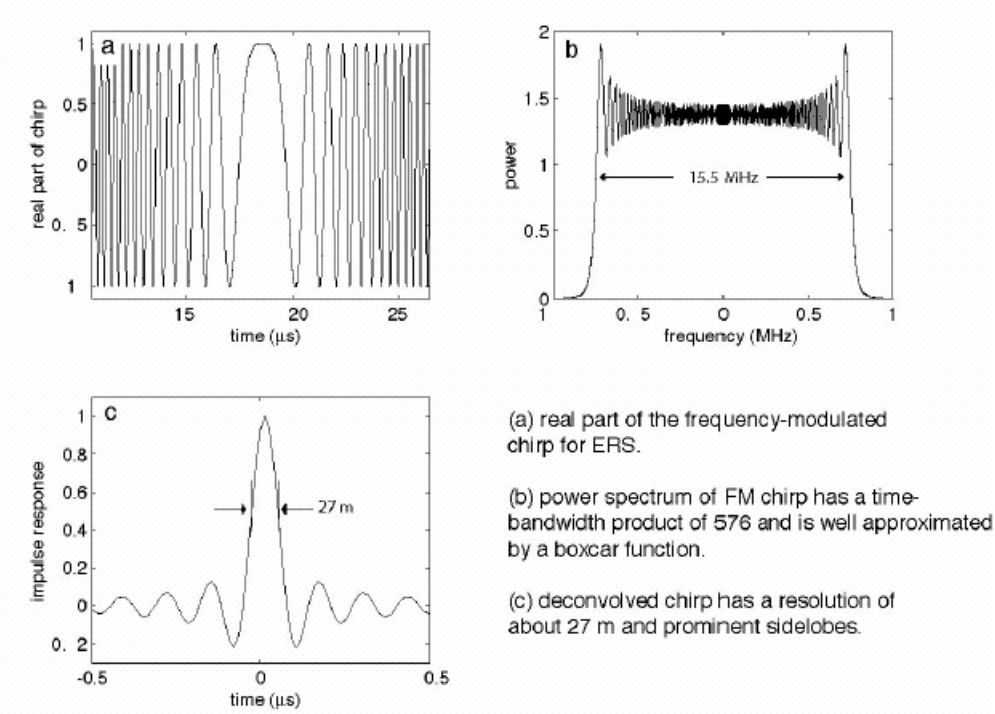

Figure 2-12. Chirp signal properties. (Sandwell, 2002).

The signal transmitted is usually a frequency modulated "chirp" with a large time-bandwidth product. According to Curlander and McDonough (1991), the spectrum has a nominal bandwidth of *B*, where *B* is the bandwidth of the chirp itself (Figure 2-12).

Assuming that the radar transmits a chirp signal (Equation 2-78) (Picardi, 2000) the backscattered echo that reaches the target is (neglecting amplitude factors that do not affect signal focussing) given in Equation 2-79.

$$s(t) = Ae^{j2\pi(f_0+\alpha t)} \qquad \text{Equation 2-78}$$

$$r(t) = e^{j2\pi\left[f_0(t_n-t_D)+\alpha(t_n-t_D)^2\right]} \qquad \text{Equation 2-79}$$

In Equation 2-79, t_n is the time measured from the centre of the nth pulse;
t_D is the round-trip time;
α is the *Chirp Bandwidth/2T*, where *T* is the length of the pulse.

On receipt of each pulse, the radar coherently mixes the centre frequency f_0 down to the offset video frequency f_1. The received echo is then given in Equation 2-80.

$$r(t) = e^{j2\pi\left[f_1 t_n - f_0 t_D + \alpha\left(t_n - t_D\right)^2\right]} \qquad \text{Equation 2-80}$$

2.7.1.1 Range compression in frequency domain

Barber (1985) points out that the range compression could be performed efficiently in the frequency domain. Moreover, at this step the real-valued signal is turned into an exponential to obtain the analytic signal that has the advantage of reducing the required bandwidth to one-half. Appendix A provides some relations that characterise Fourier processing.

To obtain the analytic signal the negative frequencies are all set to zero. The result is inverse Fourier transformed to obtain the final range compressed point spread function. The video frequency f_1 is mixed to zero by the simple procedure of moving all the frequency samples.

Range compression is usually performed in the frequency domain using the DFT. The most efficient way of implementing the DFT is the FFT (Fast Fourier Transform). This particular algorithm requires that the number of samples must be a power of two. The pulse is sampled at the range sampling rate to obtain the pulse record.

Every single pulse is correlated against the same chirp replica (Equation 2-78). The chirp is sampled at the same rate as the data. The record obtained is then packed with zeros to obtain the same length as each pulse record length.

The chirp record is then Fourier transformed and conjugated. The result is then multiplied for the pulse record to obtain the range point spread function $g_R(\tau_R)$ where τ_R is the correlation variable. The final function in the time domain is obtained via inverse Fourier transform (Equation 2-81).

$$g_R\left(\tau_R\right) = \sqrt{\Delta F_R T}\, e^{-j2\pi\left[-f_0 t_D - \alpha\left(t_D - \tau_R\right)\right]} \frac{\sin \pi \Delta F_R \left(t_D - \tau_R\right)}{\pi \Delta F_R \left(t_D - \tau_R\right)} \qquad \text{Equation 2-81}$$

In Equation 2-81, ΔF_R is the chirp video bandwidth $2\alpha T$.

2.7.1.2 Corner turning

After range compression, in order to set the data for azimuth compression, it is necessary to take samples from each pulse that have to be used in azimuth focussing.

Data are usually stored pulse by pulse in a row order (i.e. line by line). This implies that data have to be read along the columns of the ideal storage matrix. The process of reading data column by column, commonly known in literature as “corner turning”, has to be well organised or it is a source of inefficiency in the algorithm.

2.7.2 Azimuth compression

It is essentially the same process as range compression. In this case, the frequency modulation comes from the Doppler effect and the change in t_D from pulse to pulse. The round-trip distance is a quadratic function of time as it depends from the slant range. Expanding the slant range in a Taylor series about t=0 (i.e. the time at closest approach) and including only the terms up to the quadratic.

$$t_D = \frac{2R(t)}{c} = \frac{2}{c}\left(R_0 + \dot{R}t + \frac{1}{2}\ddot{R}t^2 + ... \right) \qquad \text{Equation 2-82}$$

In Equation 2-82, R_0 is the slant range at the centre of the synthetic aperture;
$\dot{R}$ is the slant range velocity at *t=0*;
$\ddot{R}$ is one-half of the slant range acceleration at *t=0*;
c is the speed of light.

The derivatives in Equation 2-82 are identified in terms of the Doppler centre frequency and Doppler rate. The phase of the signal ϕ and its first and second derivatives are given in the following equations where λ is the signal wavelength.

$$\phi = -\frac{4\pi R}{\lambda} \qquad \text{Equation 2-83}$$

$$\frac{\dot{\phi}}{2\pi} = f_{DC} = -2\frac{\dot{R}}{\lambda} \qquad \text{Equation 2-84}$$

$$\frac{\ddot{\phi}}{2\pi} = f_R = -2\frac{\ddot{R}}{\lambda} \qquad \text{Equation 2-85}$$

To compress in azimuth we have to perform a correlation in the azimuth direction considering a temporal slant-range displacement from t_D of τ_R. τ_R is not constant but it tracks t_D with an offset that is a function of the displacement from the centre of the range point spread function (Barber, 1985).

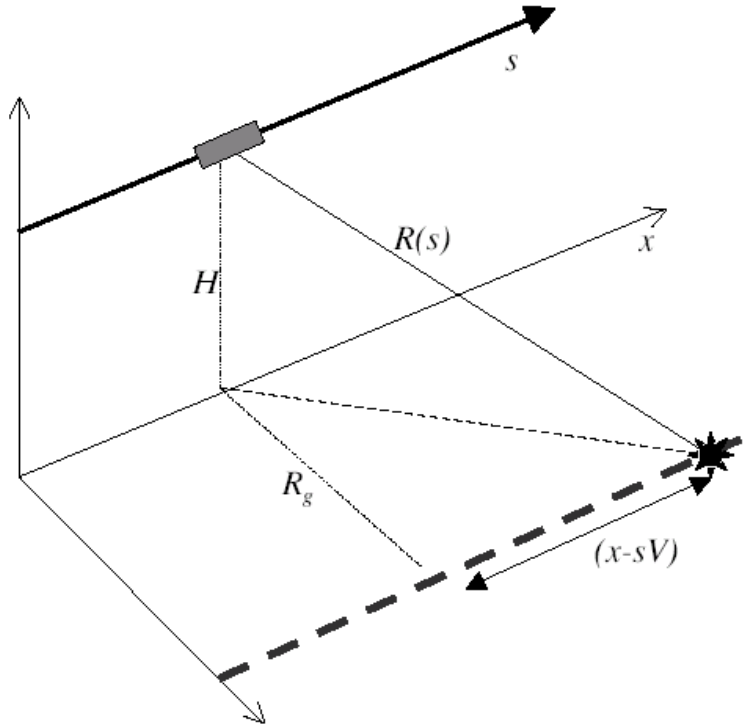

Figure 2-13. Geometry involved in the azimuth processing. (Sandwell, 2002).

If a small change in slant range is considered, then only the first-order change to the range polynomial ΔR_0 has to be taken into account as the changes in the other terms in the polynomial are negligible. This implies that the slant range that contributes to the time variable t_D is:

$$R'(t) = R_0 + \Delta R_0 + \dot{R}t + \frac{1}{2}\ddot{R}t^2 \qquad \text{Equation 2-86}$$

The actual phase history of the point is:

$$e^{-j2\pi f_0 t_D} \qquad \text{Equation 2-87}$$

In Equation 2-87, t_D is the round-trip time given by Equation 2-82.

The phase history against which it has to be correlated is $\exp(-j2\pi f_0 t_D')$ where:

$$t_D^{'} = \frac{2}{c}\left[R_0 + \Delta R_0 + \dot{R}\left(t+\tau_A\right) + \frac{1}{2}\ddot{R}\left(t+\tau_A\right)^2 \right] \qquad \text{Equation 2-88}$$

In Equation 2-88, τ_A is the correlation variable.

The slant range velocity and acceleration can be estimated in terms of spacecraft parameters. It is important to appreciate that these constitute another frequency-modulated chirp.

As derived by Sandwell (2002), the slant range velocity is expressed as in Equation 2-89. The notation used is that included in Figure 2-13.

$$\dot{R} = -V\frac{\left(x - sV\right)}{R_0} = \frac{\lambda}{2} f_{DC} \qquad \text{Equation 2-89}$$

In Equation 2-89, f_{DC} is the Doppler centroid frequency;
R_0 is the minimum slant range (squint angle=0);
s is time;
x is the along-track position of the scatterer on the ground surface;
V is the spacecraft ground velocity.

Slant range acceleration is approximated as in Equation 2-90.

$$\ddot{R} = \frac{V^2}{R} = \frac{\lambda}{2} f_R; \qquad \text{Equation 2-90}$$

In Equation 2-90, f_R is the Doppler frequency rate.

In azimuth processing, the matched filter is simply the complex conjugate of the azimuth phase function.

The Doppler Centroid frequency and the Doppler rate depend on some spacecraft parameters. The ground velocity V of the spacecraft is related to the orbital velocity at satellite altitude v_{sc} using the simple relation:

$$V = \frac{v_{sc}}{\left(1 + \frac{H}{R_e}\right)^{1/2}} \qquad \text{Equation 2-91}$$

In Equation 2-91, H is the local spacecraft altitude;
R_e is the local Earth radius.

Another crucial parameter is the factor $\frac{x-sV}{R_0}$ that is the squint angle and can be related directly to the observation geometry.

Considering a synthetic aperture interval of $\pm T_A/2$ centred about zero, the final expression for the point spread function is:

$$g_A(\tau_A) = \sqrt{B_D T}\, e^{-j2\pi\left[-\frac{2f_0}{c}\left(R_0+\Delta R_0+\dot{R}(t+\tau_A)+\frac{1}{2}\ddot{R}(t+\tau_A)^2\right)\right]} \frac{\sin \pi B_D \tau_A}{\pi B_D \tau_A} \quad \text{Equation 2-92}$$

In Equation 2-92, B_D is the Doppler bandwidth.

The system point spread function is derived multiplying Equation 2-81 and Equation 2-92, taking into account both range and azimuth PSFs.

$$g(\tau_{R,}\tau_A) = g_R(\tau_R)\, g_A(\tau_A) \quad \text{Equation 2-93}$$

2.7.2.1 The azimuth spectrum

A SAR periodically emits pulses at a pulse repetition frequency (PRF) f_p. In the frequency domain, the time series of the transmitted pulses is represented by a line spectrum (Ulaby *et al.*, 1986). Each line of the spectrum moves due to the Doppler effect. In this case, it is crucial to highlight the importance of using an analytic signal. A cosine function, in the frequency spectrum, has both positive and negative frequencies; hence, a Doppler shift splits the line into two lines that are indistinguishable. On the contrary, an analytic signal has only one line in the spectrum. This implies that positive and negative Doppler shifts are separate.

The use of analytic signals is crucial where there are both positive and negative Doppler shifts. The use of a simple real signal is possible in squinted mode where there is no Doppler ambiguity. Otherwise, the Doppler band can be aliased into a wholly positive or negative band with a carefully selected PRF, e.g. azimuth offset processing (Ulaby *et al.*, 1986).

2.7.2.2 Azimuth focussing

This part of the processing is more or less the same as the range focussing. The reference signal in the correlation process or the azimuth chirp signal is simply the complex conjugate of the azimuth phase signal.

The azimuth compression processing is much more complicated as there are some other phenomena to be taken into account deriving from the geometry of the problem.

Assuming a radar platform flying with velocity v_{sc} and emitting pulses with a given PRF, if the image has a length *L,* the number of pulses that are required is $L\ PRF/v_{sc}$. The required Doppler bandwidth B_D is approximated as (Barber, 1985):

$$B_D = 2\frac{v_{sc}^2 T_{obs}}{\lambda R_0} \qquad \text{Equation 2-94}$$

In Equation 2-94, R_0 is the minimum slant range, i.e. at broadside;
T_{int} is the integration time.

The resolution is directly proportional to B_D thus, to obtain a constant resolution throughout the image, T_{int} has to be increased across track together with the slant range at broadside R_0. This problem influences the number of samples in the Doppler replica against which the signal has to be correlated in the FFT processing. To take into account slant range variation across-track, each azimuth line should be correlated against a different replica.

2.7.2.3 Range migration

In azimuth processing, frequency modulation derives from the Doppler effect and from the change in t_D from pulse to pulse. The changing phase is a quadratic function of time because of the change in slant range between radar and target. For a relatively large range resolution cell (typically in the airborne case), the change in range due to range migration is smaller than half-range cell and this effect can be neglected; otherwise the different terms in Equation 2-88 have to be evaluated and considered carefully.

The linear term is generally called range walk while the quadratic component is called range curvature. Together they constitute the range migration effect.

The range walk component is due to orbit eccentricity, squint angle and Earth rotation (Barber, 1985). Moreover, the rotation term is a function of the ground track latitude. Even the quadratic term is a function of latitude, but its dependence is much weaker.

The simplest way of dealing with range migration is in the time domain. The processing required can be summarised easily. Once defined a reference on the ground with an azimuth coordinate, it is possible to define the slant range of each point on the image as a function of its distance from the centre of the swath:

$$R(s) = R_0 - \left(\frac{\lambda f_{DC}}{2}\right)(s - s_c) - \left(\frac{\lambda f_R}{4}\right)(s - s_c)^2 \qquad \text{Equation 2-95}$$

In Equation 2-95, R_0 is the slant range at broadside;
S_c is the azimuth coordinate that corresponds to R_0;
f_{DC} and f_R can be easily estimated from orbit parameters.

Using Equation 2-95 it is possible to determine the range points that have to be correlated to obtain the right azimuth focussing. To obtain the data points in the required range bins usually data available have to be interpolated.

2.7.3 SAR processors

Concepts and relations that have been briefly presented in the previous sections will be partly applied in the present research, as the investigation of the key properties of a geosynchronous SAR does not require the setup of a complete SAR processor. In the chapters dedicated to methodology will be shown that the focus has been limited to azimuth SAR processing as the phenomena that we would like to investigate regards mainly slow-time (i.e. azimuth) processing.

Appendix C provides a brief background about SAR processors; it has not been included in this chapter as it is beyond the scope of this research. The appendix provided can be used as a reference for eventual further activities to be carried out in the field.

2.7.4 GeoSAR processing

As it will be discussed in the relevant chapters, GeoSAR will not probably use standard SAR processing. Different aspects have to be taken into account when focussing GeoSAR images:

- Velocity is not constant during the integration time;
- Azimuth pre-summing is required to achieve a reasonable SNR;
- A bi-static SAR cannot use a chirp signal as it has to re-use the signal of a transmitter of opportunity.

2.7.4.1 SAR autofocus

SAR data is subject to a number of perturbations that come from various causes such unpredictable platform motion or heterogeneities in the propagation medium. They lead to unknown phase changes in the raw data that cause image de-focus.

In general, SAR autofocus is an iterative procedure applied to SAR processing that allows to estimate (and consequently compensate) unknown phase delays. Koo *et al.* (2005) provide a review of the existing autofocus methodologies. They could be divided in two main categories: model-based and non-parametric.

Model-based methodologies such as Quadrature Phase Error (QPE) or Map Drift (MD) or Multiple Aperture Map Drift (MAM) are appropriate for low-frequency noise that could be correctly modelled.

Non-parametric models do not require a specific knowledge of phase errors. Phase Gradient Autofocus (PGA) and its variants (Jakowatz *et al.*, 1989) has proven to be able to filter out high frequency noise sources.

The procedure is usually space-invariant (within one image), the same correction is applied to the whole image; however, when position-dependent phase errors are relevant, autofocus has to be space-variant. This is usually carried out splitting the image in sub-images that are mosaicked together after the focussing procedure (Koo *et al.*, 2005).

2.8 Multi-static SAR

The present research will provide some insights about a possible multi-static constellation made of geosynchronous SARs. Some literature background about multi-static SAR will be included in the following sections.

Paragraph 2.8.1 provides an explanation of the fundamentals related to multi-static SAR configurations. The following parts discuss the basic multi-static SAR principle and the concept of antenna phase centre. The final paragraph of this section presents the SAR train concept, a patent developed at CNES in 2003 (Aguttes, 2003; Aguttes, 2004).

2.8.1 Rationale

The need for high-resolution systems over a wide area of surveillance is the major driver to the design of multi-static SARs. The basic limitation for the design of space-borne synthetic aperture radar is the minimum antenna area constraint A_{min}, which is presented as in Equation 2-96 according to Ulaby *et al.* (1986).

$$A_{\min} = 4 v_{sc} \lambda R \frac{\tan\theta}{c}; \qquad \text{Equation 2-96}$$

In Equation 2-96, θ is the ground incidence angle;
v_{sc} is the satellite velocity;

The minimum area for a passive bi-static SAR is half the value reported in Equation 2-96. This expression highlights a compromise between achieving good azimuth resolution and wide spatial coverage.

The multi-static concept with a broad illumination source and many receiving antennas can overcome this problem. The coherent combination of recorded multichannel signals will allow the unambiguous SAR mapping of a wide area with fine azimuth resolution.

Although an individual antenna does not satisfy the minimum area criterion and collects signals that are ambiguous in Doppler domain, the total receiving antenna of the multichannel SAR achieves a non-ambiguous signal by combining coherently the output from the different channels. The constraint on the pulse repetition frequency (PRF) is determined by the total length of the receiving antenna (Equation 2-97).

$$PRF \geq \frac{2v_{sc}}{L_{tot}}; \qquad \text{Equation 2-97}$$

In Equation 2-97, L_{tot} is the sum of the lengths of the individual antennas.

Obviously, the PRF is much lower than that required by an individual small antenna.

The SAR train concept (Aguttes, 2003; Aguttes, 2004) will be presented in more details as it can be applied straightforwardly to GeoSAR.

2.8.2 Basic Principle

A significant development in SAR systems is the introduction of phase array antennas in space-borne systems. These types of antennas allow great flexibility in generation and control of radar beams.

Curie and Brown (1992) described all the different operating modes that could be exploited to enhance the effectiveness of the use of space-borne SAR in terms of swath widening and increasing resolution. The modes have been split in two main areas: those using multiple beams in the across-track (i.e. range) direction and those that utilise multiple beams in the along-track direction (i.e. azimuth).

The present research is looking towards possible applications for high altitude SARs where one of the major issues is antenna dimension that is quite a serious constraint for this kind of system; therefore multiple beam SARs are considered as a means for sharing antenna area between many satellites cooperating among them. For this reason, only along-track configurations have been considered.

Spatial sampling is used to increase the maximum unambiguous illumination area using multiple receivers. A typical concept is a constellation of micro-satellites flying in formation. A possible implementation of this concept is the TECHSAT 21 flight experiment with antennas randomly scattered (Martin and Kilberg, 2003).

In presence of a sparse aperture an unambiguous Doppler signal has to be reconstructed using the various ambiguous contributions (coming from the different antennas). A possible solution is the application of Space Time Adaptive Processing (STAP). Zhenfang *et al.* (2005) provide a clear explanation of the STAP processing: "*the main idea of the STAP approach is to retrieve the unambiguous azimuth wide (full) spectrum signal from the received data by properly overcoming the aliasing effect caused by the lower PRF through the application of a STAP algorithm (post-Doppler architecture)".*

The analysis of the STAP algorithm will not be presented here, as at the moment an application of this concept to a real case is not foreseeable. A complete STAP analysis has been reported in literature by Mengdao *et al.* (2004) and Zhenfang *et al.* (2005).

2.8.3 The SAR Train concept

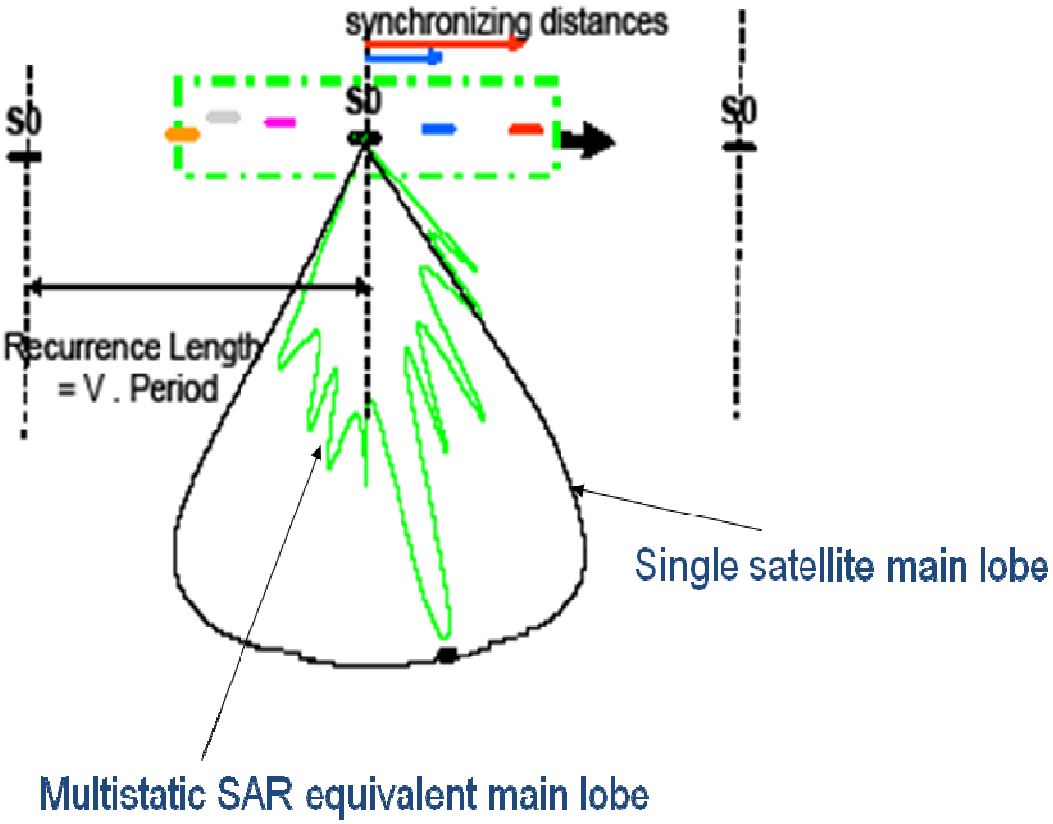

Figure 2-14. SAR train concept (Aguttes, 2003; Aguttes, 2004).

The SAR train concept (Aguttes, 2003; Aguttes, 2004), developed and patented by CNES in 2003, is a particular signal processing algorithm used to generate a large

synthetic aperture antenna through a constellation of relatively small SAR antennas flying on the same track. The sum of N synthetic antennas can be interpreted as the sum of N signals coming from N different satellites (corrected in range) and the subsequent sum of the signals received by the composite global antenna along its flight path.

Theoretically, the signals received by N SAR instruments flying on the same track can be summed coherently to obtain an equivalent SAR. There could be a benefit on the Signal to Noise Ratio or on the SAR *Merit Factor* (the SAR *Merit Factor* is given by Equation 2-98).

$$\text{SAR } \textit{Merit Factor} = \frac{Swath}{\Delta R_{az}} \qquad \text{Equation 2-98}$$

The merit factor is improved by enlarging SAR swath (reducing antenna dimension in range) or reducing azimuth resolution cell size (longer antenna in the along-track dimension). The two above-mentioned benefits cannot be obtained at the same time.

In a SAR, the azimuth resolution is set by ambiguities in azimuth. The angular separation of the ambiguous directions is $k\lambda(PRF/v_{sc})$ where k is an integer, v_{sc} is satellite velocity with respect to the target and PRF is the Pulse Repetition Frequency.

The first ambiguity lobe is crucial to determine the minimum size required for the SAR antenna in the along-track direction. If the antenna is too short (this is desirable as it could provide a better azimuth resolution according to basic SAR theory where SAR azimuth resolution is given by $L/2$); the SAR main lobe includes some ambiguities, generating a Doppler ambiguous signal. This poses a requirement on the minimum real antenna length that should be long at least $2v_{sc}/PRF$.

The aim of the SAR train concept is to relax the constraints on SAR power and on antenna physical dimension, diluting the requirements on a set of smaller SARs. At the same time, particular spread-spectrum waveforms have been chosen in order to attenuate the requirements on orbit accuracy (Aguttes, 2004).

2.8.3.1 Different modes

Aguttes (2004) describes three different SAR train operating modes. It is worthwhile presenting all of them. The common assumption is that they are based on a constellation of $\boldsymbol{n_{sat}}$ different SAR satellites flying on the same ground track (they have to be on different orbital planes). The benefits of each configuration proposed are described providing details about formation requirements, the knowledge of the terrain and of the waveforms required. As already mentioned all the configurations require a coherent combination of the SAR signals.

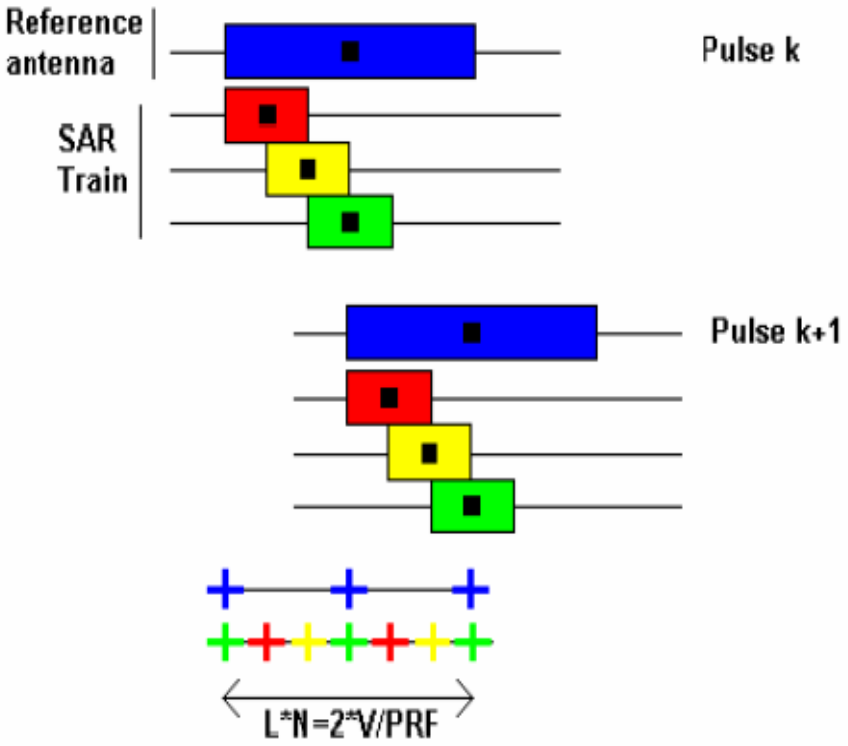

Figure 2-15. SAR Train principle (Marechal *et al.* 2005)

2.8.3.2 First mode – operating principle

The first mode considers n_{sat} SAR antennas flying with a random separation. The n_{sat} SAR images are added coherently thus the resultant image has an intensity that is the sum of the intensities in the n_{sat} images. Therefore, it is possible to achieve an improvement in the SNR and a reduction in the ambiguity level.

The first operating mode does not reduce the minimum antenna area required for proper SAR focussing but provides an advantage on the SNR and on the ambiguity level. Moreover, this configuration has the advantage of a loose constraint on signal coherence. The main one is related to the width of the tube (across-track dimension) that contains the n_{sat} flight paths.

Azimuth ambiguities are included in the main lobe of the single antenna. The reduction in ambiguity noise level can be achieved considering that the ambiguities are summed non-coherently and their intensity is reduced by a factor n_{sat}. If the n_{sat} satellites are distributed randomly in the section (the section is long v_{so}/PRF, the separation between the positions of one satellite between two different samples), the n_{sat} contributions to each ambiguity are summed non-coherently while the signals coming from the pixel are

summed coherently. This implies that we have a reduction of ambiguity noise level of a factor $\boldsymbol{n_{sat}}$.

The first operating mode can be applied to passive multi-static configurations. In the parasitic bi-static SAR constellation, it is not possible to reduce antenna physical dimensions with respect to monostatic case. However, multiple antennas could be used to improve SNR and reduce ambiguities.

2.8.3.3 Second mode – operating principle

The second mode wants to exploit the reduction in the ambiguity level to allow the ambiguities to enter the main lobe, thus to operate with signals ambiguous in Doppler. This gives an improvement of the merit factor and a reduction of antenna size.

The second operating mode allows the antenna area to be reduced in $\boldsymbol{n_{sat}}$ smaller antennas thus multiplying by $\boldsymbol{n_{sat}}$ the merit factor. The second mode is feasible only for a constellation with $\boldsymbol{n_{sat}}$=2 satellites due to coherence constraints.

This mode requires a precise positioning of the satellites. As specified in the previous paragraph, the section (the separation between the positions of one satellite between two different samples) is long v_{so}/PRF. To cancel the first $\boldsymbol{n_{sat}}$ ambiguities, the separation among the satellites constituting the train should be $v_{so}/\boldsymbol{n_{sat}}$PRF plus an interval modulo (v_{sc} /PRF). This factor is the separation between subsequent pulses in the SAR train distributed antenna.

In this operating mode (Figure 2-16), "*while ambiguities could raise because the PRF is inadapted to the elementary antennas that constitute the SAR train, (*$\boldsymbol{n_{sat}}$*-1) ambiguities out of* $\boldsymbol{n_{sat}}$ *fall into the zeros of the array pattern*" (Marechal *et al.,* 2005).

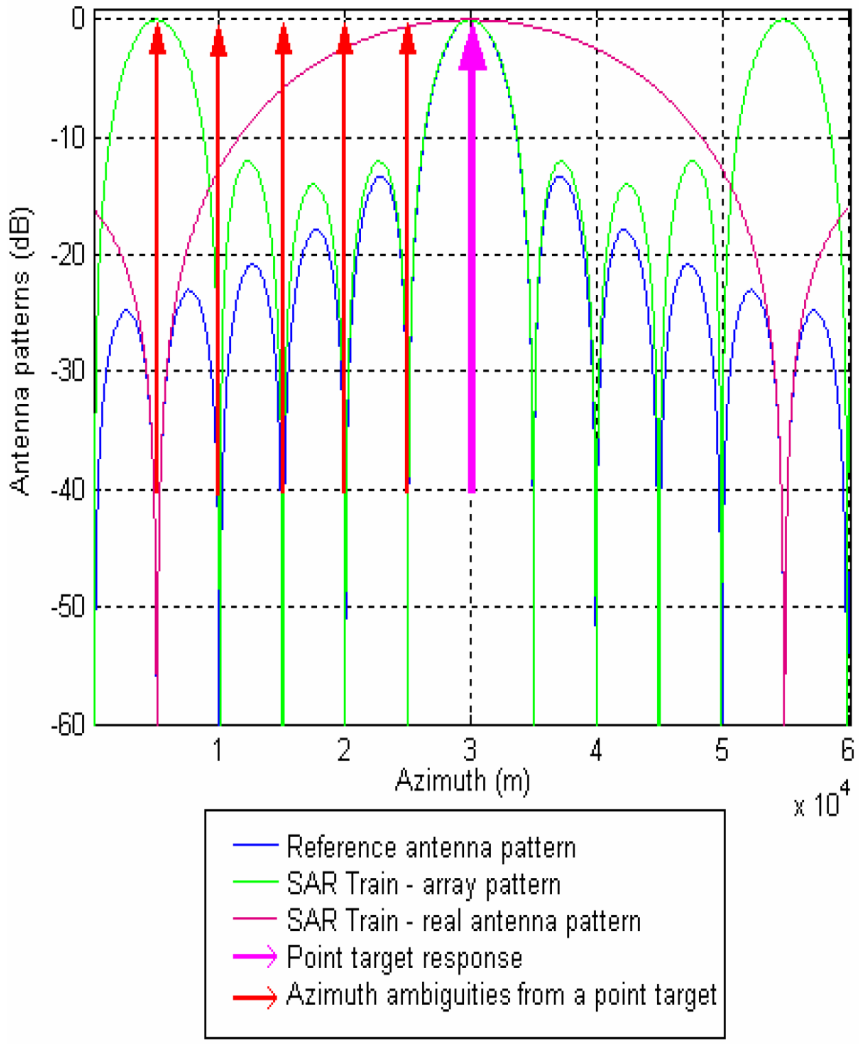

Figure 2-16. Second operating mode. Antenna pattern comparison, the x-axis is the along-track spatial distance (Marechal *et al.*, 2005)

It can be assumed that the superposition of n_{sat} satellites with the same PRF is equivalent to a single antenna with a new PRF equal to n_{sat}xPRF. The distance between ambiguities is increased by a factor n_{sat} and this improvement is used to reduce the size of the antenna in the along-track direction thus improving the resolution by a factor n_{sat}.

The second operating mode has a second possible implementation with different peculiarities. Instead of reducing the along-track dimension of the antenna, it is possible to decrease the PRF by a factor n_{sat} achieving the same level of ambiguity. The antenna size can be reduced in the range dimension achieving a wider swath with

the same level of range ambiguity. This second opportunity is used to tackle the range ambiguity issue.

It is important to point out that the reduction by n_{sat} of the antenna dimension has the consequence of reducing by n_{sat}^2 the power received by each antenna (monostatic case) as the beam-width increases by the factor n_{sat}. Even considering that there is a factor n_{sat} improvement in the power budget provided by the SAR train, the SNR is n_{sat} times lower than in the original case.

2.8.3.4 Third mode – operating principle

The third mode (Aguttes, 2004) uses the same processing required for the second mode. The main difference is that the use of wide spectrum waveforms relaxes the constraint of in-orbit placement of the n_{sat} satellites constituting the SAR train. The use of new waveforms allows the use of the second operational mode even with constellations with n_{sat} >2 satellites.

A spread-spectrum signal has an autocorrelation function with a shape significantly different from conventional signals. In fact, while for a conventional chirp signal the ambiguity function has many peaks displaced in range and in azimuth a spread-spectrum waveform has only one peak and a constant pedestal *1/4BT* (where *B* is the bandwidth of the signal and *T* is the period of the waveform).

The ambiguities contributing to noise are only those ones that are included in the main lobe. For a spread spectrum waveform, the energy level of ambiguities is proportional to the SAR *Merit Factor* (Swath/azimuth resolution). If the waveform is periodic with a period T_e, the ambiguity function has a peak and the ambiguities are concentrated in lines separated by a distance $1/T_e$.

If the n_{sat} SAR use N different waveforms, the N contributions are non-correlated thus there is a factor N reduction in ambiguity level. If only N' waveforms uncorrelated are used and the waveforms are synchronised along the orbit only a factor N' improvement is achieved in ambiguity reduction.

2.8.3.5 Analysis of the coherence of the signal

For all the operating modes, there are some coherence constraints to be verified. The vector between two different elements of the array has three components. In particular, it is possible to define a geometrical baseline (equivalent to the interferometric geometric baseline) that causes decorrelation among the signals collected from the same pixel by the various satellites.

The so-called critical baseline concept could be applied to the SAR train as well. The phase difference between the signals received by two different satellites can be corrected if the relief of the terrain is well known. The correction is performed with respect to an ideal reference trajectory. Phase deviations are modelled stochastically assuming that the interferometric baselines of all the satellites of the train are distributed normally with a zero mean value and a standard deviation σ (Aguttes, 2004).

$$\sigma = \frac{\omega}{6\sqrt{2}} \qquad \text{Equation 2-99}$$

In Equation 2-99, ω is the width of the tube containing all satellite trajectories, distributed following a normal distribution with zero mean

Therefore, the phase deviation of each of the n_{sat} contributions is given in Equation 2-100.

$$\varepsilon = \frac{4\pi\Delta h\omega}{6\sin i R\lambda\sqrt{2}} \qquad \text{Equation 2-100}$$

In Equation 2-100, Δh is the terrain altitude
i is the ground incidence angle (flat Earth geometry)

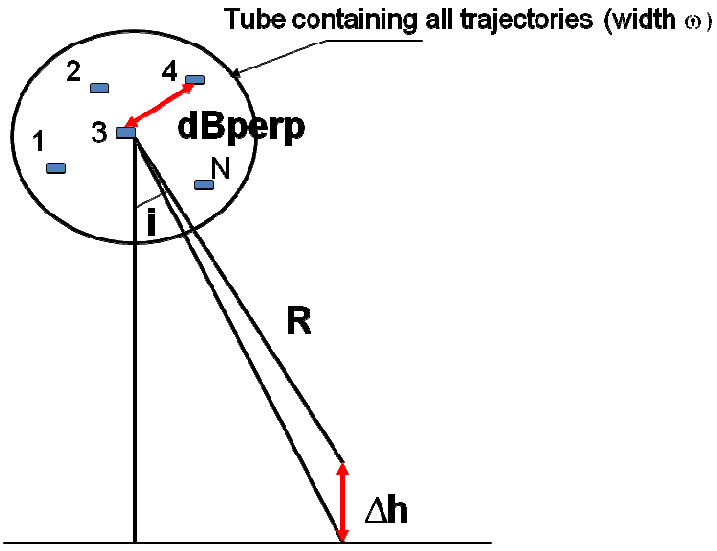

Figure 2-17. Phase decorrelation induced by topographic height and perpendicular baseline.

The effect of this phase deviation reduces the coherence of the signals collected by the SAR train. The limit imposed on power losses poses some constraints on the knowledge of topography and on the width of the tube that includes all the satellites.

The accuracy in the knowledge of the perpendicular component of the baseline has a consequence on phase accuracy as well. The following error term has to be negligible; this poses a constraint on the accuracy of the term dB_{perp}.

$$\varepsilon' = \frac{4\pi dB_{perp} h_{\max}}{\sin iR\lambda} \qquad \text{Equation 2-101}$$

In Equation 2-101, h_{max} is the maximum altitude of the terrain being imaged.

The first operating mode does not assign serious constraints on orbit control as ambiguity reduction is provided by the sum of different random phase contributions from the N satellites.

The second operating mode uses precise orbit control to cancel the first $\boldsymbol{n_{sat}}$ ambiguities. The phase error of each ambiguity is $k\alpha$ where k is the number of the ambiguity and α is the error in radians. Due to this phase error, the intensity on the ambiguity k is decreased by a factor (Equation 2-102) with respect to the ideal ambiguity suppression achievable with exact spacing between the satellites in the SAR train (Figure 2-16).

$$\frac{Nk^2\alpha^2}{N^2} \equiv \frac{k^2\alpha^2}{N} \qquad \text{Equation 2-102}$$

The residual protection on the $2(\boldsymbol{n_{sat}} -1)$ ambiguities ($\boldsymbol{n_{sat}}$ -1 ambiguities forward and $\boldsymbol{n_{sat}}$ -1 ambiguities backward with respect to the mid-point of the antenna beam) is given in Equation 2-103:

$$\left(\frac{\alpha^2}{N}\right)\left(\sum_{k=1}^{N-1} k^2\right) \qquad \text{Equation 2-103}$$

Ambiguity protection has to be better than -30 dB (Aguttes, 2004). This implies that the constraint on α is very strict even for $\boldsymbol{n_{sat}}$=2 (α=1/22). The case with only two satellites is the only one feasible according to the limitation provided by ambiguity reduction.

2.9 Phenomena affecting temporal decorrelation

A measurement system that requires a given time lapse s (seconds) to carry out a measurement is sensible to phenomena that happen on frequencies lower than 1/s Hz

(Hobbs, 2009). This implies that only phenomena that cause a signal delay comparable with the radar wavelength during the whole integration time affect the system. The present research looks into the effects of the long integration time on geosynchronous SAR processing. There are some phenomena that are not usually considered an issue in LEO SAR imaging (due to their time scale) but that can hamper significantly the image formation process of a SAR in a geo-synchronous orbit that require, as will be discussed in subsequent chapters, an integration time of hours. For this reason, this research will not include in the analysis decorrelation factors such as vegetation that, due to their timescale, are not likely to produce any effect on a geo-synchronous SAR system.

Three main issues have been tackled in the present research. Section 2.9.1 reminds the effects of phase noise on SAR images. The following sections provide a background on Earth tides (section 2.10), tropospheric propagation (section 2.11) and ionospheric propagation (section 2.12).

2.9.1 Rationale

Prior to discussing each issue in further details, this section discusses the main effect on SAR images caused by Earth tides and atmospheric propagation effects that have been considered in the present research. A comparison with their effects on LEO SAR systems will provide additional information on GeoSAR peculiarities.

2.9.1.1 Earth tides

Earth tides induce a variation in a scatterer's position that generates a fluctuation in its backscattered phase that affects the signal collected by the system during the whole integration time. This effect is usually neglected in LEO SAR systems that have an integration time shorter than 1 second as it is considered negligible; however, GeoSAR processing requires considering this aspect as Earth tides can cause a coherence loss in the target.

2.9.1.2 Atmospheric effects

Propagation medium affects electromagnetic wave propagation at all frequencies, resulting in a bending of the signal path, time delays of arriving modulations, advances of carrier phases, scintillation and other changes (Leick, 2004). These effects vary with location and time in a complex manner. The relevant propagation regions are the troposphere and the ionosphere. There are some phenomena associated with tropospheric and ionospheric turbulence that can affect the amplitude, the phase and the polarisation state of the signal received by the radar.

Tarayre and Massonet (1996) suggest a simple break down of the various atmospheric effects on radio waves propagation. They assume that two different contributions may be highlighted: the consequence of a homogeneous neutral atmosphere and the outcomes of local heterogeneities.

The heterogeneities can be produced in the neutral layer of the atmosphere by turbulent scatter or in the ionosphere, the ionised part of the atmosphere, by fluctuations in the local electronic density.

Figure 2-18 presents a sketch with different atmospheric layers.

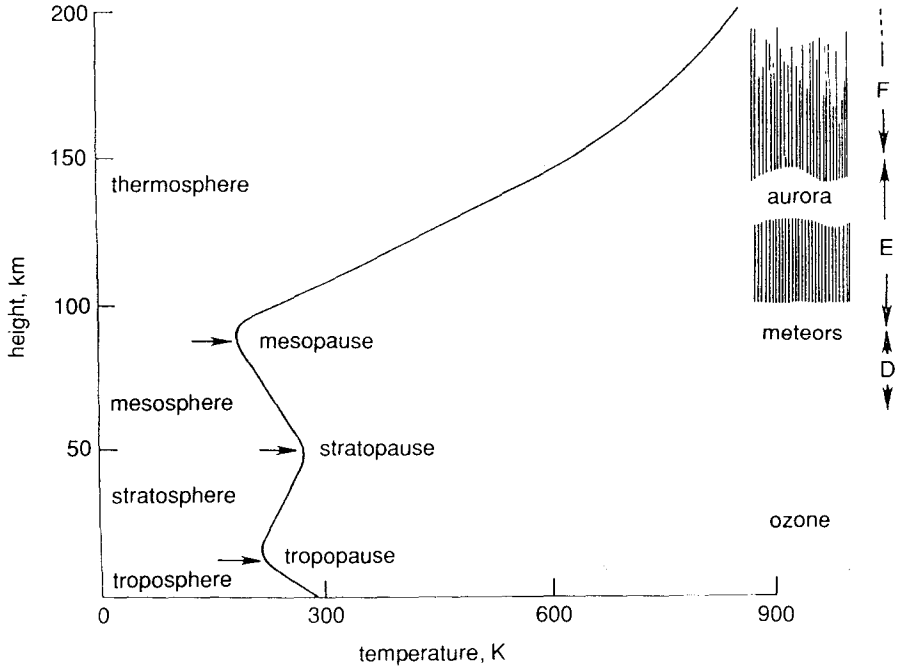

Figure 2-18. Different regions of the Earth's atmosphere, showing the mean temperature profile and the ionospheric layers (Hall *et al.*, 1996).

In LEO SAR the effects of propagation do not affect single image SAR processing, due to its short integration time; nevertheless this problem has been tackled in literature and receives a growing interest as it has an effect on SAR interferometry. InSAR compares the phases of corresponding pixels imaged at different epochs. Atmosphere can be considered as frozen during the integration time required to focus each image however, the difference in the states of the atmosphere causes some phase artefacts in the interferogram.

GeoSAR requires a different approach to atmospheric heterogeneities. Due to the long integration time, there are atmospheric heterogeneities that cause pulse-to-pulse temporal decorrelation. Therefore, while atmospheric propagation affects LEO SAR

interferometry, heterogeneities in the propagation medium affect GeoSAR's processing itself as they modify the phase collected by the system.

2.10 Earth tides

Earth tides induce a fluctuation in the position of a scatterer on the Earth's surface during the integration time. The following sections provide the fundamentals about Earth surface tidal motion and then look into the various contributions to target displacement.

2.10.1 Rationale

Many different phenomena related to Earth tides that affect the position of a site on the Earth surface have been described in the literature (McCarthy and Petit, 2004). They include:

- deformations of the solid Earth due to ocean tidal loading;
- deformations due to the body tides arising from the direct effect of the external tide generating potential;
- minor effects such as centrifugal perturbations caused by Earth rotation variations, the pole tide and atmospheric loading.

McCarthy and Petit (2004) is the reference publication dealing with the estimation of Earth tide effects. In the introduction of their document, they establish the concept that Earth tide effects can be analysed from two different perspectives: perturbations in the gravitational potential in the vicinity of the Earth and displacements in site positions.

"Some geodetic parameters are affected by tidal variations. The gravitational potential in the vicinity of the Earth, which is directly accessible to observation, is a combination of the tidal gravitational potential of external bodies (the Moon, the Sun, and the planets) and the Earth's own potential, which is perturbed by the action of the tidal potential. The (external) tidal potential contains both time independent (permanent) and time dependent (periodic) parts, and so does the tide-induced part of the Earth's own potential. Similarly, the observed site positions are affected by displacements associated with solid Earth deformations produced by the tidal potential; these displacements also include permanent and time dependent parts" (McCarthy and Petit, 2004).

Both the aspects of this problem are of interest for GeoSAR as Earth tides affect both the satellite that is orbiting and the targets on the Earth surface.

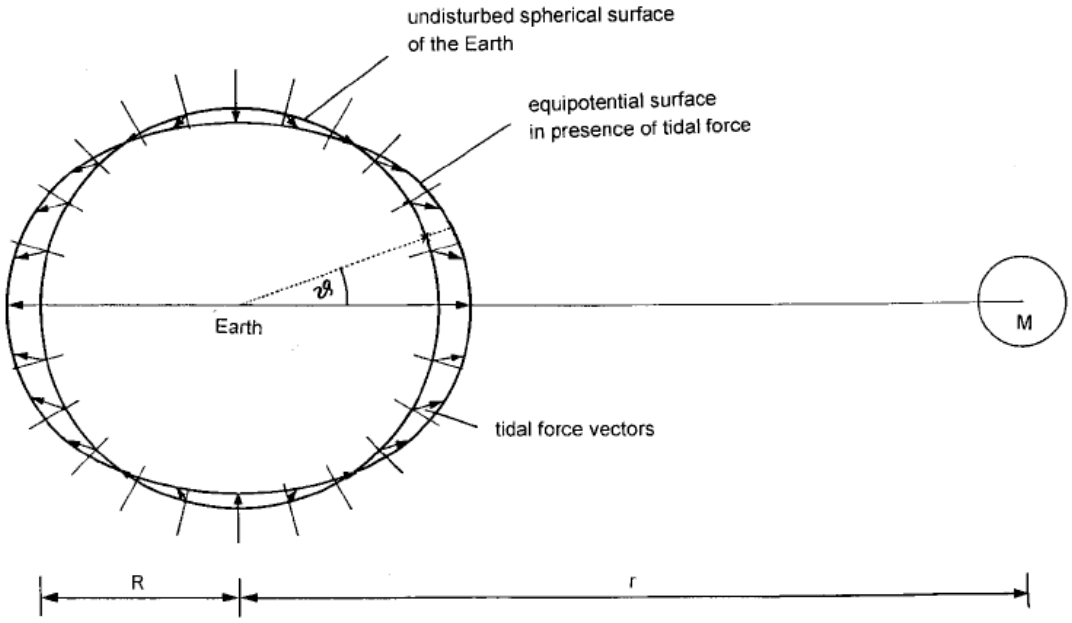

Figure 2-19. Magnitude and direction of tidal forces on the Earth's surface; the forces are caused by an external mass M (i.e. the moon) on the horizontal axis. The figure can be rotated around its axis to get the distribution in space (Brosche and Schuh, 1998).

Brosche and Schuh (1998) provide a thorough review of solid Earth tides. Tidal forces are differential gravitational forces. Both the Moon and the Sun exert tidal forces on the Earth that are significant for most practical requirements, therefore a precise knowledge of their positions allows an accurate estimation of the tidal acceleration for any point at any time on the Earth's surface.

Figure 2-19 describes the basic principle that generates Earth tidal motion on the Earth surface.

There are different contributions to site displacements. Solid Earth tides affect the Earth's potential adding a deformation. Seawater movement causes a loading on the elastic mantle of the Earth that is commonly known as ocean loading effect. The so-called "polar motion", that is the motion of the instantaneous rotation axis of the Earth, (described by IERS bulletins) leads to a change in the rotational centrifugal force. This effect causes an additional deformation of the Earth that is known as the solid pole tide (Xiao and Xia, 2003).

2.10.2 Gravitational models

The induced variations in the Earth's gravitational field cause perturbations in satellites' orbits. McCarthy and Petit (2004) in their technical note provide a well-recognised description of the procedure to include Earth tide induced potential into gravitational models currently in use.

IERS recommendations have to be implemented in all accurate procedures for orbit determination. According to Kudryatsev (2002), an accuracy of 1-2 cm might be achieved for a satellite in a MEO orbit (similar to GLONASS) applying the prescriptions included in McCarthy (1996). IERS 2003 models are implemented in practically all geodetic applications therefore Earth tides' effects on orbiting satellites can be modelled precisely.

2.10.3 Site displacements models

McCarthy (1996) and McCarthy and Petit (2004) provide the methodology to reconstruct site displacements on the Earth crust induced by tidal phenomena.

This phenomenon is usually represented referring to an Earth-fixed frame. Solid Earth tides cause displacements of the order of up to several decimetres, the pole tide may have an impact of up to a few centimetres depending on the pole position and ocean loading effects are usually in the range of some centimetres.

These displacements cannot be neglected when focussing a SAR image with a very long integration time as these displacements might cause image defocussing and blurring. Displacements introduced by Earth tides vary smoothly therefore, their variations along the synthetic aperture can be neglected (Milbert, 2002).

2.10.4 Analysis of site displacements

The different contribution to site displacements will be presented in the following sections. Section 2.10.4.1 presents the effect of solid Earth tides; ocean loading is discussed in section 2.10.4.2 , pole tide has been covered in section 2.10.4.3 , atmospheric loading has been looked into in section 2.10.4.4 .

2.10.4.1 Solid Earth tide

McCarthy and Petit (2004) provide a detailed algorithm that provides site displacements induced by solid Earth tides. A detailed description of the procedure

implemented to estimate solid Earth tide contribution is beyond the scope of the present research. Schuler (2001) provides a simple explanation of the phenomenon. A complete analysis is included in McCarthy (1996) and McCarthy and Petit (2004) as well in many other publications in literature.

Milbert (2002) implemented the recommendations included in IERS Convention 2003 as this is the current reference publication and provides, given ellipsoidal latitude and longitude, the values of the displacement in an Earth-fixed reference system at a given date.

An output file that has been obtained running the code *solid*, a free-ware code provided by Milbert (2002) has been enclosed in Appendix D.

2.10.4.2 Local site displacement due to ocean loading

McCarthy and Petit (2004) provide a clear description of the displacements due to ocean loading. *"Ocean tides cause a temporal variation of the ocean mass distribution and the associated load on the crust and produce time-varying deformations of the Earth.*"

IERS Convention 2003 provides an analytical scheme to estimate site displacement induced by ocean loading starting from Ocean tide models.

Yi *et al.* (2000) describe the procedure to estimate the load tide time series at a given location using a Green's function and an ocean tide model. Following the treatment presented by McCarthy (1992), also included in Schuler (2001), the displacement ΔC at a given location is given by:

$$\Delta C = \sum_j f_j A_j \cos\left(\omega_j t + \mu_j + \chi_j - \Phi_j\right) \qquad \text{Equation 2-104}$$

In Equation 2-104, j refers to a particular tidal constituent;
f_j and μ_j are coefficients that depend on the lunar mode;
χ_j is the astronomical argument at t=0;
A_j, ω_j and Φ_j are the amplitude, frequency and phase of the ocean tide constituent taken into account.

Equation 2-104 can be evaluated for all the different constituents that contribute to ocean tidal effects: semidiurnal waves (M_2, N_2, S_2, and K_2) and diurnal waves (K_1, O_1, P_1, and Q_1). The coefficients that relate to each constituent are estimated using an ocean tide model. The different ocean tide models produce results that are similar within 5% of their absolute displacement. This value could be considered as the accuracy of the prediction (Scherneck, 2006).

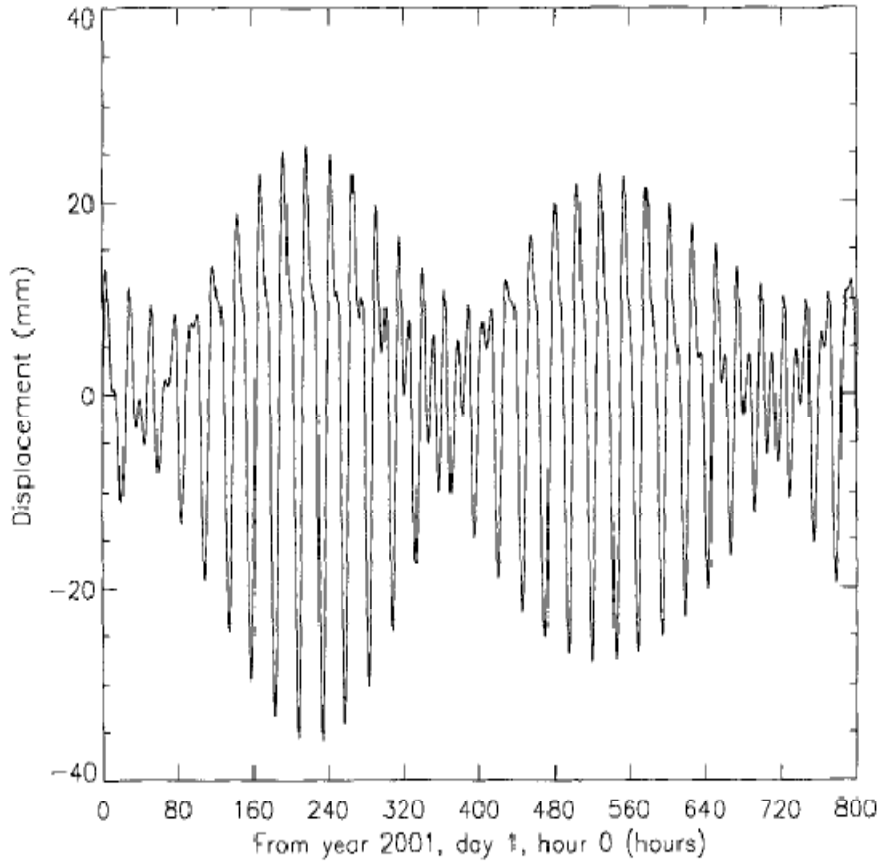

Figure 2-20. Vertical displacements due to ocean loading calculated at 1 hour interval at latitude 66.0° S and longitude 120.0° E. (Yi *et al.*, 2000).

The above-mentioned parameters are estimated using the models described by Scherneck (1991) for any station on the globe. A typical output has been generated using the software provided by the Onsala Space Observatory (Scherneck, 2006). The output has been enclosed in Appendix D.

The amplitude of this displacement is relatively small (a few centimetres). According to McCarthy (1992) (reported in Yi *et al.*, 2000) the accuracy of the vertical displacement predicted by this model is thought to be about +/- 3 mm.

Figure 2-21 shows the amplitude of the ocean loading effect due to M_2 load tide. Simulations have been carried out with a numerical model described in Egbert and Erofeeva (2002). The picture shows that the influence of ocean loading can be significant over coastal areas but can be neglected (or is far reduced) over continental areas.

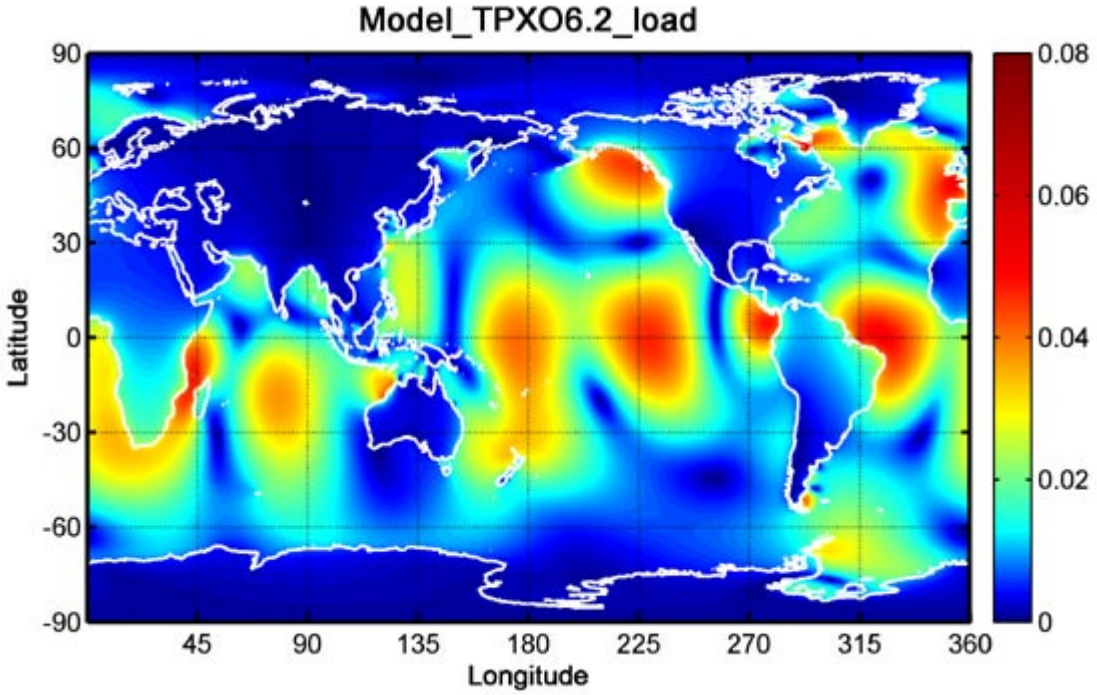

Figure 2-21. Map of M_2 load tide height amplitude (m) from the model developed by Egbert and Erofeeva (2002).

Advanced modelling techniques that take advantage of GPS networks proved to be able to model ocean loading effects with sub-millimetre accuracy (Vergnolle *et al.*, 2008).

2.10.4.3 Pole tide

The variation of station coordinates caused by the pole tide is of about a couple of centimetres. The maximum radial displacement is approximately 25 mm, and the maximum horizontal displacement is about 7 mm (McCarthy and Petit, 2004). The use of measured pole locations instead of predicted ones has probably little impact on the pole tide height accuracy. A pole location accuracy of about 50 cm is needed to get 1-mm accuracy on the pole tide height (ESA Envisat, 2006).

The pole tide is the response of the ocean (and of the elastic earth) to variations in the centrifugal force caused by wobbling of the earth's rotation axis. The pole tide has two dominant frequencies: annual and 14-month (Figure 2-22), the latter being the period of the Chandler Wobble (NASA JPL, 2005).

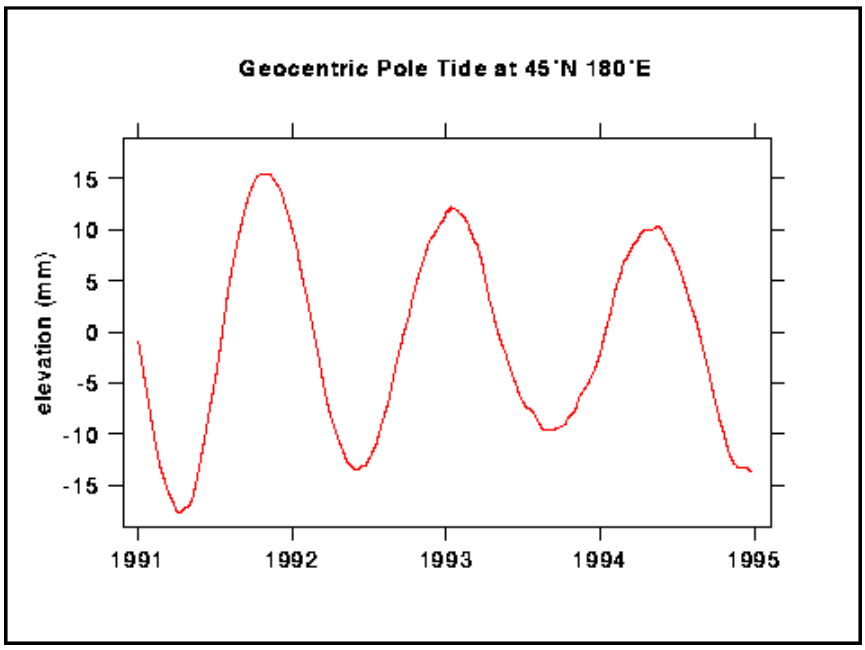

Figure 2-22. Geocentric (i.e. earth plus ocean) pole tide, at a point along the dateline at latitude 45 N and longitude 180° (NASA JPL, 2005).

2.10.4.4 Atmospheric loading

McCarthy and Petit (2004) describe atmospheric loading as another source of site displacement. For geodetic applications, its contribution is modelled using geophysical or empirical models.

The temporal and spatial scale of a GeoSAR image does not allow atmospheric loading to provide a significant contribution to differential site displacement. McCarthy and Petit (2004) report that pressure variations of about 20 hPa can cause a significant atmospheric loading effect. Such pressure changes might happen on spatial scales of 1000-2000 km and time scales of several weeks (McCarthy and Petit, 2004). This time scales are not relevant to GeoSAR processing.

2.10.5 Earth tides phase delay – summary

Earth tides are relevant to GeoSAR as they cause a significant terrain displacement during the long integration time. Background information provided in this section has the purpose of estimating the order of magnitude of this perturbation and the accuracy of the models available in literature. Further details about Earth tides effects on SAR imaging are provided in section 6.2

2.11 Tropospheric phase delay

The following sections briefly outline the principles on which tropospheric delay modelling is based. Meteorological inputs are required to run delay models.

Section 2.11.1 presents the rationale about tropospheric phase delay.

Section 2.11.2 provides a review about the tropospheric delay models that are available in literature without considering their theoretical background but focussing on their expected accuracy.

Section 2.11.3 provides the reader with the required background about turbulence and its effect on tropospheric phase delay.

2.11.1 Rationale

Hall *et al.* (1996) define the troposphere as "*the lowest region of the atmosphere, in which temperature usually decreases with height. Its upper limit is the base of the tropopause and is about 17 km high at the equator and 9 km high at the poles*".

The refractive index of clear air in the troposphere has a great influence on propagation of radio waves at frequencies greater than 30 MHz. The electric field **E** of a plane wave propagating in a medium of constant refractive index *n* has a space-time variation given by (Hall *et al.*, 1996).

$$\mathbf{E}(\mathbf{r},t) = \mathbf{E}_0 \exp\left\{i\left(n\ \mathbf{k}_0 \bullet \mathbf{r} - \omega t\right)\right\} \qquad \text{Equation 2-105}$$

In Equation 2-105, characters in bold represent vectors;
$\mathbf{k_0}$ is a vector perpendicular to the wave front;
r is the distance vector;
n is the refractive index.

Variations in the refractive index are crucial to understanding the propagation of electromagnetic waves in the troposphere. Hall *et al.* (1996) provide a thorough description of the main properties of the refractive index.

For the phase of an electro-magnetic wave, the geometrical distance differs from the optical path by the difference δS_{NEU} that is called neutral slant range delay.

$$\delta S_{NEU} = \int_{ATM} n(s)\, ds - \int_{VACUUM} ds \qquad \text{Equation 2-106}$$

In Equation 2-106, δS_{NEU} is the total/neutral slant path delay from receiver antenna to satellite;
n is the index of atmospheric refraction;
ds: differential increment in distance with respect to the line of sight;
ATM: ray path from the target to the satellite through the atmosphere;
VACUUM: virtual path of a ray from the target to the satellite through vacuum.

Refractive index is not equal to one (vacuum) due to the molecular constituents of the air, principally nitrogen, oxygen, carbon dioxide and water vapour. There is also a contribution given by polarisability of the molecules (Hanssen, 2001). It is usual to work with the non-dimensional parameter *N* defined in Equation 2-107.

$$N=(n-1)\times 10^{-6} \qquad \text{Equation 2-107}$$

Zenith delays are obtained using the radio refractive index of air as a starting point (Leick, 2004).

$$N = k_1 \frac{p_d}{T} Z_d^{-1} + k_2 \frac{e}{T} Z_w^{-1} + k_3 \frac{e}{T^2} Z_w^{-1} \qquad \text{Equation 2-108}$$

In Equation 2-108, *N* is the reduced index of refraction;
$k_{1..3}$ are the indexes of refraction;
$Z_{d/w}$ are the compressibility factors for dry and wet air;
e is partial water vapour pressure;
p_d is dry pressure.

Davis *et al.* (1985) give the following interpretation of Equation 2-108. The very first term characterizes the effect of the induced dipole moment of the dry constituents, the second term is due to the dipole moment of water vapour and the third term represents dipole orientation effects of the permanent dipole moment of water molecules.

Introducing the equation of state for the gas constituents and including various constants, Leick (2004) defines a hydrostatic (Equation 2-109*)* and wet (non-hydrostatic) refractivity (Equation 2-110).

$$N_d = k_1 \frac{p}{T} \qquad \text{Equation 2-109}$$

$$N_{wv} = k_2^{'} \frac{p_{wv}}{T} Z_{wv}^{-1} + k_3 \frac{p_{wv}}{T^2} Z_{wv}^{-1} \qquad \text{Equation 2-110}$$

Zenith Wet Delay (ZWD) and Zenith Hydrostatic Delay (ZHD) can be obtained integrating the refractivity index in Equation 2-109 and Equation 2-110. Zenith Neutral Delay or Total Delay (ZND) is the sum of the two components.

$$ZHD = 10^{-6} \int N_d (h)\, dh \qquad \text{Equation 2-111}$$

$$ZWD = 10^{-6} \int N_{wv} (h)\, dh \qquad \text{Equation 2-112}$$

$$ZND = ZHD + ZWD \qquad \text{Equation 2-113}$$

ZWD is often called the "*wet component*". This is not too wrong as it is mainly caused by the vertical distribution of water vapour in the troposphere. According to Bevis *et al.* (1992), the hydrostatic delay is often referred to as "dry component". This omits the fact that water vapour actively influences both the wet and the hydrostatic delay components. Nevertheless, the largest contribution to the hydrostatic delay can be traced back to dry air (Hanssen, 2001).

Tropospheric delay is shorter in zenith direction and increases with the zenith angle as the air mass traversed by the signal increases (Leick, 2004). Therefore, slant delays (i.e. SHD, Slant Hydrostatic Delay, SWD, Slant Wet Delay, STD, Slant Total Delay) are usually larger than the equivalent zenith delays.

$$SHD = ZHD\, m_h (\vartheta) \qquad \text{Equation 2-114}$$

$$SWD = ZWD\, m_{wv} (\vartheta) \qquad \text{Equation 2-115}$$

$$STD = ZHD\ m_h (\vartheta) + ZWD\ m_{wv} (\vartheta) \qquad \text{Equation 2-116}$$

In the previous equations, $m_h(\vartheta)$ is the hydrostatic delay mapping function;
$m_{wv}(\vartheta)$ is the wet delay mapping function.

The mapping functions model the temporal and spatial variability of the troposphere (Leick, 2004). They will be discussed in further details in the following sections.

The troposphere is not a dispersive medium and its effects cannot be removed through dual-frequency chirps. The effect of the dry component is relatively weak because it has slow scale variations. Sparse calibration points could be used to reduce its effects.

The wet delay can be as small as a few centimetres or less in arid regions. Although the wet delay is much smaller, it is usually far more variable and more difficult to remove (Bevis *et al.*, 1996).

To investigate the sensitivity Hanssen (2001) suggests the evaluation of the following derivatives:

$$\frac{\partial N_{wet}}{\partial e} = \frac{k_2}{T} + \frac{k_3}{T^2}; \qquad \text{Equation 2-117}$$

$$\frac{\partial N_{wet}}{\partial T} = -\frac{k_2 e}{T^2} - \frac{k_3 e}{T^3}; \qquad \text{Equation 2-118}$$

The ratio *R* of the two derivatives (Equation 2-117 and Equation 2-118) is usually in the range $4 \leq |R| \leq 20$ (Hanssen, 2001). This means that the refractivity *N* is *R* times more sensitive for a 1 hPa change in the partial pressure of water vapour *e* than for a 1°C change in *T* (both estimated on the Earth's surface). The lowest region of the parameter *R* is possible only where there are high temperatures and high water vapour partial pressure values.

Methods to estimate wet delay from surface measurements show quite poor accuracy (Askne and Nordius, 1987). Kolmogorov's model (Tatarski, 1961) shows that the local spatial variability has power law behaviour. The scale factor depends on time and on global location. There is a strong need for calibration points that could be used to identify at least the slow varying phase terms of the tropospheric wet delay. For the purpose, GPS water-vapour estimates might be used as well as Water Vapour Radiometer (WVR) instruments (Williams *et al.*, 1998).

In interferometric applications, the use of calibration and of multiple interferometric data stacked could be used to average tropospheric artefacts (NASA JPL, 2003). Nevertheless, at the present state of the art tropospheric delay is the major limiting factor in the accuracy achievable with interferometric techniques applied to conventional LEO SAR system.

As previously mentioned, the wet tropospheric delay cannot be accurately predicted. Treuhaft and Lanyi (1987) suggested a statistical model that has been confirmed in literature (Williams *et al.*, 1998). Their model is based on the assumption that the spatial structure of the delay fluctuations could be approximated by Kolmogorov's turbulence theory (Tatarski, 1961). The second hypothesis is that temporal variations are due to spatial patterns moved by the winds. The last assumption, given the value of wind velocity, relates the temporal structure function to the spatial structure function.

Zhu *et al.*, 2007 describe some models, currently still under development, that allow a 3D water vapour mapping and a consequent very accurate tropospheric error prediction.

2.11.2 Tropospheric delay models

Tropospheric delay has been divided into hydrostatic and wet components. The following sections outline the analytical models present in literature. The theoretical background of the models is not taken into account as it is beyond the scope of the

research. The accuracy of the predictions have been discussed as it is a crucial aspect in tropospheric delay compensation

2.11.2.1 Zenith Hydrostatic Delay (ZHD)

Three different models that provide zenith hydrostatic delay in closed form will be hereafter presented (Table 2-2). They are based on a range of assumptions and therefore different levels of accuracy are expected.

Table 2-2. Hydrostatic delay models.

Model	*Section*
Hopfield hydrostatic delay model	Section 2.11.2.1.1
Saastamoinen hydrostatic delay model	Section 2.11.2.1.2
MOPS hydrostatic delay model	Section 2.11.2.1.3

2.11.2.1.1 Hopfield hydrostatic delay model

This model (Schuler, 2001) is based on the assumption that air behaves as a perfect gas and that there is a constant temperature. ZHD is expressed in the form:

$$\mathrm{ZHD}=1.552\ 10^{-5}\left[\frac{K}{hPa}\right]\frac{p_0}{T_0}\left(40136\left[m\right]+148.72\left[\frac{m}{K}\right]T_0\right) \quad \text{Equation 2-119}$$

In Equation 2-119, p_0 is the static pressure at the target site in *hPa*;
T_0 is the static temperature at the target site in *K*.

2.11.2.1.2 Saastamoinen hydrostatic delay model

This model has become very popular due to its high accuracy. Elgered *et al.* (1991) give the following *rms* error budget: the error in the refractivity constant contributes to about 2.4 mm. The uncertainty in the gravity reduction has a marginal influence of 0.2 mm as well as the uncertainty of the universal gas constant (0.1 mm) and the variability of the dry mean molar mass (0.1 mm). Furthermore, it should be noted that no temperature measurements are needed in contrast to the Hopfield model, but the

height of the station and its latitude are used for the computation of the gravity correction.

$$ZHD = \frac{0.0022767\left[\frac{m}{hPa}\right]p_0}{1-0.00266\cos(2\varphi)-0.00028\left[\frac{1}{km}\right]h} \qquad \text{Equation 2-120}$$

In Equation 2-120, φ is the ellipsoidal latitude;
h is the site height over the ellipsoid in *km*;
p_0 is the static pressure at the scatterer site in *hPa*.

2.11.2.1.3 MOPS Hydrostatic Delay Model

If meteorological data are not available, MOPS (1998) hydrostatic delay model could be applied as it uses only standard meteorological data that depend only on latitude and consider seasonal variations.

Meteorological measurements are modelled with the help of default data sets. This advantage is also the major drawback of this model as no one can expect a superior accuracy from this approach. Poorly modelled pressure values, for example, will quickly degrade the accuracy of the hydrostatic delay. An error of 10 hPa contributes to approximately 2.2 cm, which may likely occur in some regions.

2.11.2.1.4 Comparison between the different hydrostatic delay models

Schuler (2001) provides an evaluation of the accuracies expected for the presented tropospheric delay models. As the Saastamoinen model is accepted to be the most accurate, it is considered as a reference. Statistics have been evaluated for about 100 different IGS network station location.

The Hopfield model only shows a very small standard deviation of 0.2 mm with respect to the Saastamoinen reference model. The *rms* values show a systematic trend with increasing latitude. Smallest deviations occur near the equator, largest (more than 9 mm) in polar regions. This effect is mainly due to the missing gravity reduction in the Hopfield approach, which treats the gravity as a constant value. In global average, the systematic error is about 4 mm.

As expected, the MOPS model performs much worse than the Hopfield model in comparison to Saastamoinen's theory since systematic effects are the dominant contributors to its error budget.

Pressure prediction is especially poor for some sites in the polar regions of the southern hemisphere. In global average, the *rms* is about 16 mm. This is more than 4 times larger than the *rms* of the Hopfield model.

2.11.2.2 Zenith Wet Delay (ZWD)

Zenith Wet Delay is affected by the vertical distribution of water vapour therefore it is very difficult to retrieve this parameter from a model that includes only surface measurements. Schuler (2001) provides a review of the main zenith wet delay models and estimates their accuracy. Models described in the following sections have been listed in Table 2-3.

Table 2-3. Wet delay models.

Model	*Section*
Hopfield wet delay model	Section 2.11.2.2.1
Ifadis wet delay model	Section 2.11.2.2.2
Mendes hydrostatic delay model	Section 2.11.2.2.3
MOPS hydrostatic delay model	Section 2.11.2.2.4

2.11.2.2.1 Hopfield Wet Delay Model

Hopfield models the wet component of the refractivity in closed form as a function of the partial water vapour pressure at the scatterer position (Schuler, 2001).

$$ZWD = \left\{ 555.7\left[\frac{mK^2}{hPa}\right] + 1.792 \bullet 10^{-4}\left[\frac{mK^2}{hPa}\right] \exp\left(\frac{t_0}{22.90[°C]}\right)\right\}\frac{e_0}{T_0^2} \quad \text{Equation 2-121}$$

In Equation 2-121, T_0 is the temperature at the scatterer site in *K*;
t_0 is the temperature at the scatterer site in ℃;

e_0 is the partial water vapour pressure at the scatterer site in *hPa*.

2.11.2.2.2 Ifadis Wet Delay Model

Ifadis (1986) proposes to model the zenith wet delay as a function of surface pressure, partial water vapour pressure and temperature:

$$ZWD = 0.554 \cdot 10^{-2}\left[m\right] - 0.880 \cdot 10^{-4}\left[\frac{m}{hPa}\right](p - 1000) + 0.272 \cdot 10^{-4}\left[\frac{m}{hPa}\right]e + 2.771\left[\frac{m°C}{hPa}\right]\frac{e}{T} \qquad \text{Equation 2-122}$$

In Equation 2-122, p is the surface pressure in *hPa*;
e is the partial water vapour pressure at the scatterer site in *hPa*;
T is the temperature at the scatterer site in °C.

2.11.2.2.3 Mendes Wet Delay Model

Mendes and Langley (1998) derived a linear relation between wet delay and partial water vapour pressure:

$$ZWD = 0.122\left[m\right] + 0.00943\left[\frac{m}{hPa}\right]e \qquad \text{Equation 2-123}$$

In Equation 2-123, e is the partial water vapour pressure at the scatterer site in *hPa*.

2.11.2.2.4 MOPS wet delay model

The MOPS model (MOPS, 1998) reduces the wet delay estimate to the observation height H above the sea level in metres:

$$ZWD = ZWD_0\left(1 - \frac{\beta H}{T}\right)^{\frac{(\lambda-1)g}{R_d\beta}-1} \qquad \text{Equation 2-124}$$

With a mean gravity of g=9.80665 m/s^2. β and λ are parameters that come from the latitude of the site (MOPS, 1998).

$$ZWD_0 = \frac{10^6 k_3 R_d}{g_m(\lambda+1)-\beta R_d}\frac{e}{T}$$ Equation 2-125

In Equation 2-125, k_3 = 382000 K^2hPa^{-1};
R_d=287.054 J kg^{-1} K^{-1};
G_m=9.784 m s^{-2}.

2.11.2.2.5 Comparison between the different wet delay models

Schuler (2001) provides a useful comparison between the different wet delay models described in the previous sections. The truth data has been obtained using total delays measured from the IGS network and subtracting the Saastamoinen hydrostatic delay, which is commonly considered as a reference.

The Hopfield and the Mendes models present an *rms* error of about 3 cm. The mean error is 6 mm for Mendes (1 mm for Hopfield) while the standard deviation is 12 mm for Mendes (12.4 mm for Hopfield).

The MOPS model has an *rms* error of about 5 cm.

2.11.2.2.6 Advanced atmospheric modelling

Holley *et al.* (2008) provide a description of a procedure for atmospheric water vapour modelling that allows predicting very accurate wet delay corrections.

The UK Met Office's Unified Model (UM) is a non-hydrostatic, semi-Lagrangian forward numerical model, which was used to produce 3D water vapour fields corresponding to SAR acquisition dates. The UM's representation of initial and boundary conditions uses a nested domain scheme. Outer domain, with coarser grid spacing and resolution, provide boundary conditions for inner domains (Figure 2-23). The smallest domain covers the site of interest at 300m grid spacing, with ten second sampling (Holley *et al.* 2008).

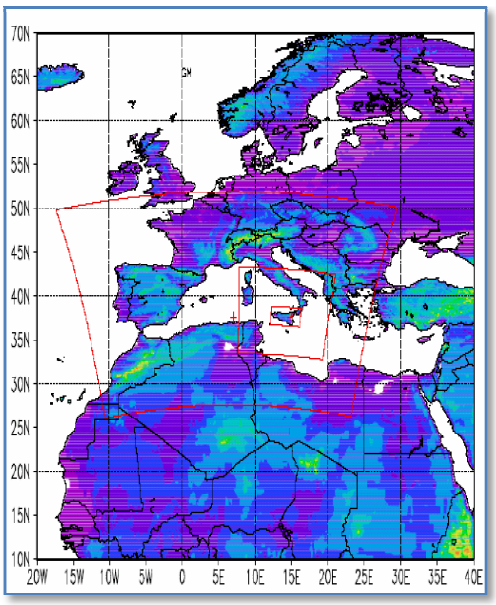

Figure 2-23. Nested domain for atmospheric water vapour mapping (Holley *et al.* 2008).

The input information dataset is extremely complex: global atmospheric parameters, orography, land use and vegetation. However, the outcome of the simulations provides an accurate 3D map of temperature, pressure, water vapour, liquid cloud-water, solid cloud-water, wind speed and direction.

Zhu *et al.* (2007) compare the output of this model with instantaneous MERIS (Medium Resolution Imaging Spectrometer). The mismatch between the model and the MERIS fields (*rms* = 1.1 and 1.6 mm, for two different test cases) is comparable with the accuracy of the MERIS sensor itself.

Boehm *et al.* (2008) describe the Vienna Mapping Functions (VMF), a very accurate GPS-derived mapping function for tropospheric delay estimation. Their methodology has been developed for space geodetic techniques, such as GNSS or VLBI, which are based on data from numerical weather models. Their analysis shows a very good accuracy in wet delay measurements at the 1 mm level.

2.11.2.3 Mapping functions

Mapping functions have been introduced when the difference between slant delay and zenith delay has been discussed. Tropospheric delay is shortest in the zenith direction and its projection on the slant range direction requires a specific function, called the mapping function.

$$m(z,p,T)=\frac{SND}{ZND}$$ Equation 2-126

In Equation 2-126, z is the zenith angle;
p,T are pressure and temperature at the scatterer site.

For the neutral (total) component, a simple conversion could be used that is accurate up to zenith angle (i.e. ϑ) of about 60°.

$$m(\vartheta)=\frac{1}{\cos\vartheta}=\csc\vartheta$$ Equation 2-127

Leick (2004) suggests the use of a more complex model. The one that is in common use is reported in Niell (1996). It is valid for both hydrostatic and wet delays.

$$m(\vartheta)=\frac{1+\dfrac{a}{1+\dfrac{b}{1+c}}}{\cos\vartheta+\dfrac{a}{\cos\vartheta+\dfrac{b}{\cos\vartheta+c}}}$$ Equation 2-128

The coefficients a, b and c are a function of the latitude of the station. Their values could be easily found in literature for both hydrostatic and wet delays (Leick, 2004, Schuler, 2001).

2.11.2.4 Wet delay and PWV

Models presented in previous sections allow to estimate wet tropospheric delay using measurements carried out on the Earth's surface (i.e. static pressure, temperature, humidity). Using dedicated instruments such as radiosondes, according to Snider (2000), Precipitable Water Vapour (PWV) could be determined with an accuracy of about 0.5 mm. This could be used to model wet tropospheric delay with an extremely good accuracy.

According to Bevis *et al.* (1996), Hanssen (2001) and other authors, slant tropospheric wet delay is expressed as a function of the precipitable water vapour. The delay is expressed as:

$$SWD=\Pi^{-1}PWV$$ Equation 2-129

In Equation 2-129 Π is a dimensionless constant of proportionality that is about 0.15 (Bevis *et al.*, 1996; Hanssen, 2001).

"*Meteorology, ground-based GPS has become an operational tool that can measure precipitable water vapour (PWV) with high accuracy (1~1.5mm) during all-weathers, and with high temporal resolution (e.g. 5 minutes) at low cost*". (Li, 2004).

2.11.2.5 Liquid water contribution

Hanssen (2001) specifies that, for SAR imaging, liquid water present along the ray path has a contribution in the determination of the refraction index. In many geodetic applications where the total slant delay is measured, this term is neglected as it is only a few millimetres. As a SAR system is sensitive to spatial and temporal variations of the wet delay while it is blind to total slant delays, this term cannot be neglected. However, liquid water (i.e. precipitations and clouds) varies in space and time more than water vapour, its effect is minor after the averaging carried out in SAR focussing. Calculations are usually carried out assuming a homogeneous cloud layer of 1 km thick. Variations in air refractivity *N* are usually estimated assuming an empirical expression (Hanssen, 2001).

$$N_{liq} = 1.45 \ \frac{m^3}{g} [W]_{\frac{g}{m^3}} \qquad \text{Equation 2-130}$$

In Equation 2-130, *W* is the liquid water content in g/m^3.

The integral of Equation 2-130 is usually labelled as liquid delay.

2.11.3 Turbulent scatter

Local heterogeneities in the troposphere are usually related to oscillations in wet delay. They are caused by small deviations of temperature and humidity from the background value. Shear forces between two moving air masses create these irregularities. The main effect is the creation of turbulent eddies at the outer scale of turbulence (about 100 m) (Hall *et al.*, 1996). In fully developed turbulence, this mixing continues down to the inner scale of turbulence (about 1 mm) where the energy is dissipated.

Spatial statistics of a turbulent medium are described by a quantity called the structure function. For a random field the structure function D_x between two points is (Tatarski, 1961).

$$D_x\left(\vec{r},\vec{R}\right) = \left\langle \left[x\left(\vec{r}+\vec{R}\right) - x\left(\vec{r}\right) \right]^2 \right\rangle; \qquad \text{Equation 2-131}$$

In Equation 2-131, angle brackets indicate the ensemble averages;
x is the random field considered (e.g. temperature, humidity);

$\vec{r}, \vec{R}$ are distance vectors.

The statistical model adopted for turbulence is the power law model. According to this assumption that has been verified by many experimental tests, the structure function has the form presented in Equation 2-132.

$$D_x(R) = C^2 R^{\nu}; \qquad \text{Equation 2-132}$$

In Equation 2-132, ν is the power spectrum index.

The power law spectrum is:

$$P_x(f) = P_0 \left(\frac{f_0}{f} \right)^{\beta}; \qquad \text{Equation 2-133}$$

In Equation 2-133, f is the spatial frequency;
β is the spectral index;
P_0, f_0 are normalising constants.

The relation between structure function and the power spectrum of a power law process is:

$$D_x(R) = C^2 R^{\beta-1}; \qquad \text{Equation 2-134}$$

From dimensional considerations, Tatarski (1961) showed that $\nu=2/3$ for elementary turbulence according to the Kolmogorov's theory.

2.11.4 Tropospheric phase delay – summary

The variations of the local meteorological variables P_d, T and e cause variations in the refractive index at various scales:

- on the medium scales (100 m – 100 km) the ground and micro meteorological phenomena can produce spatial and temporal variations;
- on the small scales (<100 m) turbulent mixing causes scattering and scintillation (Hall *et al.*, 1996).

The tropospheric delay has been divided in two terms: dry and wet delay.

The dry term is related to the surface static pressure (Hanssen, 2001). High and low pressure zones have usually minimal spatial variations with dimensions larger than the SAR image. This implies that the dry term has only a limited influence even on quite

large SAR images. However, during the integration time there could be a significant pressure variation (i.e. 8 hours).

The wet part of the refractive index has much more significant spatial and temporal variations that have to be taken into account when focussing a GeoSAR image. It is a function of the relative humidity. This atmospheric property can vary strongly both spatially and temporally thus causing unpredictable variations in the tropospheric wet delay.

Moisture variations of 1 g/kg^{-1} are quite frequent even on a 1 km spatial scale. This confirms the severe variability of the wet delay term.

Background information provided in this section has the purpose of estimating the order of magnitude of this perturbation and the accuracy of the models available in literature. Further details on tropospheric effects on SAR imaging are provided in section 6.3

2.12 Ionospheric phase delay

This section provides a literature background about the ionosphere and its influence on SAR signals and on SAR focussing.

Section 2.12.1 provides some basic information about the ionosphere and phase delays induced by ionosphere. The following section (2.12.2) discusses the effects of phase delays on SAR signal.

Section 2.12.3 presents the effects of ionospheric heterogeneities on SAR images. Section 2.12.4 discusses the aspects related to spatial and temporal TEC variations. The discussion follows with an analysis of the probability of occurrence of ionospheric perturbations (2.12.5) and with the presentation of some TEC datasets that are freely available in literature and that have been used in the present research (2.12.6).

2.12.1 Rationale

When solar radiation strikes the molecules of the upper atmosphere, electrons are dislodged from atoms and produce the ionospheric plasma. The ionosphere is the region of the atmosphere in which ionisation of gases is particularly intense and it extends from heights of about 60 km to 600 km. The effect of this layer is very much dependent on frequency (Hall *et al.*, 1996).

This effect occurs mostly on the sunlit side of the Earth. Only the most energetic part of the spectrum (the extreme ultraviolet and X-ray) produces this ionization. The presence of these charged particles makes the ionosphere an electrical conductor, which supports electric currents and affects radio waves.

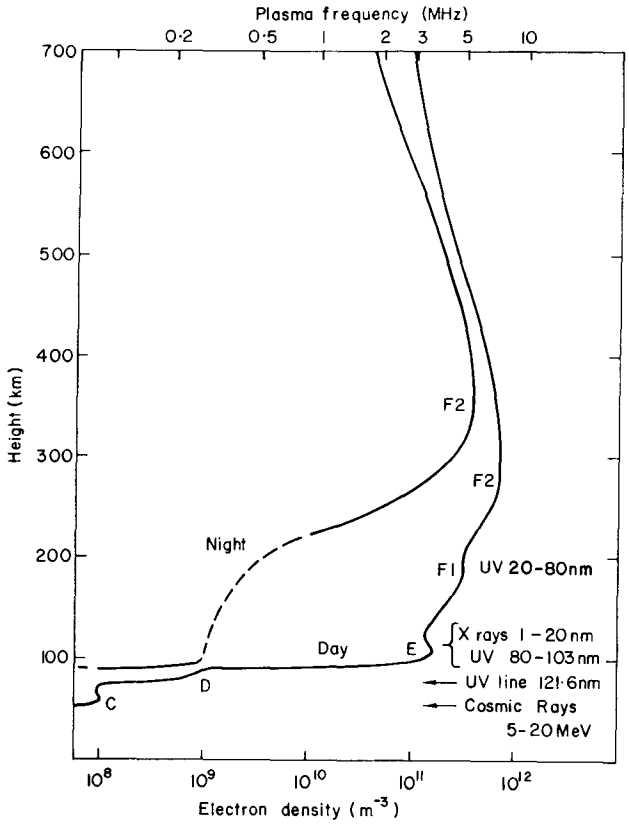

Figure 2-24. Typical mid-latitude electron density profiles for moderate solar activity showing the radiations that produce the ionospheric layers. (Hall *et al.*, 1996).

As plasma diffusion along the magnetic field lines proceeds much more rapidly than across the magnetic field, structures orthogonal to the magnetic field in the lower ionosphere are maintained at all altitudes giving to the ionosphere a tube-like structure.

The vertical distribution of electron concentration has a typical profile where three different zones are identified (i.e. D, E and F zones). The electron density profile is obviously influenced by solar activity (Figure 2-24). Its value is higher during daylight hours than during the night. There is even a strong influence of the 11-year solar cycle (Figure 2-25). All the ionospheric disturbances can be traced back to anomalies in the solar energy production.

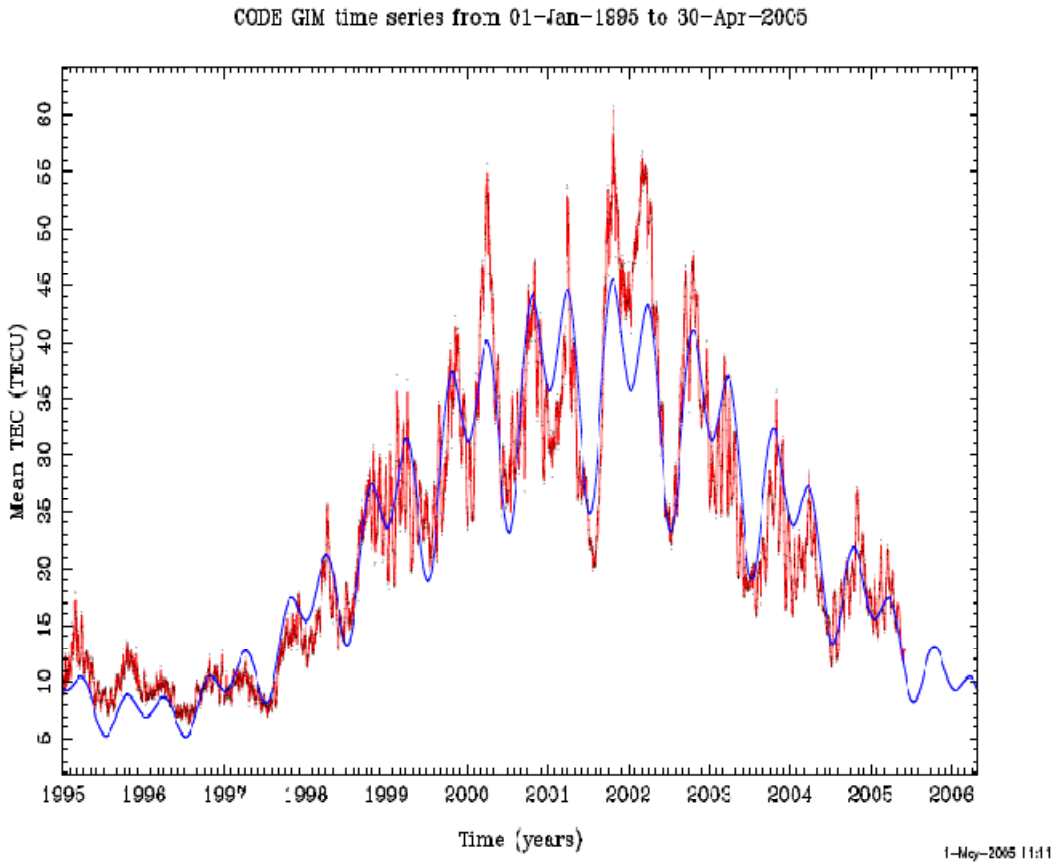

Figure 2-25. Temporal variation of the total electron content (TEC) of the ionosphere during the last 11 years. The temporal axis covers a complete 11-year period of solar irradiance (from CODE Centre, Bern). The bold line shows a 7-parameter trend function (Meyer *et al.* 2006).

The *D-layer* (80-100 km) is the lowest part of the ionosphere and receives only a minor part of the ionising solar radiation. This layer disappears after sunset. The *E-layer* (100-140 km) has little more ionisation, but it fades in the upper layer after sunset, too. The most important and energetic layers are the *F1* (140-200 km) and *F2* (200-400 km).

The peak value is known as *NmF2*. The electron density profiles at altitudes higher than the electron peak are largely derived from the *NmF2* value.

"*In dispersive media like the ionosphere the phase velocity of a traversing electromagnetic wave is slightly higher than it would be if it was travelling through a vacuum"* (Meyer *et al.* 2006). The local electron density determines the refractive index μ of the ionosphere. The deviations of μ from unity are very small but the two-way path lengths are quite large for space borne radars thus this contribution has to be taken into account.

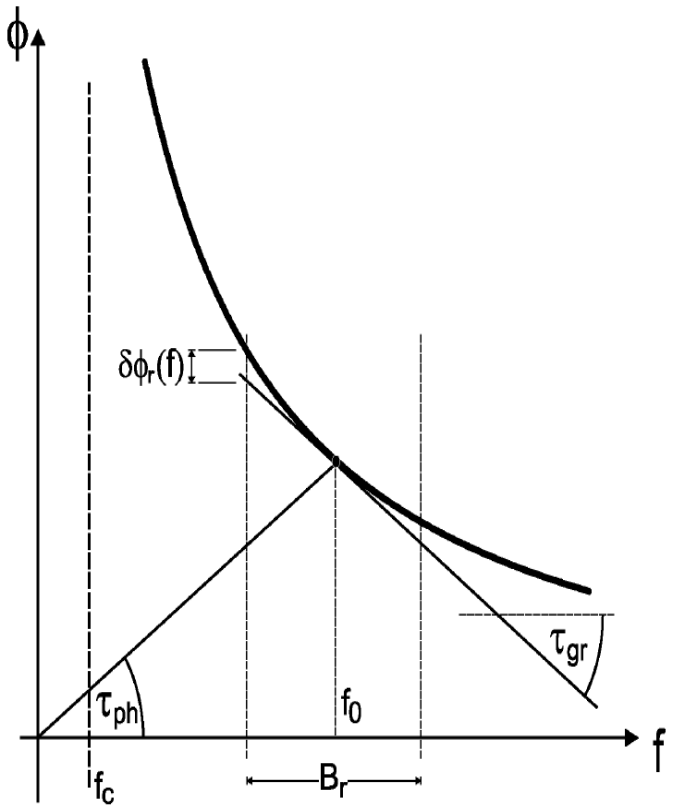

Figure 2-26. Phase behavior of the ionosphere and its parameterization by phase delay τ_{ph}, group delay τ_{gr}, and residual phase curvature $\delta\phi$(f). The traversing signal has the bandwidth B_r centred on centre frequency f_0. (Meyer *et al.* 2006).

The ionosphere can be treated as a perfect dielectric with a refractive index n_{iono} as in Equation 2-135 (Meyer *et al.* 2006).

$$n_{iono} \approx \left(1 - \frac{1}{2}\frac{e_l^2}{4\pi^2 m\varepsilon_0}\frac{n_e}{f^2}\right) = 1 - k\frac{n_e}{f^2} \qquad \text{Equation 2-135}$$

In Equation 2-135, k=40.28 m^3/s^2;
e_l is the elementary charge;
m is the electron mass;
ε_0 is the dielectric permittivity of vacuum;
f is the signal frequency.

It is convenient to introduce the column density of free electron, TEC (Total Electron Content), the integral of the number of free electrons over a column with unit area and length h.

$$TEC = \int_0^h n_e dh \qquad \text{Equation 2-136}$$

In Equation 2-136, TEC is measured in electrons/m^2;
n_e is the spatial density of free electrons (electrons/m^2).

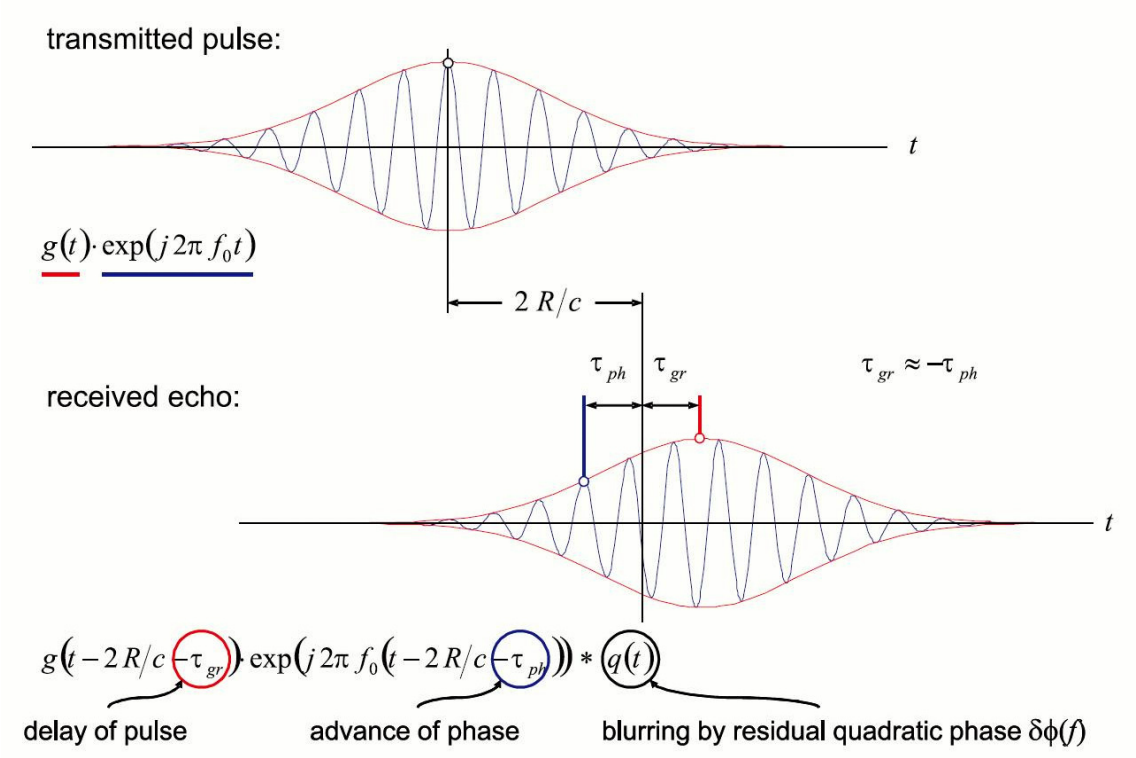

Figure 2-27. Schematic explanation of ionospheric propagation effects on a wide-bandwidth SAR signals (Meyer *et al.* 2006).

The two-way shift induced by the ionosphere is given by Equation 2-137.

$$\phi = -2\pi \frac{2k}{cf} \int_H n_i dh = -2\pi \frac{2k}{cf} TEC \qquad \text{Equation 2-137}$$

Hanssen (2001) points out that the effect of ionosphere is different on phase and on group delay. Group delay depends on electron content and affects carrier signal; phase delay is caused by dispersions in the ionosphere and affects even signal modulation. The group signal delay τ_{gr} and consequently the phase delay τ_{ph} is expressed by a series in the reciprocal of the carrier frequency f (Hanssen, 2001):

$$\tau_{gr} \approx \frac{A}{f^2} + \frac{B}{f^3} + \frac{C}{f^4}$$ Equation 2-138

Meyer *et al.* (2006) report the expression that is commonly used to express group delay.

$$\tau_{gr} \approx -\frac{1}{2\pi}\frac{d\phi(f)}{df} = -2\frac{k}{cf_0^2}TEC$$ Equation 2-139

The ionospheric layer is an all-pass filter that introduces a signal group delay τ_{gr}, a phase delay τ_{ph} and a residual phase curvature $\delta\phi$ that can cause an additional range blurring (Meyer *et al.*, 2006). Equation 2-140 shows the relation between phase and group delay.

$$\tau_{ph} = -\frac{4\pi f}{c}\delta_{gr} = -\frac{4\pi f}{c}\left(c\tau_{gr}\right) = -4\pi f\tau_{gr}$$ Equation 2-140

The effect of the ionosphere on radio waves is frequency dependent. This property is critical to estimate the ionospheric delay in application such as GPS.

Dual-frequency GPS receivers observe the delay between the two frequencies L_1 and L_2, which enables estimations of the unknowns in Equation 2-138.

Radio signals not incident from zenith are generally delayed as well as bent. To derive a mapping function that takes into account these effects, ionosphere is usually modelled as a single layer. The height of this layer is the altitude at which a ray coming from the satellite and directed towards the Earth's surface pierces the layer with maximal electron density. In general an effective ionospheric height h_{sp}=400 km is used.

Both phase and group delays are directly proportional to the total electron content (TEC), which is the summation of the electronic density along the path of the electro-magnetic wave.

The expression that relates vertical TEC (*VTEC*) and slant range TEC (*STEC*) is (Nava *et al.*, 2007):

$$VTEC = STEC\cos\chi$$ Equation 2-141

In Equation 2-141, *VTEC* is the vertical TEC;
STEC is the slant range TEC;
$cos\chi$ is the mapping function.

The mapping function is obtained from geometric considerations:

$$M = 1/\cos\chi \qquad \text{Equation 2-142}$$

$$\cos\chi \approx \sqrt{1-\left(\frac{R_e\cos\varepsilon}{R_e+h_{sp}}\right)^2} \qquad \text{Equation 2-143}$$

In Equation 2-143, R_e is the Earth's radius;
ε is the elevation angle relative to the horizon.
χ is the zenith angle.

2.12.2 Effects on SAR signal

This section discusses ionospheric effects on SAR signals focussing on group delay and phase delay.

2.12.2.1 Group delay

For a SAR acquisition with a look angle of χ degrees, the slant range delay (single way) in meters is expressed as (Xu *et al.*, 2004):

$$\delta_{p,iono} = \frac{K}{f^2} M(\chi) TEC \qquad \text{Equation 2-144}$$

In Equation 2-144, f is the SAR carrier frequency in Hz;
K is a constant = -40.28 m^3s^{-2} (Hanssen, 2001).
TEC is the total electron content (measured in electrons/m^2).

For a C band SAR with a quite steep look angle (23°) the sensitivity of the ionospheric delay to the total electron content is (Hanssen, 2001) given in Equation 2-145 (measured in m^3/electrons).

$$\partial\delta_{p,iono} / \partial TECU = -0.015 \qquad \text{Equation 2-145}$$

The one-way zenith ionospheric delay is given by Equation 2-144. At L band (1.5 GHz) the one-way ionospheric delay associated to a 1 TECU (1 TECU = 1 × $10^{16}m^{-2}$) variation is 0.17 m (i.e. about 1 wavelength). TEC units are usually used instead of the original TEC values.

Daily TEC varies between 20 TECU during the solar minimum and 100 TECU during the maximum of the solar cycle.

2.12.2.2 Phase delay

Following Equation 2-140 in section 2.12.1, the phase delay induced on the SAR signal is:

$$\tau_{ph} = \Delta\psi = -\frac{4\pi}{c_0}\frac{40.28}{f}TEC \qquad \text{Equation 2-146}$$

The phase advance of a SAR signal is calculated from the delay of its envelope (Xu *et al.* 2004; Meyer *et al.* 2006). Assuming a 1 TECU error in the knowledge of TEC the advance in SAR phase (two way) is 13.4 rad for L band (slightly larger than two wavelengths).

2.12.3 Ionospheric effects on SAR images

Ionospheric effects on SAR images have been discussed in many recent papers. All the results that have been published share a common assumption: a static ionosphere during the whole integration time (assumption that is acceptable for a LEO SAR but not for a GeoSAR). Therefore, ionospheric heterogeneities are usually considered a concern for SAR interferometry (that requires the knowledge of the ionosphere at two different epochs) more than for SAR image formation. It has to be said that variations in the ionosphere on time scales of about 1 second, are extremely unlikely therefore, the assumption of a frozen ionosphere becomes totally acceptable.

However, spatial TEC heterogeneities can affect SAR focussing causing blurring and distortion even if the integration time is very short. Meyer *et al.* (2006) provide a recent review on the effect of TEC heterogeneities on SAR images. They consider three different aspects:

- phase delays;
- group delays;
- non-linear phase terms.

Phase delays and non-linear phase terms affect mainly azimuth SAR processing as they perturb the phase of the signals processed. Group delay, on the other hand, affects range processing and introduces geometric distortions in the image.

Spatial scales of these disturbances reach from several meters up to several 100 km. Their magnitude is relatively small and is below 1 TECU for small-scale structures

(smaller 10 km), and about 1 TECU for medium scale structures (100 km to several 100 km).

The effect of TEC variations on SAR images strongly depends on their scale. The presence of small-scale electron density heterogeneities across the synthetic aperture length will cause quick phase fluctuations that result in a decrease of the along-track resolution of a SAR.

Inhomogeneities of larger spatial wavelengths may cause phase ramps across the along-track chirp, which result in an azimuth shift of objects in the affected region. These effects, dubbed *azimuth streaks*, were attributed to ionospheric effects the first time in Gray *et al.* (2000). TEC variations with spatial wavelength larger than the SAR image itself might be neglected.

2.12.3.1 Phase delays

Phase delays cause a distortion in azimuth processing, linear TEC gradient along the synthetic aperture causes an azimuth displacement of the target. Ionospheric perturbations with a spatial scale larger than the SAR image itself generate a slope in the range direction due to the different path lengths through the ionosphere. Small-scale disturbances generate local reduction of azimuth resolution as they reduce the actual coherent integration time.

According to Meyer *et al.* (2006), "*inhomogeneities of medium spatial wavelengths may cause "phase gradients" across the azimuth chirp, which result in an azimuth shift of objects in the focused image*".

According to Meyer *et al.* (2006), group delay affects the range envelope of the SAR image. A constant TEC phase screen introduces a cross-track displacement that is range dependent in the whole image while local heterogeneities will lead to geometric distortions in the final focused SAR image.

Across-track variations cause an incorrect location of the target on the ground. Given an additional group delay $\Delta\tau$ the slant range delay is (Curlander and McDonough, 1991):

$$\Delta r = \frac{c\Delta\tau}{2\sin\theta} \qquad \text{Equation 2-147}$$

In Equation 2-147, θ is the ground incidence angle (i.e. 50°).

A TEC variation of 1 TECU generates a group delay of about one wavelength at L band. The effect on range displacement is therefore negligible.

Spatial or temporal variations in the ionosphere cause phase variations that could be expressed as in Equation 2-148 (Belcher, 2008).

$$\delta\varphi = \beta_a x^2 \qquad \text{Equation 2-148}$$

In Equation 2-148, β_a is the azimuth focus parameter;
x is the along-track coordinate.

The parameter β_a could be determined applying the maximum contrast auto-focus technique, "that iteratively searches for the highest contrast range profile by adjusting the focussing parameter until a focus is achieved" (Belcher, 2008). The estimated accuracy is given in Equation 2-149 where L_W is the antenna beam-width on the ground and L_{SA} is the length of the synthetic aperture.

$$\left\langle \delta\beta_a^{\,2} \right\rangle = \frac{L_W}{L_{SA}^5}\frac{90}{SNCR} \qquad \text{Equation 2-149}$$

In case of a SAR that is exploiting its full synthetic aperture the expression of the *rms* focussing error $\delta\beta_a$ as a function of the SNCR (Signal to Noise Clutter Ratio) is expressed as in Equation 2-150.

$$\sqrt{\left\langle \delta\beta_a^2 \right\rangle} = \frac{1}{L_{SA}^2}\frac{\sqrt{90}}{\sqrt{SNCR}} \qquad \text{Equation 2-150}$$

2.12.3.2 Group delay

Ionospheric group delay affects range focussing in SAR image formation. The absolute level of TEC can cause a target range displacement in the image. The effect is also frequency-dependent and therefore could potentially cause range de-focus. Belcher (2008) reports that for a 1 GHz SAR (3 m ground resolution) a TEC level of about 7.4 TECU will cause a range delay of one resolution cell while range de-focus can happen if there is a TEC level of 149 TECU. Therefore range defocus is quite unlikely to happen.

Belcher (2008) investigates the effect of spatial TEC variations that affect SAR range focussing. This effect has been modelled assuming a phase contribution shown in Equation 2-151:

$$\delta\varphi = \beta_r f^2 \qquad \text{Equation 2-151}$$

In Equation 2-151, β_r is the range focus parameter;
f is the signal frequency.

The parameter β_r could be determined, as for β_a, applying auto-focus techniques such as maximum contrast (Belcher, 2008).

The theoretical accuracy of the maximum contrast method has been determined for airborne SARs and allow to estimate the *rms* focussing error $\delta\beta_r$ as a function of the SNCR (Belcher, 2008).

$$\sqrt{\left\langle \delta\beta_r^{\,2} \right\rangle} = \frac{1}{B^2}\frac{\sqrt{90}}{\sqrt{SNCR}} \qquad \text{Equation 2-152}$$

In Equation 2-152, B is the bandwidth of the signal.

2.12.3.3 Range distortions - Non linear phase term

Meyer *et al.* (2006) provide a simple methodology to evaluate the residual phase noise induced by ionosphere that has not been modelled using phase and group delays as their expression is usually limited to quadratic terms.

$$\delta\varphi_r(f) = \frac{4\pi}{c_0}\frac{K}{f_0^3}TEC\left(f - f_0\right)^2 \qquad \text{Equation 2-153}$$

This residual phase term results in a blur in the range azimuth PSF.

Assuming that our GeoSAR system reuses an L band (i.e. 1.5 GHz) and 8 MHz channel the maximum residual phase per TECU is:

$$\delta\varphi_{r,\max} = \frac{4\pi}{c_0}\frac{40.28}{\left(1.5\cdot 10^9\right)^3}TEC\left(8\cdot 10^6\right)^2 \simeq 0.02° \qquad \text{Equation 2-154}$$

Therefore, for the given GeoSAR configuration parameters, the effect of the non-linear phase term is negligible.

2.12.3.4 SAR interferometry and TEC estimation

In literature, SAR interferometry has been presented as a means to look into TEC distributions under the assumption that the ionosphere is steady during the integration time. This assumption fails for GeoSAR; nevertheless, the following section shows that

this approach is not applicable in this research as the limited range resolution prevents from evaluating small TEC variations.

Meyer *et al.* (2006) as well as other authors in the past (Hanssen, 2001; Quegan and Lamont, 1986) specified that interferometric pairs can be used to estimate differential TEC variations (∆TEC) between different acquisitions. This approach could be applied in order to estimate ionospheric perturbations that take place within a single SAR scene.

Meyer *et al.* (2006) provide an analytical procedure that could be used in order to investigate if this approach is applicable to GeoSAR as well. A GeoSAR image has been focused taking into account TEC variations with an accuracy of 0.1 TECU therefore only variations smaller than this value are expected to be present in the interferogram.

Applying the equations in Meyer *et al.* (2006) to monitor ∆TEC with an accuracy of 0.05 TECU range displacement, the interferogram has to be measured with an accuracy of 2 cm.

Bamler and Eineder (2005) provide an expression for the standard deviation of the range shift estimation $\sigma_{\Delta r}$:

$$\sigma_{\Delta r} = \sqrt{\frac{3}{2N}}\sqrt{\frac{1-\gamma^2}{\pi\gamma}}\rho_{sr} \qquad \text{Equation 2-155}$$

In Equation 2-155, N is the number of samples averaged in the estimation
γ is the interferometric coherence
ρ_{sr} is the slant range resolution.

Assuming an average coherence of 0.5 with the given slant range resolution (i.e. 10 m) about 10^5 samples should be averaged in order to achieve the desired range shift accuracy.

The figures proposed show clearly that ∆TEC cannot be used as a procedure to improve the quality of the TEC mapping carried out in order to focus a GeoSAR image.

A similar methodology could be applied to estimate the differential along-track TEC gradient between the two images of an interferometric couple. Due to the limited azimuth resolution in the GeoSAR case, this approach would provide extremely poor results.

2.12.4 Spatial and temporal TEC variations

Ionospheric TEC variations affect SAR image formation; some simulations have been carried out in the present research to investigate their effect on a geosynchronous SAR system. The following sections provide some background information about spatial and temporal TEC variations. Figure 2-28 shows ionospheric TEC variations for a 24-hour observation time obtained from the *spectre* dataset (see 2.12.7.2 and Crespon *et al.*, 2007).

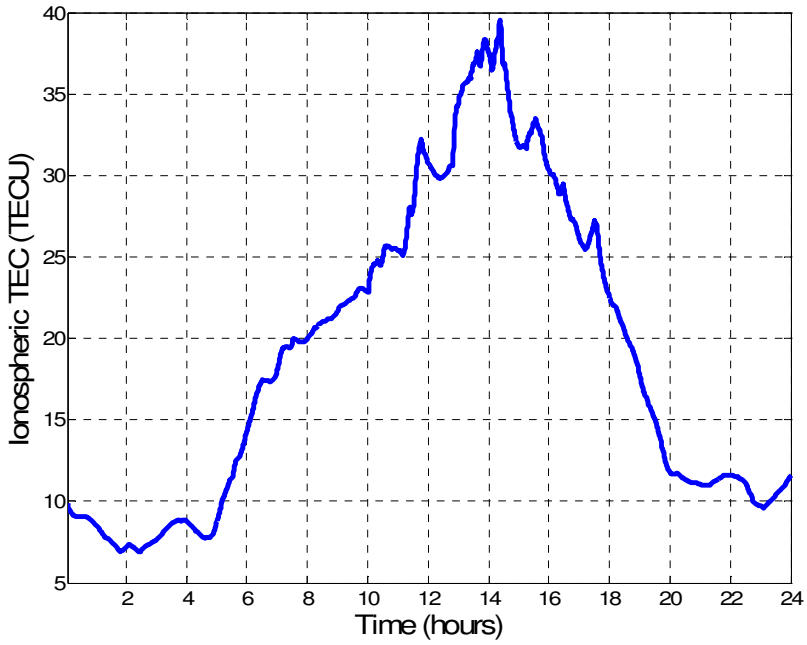

Figure 2-28. Ionospheric TEC variations observed in 24 hours with respect to local time, from *spectre* data (Crespon *et al.*, 2007).

2.12.4.1 TEC spatial gradients

McGraw *et al.* (2000) in their analysis of GPS Local Area Augmentation System (LAAS) provide some insights about TEC spatial gradients. Under normal daytime ionospheric conditions, the spatial gradient in ionospheric delay is about 3-5 mm/km (1 sigma). Under severe ionospheric storms, Konno *et al.* (2005) report that the spatial gradients can increase up to 316 mm/km, about 60 times larger than in normal circumstances.

Figure 2-29 shows four histograms for different geomagnetic storms that have been recorded over Japan. The elevation angle of a gradient is the average elevation of the

two lines of sight that generate the gradient. The z-axis shows the (base-10) logarithm of the number of occurrences recorded during each geomagnetic storm.

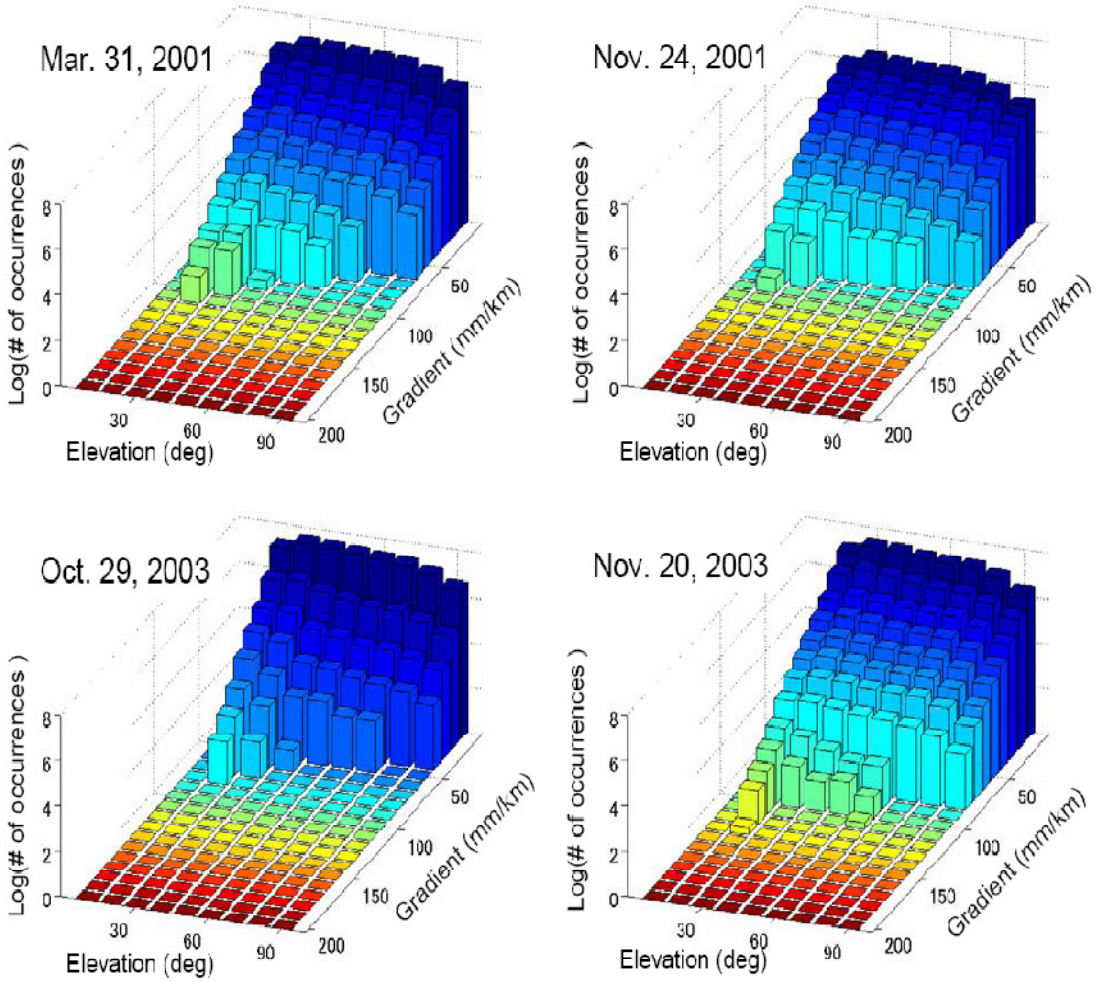

Figure 2-29. Histograms of slant gradients for four different magnetic storms (Konno *et al.* 2005).

Meyer *et al.* (2006) report that a typical ionospheric anomaly may have amplitude of about 0.3 TECU and a width of 5 km as presented in Figure 2-30.

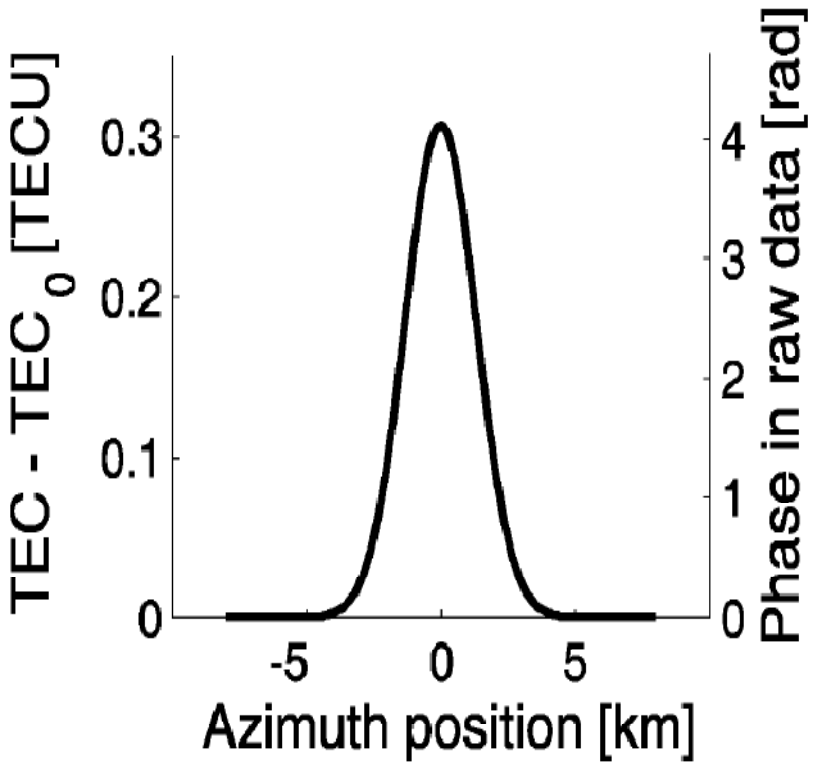

Figure 2-30. Typical ionospheric anomaly (Meyer *et al.*, 2006).

The plots in Figure 2-29 and Figure 2-30 show that spatial TEC gradients are very large and concentrated in the area of few kilometres (much shorter that the synthetic aperture length of a geosynchronous SAR).

2.12.4.2 TID (Travelling ionospheric disturbances)

"*It appears that TEC smaller-scale variability is mainly related to three types of phenomena: travelling ionospheric disturbances (TIDs), scintillations or "noise-like" variability*" (Lejeune and Warnant, 2008). TIDs appear as waves in the electron density, which are due to interactions between the ionosphere and the neutral atmosphere. Figure 2-31 presents TEC variations that take place during the disturbance.

An ionospheric perturbation, to be visible in an SAR image, has to be smaller in scale than the image itself. The only effects with relatively small scales are TID (Travelling Ionospheric Disturbances). Medium scales TID have scale lengths of 100-200 km, time scales of 10-20 minutes and amplitude with variations of about 0.5-5% in the TEC. Large-scale TID are relatively uncommon. Their scale lengths are about 1000 km and the TEC variation up to 8% (Hanssen, 2001).

Subsequent to sudden electron density disturbances, ionospheric gravity waves occur. These waves have a very long wavelength (up to 400 km) and have gravity as restoring force.

As an example, strong TIDs were detected on December 24, 2004 (TEC variability up to 0.6 TECU/min). Figure 2-31 shows DTEC (Differential Total Electron Content), i.e. the derivative of TEC with respect to time. This plot shows clearly that in presence of TID, TEC values are highly unpredictable with significant temporal variations.

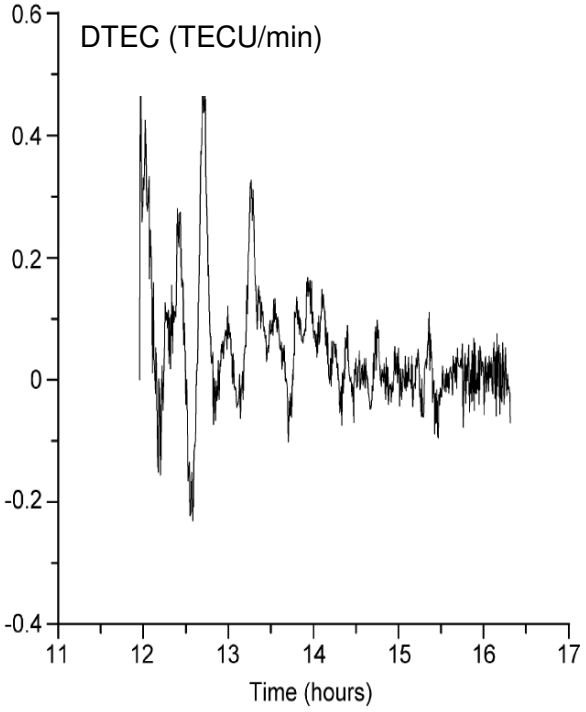

Figure 2-31. TEC variability (TECU/min) due to a TID detected at Brussels on DOY 359 in 2004 along the track of satellite 21 (Lejeune and Warnant, 2008).

Tsugawa (2006), using GPS observations, presents a brief summary of the TID recorded over Japan in 2002. The paper shows a useful classification of medium scale and large-scale disturbances.

Large Scale TIDs (LSTID) have amplitude of about 20%; their spatial scale is between 1000 and 3000 km; the propagation velocity is between 300 and 600 m/s. They show a clear dependence on geomagnetic activity (Kp index).

Medium Scale TIDs (MSTID) have amplitude of about 10%; their spatial scale is between 100 and 500 km; the propagation velocity is between 50 and 200 m/s.

Tsugawa (2006) provides some values (reported in the following table) that can be useful in order to summarize the main peculiarities of night-time and daytime Medium

Scale TID. Night-time perturbations are less fast and have a shorter spatial scale with respect to daytime perturbations. The statistical analysis has been carried out in the period between April 1999 and December 2002. In Table 2-4 the occurrence rate refers to the number of days (or nights) in the observation period when MSTID have been recorded.

Table 2-4. Morphology of MSTID observed in Japan (Tsugawa, 2006)

	Nighttime MSTID	Daytime MSTID
Occurrence Rate	~ 80 %	> 50 %
Amplitude (in 2002)	0.4 - >1.2 TECU	0.5-1.0 TECU
Wavelength	150-500 km	100-350 km
Velocity	50-150 m/s	100-200 m/s
Direction	southwestward	south-southeastward
Seasonal dependence	summer (1st max), winter (2nd max)	winter
Geomagnetic activity dependence	no	–
Solar activity dependence	negative	not clear
Remarks	Electrodynamic forces play an important role in their generation.	Atmospheric gravity waves would be responsible for their generation.

2.12.4.3 Ionospheric scintillations

Scintillations are fluctuations in phase and amplitude of the signal, which are due to the presence of small-scale irregularities in the electron concentration.

There are certain regions of the ionosphere (mainly the high latitude and low latitude F-regions) and certain local times (principally after sunset) when the ionosphere may become highly turbulent. According to Anderson and Fuller-Rowell (1999) "*turbulence is defined as the presence of small-scale (from centimetres to meters) structures or irregularities embedded in the large-scale (tens of kilometres) ambient ionosphere*".

As shown in the following figure, ionospheric irregularities are generated just after sunset in the equatorial region. Around the magnetic poles, these irregularities may be generated either during the daytime or at night. In both cases, these small-scale irregularities can last for a few hours and occur most frequently during the solar cycle maximum.

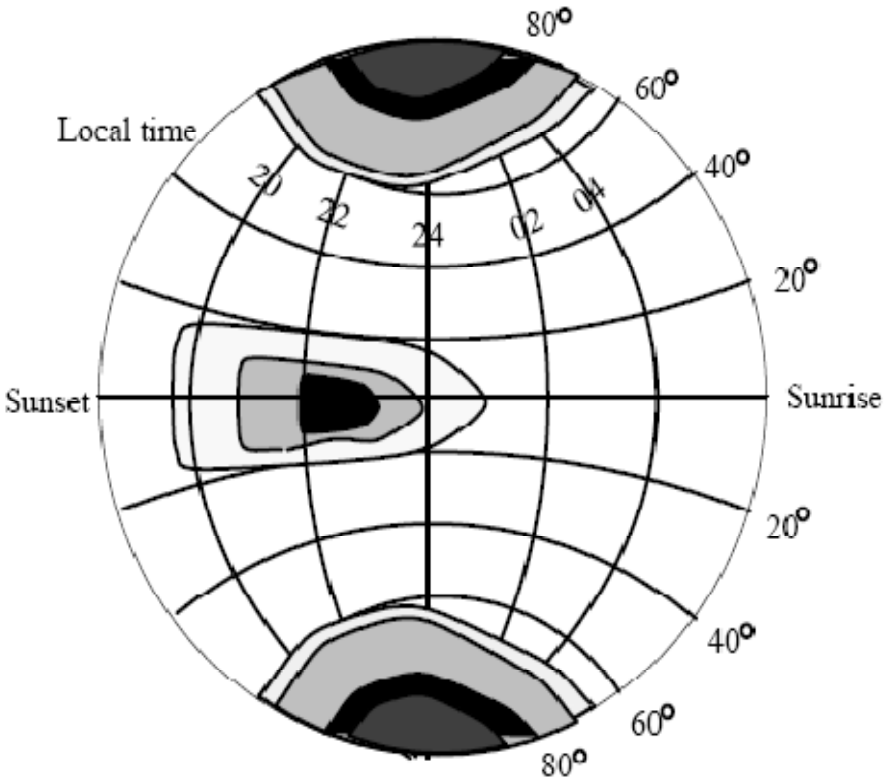

Figure 2-32. Ionospheric scintillation areas during low and moderate solar activity (Anderson and Fuller-Rowell, 1999).

2.12.4.4 Geomagnetic storms

They are mainly observed in the polar and in the equatorial ionosphere. In mid-latitude stations, ‘‘noise-like’’ variability in TEC can also be observed. Such a variability is mainly detected during geomagnetic storms; Figure 2-33 shows noise-like variability in TEC due to a severe geomagnetic storm observed at Brussels on DOY 324 in 2003 (November 20, 2003). TEC variations due to geomagnetic storms can be up to 2 TECU/min.

Section 2.12.5 will discuss the probability of occurrence of geomagnetic storms and will correlate their strength with their effect on ionospheric perturbations.

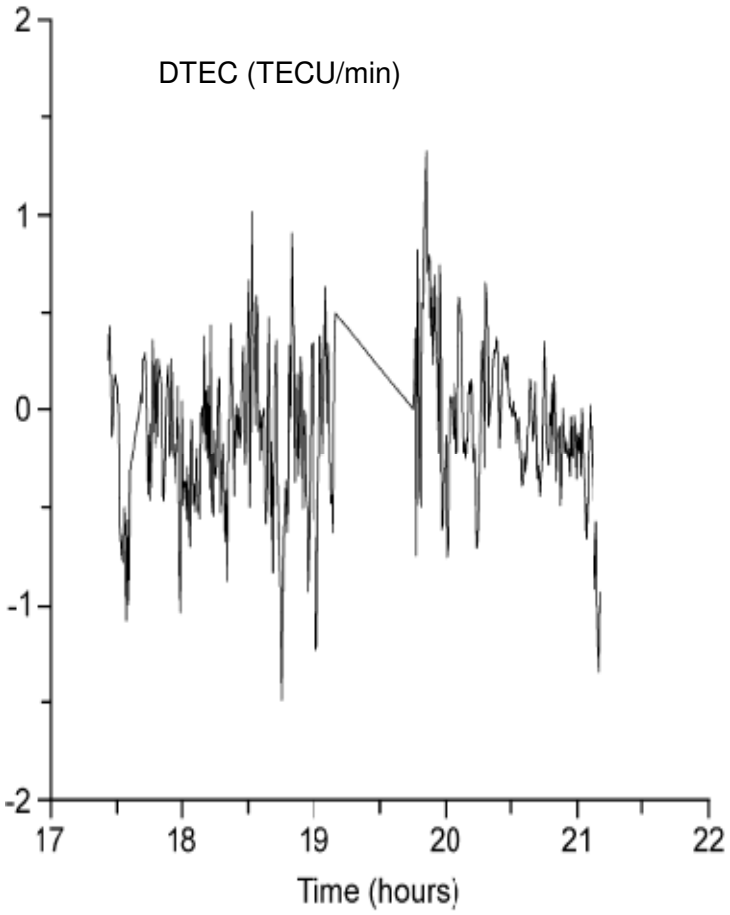

Figure 2-33. TEC noise-like variability observed at Brussels on DOY 324 in 2003 along the track of satellite 15 (GPS) (Lejeune and Warnant, 2008).

NOAA SEC (2005) provides a quantitative scale that uses the parameter *Kp* to measure the intensity of geo-magnetic activity.

The *Kp* index is a quasi-logarithmic local index of the 3-hourly range in magnetic activity relative to an assumed quiet-day curve for a single geomagnetic observatory.

Section 2.12.5 will provide further details on this activity scale. Figure 2-34 shows the variations of the geo-magnetic index that have been recorded during a geo-magnetic storm, values of the parameter *Kp* larger than four correspond strong geomagnetic activity (see section 2.12.5).

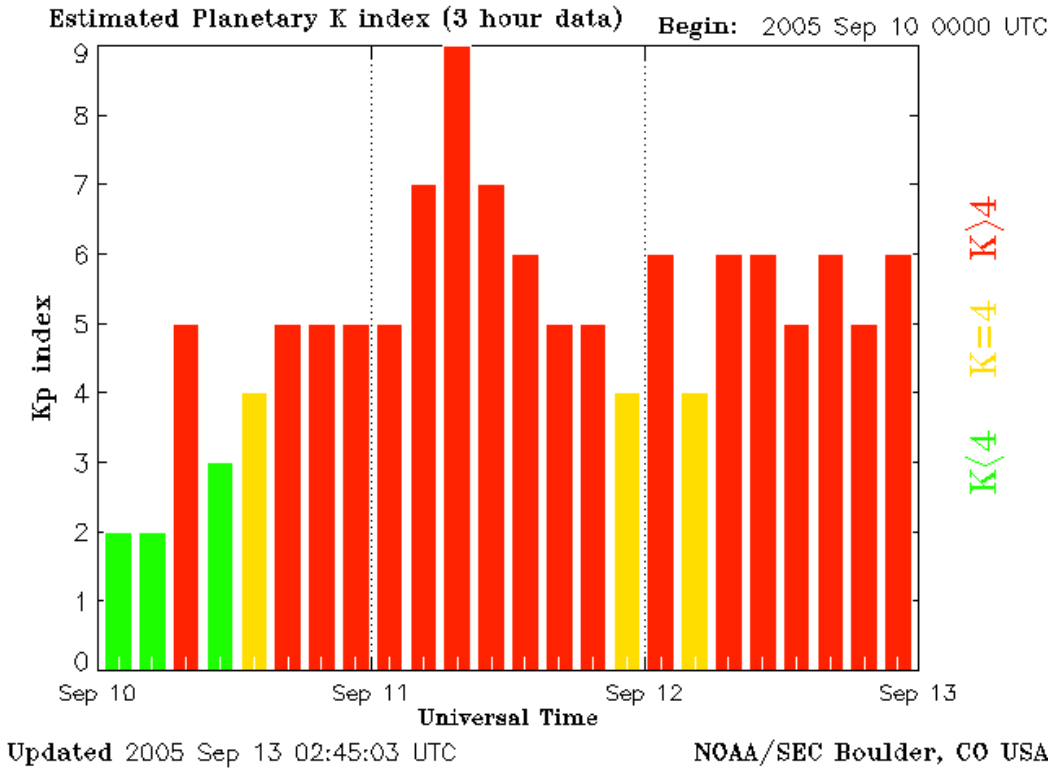

Figure 2-34. Geo-magnetic storm 11/12 September 2005 - Estimated Planetary *Kp* index (ftp.sec.noaa.gov).

2.12.5 Occurrence of ionospheric disturbances

Ionospheric disturbances are related to phenomena that characterize the space environment.

Anderson and Fuller-Rowell (1999) address the issue of ionospheric variability and include solar flares and geomagnetic storms as the two major sources of ionospheric variability.

NOAA space environment centre (SEC) (NOAA SEC, 2005) defined three different scales to classify space weather disturbances (Table 2-5, Table 2-6 and Table 2-7). In all the tables, the frequency is the rate of occurrence during a whole solar cycle.

The *Kp* index is the planetary average of all the *K* indices measured at observatories around the globe. This planetary index is designed to measure solar particle radiation by its magnetic effects (Poole, 2002).

Table 2-5. Extract from NOAA Space Weather Scale for Geomagnetic Storms (NOAA SEC, 2005)

Category	Descriptor	Kp values	Frequency (number per solar cycle)
Extreme	G5	9	4
Severe	G4	8	60
Strong	G3	7	130
Moderate	G2	6	360
Minor	G1	5	900

Table 2-5 includes some information from the NOAA Space Weather Scale for Geomagnetic Storms. Ionospheric disturbances that affect GPS-like (i.e. L band) signals become significant with strong (G3 class) storms. "*Although geomagnetic and ionospheric storms are interrelated, it is worth noting that they are different. A geomagnetic storm is a disturbance of the Earth's magnetic field and an ionospheric storm is a disturbance of the ionosphere*" (Poole, 2002).

The intensity of the solar radiation is measured considering the flux level, i.e. the flux level of particles with energy larger than 10 MeV. The flux is averaged every five minutes and it is measured in particles·s^{-1}·$ster^{-1}$·cm^{-2} (NOAA SEC, 2005).

Table 2-6. Extract from NOAA Space Weather Scale for Solar Radiation Storms (NOAA SEC, 2005)

Category	Descriptor	Flux level	Frequency
Extreme	S5	10^5	1
Severe	S4	10^4	3
Strong	S3	10^3	10
Moderate	S2	10^2	25
Minor	S1	10	50

Table 2-6 includes some information from the NOAA Space Weather Scale for Solar Radiation Storms. Ionospheric disturbances that affect GPS-like (i.e. L band) signals become significant with strong (S3 class) storms.

Table 2-7. Extract from NOAA Space Weather Scale for Radio Blackouts (NOAA SEC, 2005)

Category	Descriptor	X-ray peak	Frequency
Extreme	R5	X20	1
Severe	R4	X10	8
Strong	R3	X1	175
Moderate	R2	M5	350
Minor	R1	M1	2000

Table 2-7 includes some information from the NOAA Space Weather Scale for Radio blackouts induced by solar flares. Solar flares are classified using the brightness of their peak or equivalently using the amount of energy (measured in W m^{-2}) in the 0.1-0.8 nm range (NOAA SEC, 2005).

As with the previous scales, ionospheric disturbances that affect GPS-like (i.e. L band) signals become significant with strong (R3 class) storms.

In conclusion, considering the main space weather phenomena that can induce significant variations in the ionosphere, there should be about 400 events for every solar cycle (11 years ≈ 4000 days). Most of the problems are likely to be concentrated about the maximum of the solar cycle or about a local peak of solar activity.

Only 10 out of 400 are the “extreme” phenomena that are likely to hamper completely GeoSAR operations.

2.12.6 Effect of ionospheric turbulence

Belcher (2008) summarises the effect of ionospheric turbulence on along-track focussing: “*Both ionospheric and tropospheric turbulence has a power-law spectrum, therefore there is no distance over which there are no TEC changes, but a coherence length can be defined where the TEC variations can be considered negligible. Over this length, the along track autofocus algorithm can be applied and any constant TEC removed and the focus restored. Autofocus algorithms generally require a minimum initial coherence length to start the autofocus procedure, and can then extend the coherence length for image formation by represents the limiting factor for along track image formation: if the ionosphere is so turbulent that it is not coherent over this minimum interval, no image can be generated. It is the turbulence that limits image formation, not the absolute TEC*”.

Figure 2-35 shows an example of ionospheric turbulence PSD (Belcher, 2008).

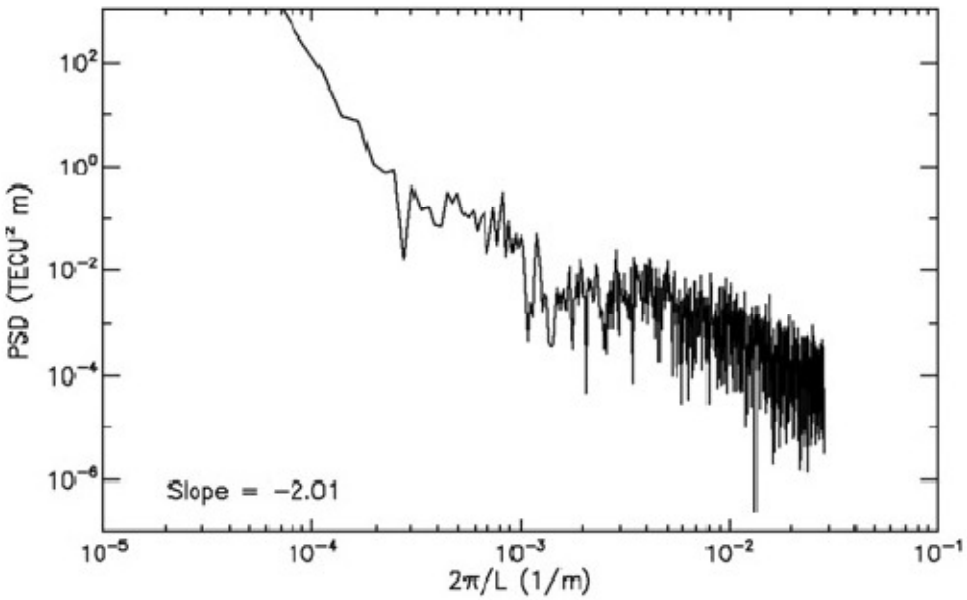

Figure 2-35. Example of ionospheric power spectrum (Belcher, 2008)

A suitable upper limit for ionospheric turbulence (measured by the factor C_kL) to allow for image formation is shown in Figure 2-36 (Belcher, 2008).

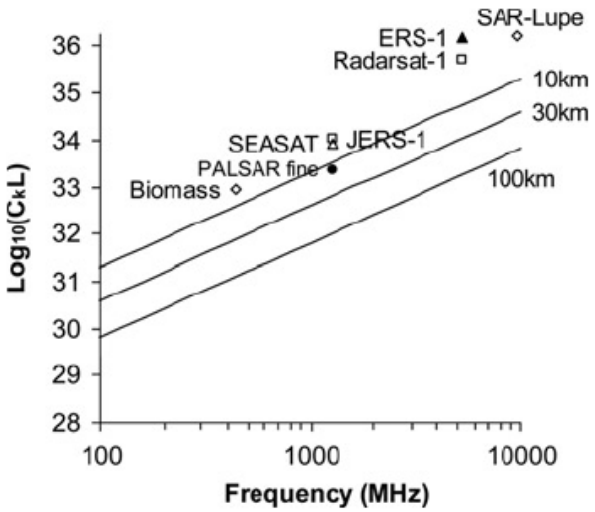

Figure 2-36. Maximum value of the coefficient *CkL* for several different coherence lengths (Belcher, 2008).

2.12.7 Historical TEC data

Some datasets including TEC time series freely available have been used in the present research.

2.12.7.1 NOAA Data

NOAA provides (www.ngdc.noaa.gov/stp/IONO/USTEC/products/) an archive of historical slant range ionospheric TEC time series sampled every 15 minutes on a grid 0.1° lat x 0.1° longitude. These data have an accuracy of about 2 TECU.

Data for 72 different locations (inside continental USA) have been presented in Figure 2-37. The trend is clearly periodic with a 24-hour period. The maximum amplitude of the oscillation is larger than 5 TECU.

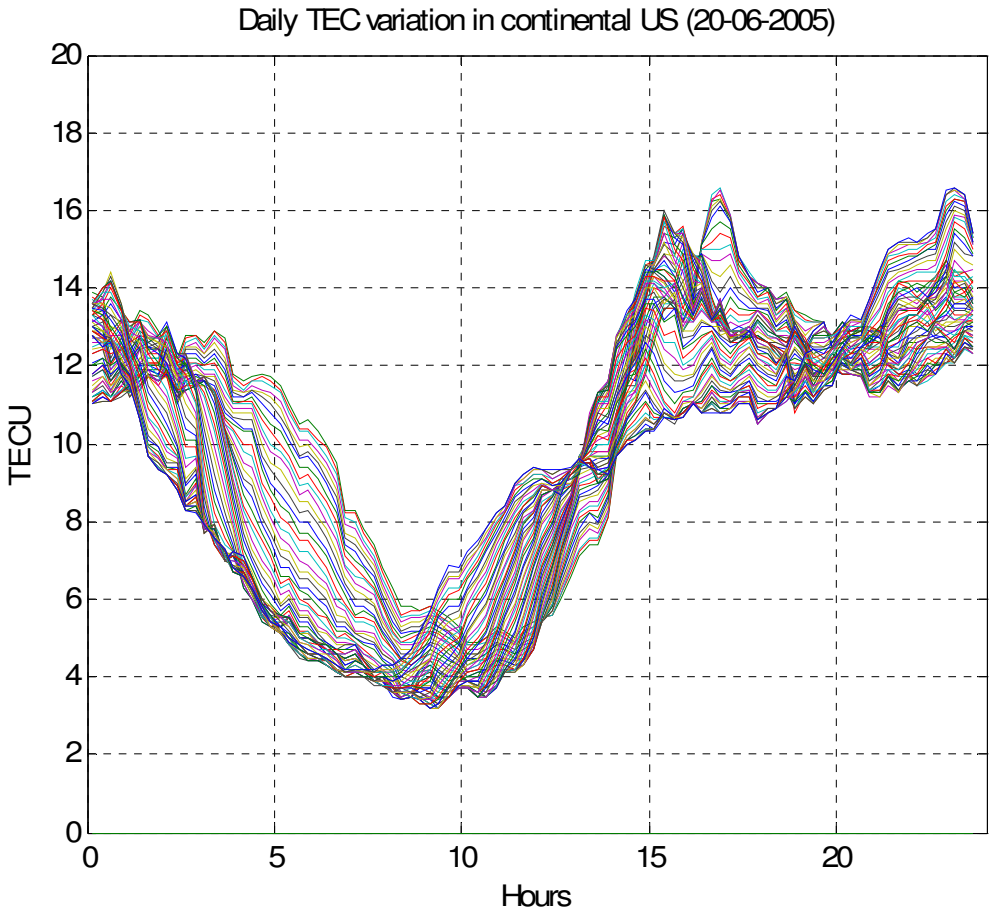

Figure 2-37. Daily TEC variation for 72 locations in continental US. The abscissa is local solar time.

2.12.7.2 *Spectre* dataset

The Noveltis project provided ionospheric data sampled every 30 seconds on a grid 2.5° lat x 2.5° longitude all over Europe (Crespon *et al.*, 2007). These data have an accuracy of about 2 TECU. As will be discussed in Chapter 6 these data are not accurate enough to allow a precise phase compensation for SAR image formation. Figure 2-38 shows VTEC contours over Europe for 14 September 2005.

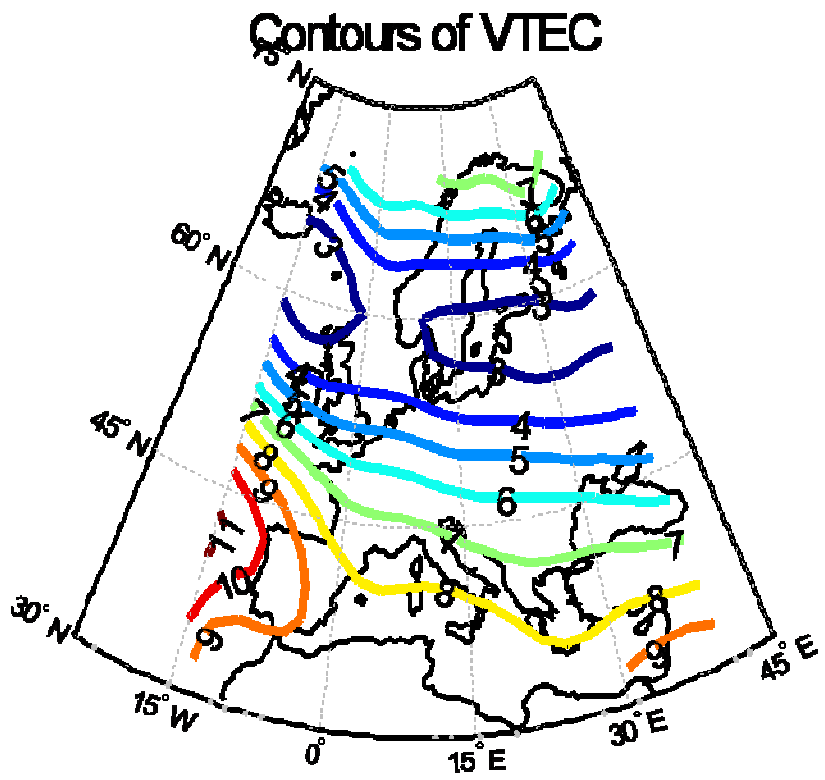

Figure 2-38. VTEC contours plotted from spectre data (Crespon *et al.* 2007) (14 September 2005).

Spectre data are provided in *netcdf* format. To import the data the routine *cdf2idl.pro* (Rupert, 1998 in Appendix B) has been used.

2.12.7.3 Ionospheric models

"*The International Reference Ionosphere (IRI) is a widely used standard for the specification of ionospheric parameters and is recommended for international use by the Committee for Space Research (COSPAR) and the Union for Radio Science (URSI).*" (Bilitza, 2001)

Ionospheric models do not include accurate models for TEC perturbations. Therefore, IRI models can be used only for a rough estimation of TEC profiles during SAR integration time.

2.12.8 Ionospheric phase delay – summary

Ionospheric phase delays, due to their unpredictability, are relevant to GeoSAR as they are likely to be the most important source of decorrelation in GeoSAR image formation. This aspect has only been marginally considered in relevant SAR literature as conventional LEO SAR systems usually have integration time of the order of 1 second. Such time lapse is too short for any ionospheric contribution to decorrelation to become significant.

Background information provided in this section has the purpose of estimating the order of magnitude of ionospheric TEC perturbations and their probability of occurrence

The scope of this review is to model ionospheric phase delays thus allowing a realistic simulation of their effects on GeoSAR imaging.

Further details on ionospheric effects on SAR imaging are provided in section 6.4 .

2.13 Summary

This chapter provided a background on SAR systems, both monostatic and bi-static. Fundamentals of SAR interferometry have been provided as this is a potential field of application for a SAR working from a geosynchronous orbit. The concept of coherence has been explained referring to SAR image processing and SAR interferometry highlighting differences and properties.

SAR processing has been explained as the present research required the development of a SAR signal processor. The latter part of the chapter provides some information about multi-static SAR and about temporal decorrelation aspects (i.e. earth tides, tropospheric and ionospheric delay). In particular for each of the decorrelation sources under consideration a literature review has been provided in order to assess their relevance to SAR image formation.

3 GeoSAR configuration

The literature review presented in the introduction included both passive and active geosynchronous SAR configurations. This chapter will provide a preliminary discussion about the geosynchronous orbit (section 3.1) and geosynchronous SAR systems both monostatic (section 3.2) and bi-static (section 3.3). Section 3.4 presents a system trade-off to select the most suitable system design configuration and the optimal frequency. Section 3.5 summarises the conclusions of these analyses.

3.1 Geo-synchronous orbit

A SAR system requires relative motion between the transmitter (or the receiver) and the target.

For a monostatic configuration, a geostationary orbit (a geosynchronous orbit with zero inclination and zero eccentricity) is not acceptable for SAR imaging as the satellite is stationary with respect to an observer on the Earth. With respect to a GEO orbit, a geosynchronous orbit has non-zero inclination and/or eccentricity. This allows relative motion between the target and the antenna that generates a synthetic aperture.

The same considerations could be applied as well to a bi-static GeoSAR configuration under the assumption that the transmitter is stationary with respect to the target on the ground (i.e. transmitter in GEO) as considered by Prati *et al.* (1998).

3.1.1 Shapes of geosynchronous orbits

If an otherwise geostationary Earth orbit is given a non-zero inclination, it will move along a figure-of-eight ground track through a latitude range, both north and south, equal to the inclination, taking one sidereal day to complete the cycle. The ground track will be a figure-of-eight line as shown in Figure 3-1 generated using the software Satellite Tool Kit (STK). The motion along this orbit, and therefore the synthetic aperture, is mostly in the north-south direction.

Instead, if inclination is kept at zero and eccentricity becomes non-zero, the spacecraft will be alternately closer to the Earth than GEO and further from it. The speed of the spacecraft will be alternately faster and slower than GEO speed, and so there will be an east-west drift of the ground position (Bate *et al.* 1971).

If we combine non-zero inclination and eccentricity, a variety of relative orbit shapes could be achieved. For example in Figure 3-2, the satellite has inclination of 0 degrees and eccentricity of 0.05. This results in the synthetic aperture radar having much better resolution imaging to the north and south than to the east and west.

Figure 3-1. Trajectory of the satellite for a geosynchronous orbit with zero eccentricity and 5° inclination.

Figure 3-2. Trajectory of the satellite for a geosynchronous orbit with zero inclination and 0.05 eccentricity.

In order to achieve coverage in all directions and to have equal resolution, the relative orbit must be as nearly circular as possible. The diameter of this circle is dictated by the required radar resolution; once this is known, the required inclination and eccentricity can easily be calculated, as explained in the following sections.

The geometry of this kind of orbit will be further investigated in section 4.1.1 when the chosen GeoSAR orbit will be presented.

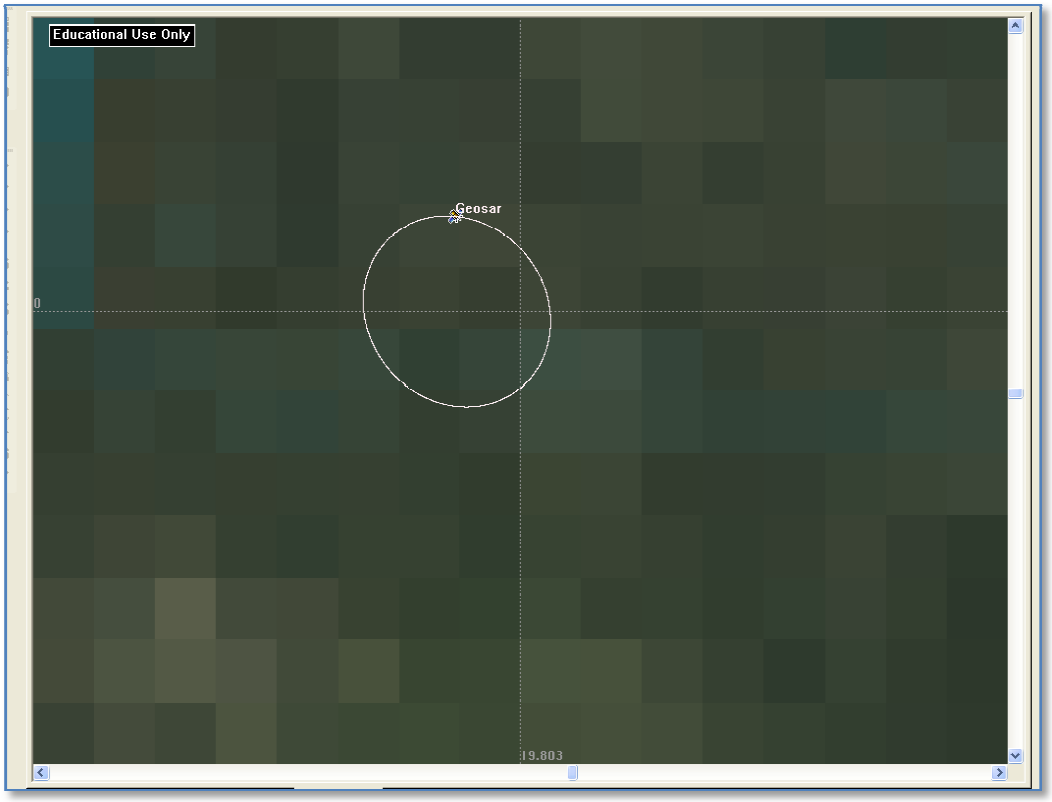

Figure 3-3. Trajectory of the satellite for a geosynchronous nearly circular orbit with non-zero inclination and non-zero eccentricity.

3.1.2 Effects of orbital elements on relative orbit

A circular ground-track orbit allows the satellite to form a synthetic aperture while flying along the north-south or the east-west direction.

The six classical orbital elements are as follows:

- semi-major axis;
- eccentricity;

- inclination;
- argument of perigee;
- right ascension of the ascending node;
- true anomaly.

Each of these elements affects the shape, size or location of the relative orbit or the satellite's position on it. Their effects will be investigated in the following sections focussing on the constraints required to achieve a circular ground-track orbit.

Cazzani *et al.* (2000) provide some linearised equations to estimate longitude, latitude and altitude of a geosynchronous satellite assuming that its orbit is not perfectly geostationary and there are residual eccentricity (*e*) and inclination (*i*). Satellite altitude is as well slightly different (δR) from the GEO one. These equations are derived from Kepler's equations neglecting second order terms.

$$\begin{cases} r = R_{GEO} + \delta R - R_{GEO} e \cos\left[\omega_T \left(t - t_0\right)\right] \\ long - long_0 = 2e\left(\frac{180}{\pi}\right)\sin\left[\omega_T \left(t - t_0\right)\right] - \frac{3}{2}\frac{\delta R}{R_{GEO}}\left[\omega_T \left(t - t_0\right)\right] \\ lat = i \sin\left[\omega_T \left(t - t_0\right)\right] \end{cases}$$ Equation 3-1

In Equation 3-1, *r, lat and long* describe the position of the satellite;
$long_0$ is the initial longitude of the satellite;
ω_T is the Earth's angular velocity;
R_{GEO} is the altitude of GEO orbit.

3.1.2.1 Semi-major axis

This must remain the same as that of GEO, which is 42164.2 km. If it is allowed to change even slightly, the satellite will not be synchronous, but will drift east or west.

3.1.2.2 Eccentricity

This controls the magnitude of the spacecraft's east-west relative motion. According to Agrawal (1986) the longitude variation east and west from the centre point is:

$$\Delta long = 2e$$ Equation 3-2

In Equation 3-2, *e* is the orbit eccentricity,

$\Delta long$ in radians is the amplitude of the east-west oscillation.

3.1.2.3 Inclination

Inclination *i* controls the magnitude of north-south relative motion. Therefore, in a circular ground-track orbit, it has to be equal to $\Delta\lambda$ that controls the east-west wander.

$$i = \tan^{-1}\left(\frac{r}{R}\right) \qquad \text{Equation 3-3}$$

In Equation 3-3, *r* is the radius of the relative orbit;
R is the GEO radius (42164.2 km).

3.1.2.4 Argument of Perigee

The location of the perigee on the orbital plane, measured in the direction of motion starting from the ascending node, has to be 90° or 270° for a circular relative orbit. The spacecraft will describe a clockwise near-circle as seen from above if argument is 90°, since perigee – the point of greatest speed – is at the northernmost part of the orbit. At 270°, the motion will be anticlockwise.

3.1.2.5 Right ascension and True anomaly

Right ascension controls the location of the satellite on the relative orbit and the location of the relative orbit on the equator. A right ascension of 0° means the satellite crosses the equator heading north under the first point of Aries.

True anomaly describes the position of the spacecraft on its orbit, measured from perigee in the direction of motion.

3.1.2.6 Circular track orbit parameters

Following the considerations carried out in the previous sections, parameters that will allow a geosynchronous circular track will be hereafter summarised. The parameters considered hereafter refer to the position of the satellite in the ECF (Earth Centred Fixed) reference system.

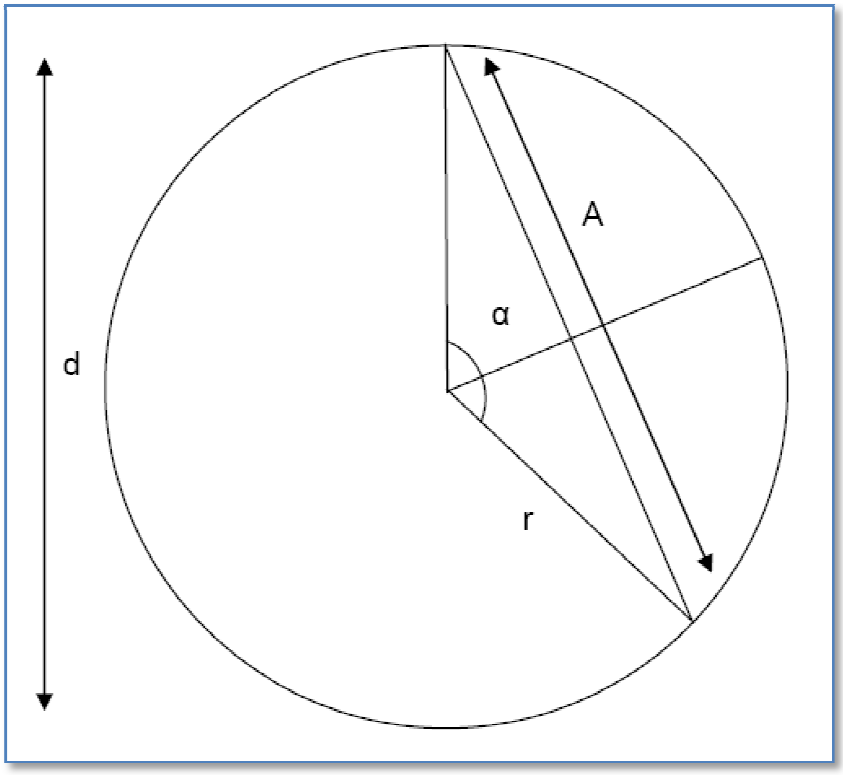

Figure 3-4. Geometry of the geosynchronous circular ground track orbit.

According to the geometry presented in Figure 3-4, the angle α and the diameter d are related by the following equations.

$$\sin\left(\frac{1}{2}\alpha\right)=\frac{1}{2}\frac{A}{r} \qquad \text{Equation 3-4}$$

$$d=\frac{A}{\sin\left(\frac{1}{2}\alpha\right)} \qquad \text{Equation 3-5}$$

The angle α (in degrees) in previous equations could be calculated from the integration time T (in hours) taking into account that the orbit period is 24 hours.

$$\alpha=\frac{T}{24}\times 360 \qquad \text{Equation 3-6}$$

Following Equation 3-6 d, the diameter of the circular ground-track, is expressed as in Equation 3-7.

$$d = \frac{A}{\sin\left(\frac{T}{48}\times 360\right)}$$ Equation 3-7

The geometrical model presented in Figure 3-4 can also be used to find the satellite velocity *V*, measured in ms^{-1} (assumed constant around the circle) if the imaging time *T* is given in hours and the aperture length is in meters:

$$V = \frac{\pi d}{24} = \frac{\pi A}{24\times 3600\times \sin\left(\frac{T}{48}\times 360\right)} = \frac{\pi A}{86400\sin\left(\frac{15\ T}{2}\right)}$$ Equation 3-8

Orbital parameters required to put the spacecraft in a relative orbit with that radius are obtained using the equations derived in previous sections (i.e. Equation 3-9).

$$i = \tan^{-1}\left(\frac{r}{R}\right)$$ Equation 3-9

In a circular relative orbit, it is also the case that $\Delta\lambda=i$, therefore applying Equation 3-10 (Agrawal, 1986), eccentricity is half $\Delta\lambda$ (in radians).

$$i = \Delta long = 2e$$ Equation 3-10

As shown in Equation 3-1, satellite motion has a radial motion with one-day period that has to be taken into account when considering SAR processing as the distance between the antenna and the target is constantly varying.

3.1.3 Altitude factor

The imaging geometry from a geosynchronous SAR to the illuminated target is very different compared to conventional LEO system. Earth curvature introduces a sort of spotlight mode as the satellite flies along a flight path that is longer than the actual track on the Earth's surface. This implies that a scaling factor has to be included in all performance equations while it is usually neglected in traditional SAR literature. This altitude factor A_F (Equation 3-11) is negligible in LEO systems as it is practically one while it is significant in imaging radars from very high altitude orbits (Madsen *et al.* 2001).

$$A_F = \frac{R_E + h}{R_E} \approx \frac{42}{6.4} = 6.56$$ Equation 3-11

The altitude factor is obviously the scaling factor used to derive nadir-point velocity magnitude from the velocity of the satellite itself. It has to be included in all performance equations such as those to derive azimuth resolution Δy, synthetic aperture A, and integration time T_{int}.

$$v_{sc} = v\frac{R_E}{R_E + h} \qquad \text{Equation 3-12}$$

In Equation 3-12, v_{sc} is the ground-track velocity of the spacecraft;
v is the orbital velocity relative to the rotating Earth.

The aperture of the synthetic antenna θ_{synth} is given in Equation 3-13.

$$\theta_{synth} = \frac{\lambda}{L_A} = \frac{\Delta y}{R} \qquad \text{Equation 3-13}$$

In Equation 3-13, λ is the radar wavelength;
L_A is the length of the synthetic aperture;
Δy is the azimuth resolution;
R is the slant range.

The following equations provide expressions for the integration time T_{int}, the synthetic antenna aperture L_A and the azimuth resolution Δy. Following equations apply to a conventional SAR where the maximum azimuth resolution is achieved exploiting the full synthetic aperture. However it has to be said that the law of inverse proportionality to the altitude factor A_F applies to all SAR systems.

$$T_{\text{int}} = \frac{R\theta}{v_{sc}} = \frac{R\lambda}{Dv_{sc}} = \frac{R\lambda}{Dv}\frac{R_E + h}{R_E} \qquad \text{Equation 3-14}$$

$$L_A \approx vT_{\text{int}} = \frac{v}{v_{sc}}\frac{\lambda R}{D} = \frac{\lambda R}{D}\frac{R_E + h}{R_E} \qquad \text{Equation 3-15}$$

$$\Delta y = \frac{D}{2}\frac{R_E}{R_E + h} \qquad \text{Equation 3-16}$$

In the previous equations, R is the slant range;
R_E is the Earth's radius;
h is the altitude of the satellite;
T_{int} is the integration time;

L_A is the length of the synthetic aperture;
Δy is the azimuth resolution;
θ is the antenna beam width.

Equation 3-15 assumes that velocity is constant along the whole flight path of the antenna.

Equation 3-16 assumes a monostatic configuration. In a bi-static configuration, the azimuth resolution is equal to twice Δy.

3.1.4 Imaging geometry

Imaging from a geosynchronous orbit allows having a wide swath on the Earth's surface.

Figure 3-5. 60° geosynchronous orbit, ground track and instantaneous field of view (NASA JPL, 2003).

Figure 3-5 comes from the GeoSAR monostatic concept (Madsen *et al.*, 2001) in a highly inclined geosynchronous orbit that has been used to define the GESS constellation (NASA JPL, 2003). The plot shows the instantaneous field of view achievable with such a system.

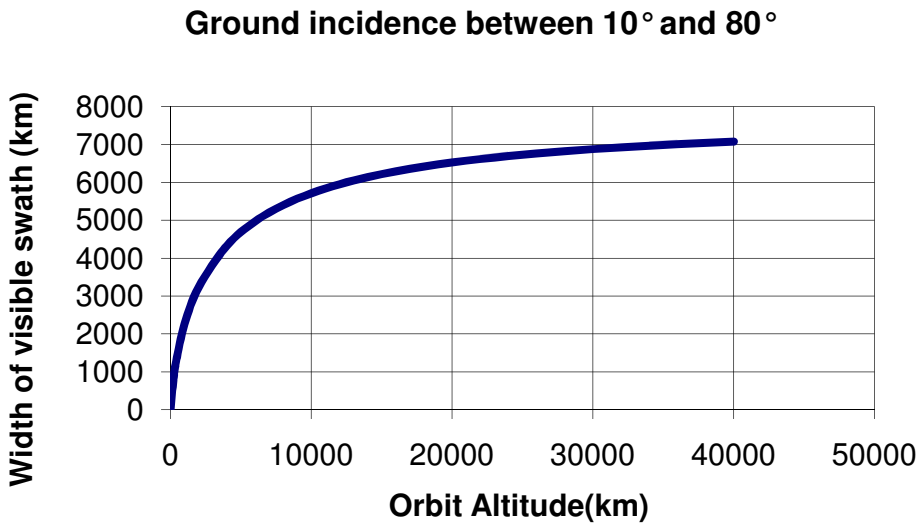

Figure 3-6. Relation between orbit altitude and visible swath. Ground incidence angle is between 10° and 80°.

Figure 3-6 shows the width of the visible swath achievable from orbits with different altitudes. A major advantage that comes from the use of a geosynchronous orbit for remote sensing is a large potential coverage.

The high altitude and the need of operating with high squint angles require an accurate definition of the geometric parameters that will be used to assess coverage and resolution.

The angle ρ (Figure 3-7) is derived from Equation 3-17:

$$R_E = (R_E + h)\sin\rho \qquad \text{Equation 3-17}$$

The nadir angle ξ (Figure 3-7) can then be expressed as:

$$\tan\xi = \frac{R_E \sin\gamma}{h + R_E(1-\cos\gamma)} = \frac{\sin\gamma}{\frac{h+R_E}{R_E} - \cos\gamma} = \frac{\sin\gamma}{\frac{1}{\sin\rho} - \cos\gamma} = \frac{\sin\rho\sin\gamma}{1-\sin\rho\cos\gamma} \qquad \text{Equation 3-18}$$

Applying the law of sines:

$$\frac{R_E}{\sin\xi} = \frac{(R_E+h)}{\sin(90°+\varepsilon)} = \frac{(R_E+h)}{\cos\varepsilon} \qquad \text{Equation 3-19}$$

The grazing angle ε, or the spacecraft elevation angle is (Equation 3-20):

$$\cos\varepsilon = \frac{\sin\xi}{\sin\rho} \qquad \text{Equation 3-20}$$

The angle ρ is 0.15 radians (i.e. 8.7°) from a 36000 km altitude. The angle of incidence, the one that limits the field of view of the SAR sensor is given by Equation 3-21:

$$\phi = 90^{\circ} - \varepsilon \qquad \text{Equation 3-21}$$

For the sake of coverage estimation, it is useful to use an equivalent flat Earth geometry (Figure 3-8).

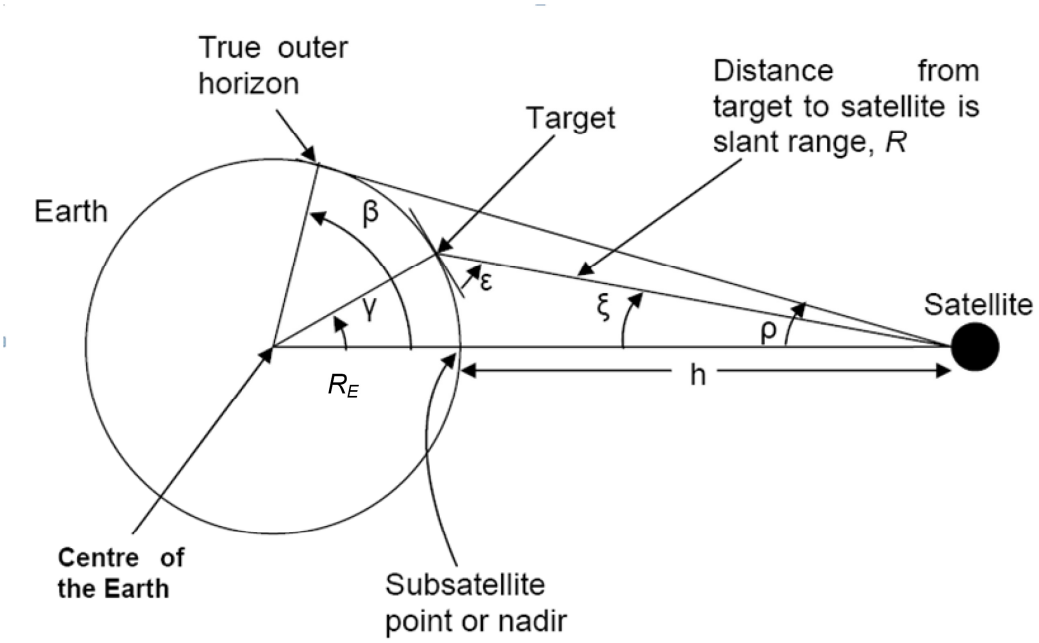

Figure 3-7. Earth viewing geometry (Lee, 2003).

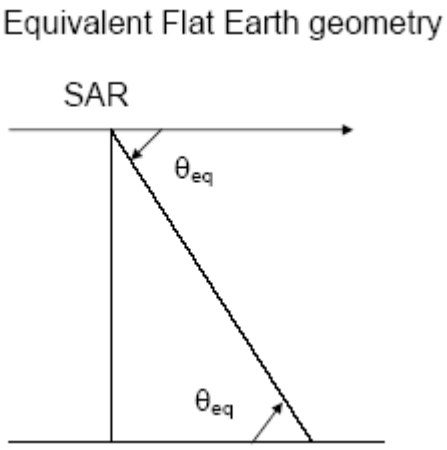

Figure 3-8. Equivalent flat Earth imaging geometry.

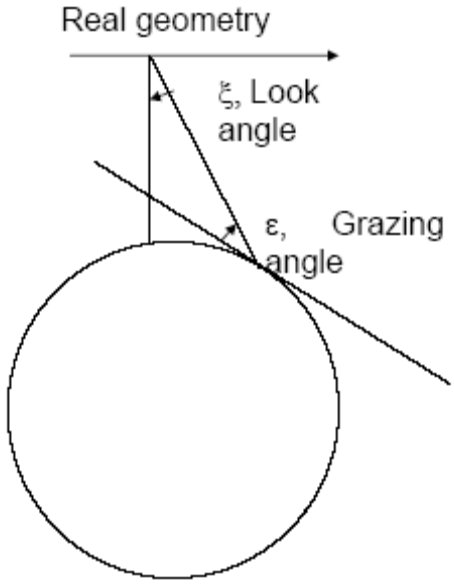

Figure 3-9. Real or "curved Earth" imaging geometry.

The real imaging geometry (Figure 3-9) takes into account the effect of Earth curvature. The angle θ_{eq} in the flat Earth geometry is equal to the grazing angle ε in the curved Earth geometry. SAR look angle (the angle between radar's boresight and the nadir) is clearly different in the two cases: in the "flat Earth" geometry, the look angle is ϕ=90 ^{o}- θ_{eq}; in the curved Earth geometry, the radar look angle is related to the grazing angle by Equation 3-20.

The same considerations may be applied to the azimuth imaging geometry where θ_{eq} is the ground squint angle. The squint angle has been defined in a way that a broadside observation corresponds to 90° squint angle.

Table 3-1 shows a correspondence between the radar look angle and the grazing angle in a geosynchronous geometry.

Table 3-1. Radar look angle (Curved Earth geometry) ξ, grazing angle ε and radar look angle (Flat Earth geometry) ϕ (ϕ=90°–ε).

ξ	ε	ϕ
0°	90°	0°
1°	84°	6°
2°	77°	13°
3°	70°	20°
4°	62°	28°
5°	55°	35°

In the equivalent planar or flat Earth geometry, the ground incidence angle is equal to the radar look angle ϕ (Figure 3-8).

3.1.5 Geosynchronous orbit - summary

This section summarises the peculiarities of geosynchronous orbits. The effect of orbital elements on the fight path has been investigated. The relations between orbital parameters to have a circular flight path have been estimated.

The main advantage of the geosynchronous orbit is in terms of coverage as the high altitude allows imaging a very large swath on the ground.

The Earth curvature and the consequent altitude factor (A_F=6.56, usually neglected in LEO SAR) influences all the basic relations used to calculate SAR main performance parameters. The difference between the radar look angle ξ and the grazing angle ε (sometimes neglected in LEO SAR) has to be considered when implementing a GeoSAR simulator.

3.2 Active monostatic configuration

This section investigates the main issues related to a monostatic active SAR design. This analysis is based on the GESS system (NASA JPL, 2003), a spacecraft concept that has been discussed in literature. This satellite flies along an inclined geosynchronous orbit with zero eccentricity and a figure-of-eight ground track due to a 60° inclination. The analyses in this section apply to systems that fly along a highly inclined geosynchronous orbit.

All the data presented in the following paragraphs use the following assumptions:

- radar wavelength λ=0.25 m;
- slant range R= 36000 km.

The following sections will discuss the implication of geosynchronous orbit on satellite velocity, minimum integration time, antenna size and average transmitted power.

3.2.1 Satellite velocity

Table 3-2 shows velocities of the spacecraft relative to the sub-satellite point at the equator (t=0) or at the northern-most point (6 hours after crossing the equator) of its trajectory. The values are clearly influenced by the inclination of the orbit. The nadir (sub-satellite point) velocity is derived dividing the values in the following table by the altitude factor A_F.

Table 3-2. Velocity (relative to the sub-satellite point) of a spacecraft flying along a geosynchronous orbit with given inclination and zero eccentricity. Data are given for the passage at the equator and for the northern-most (southern-most) point of the trajectory.

Orbit inclination (degrees)	***Velocity (m/s) at the equator***
1	53.66
5	268.23
10	535.95
20	1067.82
30	1591,56
40	2103.19
50	2598.81
60**	3074.66**

** 60° is the orbit inclination planned for the GESS constellation.

3.2.2 Integration time

Integration time, for a given orbit, is a function of the synthetic aperture length and of the radar velocity. The influence of the orbit is given by the radar slant range and by the velocity of the satellite. Under the assumption that the orbit has zero eccentricity, only orbit inclination and the physical length of the SAR antenna determine the integration time.

The expression for the integration time T_{int} is given in Equation 3-22 (Curlander and McDonough, 1991). The expression has been modified to include the altitude factor, A_F.

$$T_{\text{int}} = \frac{\lambda R}{v_{sc} D} A_F \qquad \text{Equation 3-22}$$

In Equation 3-22, λ is the radar wavelength;
v_{sc} is the ground-track satellite velocity;
D is the physical dimension of the antenna;
R is the slant range.

The expected integration times for three different antenna diameters (i.e. 10, 20 and 30 metres) are plotted in Figure 3-10. These results assume that SAR is operated to achieve the full azimuth resolution.

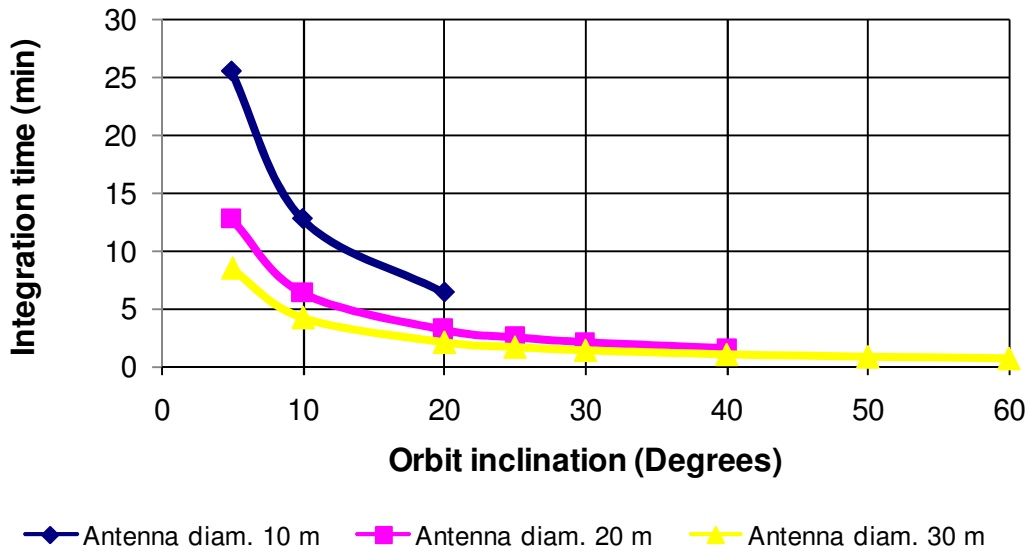

Figure 3-10. Integration time at the equator (maximum velocity and minimum integration time) for a monostatic geosynchronous SAR as a function of orbit inclination and antenna diameter.

3.2.3 Antenna diameter

The minimum antenna area is affected by ambiguities constraints. Madsen *et al.* (2001) reports the following expression:

$$A_{ant} \geq 4\rho\lambda \tan\theta \frac{v_{sc}}{c} \qquad \text{Equation 3-23}$$

Equation 3-23 assumes that the satellite is flying along the full synthetic aperture to achieve its maximum azimuth resolution. A 2x margin is also included. The minimum antenna size is required to avoid both range and azimuth ambiguities.

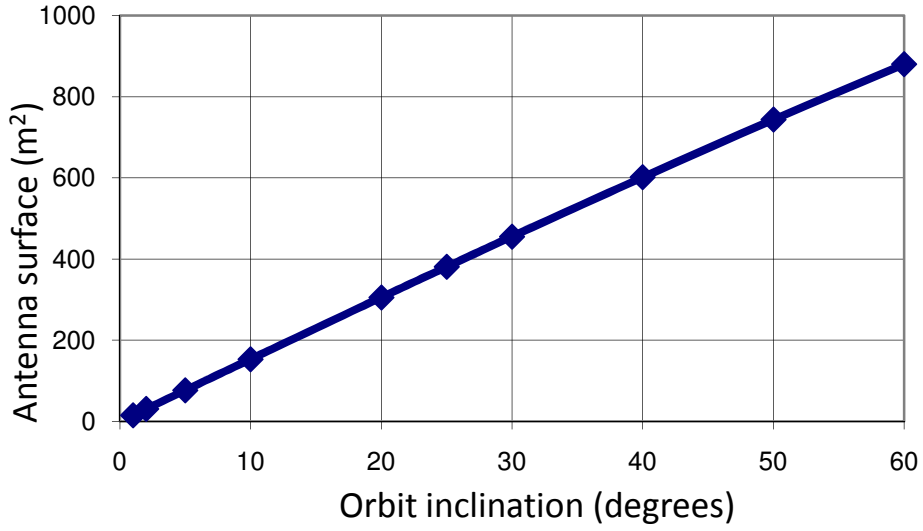

Figure 3-11. Minimum antenna surface (with a factor 2 margin with respect to the minimum acceptable value) as a function of orbit inclination.

Figure 3-11 presents the value of the minimum antenna surface area (with a factor 2 margin). Orbit inclination is the driving factor in system design. A satellite in a highly inclined orbit has a fast-moving ground track and requires a large antenna to avoid Doppler ambiguities (i.e. 30 m for a 50° inclined orbit).

3.2.4 Average transmitted power

In section 2.2.4 (Equation 2-28) the radar equation has been derived, Equation 3-24 recalls the final expression for the average transmitted power, a critical parameter in SAR design.

$$P_{avg} = \frac{SNR_{Ns} 8\pi R^3 k T_{\text{int}} F \lambda v}{A^2 \sigma^0 \Delta R_{range} \sin\theta}; \qquad \text{Equation 3-24}$$

In Equation 3-24,

T_{int} is the integration time;
k is the Boltzmann constant;
v is the spacecraft ground track velocity;
A is the receiver area (Figure 3-11);
SNR_{Ns} is the SNR achieved in the integration time (taking into account pulse compression);
θ is the ground incidence angle.

The relation between peak (P_t) and average power (P_{avg}) is presented in Equation 3-25 where τ_p is the radar pulse length.

$$P_t = \frac{P_{avg}}{\tau_p PRF} \qquad \text{Equation 3-25}$$

Equation 3-24 has been used to calculate results for GeoSAR assuming that:

SNR_{Ns} is 10 dB;
F, the noise figure is 6 dB;
σ^0, the normalised radar cross section is -20 dB;
T_0, the noise temperature is 290 K;
λ, the wavelenth is 0.25 m;
v, satellite ground track velocity is according to the chosen orbit;
other system losses are 3dB.

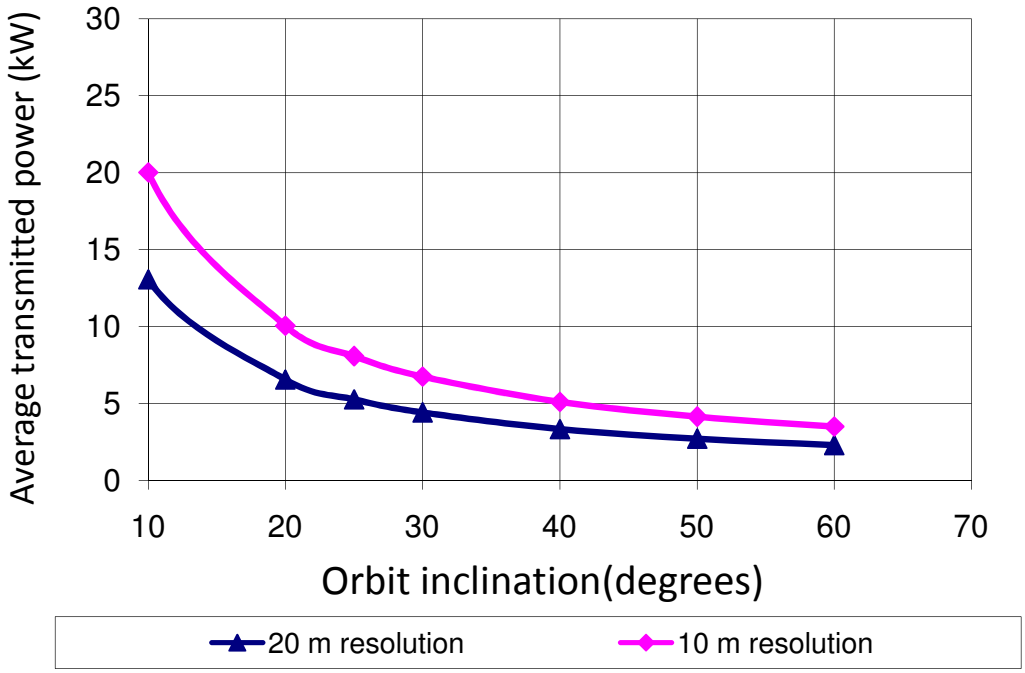

Figure 3-12. Average transmitted power (kW) as a function of orbit inclination for two different range resolutions (antenna dimension has been doubled to achieve a margin with respect to the minimum acceptable value as in Figure 3-11).

Figure 3-12 shows the value of the average transmitted power that is required (assuming an antenna surface doubled to achieve a margin). Once again, orbit inclination is the driving factor in system design. Average transmitted power decreases with orbit inclination as the minimum antenna area increases; moreover area coverage decreases at higher inclinations.

3.2.5 Active monostatic configuration - summary

The minimum antenna size and the level of transmitted power are the two major drivers in monostatic geosynchronous system design. These two parameters are closely related to orbit inclination (i.e. orbital velocity). This implies that, considering the analysis carried out in previous sections, an L band active monostatic configuration can be implemented only in a highly inclined orbit. On the other hand, due to range and azimuth ambiguities, a very large antenna is required increasing system cost and complexity. This issue can be improved using shorter wavelengths.

The configuration proposed by NASA JPL (2003) with a 60° inclined orbit and a 30 m diameter antenna, seems to be one of the possible compromise to implement a monostatic geosynchronous SAR system. This solution is not feasible now due to its technical complexity. The two main issues to tackle are the development of a very large deployable antenna and a significant improvement of the power generation sub-system capacity.

3.3 Bi-static configuration

The implementation of a geosynchronous SAR system has a second option, a receiver-only system that reuses the signal transmitted by a dedicated transmitter or by any transmitter of opportunity (passive bi-static). This will reduce the complexity of the system design. A bi-static configuration cannot fly along a highly inclined orbit, as it requires a very long integration time to achieve a reasonable SNR. Therefore, conclusions carried out in this section, apply to systems that fly along a nearly geostationary orbit (inclination smaller than few degrees).

The bi-static SAR configuration solves the power generation issue as it re-uses any signal transmitted by another satellite. The transmitter can be in GEO as well.

A relevant example in literature for a passive bi-static SAR system that re-uses the signal generated by a transmitter of opportunity such as Digital Audio Broadcasting (L band) is provided by Prati *et al.* (1998).

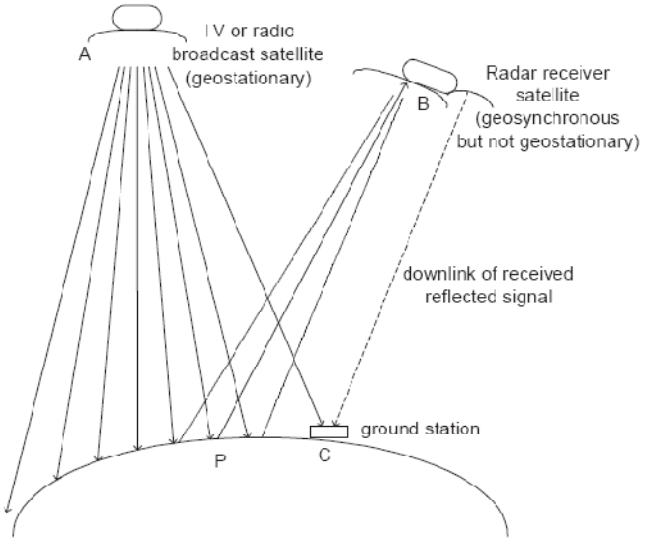

Figure 3-13. Passive bi-static geosynchronous SAR, system geometry (Hobbs, 2006).

Figure 3-13 presents the geometry of the system that reuses the signal transmitted by a satellite in a GEO orbit.

As in the active monostatic case, system design is heavily affected by the link budget. The brief analysis carried out in the following section will show that, given the average power transmitted by a transmitter, only a nearly geostationary orbit (an ideal geostationary orbit could not provide the relative motion required to create the synthetic aperture) with a small inclination can achieve a reasonable SNR.

The following sections will put a clear bridge between passive bi-static SAR and bi-static SAR with a dedicated transmitter (section 3.3.1), will present the peculiarities of the passive bi-static configurations in terms of link budget (section 3.3.2) and signal processing (section 3.3.3). Section 3.3.4 discusses the quasi-monostatic configuration and the assumption regarding the bi-static angle. As far as the orbit is concerned, the same analysis carried out for the monostatic configuration could be applied.

3.3.1 Passive bi-static or bi-static with a dedicated transmitter

As mentioned in the introduction to this section, a bi-static SAR requires a signal transmitted by a different platform. There are two different options:

- signal transmitted by a dedicated platform;

- signal transmitted by a non-cooperative platform (i.e. transmitter of opportunity) as in Prati *et al.* (1998).

If the signal is transmitted by a dedicated platform, transmitted waveform could be optimised in order to achieve better performances and easier signal processing. If the system is reusing the signal transmitted by a non-cooperative transmitter (passive bi-static) there could be a degrade in system performances due to the waveform transmitted and to the information content that is included in the transmitted signal. In literature many analysis have been carried out to investigate the potential of existing signals for radar applications. As an example, Griffiths *et al.* (2003) provide an analysis about the suitability of off-air signals for radar applications.

In the present research it has been assumed that the system re-uses the signal coming from a transmitter of opportunity and that this signal is appropriate for SAR image formation. Following this hypothesis, issues regarding the transmitted waveform and synchronisation between transmitter and receiver have not been taken into account. Therefore, when looking into bi-static SAR configurations, the present research will discuss only issues regarding passive (or parasitic) bi-static SAR systems.

3.3.2 Bi-static radar equation

Hereafter, an analytical expression for SNR at the receiver will be presented for a passive bi-static SAR. Equation 3-26 (Prati *et al.*, 1998) provides the power at the receiver.

$$P_R = \frac{P_t B}{4\pi R^2} A_r \sigma^0 \Delta R_r \Delta R_a \qquad \text{Equation 3-26}$$

In Equation 3-26, P_R is the power density at the receiver in $Wm^{-2}Hz^{-1}$;
P_t is the power density reflected from the ground surface in $Wm^{-2}Hz^{-1}$;
B is the signal bandwidth;
R is radar slant range;
A_r is the area of the receiving antenna;
σ^0 is the radar backscatter.

Under the assumption that the motion of the SAR antenna is shorter than the maximum synthetic aperture, the achievable azimuth resolution ΔR_a could be expressed in terms of ground-track satellite velocity v_{sc} and integration time T_{int} (Equation 3-27).

$$\Delta R_a = \Delta y = \frac{\lambda R}{v_{sc} T_{\text{int}}} \qquad \text{Equation 3-27}$$

Range resolution ΔR_r could be expressed using Equation 3-28 (Willis, 1991) where φ is the ground grazing angle and β is the bi-static angle.

$$\Delta R_r = \frac{c}{2B\sin\varphi\cos^2\frac{\beta}{2}}$$ Equation 3-28

Using previous equations Equation 3-26 becomes:

$$P_R = \frac{P_t \cancel{B}}{4\pi R^{\cancel{3}}} A_r \sigma^0 \frac{\lambda \cancel{R}}{v_{sc} T_{obs}} \frac{c}{2\cancel{B}\sin\varphi\cos^2\frac{\beta}{2}}$$ Equation 3-29

"*Averaging the received signal (re-phased and thus coherent) and the noise (incoherent) for T_{int}, we get an equivalent noise bandwidth of $1/T_{int}$"* (Prati *et al.*, 1998).

$$SNR = \frac{P_R}{FkT_n \frac{1}{T_{\text{int}}}} = \frac{P_t}{4\pi R^2} A_r \sigma^0 \frac{\lambda R}{v_{sc}} \frac{c}{2\sin\varphi\cos^2\frac{\beta}{2}} \frac{1}{FkT_n}$$ Equation 3-30

In Equation 3-30, the ratio between the signal and the noise power in the used bandwidth has the following expression that depends from the noise figure *F*, antenna noise temperature T_n and the Boltzmann constant *k*.

Many parameters in Equation 3-30 are constants (summarised in Equation 3-31) therefore SNR depends only on the size of the receiver antenna and on the velocity of the satellite. It has to be said that the velocity of the satellite depends on the inclination of the orbit that limits the length of the footprint on the Earth's surface (that is also the size of the synthesized aperture).

$$\text{Constant} = c_o = \frac{P_t}{4\pi R^2} \sigma_0 \frac{\lambda R c}{2\sin\varphi\cos^2\frac{\beta}{2}} \frac{1}{FkT_n}$$ Equation 3-31

For a given configuration, Equation 3-32 shows SNR in a form that allows an extremely simple trade-off analysis between the choice of the orbit and the physical dimensions of the antenna. Assuming that P_t is -171 dBWm^{-2}Hz^{-1} (Prati *et al.*, 1998), σ^0 is -18 dB, noise figure *F* is 7 dB, noise temperature *T* is 290 K, bi-static angle β is 30°, grazing angle φ is 30°, c_0 is equal to 0.50 dB therefore:

$$[A_r]_{dB} - [v_{sc}]_{dB} = SNR_{dB} + 0.5$$ Equation 3-32

In Equation 3-32, A_r is the area of the receiving antenna in m^2,
v_{sc} is the ground-track velocity in m/s.

The proposed GeoSAR configuration gives a SNR of 9.7 dB. This equation could be validated using the values presented by Prati *et al.* (1998) (i.e. bi-static angle=90°).

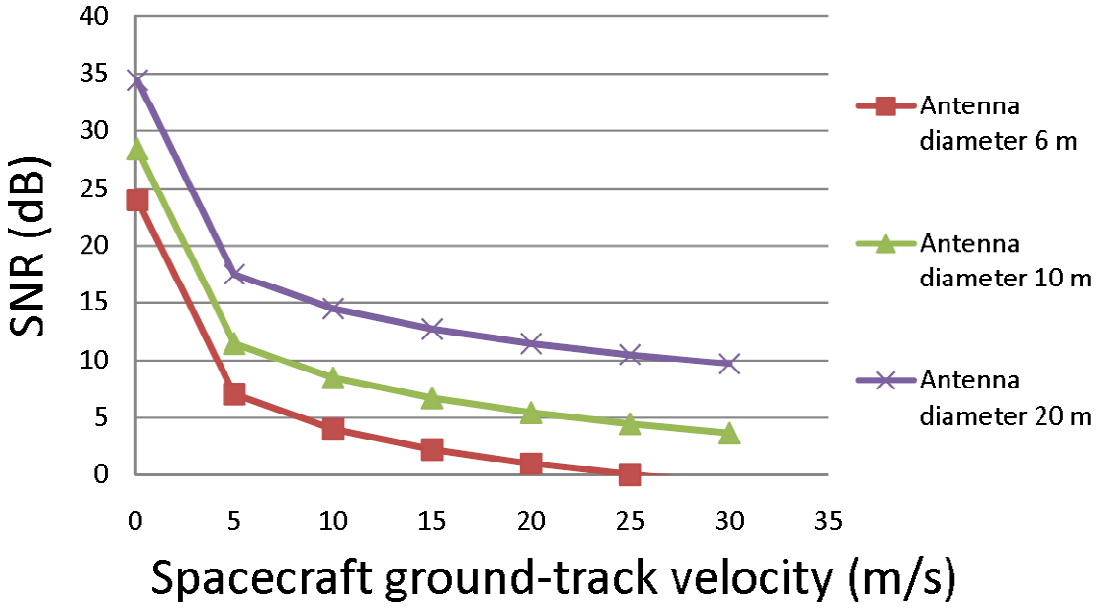

Figure 3-14. SNR for a passive bi-static geosynchronous SAR.

Figure 3-14 shows that, as the spacecraft velocity increases (i.e. orbit inclination increases) the focused SNR decreases and a larger antenna is required to keep a constant power budget.

Results plotted in Figure 3-14 are clearly influenced by the amount of power available from the transmitter of opportunity.

A relatively small antenna (i.e. 6 meter diameter) has to be placed in a nearly GEO orbit (orbit inclination smaller than 1°, see Table 3-3). This implies that the motion of the satellite along its flight path is much shorter than the maximum achievable synthetic aperture length.

Considering a zero eccentricity geosynchronous orbit with a figure-of-eight ground track, Table 3-3 presents the length of the track north-south followed by the satellite (i.e. the synthetic aperture) and the velocity with respect to the sub-satellite point. The data in the table include the values provided by Prati *et al.* (1998) and consider a simplified linear relation between motion and velocity. This assumption is acceptable for small orbit inclinations.

The synthetic aperture is limited by the motion of the satellite as the maximum achievable synthetic aperture would eventually be 1500 km for a 6 m diameter antenna (λ=0.25 m, R=36000 km).

Table 3-3. Length of the line described during the north-south motion and maximum ground track velocity.

Length of the line described (km)	*Ground-track Velocity (m/s)*
60	2
120	4
240	8

3.3.3 Azimuth pre-summing

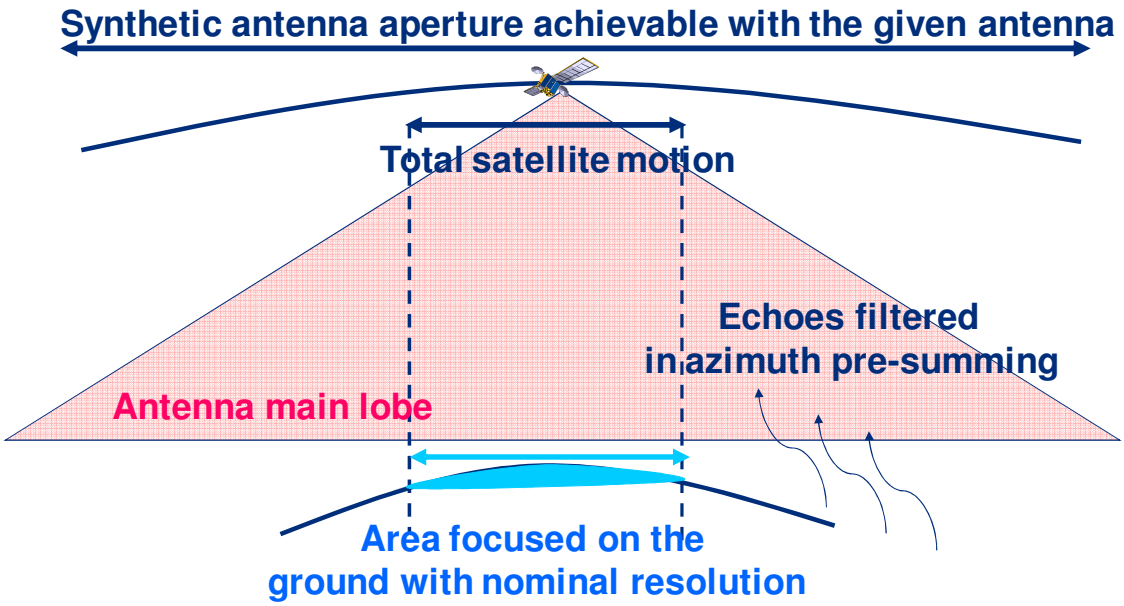

Figure 3-15. Basic principle of azimuth pre-summing for a bi-static SAR configuration (Bruno *et al.*, 2006).

In a bi-static passive configuration, the integration time is the major driver in the system design. To achieve an integration time of many hours orbit inclination has to be very shallow therefore, the motion of the satellite limits the synthetic aperture. The system is ambiguous in Doppler as the main lobe of the antenna is larger than the synthetic aperture and allows azimuth ambiguities to enter the main lobe.

To avoid azimuth ambiguities (the full azimuth resolution cannot be achieved) azimuth pre-summing could be used to low-pass filter Doppler bandwidth. Pre-summing means considering a large correlation window ΔT for each pulse. It is equivalent to considering

an antenna working stop and go at intervals $v_{sc}\Delta T$. The main effect of pre-summing is that azimuth resolution is reduced to the point of being unambiguous. The azimuth footprint is reduced as well.

As shown in Figure 3-15, the total satellite motion is much shorter than the antenna main beam. As specified by Prati *et al.* (1998), only an area as large as the total satellite motion, could be focused with nominal azimuth resolution (neglecting edge effects). *"As long as the antenna footprint after pre-summing during ΔT, is greater than the synthetic antenna aperture, the azimuth resolution ΔR_{az} remains unchanged, except for edge effects"* (Prati *et al.* 1998).

3.3.4 Quasi-monostatic or true bi-static configuration

In a bi-static SAR, the bi-static angle has a significant effect on target backscatter that can have significant fluctuations associated with small variations in the bi-static angle.

If the transmitter and the receiver are quite close in the sense that their distance is small with respect to the radar slant range, the bi-static angle is very small. This configuration is called pseudo-monostatic or quasi-monostatic (Willis, 1991). In this configuration the target backscatter is comparable to mono-static backscatter and does not show significant fluctuations.

In the present research, the assumption that the bi-static angle is 30° has been made; therefore this configuration does not qualify as a quasi-monostatic as the distance between transmitter and receiver (≈6000 km) is not small compared to the slant range (≈40000 km). The bi-static *radar cross section* (RCS) will be significantly different from the monostatic one. However, target backscatter fluctuations have not been taken into account in link budgets and other power calculations as their contribution could be neglected at this stage of the research.

3.3.5 Bi-static configuration – summary

The difference between a passive bi-static configuration and a bi-static SAR with a dedicated transmitter has been presented. This research takes into account only a passive bi-static (parasitic) configuration that reuses the signal transmitted by any transmitter of opportunity. A 30° bi-static angle has been assumed, this implies that the configuration is purely bi-static. Backscatter variations due to the bi-static angle have been neglected in the present research.

For such a system, the amount of power available is the major driver in the system design of a passive bi-static geosynchronous SAR. With the assumed power level (Prati *et al.*, 1998) the system requires a very long integration time to achieve a reasonable SNR. Therefore, the satellite has to fly along a nearly geostationary orbit.

With respect to the monostatic active SAR, the bi-static passive configuration does not require huge antennas and large power requirements. Therefore, it could be realised with current technologies.

Following the calculations proposed, antenna size should be at least about 6 meter in diameter for an L band satellite. Using shorter wavelengths, the size of the reflectors can be reduced as well.

3.4 System trade-off analysis

Having discussed the peculiarities and the main issues related to system design of both monostatic and bi-static configurations, a system trade-off analysis has been carried out in order to define the configuration that will be further investigated in the present research.

Various configurations have been assessed to compile a technical feasibility trade-off (section 3.4.1) looking into two main aspects:

- phase delays;
- link budget from GEO.

Once the feasibility of a set of possible system configurations has been evaluated, the choice of the final system design could be completed considering the results of the frequency trade-off analysis (section 3.4.2) that takes into account the following parameters:

- temporal decorrelation;
- potential transmitters of opportunity (bi-static configuration only);
- frequency allocation;
- system complexity;
- applications.

The bands listed in Table 3-4 have been considered in the discussion.

Table 3-4. Frequencies considered in the trade-off analysis.

	Frequency range	Wavelength (cm)
P	0.7	42,86
	1	30,00
L	1.2	25,00
S	2.4	12,50
C	4.5	6,67
	6	5,00
X	9	3,33
	10.5	2,86
Ku	12	2,50
	15	2,00
K	20	1,50

The analysis has been carried out considering three options for the integration time: 1 minute, 1 hour and 8 hours. In this section the observation time has not been taken into account as an integration time shorter than the actual observation time could be chosen to cope with phase delay induced complexities.

The effect of the chosen integration time on the system design is substantial. It clearly affects the phase delay and the link budget. Consequently, it affects ground azimuth resolution and possible applications. There is also an influence on system complexity as signal processing on long integration time requires phase compensation algorithms to be applied in order to guarantee signal coherence on long timescales.

The proposed configurations for a geosynchronous SAR have been presented in sections 3.2 and 3.3 .

3.4.1 Technical feasibility trade-off

This analysis takes into account only of phase uncertainty and the link budget to assess the technical feasibility of the various configurations. Frequencies in the range from P to K band have been considered with three different integration times (1 minute, 1 hour, 8 hours).

3.4.1.1 Phase uncertainty

As presented in Chapter 2, various phenomena affect signal phase delays. Earth tides, tropospheric and ionospheric delay have been looked into, as they are the major sources of concern. The effects of phase uncertainty depend mainly on the integration time; therefore, the following sections present the analysis of three different cases.

To evaluate the phase delay budget, Earth tidal displacement and tropospheric delay uncertainties have been directly converted into phase delays. Ionospheric delay uncertainty ($\Delta\varphi_{iono}$) has been estimated considering the accuracy in TEC measurement (*TEC*) and the signal frequency *f*. It is converted to phase delay using Equation 3-33.

$$\Delta\varphi_{iono} = -\frac{40,28}{f^2}TEC \qquad \text{Equation 3-33}$$

Phase uncertainty calculations assume a 2-way travel along a path $3^{0.5}$ times longer than the zenith path (to take into account the difference between slant and zenith delay). To allow image formation, residual phase delay has to be estimated during SAR focussing. Techniques such as auto-focus (Belcher, 2008) can be used effectively in presence of correlated noise up to a certain amount of residual phase noise. In the phase delay budget, 2.5 rad has been assumed as the upper limit for the sum of the three phase delays. This figure is comparable with the upper limit for phase delay assumed by Belcher (2008) for along-track autofocus (+/- π rad 2σ). It has to be said the phase compensation techniques require a large SNR.

3.4.1.1.1 1-minute integration time

On such timescale, phase uncertainties induced by Earth tides can be neglected as their period is about 12 hours. Tropospheric delay uncertainty can be neglected as well because variations in both hydrostatic and wet delay happen on longer timescales.

Table 3-5. Phase uncertainty budget for 1-minute integration time.

Band	Frequency (GHz)	Earth tide (m)	Troposphere (m)	Ionosphere (m)	Earth tide (rad)	Troposphere (rad)	Ionosphere (rad)	Sum (rad)
P	0.7	0	0	0.041	0.000	0.000	2.087	2.09
	1	0	0	0.020	0.000	0.000	1,461	1,46
L	1.2	0	0	0.014	0.000	0.000	1.218	1.22
S	2.4	0	0	0.003	0.000	0.000	0.609	0.61
C	4.5	0	0	0.001	0.000	0.000	0.325	0.32
	6	0	0	0.001	0.000	0.000	0.244	0.24
X	9	0	0	0.000	0.000	0.000	0.162	0.16
	10.5	0	0	0.000	0.000	0.000	0.139	0.14
Ku	12	0	0	0.000	0.000	0.000	0.122	0.12
	15	0	0	0.000	0.000	0.000	0.097	0.10
K	20	0	0	0.000	0.000	0.000	0.073	0.07

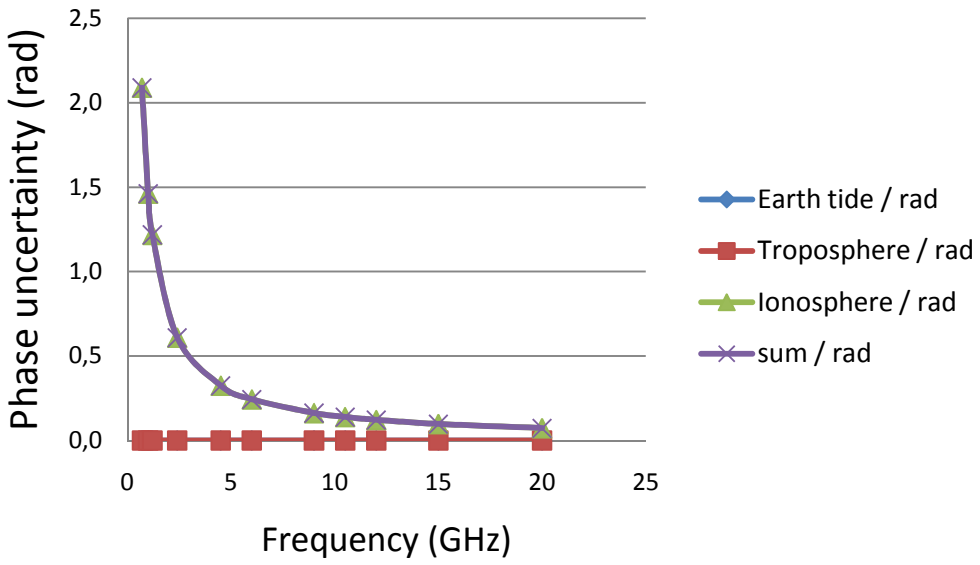

Figure 3-16. Phase uncertainty budget at various frequencies (1-min integration time).

Ionospheric correlation time, as presented in section 2.12.2, can be as short as a few minutes so the phase delay budget can be carried out taking into account a relatively small residual TEC variation (i.e. 0.05 TECU) after phase noise compensation during the integration time.

Results are summarised in Table 3-5 and in Figure 3-16. In the table, the cells with the sum of phase uncertainties smaller than 2.5 rad have been highlighted.

3.4.1.1.2 1-hour integration time

Phase uncertainties induced by Earth tides have a period of about 12 hours. Considering a 1-hour integration time, a residual 1 mm phase delay can be credited to Earth tides.

Dry tropospheric delay could be neglected as its variations happen on timescales longer than 1 hour; however, wet tropospheric delay variations has to be taken into account. At long wavelengths (P or L band), coarse models (such as MOPS, with 5 cm accuracy) are able to compensate for tropospheric delay; at shorter wavelengths more accurate prediction techniques such as measurements coming from GPS networks (1,5 mm accuracy) are required (section 2.11.2.2.6).

Ionospheric phase delay is likely to be uncorrelated over a 1-hour time period. The phase delay budget assumes that TEC measurements with an accuracy of 0.2 TECU are available. This is a quite demanding assumption; it will be discussed in more details when dealing with ionospheric effects on a geosynchronous SAR (section 6.4).

Results are summarised in Table 3-6 and plotted in Figure 3-17. In the table, the cells with total phase delay smaller than 2.5 rad have been highlighted.

Table 3-6. Phase uncertainty budget for 1-hour integration time.

Band	Frequency (GHz)	Earth tide (m)	Troposphere (m)	Ionosphere (m)	Earth tide (rad)	Troposphere (rad)	Ionosphere (rad)	Sum (rad)
P	0.7	0.001	0.0015	0.164	0.051	0.076	8.350	8.35
	1	0.001	0.0015	0.081	0.073	0.109	5.845	5.85
L	1.2	0.001	0.0015	0.056	0.087	0.131	4.871	4.87
S	2.4	0.001	0.0015	0.014	0.174	0.261	2.435	2.46
C	4.5	0.001	0.0015	0.004	0.326	0.490	1.299	1,43
	6	0.001	0.0015	0.002	0.435	0.653	0.974	1.25
X	9	0.001	0.0015	0.001	0.653	0.979	0.649	1,34
	10.5	0.001	0.0015	0.001	0,762	1.143	0.557	1,48
Ku	12	0.001	0.0015	0.001	0.871	1,306	0.487	1,64
	15	0.001	0.0015	0.000	1.088	1,632	0.390	2.00
K	20	0.001	0.0015	0.000	1,451	2.177	0.292	2.63

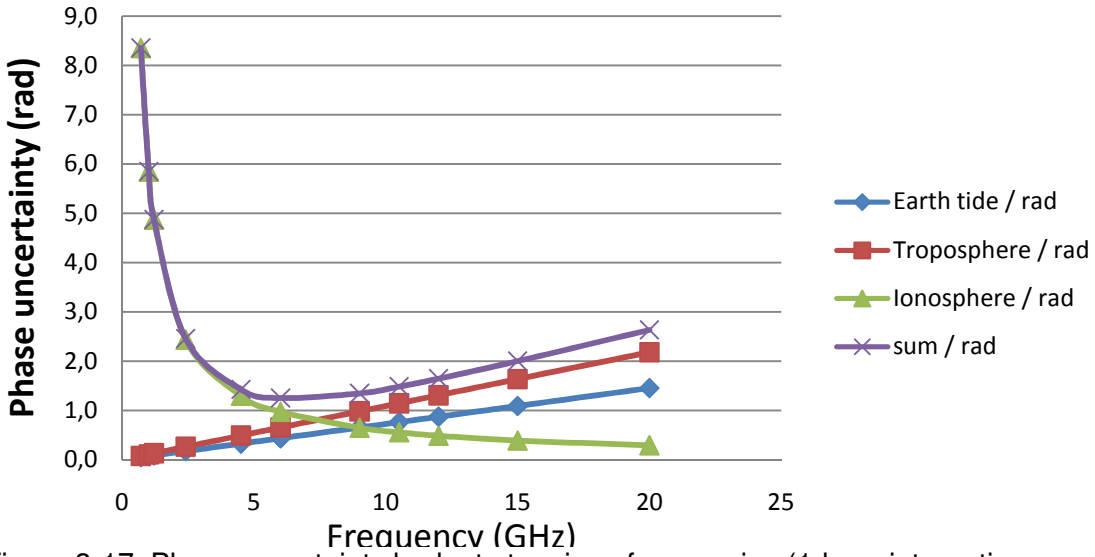

Figure 3-17. Phase uncertainty budget at various frequencies (1-hour integration time).

3.4.1.1.3 8-hour integration time

According to McCarthy and Petit (2004), Earth tides displacements could be modelled with an accuracy of 4 mm (1 mm due to solid Earth tides and 3 mm due to ocean loading effects). As discussed in section 2.10.4.2 , using more advanced ocean loading models or limiting the analysis to continental plates where the effect of ocean loading is negligible, the overall accuracy could be reduced to 2 mm (1 mm credited to solid Earth tides and 1 mm due to ocean loading).

Tropospheric uncertainties also might be considered. An overall accuracy of 2.5 mm has been assumed (1 mm due to dry delay and 1,5 mm due to wet delay).

Ionospheric phase delay is likely to be uncorrelated over an 8-hour time period. As in the previous case, phase uncertainty budget assumes that TEC measurements with 0.2 TECU accuracy are available.

Results are summarised in Table 3-7 and plotted in Figure 3-18. In the table, the cells with total phase uncertainty smaller than 2.5 rad have been highlighted.

Table 3-7. Phase uncertainty budget for 8-hour integration time.

Band	Frequency (GHz)	Earth tide (m)	Troposphere (m)	Ionosphere (m)	Earth tide (rad)	Troposphere (rad)	Ionosphere (rad)	Sum (rad)
P	0,7	0.002	0.0025	0.164	0.102	0.127	8.350	8.35
	1	0.002	0.0025	0.081	0.145	0.181	5.845	5.85
L	1.2	0.002	0.0025	0.056	0.174	0.218	4.871	4.88
S	2.4	0.002	0.0025	0.014	0.348	0.435	2.435	2.50
C	4.5	0.002	0.0025	0.004	0.653	0.816	1.299	1,67
	6	0.002	0.0025	0.002	0.871	1.088	0.974	1,70
X	9	0.002	0.0025	0.001	1,306	1,632	0.649	2.19
	10.5	0.002	0.0025	0.001	1,524	1,904	0.557	2.50
Ku	12	0.002	0.0025	0.001	1,741	2.177	0.487	2.83
	15	0.002	0.0025	0.000	2.177	2.721	0.390	3.51
K	20	0.002	0.0025	0.000	2.902	3.628	0.292	4.65

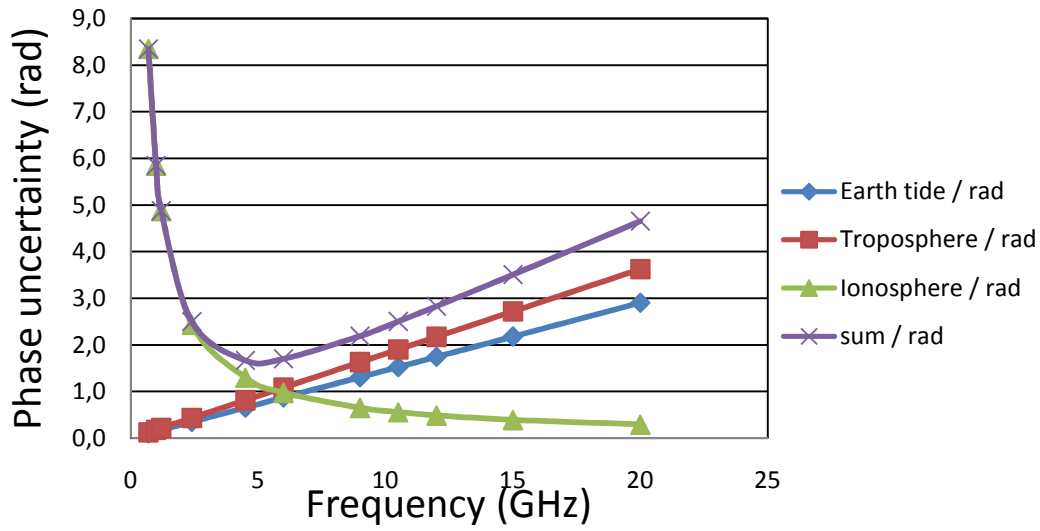

Figure 3-18. Phase uncertainty budget at various frequencies (8-hour integration time).

3.4.1.1.4 Phase delay summary

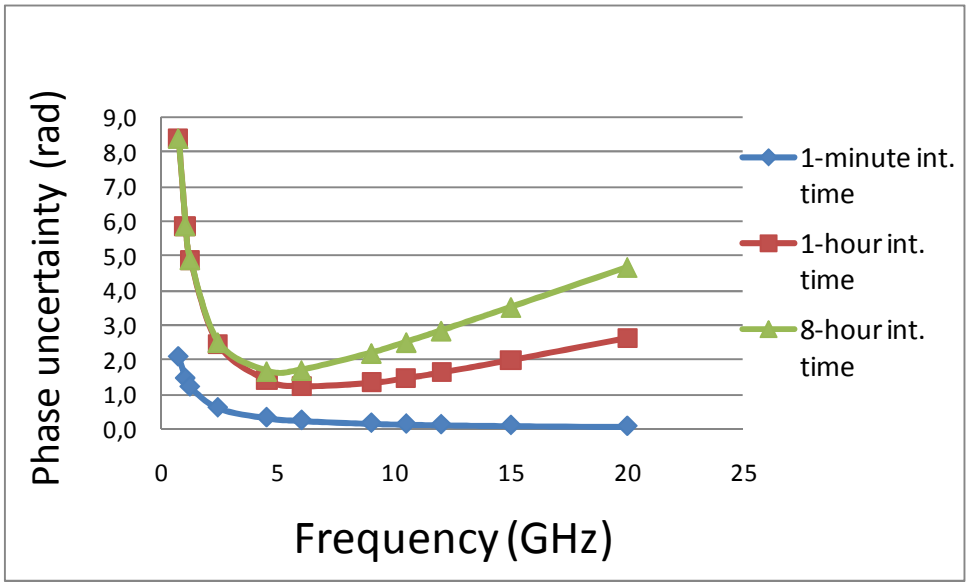

Figure 3-19. Phase uncertainty at various integration times.

Figure 3-19 summarises the outcomes of the phase uncertainty budget at various frequencies and integration times.

Phase uncertainty is not an issue if a relatively short integration time (1 minute) is used.

At intermediate integration times (about 1 hour), phase uncertainty becomes significant at long wavelengths due to ionospheric delay and at higher frequencies due to tropospheric delay.

If very long integration times are used, troposphere and Earth tides might completely hamper SAR focussing at high frequencies, on the other hand ionospheric delay uncertainty affects significantly longer wavelengths.

The effect of phase delays, in presence of correlated phase noise has to be mitigated during image formation applying autofocus algorithms. According to Belcher (2008) these procedures have two main requirements:

- Signal phase should be coherent for a portion of the synthetic aperture to start the iterative auto-focus procedure;

- SNR should be large enough (i.e. greater than 20 dB) to achieve a small error in the estimation of the autofocus parameters.

Both ionospheric and tropospheric noise are usually correlated in space and time. Autofocus procedures to mitigate the effects of phase delays could potentially be applied if SNR is large enough. The capability of coping with large phase delays is therefore closely connected to the link budget, that will be discussed in the following section.

3.4.1.2 Link budget

Hobbs (2008) describes the methodology to address link budget calculation from GEO, a useful method to assess the feasibility of different GeoSAR concepts. For the sake of completeness, the key steps of this methodology are restated hereafter.

The amount of power received P_R from a system with a circular antenna (diameter d) and horizontal resolution ΔR_{range} at a slant range R is given in Equation 3-34.

$$P_R = \frac{\cos\theta}{4\pi 1.22^2} \frac{P_T d^4 \Delta R_{range}{}^2 \sigma^0}{\lambda^2 R^4} \frac{1}{L_R^2} \qquad \text{Equation 3-34}$$

In Equation 3-34, σ^0 is the backscatter coefficient (assumed equal to -10 dB);
θ is the local incidence angle (about 43° for a location with 40° latitude);
d is the diameter of the receiving/transmitting antenna;
λ is the radar wavelength;
L_R is the signal attenuation induced by atmospheric phenomena.

The backscatter coefficient has been assumed constant for both mono-static and bi-static configuration. The effect of the bi-static angle has not been included. This simplification is acceptable in this analysis as it is only preliminary.

The same equation can be applied to the bi-static case taking into account different slant ranges and different antenna sizes.

The bandwidth B required for a given horizontal resolution is presented in Equation 3-35. Following this expression, the noise power P_N is shown in Equation 3-36.

$$B = \frac{c}{2\Delta R_{range} \sin\theta} \qquad \text{Equation 3-35}$$

$$P_N = kTB \qquad \text{Equation 3-36}$$

The SNR for a single pulse (SNR_0) is given in Equation 3-37.

$$SNR_0 = \frac{P_R}{P_N}$$ Equation 3-37

The minimum time t_{min} between pulses is determined by the time during which backscattered power is received from the footprint (Equation 3-38).

$$t_{\min} = \frac{4R\psi \tan\theta}{c}$$ Equation 3-38

In Equation 3-38, ψ is the antenna beam-width (i.e. $1.22\,\lambda/d$) for a circular antenna.

The integration gain that provides the final SNR for the assumed integration time is given in Equation 3-39.

$$g = \sqrt{\frac{\mathrm{T}_{\mathrm{int}}}{t_{\min}}}$$ Equation 3-39

The final SNR has been obtained from Equation 3-37 adding a 20 dB pulse compression gain (Skolnik, 2001).

Losses due to atmospheric phenomena have been estimated using ITU (2003). The rainfall intensity $R_{0.01}$ exceeded for 0.01% of an average year has been assumed equal to 50 mm/h taking into account values expected for continental Europe.

Following prescriptions in ITU (2003) the path in the rain for a station at sea level is given by:

$$L_{rain} = 2 \times {h_{rain}}/{\sin E}$$ Equation 3-40

In Equation 3-40, L_{rain} is the path (two-way) within the rain;
h_{rain} is the rain altitude assumed conservatively equal to 5 km as prescripted in ITU(2003) for areas with latitude between -21° and 23°;
E is satellite elevation.

Assuming a 40° satellite elevation the path in the rain is ≈15 km.

Table 3-8 provides a worst case prediction for two-way rain attenuation L_R^2 for areas over continental Europe corresponding to the values $R_{0,1}$=10 mm/h and $R_{0,01}$=50 mm/h. Data have been estimated using the normogram reported in ITU (2003) and assuming that E=40° and L_{rain}=15 km.

Table 3-8. Worst case rain attenuation L_R^2 for areas over Europe (i.e.$R_{0,1}$=10 mm/h $R_{0,01}$=50 mm/h)

Band	Frequency (GHz)	L_R^2 (db) $R_{0,1}$ 10 mm/h	L_R^2 (db) $R_{0,01}$ 50 mm/h
P	0.7	0	0
	1	0	0
L	1.2	0	0
S	2.4	0	0
C	4.5	0.15	0.5
	6	0.45	3.75
X	9	1.95	14.5
	10.5	3.3	25.5
Ku	12	4.5	27
	15	7.5	42
K	20	12	82.5

Table 3-9 summarises SNR achievable from a system with 1 kW transmitted RF, a 6 m receiving/transmitting antenna and a 1 km range resolution and neglecting rain losses (L_R=0 dB).

Table 3-9. Link budget from GEO. SNR estimated following the procedure described in Hobbs (2008) assuming a 6 m antenna, σ^0 -10 dB, 1 kW transmitted power, 1 km range resolution, 20 dB pulse compression gain and L_R=0 dB.

Band	frequency GHz	1-minute integration SNR (dB)	1-hour integration SNR (dB)	8-hour integration SNR (dB)
P	0.7	-5.95	-5.02	-0.50
	1	-2.07	-1.14	3.38
L	1.2	-0.09	0.84	5.36
S	2.4	7.43	8.37	12.89
C	4.5	14.21	15.14	19.66
	6	17.38	18.31	22.83
X	9	21.89	22.83	27.35
	10.5	23.30	24.23	28.75
Ku	12	24.91	25.84	30.36
	15	27.33	28.26	32.78
K	20	30.46	31.39	35.91

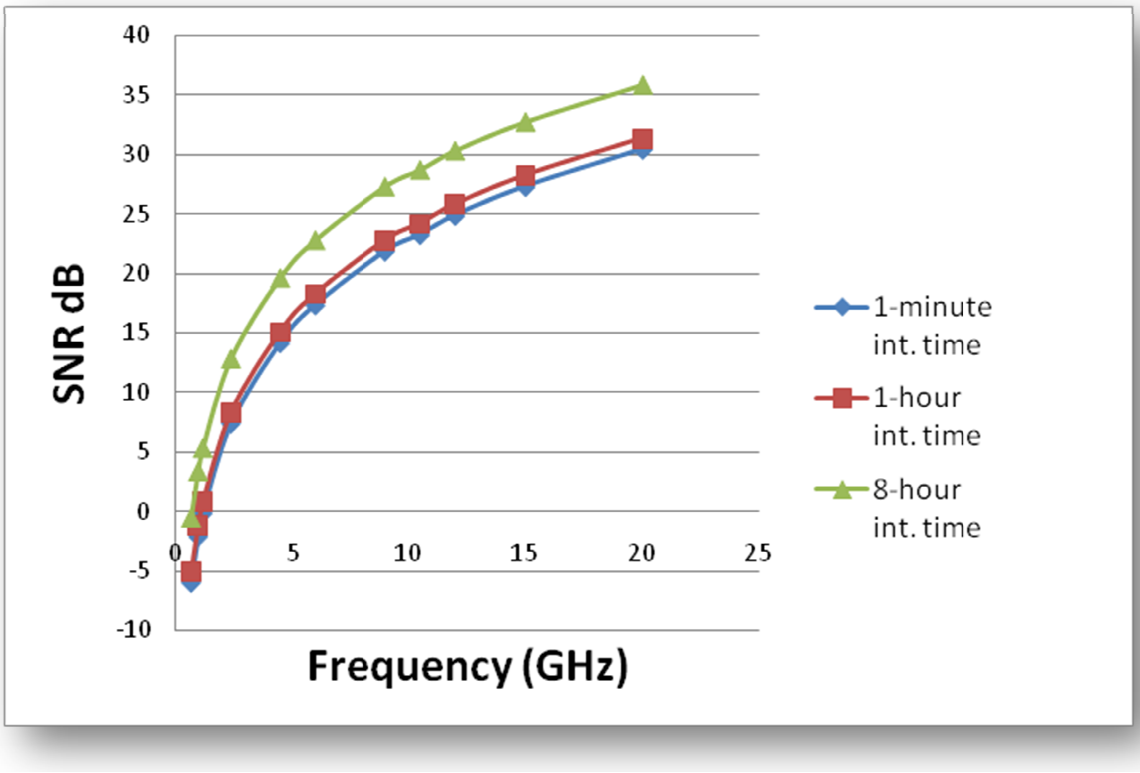

Figure 3-20. SNR in dB corresponding to different integration times.

SNR limitations could be overcome adopting a larger horizontal resolution and/or a larger antenna. Taking into account Equation 3-34, for any configuration it is possible to determine the factor how much the antenna diameter (i.e. D_d) or the horizontal resolution (i.e. D_Δ) should be increased to achieve a given SNR improvement (i.e. $[\Delta SNR]_{dB}$ in Equation 3-41 and Equation 3-42).

$$D_d = 10^{\frac{[\Delta SNR]_{dB}}{40}} \qquad \text{Equation 3-41}$$

$$D_\Delta = 10^{\frac{[\Delta SNR]_{dB}}{20}} \qquad \text{Equation 3-42}$$

Table 3-10 presents, for all configurations where the SNR (Table 3-9) is below 20 dB, the antenna diameter required to achieve the 20 dB SNR goal.

Table 3-11 presents, for all configurations where the SNR (Table 3-9) is below 20 dB, the values of the azimuth resolution required to achieve the 20 dB SNR goal.

Table 3-10. Antenna diameter required to achieve a 30 dB SNR assuming σ^0 -10 dB, 1 kW transmitted power, 1 km range resolution, 20 dB pulse compression gain and L_R=0 dB.

Band	frequency GHz	1-minute integration	1-hour integration	8-hour integration
P	0.7	16.9	10.1	7.8
	1	24.0	14.4	11.1
L	1.2	21.5	12.9	9.9
S	2.4	13.9	8.3	6.4
C	4.5	9.4	N.A.	N.A.
	6	7.8	N.A.	N.A.
X	9	6.1	N.A.	N.A.
	10.5	N.A.	N.A.	N.A.
Ku	12	N.A.	N.A.	N.A.
	15	N.A.	N.A.	N.A.
K	20	N.A.	N.A.	N.A.

Table 3-11. Spatial Resolution required to achieve a 20 dB SNR assuming σ^0 -10 dB, 1 kW transmitted power, 6 m diameter antenna, 20 dB pulse compression gain and L_R=0 dB.

Band	frequency GHz	1-minute integration	1-hour integration	8-hour integration
P	0.7	7939	2853	1695
	1	16054	5769	3428
L	1.2	12782	4593	2730
S	2.4	5374	1931	1148
C	4.5	2465	N.A.	N.A.
	6	1710	N.A.	N.A.
X	9	1017	N.A.	N.A.
	10.5	N.A.	N.A.	N.A.
Ku	12	N.A.	N.A.	N.A.
	15	N.A.	N.A.	N.A.
K	20	N.A.	N.A.	N.A.

To define which configurations are not feasible due to an unfavourable link budget, an upper limit for antenna diameter and for azimuth resolution has to be set. Therefore, considering a 15 m antenna and 1 km resolution cell the maximum achievable SNR is given in Table 3-12 (neglecting rain losses i.e. L_R=0 dB). Configurations that are not able to reach the 20 dB SNR lower limit (highlighted in the table) are considered as technical unfeasible with the assumed amount of transmitted power.

Table 3-12. Link budget from GEO. SNR estimated following the procedure described in Hobbs (2008) assuming a 15 m antenna, σ^0 -10 dB, 1 kW transmitted power, 1 km range resolution, 20 dB pulse compression gain and L_R=0 dB.

Band	frequency GHz	1-minute integration SNR (dB)	1-hour integration SNR (dB)	8-hour integration SNR (dB)
P	0.7	2.00	10.89	15.41
	1	5.89	14.78	19.30
L	1.2	7.87	16.76	21.28
S	2.4	15.39	24.28	28.80
C	4.5	22.16	31.05	35.57
	6	25.34	34.23	38.75
X	9	29.85	38.74	43.26
	10.5	31.26	40.15	44.67
Ku	12	32.87	41.76	46.28
	15	35.29	44.18	48.70
K	20	38.41	47.30	51.82

As shown in Equation 3-34, the link budget is affected by rain attenuation, especially at frequencies higher than 10 GHz, the following tables show the outcomes of the link budget when rain attenuation corresponding to $R_{0,1}$ (Table 3-13) and $R_{0,01}$ (Table 3-14) are taken into account. In the tables cells in light gray show configurations that were already not feasible neglecting rain attenuation while cells in dark gray show configurations that could become unfeasible taking into account rain attenuation.

Table 3-13. Link budget from GEO. SNR estimated following the procedure described in Hobbs (2008) assuming a 15 m antenna, σ^0 -10 dB, 1 kW transmitted power, 1 km range resolution, 20 dB pulse compression gain and L_R corresponding to $R_{0,1}$=10 mm/h.

Band	frequency GHz	1-minute integration SNR (dB)	1-hour integration SNR (dB)	8-hour integration SNR (dB)
P	0.7	1.3	10.19	14.71
	1	4.89	13.78	18.3
L	1.2	6.67	15.56	20.08
S	2.4	12.99	21.88	26.4
C	4.5	17.66	26.55	31.07
	6	19.34	28.23	32.75
X	9	20.85	29.74	34.26
	10.5	20.76	29.65	34.17
Ku	12	20.87	29.76	34.28
	15	20.29	29.18	33.7
K	20	18.41	27.3	31.82

Table 3-14. Link budget from GEO. SNR estimated following the procedure in Hobbs (2008) assuming a 15 m antenna, σ^0 -10 dB, 1 kW transmitted power, 1 km range resolution, 20 dB pulse compression gain and L_R losses ($R_{0,01}$=50 mm/h).

Band	frequency GHz	1-minute integration SNR (dB)	1-hour integration SNR (dB)	8-hour integration SNR (dB)
P	0.7	2	10.89	15.41
	1	5.89	14.78	19.3
L	1.2	7.87	16.76	21.28
S	2.4	15.39	24.28	28.8
C	4.5	21.66	30.55	35.07
	6	21.59	30.48	35
X	9	15.35	24.24	28.76
	10.5	5.76	14.65	19.17
Ku	12	5.87	14.76	19.28
	15	-6.71	2.18	6.7
K	20	-44.09	-35.2	-30.68

For systems working at frequencies higher than X band, there is a significant reduction in link budget margin caused by rain. This implies that at such wavelength there will be reduction is system availability due to rain attenuation.

3.4.1.3 Technical feasibility trade-off - conclusions

To assess technical feasibility of the various configurations and to compare their effectiveness, a score has been assigned to phase uncertainty and SNR (in absolute terms) for each wavelength. Data have been filtered to limit the analysis removing configurations that show a phase delay larger than 2.5 rad (upper limit for auto-focus compensation) and that do not allow the formation of a SNR higher than 20 dB (antenna diameter 15 m, azimuth resolution 1 km, transmitted power 1 kW).

Scores have been normalised between 0 and 10 assigning the maximum value respectively to the lowest phase uncertainty and the highest SNR (in absolute terms). The rationale of this assumption comes from the fact that a large SNR allows a better phase delay compensation using autofocus algorithms.

The outcome of this analysis is shown in the following table, where the scores assigned to SNR and to phase delays have been summed.

The label *SNR* states that this configuration is not technically feasible due to SNR limitations. The label *PHASE* states that the configuration is not technically feasible due to phase noise limitations.

The most significant considerations that could be derived from Table 3-15 and Figure 3-21 are:

- K band can be used only with short integration time due to the significant phase delay.
- 1-hour integration time can be used with bands up to Ku.
- Wavelengths from L band to X band can be used with very long integration times.
- L band requires a large antenna to achieve a significant SNR; however, it shows a large phase delay due to ionospheric contribution, this issue has to be well considered when planning an L band system.
- P-band systems are feasible only with very short integration times, but this condition is not compatible with constraints imposed by the link budget.
- SNR limitations can be removed increasing antenna diameter;

- Phase delay limitations for wavelengths up to L band are due to ionospheric delay. Increasing the accuracy of TEC measurement could make these configurations technically feasible.

- Phase delay limitations for short wavelengths (from X to K bands) are due to tropospheric and Earth tide delay. Increasing the accuracy of those measurements could make these configurations technically feasible.

Rain attenuation caused by moderate rainfalls (i.e. 10 mm/h) that correspond to $R_{0,1}$ for Europe (i.e. 10 mm/h) causes a slight decrease in system link budget but does not reduce overall system availability. Heavy rains such as those that correspond to $R_{0,01}$ for Europe (i.e. 50 mm/h) cause a signal attenuation so significant that the system is not able to achieve the desired link margin (i.e. 20 dB) at frequencies higher than 10 GHz. This effect is even more significant for higher rainfall rates (i.e. tropical rains).

However, at this stage of the trade-off analysis, the effect of rainfall rates has not been taken into account further more as it reduces system availability and does not affect system technical feasibility.

Table 3-15. Total score corresponding to phase uncertainty and SNR

Band	frequency (GHz)	1-minute	1-hour	8-hour
P	0.7	**SNR**	**SNR/PHASE**	**SNR/PHASE**
	1	**SNR**	**SNR/PHASE**	**SNR/PHASE**
L	1.2	**SNR**	**SNR/PHASE**	**PHASE**
S	2.4	**SNR**	**4.86**	**5.56**
C	4.5	**12.98**	**10.28**	**10.19**
	6	**13.92**	**11.60**	**10.67**
X	9	**15.11**	**12.09**	**9.59**
	10.5	**15.47**	**11.82**	**PHASE**
Ku	12	**15.85**	**11.48**	**PHASE**
	15	**16.42**	**10.52**	**PHASE**
K	20	**17.12**	**PHASE**	**PHASE**

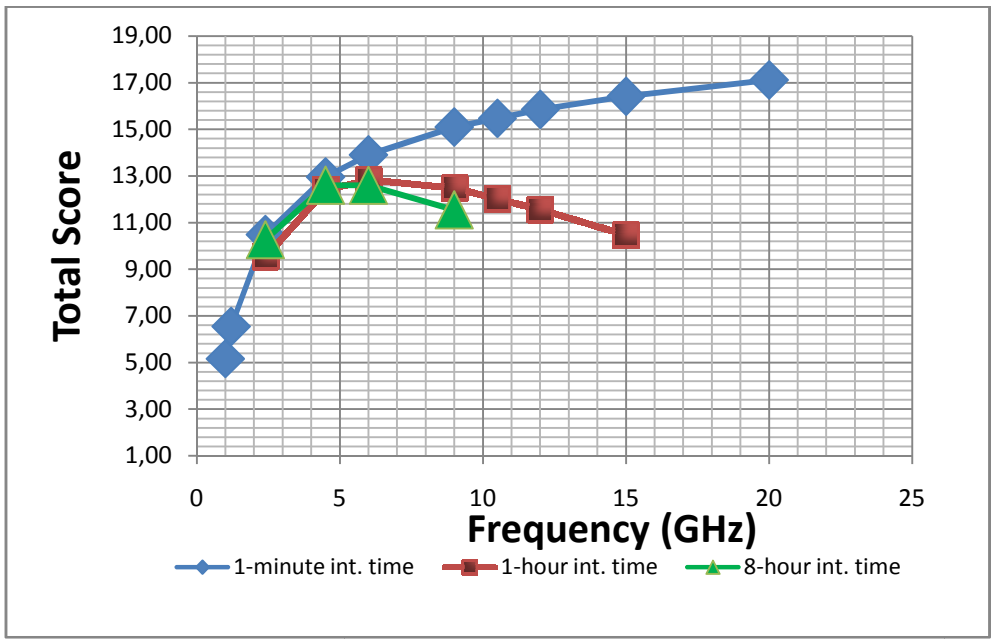

Figure 3-21. Total score assigned to phase uncertainty and SNR for three different integration times (1 minute, 1 hour, 8 hours).

The outcomes of the technical feasibility budget are clearly influenced by assumptions that have been made. As an example the following assumptions (affecting phase delay budget for 8-hour integration time) could change the outcomes of the technical feasibility study (results shown in Table 3-16):

- TEC measurement accuracy 0.1 TECU (over 8 hours). This change improves phase uncertainty budget at long wavelength and removes the phase limitation for L band.

- Tropospheric delay accuracy 1.5 mm (over 8 hours). This change improves phase uncertainty budget at short wavelengths and removes phase limitations up to Ku band.

Table 3-16. Total score corresponding to phase uncertainty and SNR

Band	frequency (GHz)	1-minute	1-hour	8-hour
P	0.7	**SNR**	**SNR/PHASE**	**SNR/PHASE**
	1	**SNR**	**SNR/PHASE**	**SNR/PHASE**
L	1.2	**SNR**	**SNR**	**4.11**
S	2.4	**SNR**	**9.54**	**10.27**
C	4.5	**12.95**	**12.41**	**12.60**
	6	**13.89**	**12.83**	**12.60**
X	9	**15.10**	**12.48**	**11.54**
	10.5	**15.46**	**12.02**	**10.75**
Ku	12	**15.84**	**11.56**	**9.97**
	15	**16.41**	**10.46**	**PHASE**
K	20	**17.11**	**PHASE**	**PHASE**

However, it has to be said that the influence of SNR is critical in assessing technical feasibility as:

- Power generation and antenna diameter are both critical issues in system design.

- Link budget affects the effectiveness of the auto-focus procedure that has to be used to compensate residual phase delays.

Three different integration times have been used in the analysis, however it has to be said that integration time clearly influences SAR azimuth ground resolution therefore, some of the configurations that appear as technically feasible could not be useful for any application as the ground resolution is extremely poor.

3.4.2 Frequency trade-off

Following the phase delay and the SNR budgets, technically feasible configurations have been identified setting lower boundaries to the focused SNR and upper boundaries to total phase delay uncertainties.

However, some other issues contribute to the final system design trade-off. They are discussed in the following sections.

3.4.2.1 Temporal decorrelation

NASA JPL (2003) states that a longer wavelength is more appropriate to guarantee a long correlation time. As an example, in a forest environment that is heavily subject to temporal decorrelation, L band or P-band are able to penetrate the canopies therefore signal is reflected from more stable targets such as the soil or the trunks. This can guarantee correlation over long time scales. This is a clear advantage in SAR interferometry. For earthquakes such as Izmir, cultivated, vegetated areas were problematic for maintaining correlation between interferograms of C band ERS data (NASA JPL, 2003).

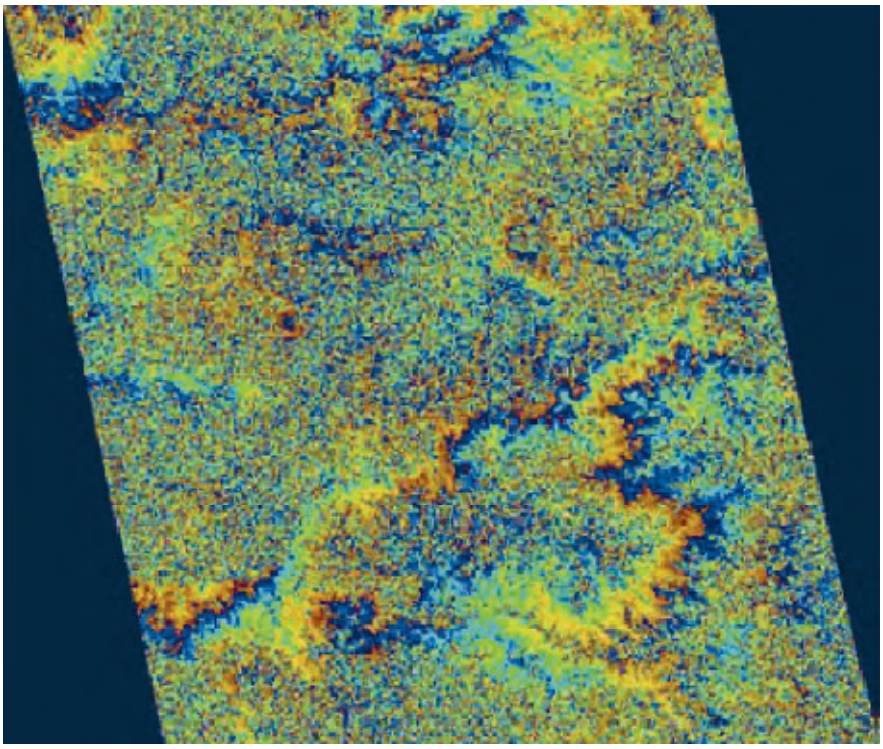

Figure 3-22. ERS Interferogram failed due to coherence loss: the Latur earthquake in India. Difficulties arose because it was monsoon time, which drastically changes the surface conditions. (Ferretti *et al.*, 2007)

Figure 3-22 from Ferretti *et al.* (2007) shows the effect of temporal decorrelation on a C band interferogram of an agricultural area.

When imaging from a geosynchronous orbit, the concept of coherence is not related only to different SAR acquisitions (interferometric coherence) but takes into account also the correlation between signals backscattered from the same target at different epochs during the integration time (pulse-to-pulse coherence). A longer wavelength

would be able to penetrate the canopies and collect signal from more stable scatterers such as trunks or the soil itself.

Seynat (2000) used the software RT2 (Knight, 1997) to estimate the backscatter of canopies at four different wavelengths (X band, λ=3 cm; C band, λ=5.6 cm; L band, λ=25 cm; P-band, λ=66 cm) as a function of stalk size with a radar incidence angle set to 45 degrees. This software models appropriately the soil surface and the canopies; subsequently it applies the radiative transfer approach to estimate the radar backscatter. This piece of information is relevant to geosynchronous SAR system design as it allows estimating the influence of canopies on SAR imaging.

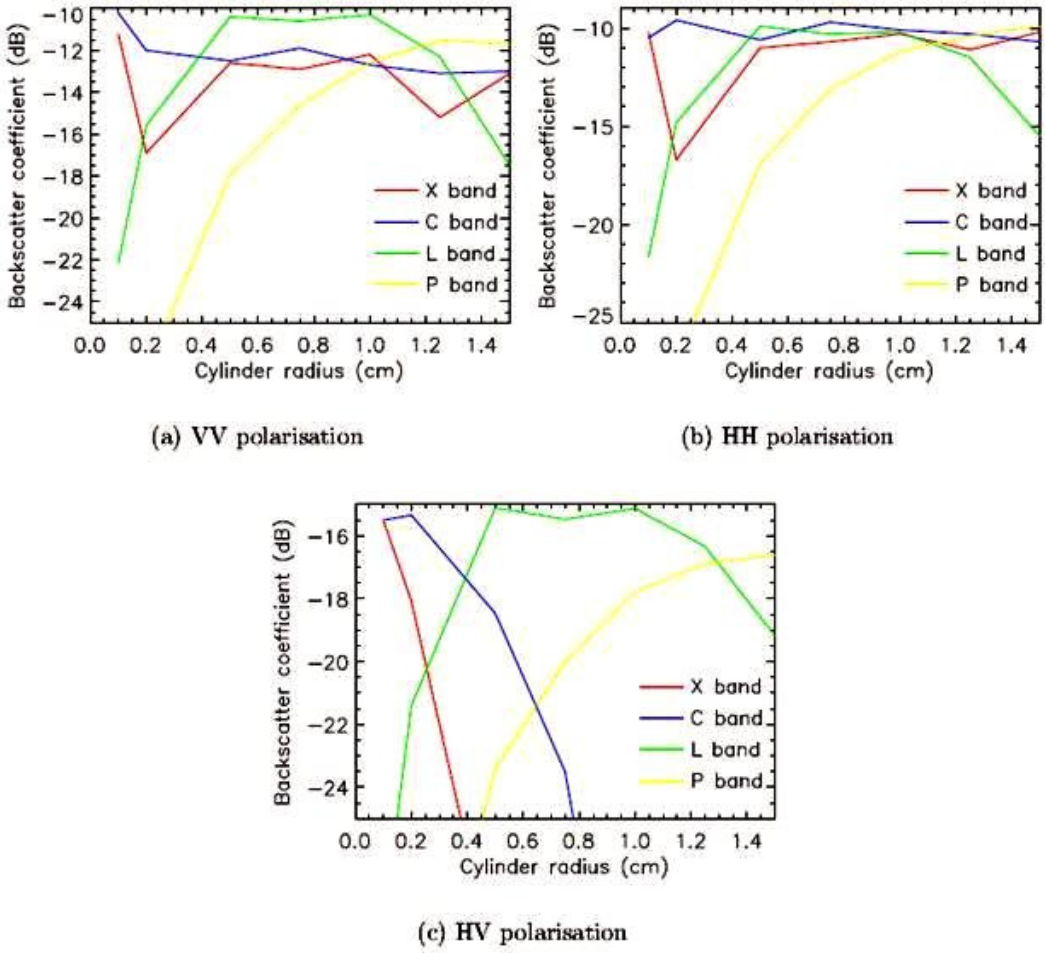

Figure 3-23. Variation of radar cross section σ^0 with the stalk radius (Seynat, 2000).

The variation of the radar cross section σ^0 for the three different polarisations is presented in Figure 3-23. The variation (VV polarisation) at L band shows that the backscatter is significant only for vegetation with stalk radius between 4 and 10 mm.

The decrease for stalk radius greater than 1 cm can be an artefact due to interference at this specific wavelength for objects of this diameter (Seynat, 2000).

Most crops like wheat have stalk radii that are in the range between 0.1 and 0.4 cm and do not influence system working at L band or P-band that, on the other hand, appear to be sensitive to tree branches that have larger radius.

L band or longer wavelengths appear suitable to monitor soil surface in presence of canopies. This property will be stressed in the chapter dealing with applications, as soil moisture monitoring is one of the possible fields of application for a geosynchronous SAR.

C, X, Ku and K bands are likely to suffer from temporal decorrelation if the integration time becomes longer than few seconds as only few targets could be considered stable on such timescales. For water or dense vegetation at L band decorrelation time is about 0.1 seconds (Prati *et al.*, 1998). Analogous conclusions could be drawn even considering a longer correlation time that appears more likely for canopies (Seynat, 2000; Hobbs, 1997).

The same concern applies to SAR interferometry; at higher frequencies, there will be a loss in interferometric coherence over areas with few stable targets.

3.4.2.2 Applications and existing SAR systems

SAR systems in P, L and C bands have been widely used in the last twenty years and there are various well-known applications, ranging from agriculture monitoring to topographic mapping. X band SAR systems (that have been deployed in the last few years), with ground resolution that might be sub-metric, provide the opportunity to match the needs of the intelligence community that, at the present stage, is the most important user of remotely sensed data and require for its applications an extremely good ground resolution.

There are currently no systems working at S, Ku and K bands, therefore the potential of these systems has still to be looked into.

As a direct consequence, existing SAR systems are concentrated only in a limited portion of the spectrum (P, L, C and X bands). The existence of other previous space missions working in the same band is relevant in the trade-off analysis as this means that space radar technology at the frequency under consideration is mature and that there is an existing archive of collected data that might be used for comparison and calibration. Table 3-17 includes a list of the main SAR missions grouped according to their band.

Table 3-17. List of main SAR missions (monostatic LEO configuration).

	Existing systems (monostatic LEO)
P (UHF)	Various airborne systems
L	SEASAT; JERS; ALOS PALSAR
S	N.A.
C	ERS; ENVISAT; RADARSAT; SRTM
X	TERRASAR; COSMO; SAR LUPE
Ku	N.A.
K	N.A.

3.4.2.3 Potential transmitters of opportunity

This aspect is relevant only to bi-static configurations that require a transmitter of opportunity that can be in GEO as well. Anderson and Bartamian (2008) provide a useful review of the global trends in communication satellites and some useful information about potential transmitters.

There are few UHF emitters in GEO that might be used as transmitter of opportunity. This band is used for military communications (in the range 200 MHz – 300 MHz). This kind of transmission (MIL-STD-181; MIL-STD-182; MIL-STD-183) has a very limited power (due to the use of omni-directional antennas) and a narrow bandwidth (from 5 to 25 kHz).

L band has been reserved for military communications in many countries (such as United States). The Electronic Communication Committee, with the ECC Decision dated 17 October 2003 designated the frequency band 1479.5 – 1492 MHz for use by Satellite Digital Audio Broadcasting (S-DAB) systems all over Europe. Several systems provide such services around the globe (i.e. Africasat 1). Apart from DAB, in L band there are also some communication services (i.e. Thuraya, Inmarsat). GPS and other GNSS systems work at L band as well; it has to be said that the applications of GNSS reflectometry from geo-synchronous altitude are hampered by the scarce SNR (Hobbs, 2008).

S band is usually used for telemetry channels, however in the United States S-DAB is provided at S band (about 2 GHz) by systems such as XM.

C and Ku bands are the most frequently used in Fixed Satellite Services. Plenty of systems emit signals in this part of the spectrum (i.e. Inmarsat, Eutelsat, Eumetsat, and Thuraya).

X band is widely used for military satellite communications (Lisi, 2006). The major drawback of this fact is that there is no information available on the availability of the transmitter and on the waveform for any possible passive bi-static application.

K-band, according to the current trends in satellite communication, is becoming widely used in satellite communication services.

3.4.2.4 Frequency band allocation

The International Radio Consultative Committe of the International Telecommunication Union (ITU) defines frequency band allocation for various communication services in its Radio Regulations (RR). In particular article 5 of Volume I provides table with the allocation of the whole spectrum to various satellite services. As confirmed by ITU (1988), there are frequencies allocated to fixed-satellite services at C, X, Ku and K bands.

Earth observation systems could potentially work as a primary or secondary service (i.e. a use that does not hamper primary services) in the bands listed below (ITU Radio Regulations, Volume I, Art.5):

- 432-438 MHz (secondary service);
- 1215-1300 MHz;
- 1525-1535 MHz (secondary service);
- 2025-2110 MHz;
- 2200-2290 MHz;
- 3100 3300 MHz (secondary service);
- 5250-5570 MHz;
- 8025-8400 MHz;
- 8.55-8.65 GHz;
- 9.5-9.8 GHz;
- 13.25-13.4 GHz;
- 13.4-13.75 GHz;
- 17.2-17.3 GHz;
- 24.05-24.25 GHz (secondary service);
- 25.5-27 GHz;
- 28.5-29.1 GHz.

The list provided shows that there are many frequency windows allocated to Earth observation (active) and therefore band allocation is not a relevant issue and will not be included in the trade-off analysis.

3.4.2.5 System complexity

For a geo-synchronous SAR, a significant part of the cost has to be ascribed to the launch. Taking into account this aspect, the mass budget plays a major role in the system design. Therefore the key parameters to measure the complexity of a given system design are the size of the antenna (in both monostatic and bi-static systems) and the amount of radiated power (monostatic systems only) that is proportional to the size of the solar panel required. This choice is based also on the assumption that RF components working at high frequencies up to K band will become COTS in the near future. This is clearly a simplification that does not include consideration on hardware complexity. This is acceptable in this preliminary stage of the trade-off.

Following this approach, the complexity (and the cost) of the system is directly related to the wavelength. A system in K-band will be far simpler than a P-band system.

3.4.2.6 Frequency trade-off- conclusions

The issues discussed in previous sections could be used to compile a trade-off analysis to identify the most convenient system frequency for both monostatic and bi-static systems. Conclusions drawn will be matched with the outcomes of the technical feasibility trade-off and with the analysis of active and passive configurations to identify potential suitable configurations.

3.4.2.6.1 Bi-static system

Following the analysis presented in previous sections, a trade-off analysis has been carried out in order to identity the most suitable frequency for a bi-static geosynchronous SAR configuration. The existence of a transmitter of opportunity has been taken into account as a bi-static system is being considered. A score in the range between 1 (very poor) and 5 (very good) has been assigned to each feature as shown in Table 3-18. All the aspects have been included in the budget with an unitary weight, therefore the sum of the weights is equal to 4.

Table 3-18. Frequency trade-off analysis for a bi-static SAR system.

	Potential transmitters of opportunities	Applications	System complexity	Temporal decorrelation	Total score
P (UHF)	2	4	1	5	12
L	3	5	2	4	**14**
S	2	1	2	4	9
C	5	4	2	2	13
X	5	3	3	2	13
Ku	5	1	4	1	11
K	5	1	5	1	12

Scores have been assigned according to an engineering judgment. Scores assigned to applications and system complexity are those that are more likely to vary if different ground rules are assumed. Considering that these scores can vary of +/-0.5 point P,C, X and K band can reach the total score assigned to L band. Therefore, the final decision has to be taken carrying out a parametric analysis that uses different weights for the various factors under evaluation.

3.4.2.6.2 Monostatic system

For a monostatic system, the list of the parameters has to be modified to take into account that there is no need for a transmitter of opportunity. As for bi-static systems, all the aspects have been included in the budget with an unitary weight, therefore the sum of the weights is equal to 3.The output of this analysis is given in the following table.

Table 3-19. Frequency trade-off analysis for a monostatic SAR system.

	Applications	System complexity	Temporal decorrelation	Total score
P (UHF)	4	1	5	10
L	5	2	4	**11**
S	3	2	3	8
C	4	2	2	8
X	3	3	2	8
Ku	1	4	1	6
K	1	5	1	7

Also in this case, scores have been assigned according to an engineering judgment. Scores assigned to applications and system complexity are those that are more likely to vary if different ground rules have been assumed. If these scores vary of +/-0.5 point only P band can reach the score assigned to L band. A parametric analysis will be carried out to choose the most suitable frequency.

3.4.2.6.3 Parametric analysis

The frequency trade-off has to be looked into considering that various aspects under investigation can have different relevance.

The sum of the weights for a bi-static configuration is equal to 4, for a monostatic configuration the sum is equal to 3. To evaluate which frequency is the most suitable according to a specific characteristic, a parametric analysis has been carried out.

Table 3-20 shows, for a bi-static system, the score calculated summing the values given to all the aspects in Table 3-18 but assigning a weight factor 1.6 to the parameter stated in the first column and a weight factor 0.8 to the other parameters. These weight factors have been chosen to keep constant the sum of the weights (i.e. 4) with respect to the previous analysis.

The same approach has been applied to monostatic configuration using the scores in Table 3-19 and applying a weight factor 1.5 to the parameters stated in the first column and a weight factor 0.75 to the other parameters. Results are shown in Table 3-21.

This analysis shows that, for a bi-static SAR, L band is the most suitable frequency regarding applications and temporal decorrelation. C and X band should be preferred looking into transmitters of opportunity while K band should be preferred to reduce system complexity.

It has to be said that temporal correlation is a major driver in the design of a geosynchronous SAR as the integration time cannot be as short as for LEO satellites. Moreover for the aspects where L band does not receive the highest score, its value is close to the maximum. Following these considerations, L band is the most suitable frequency for a geosynchronous bi-static SAR.

Table 3-20. Total score, parametric analysis for a bi-static configuration

	Total Score (Potential transmitters of opportunities)	Total Score (Applications)	Total Score (System complexity)	Total Score (Temporal decorrelation)
P (UHF)	11.2	12.8	10.4	13.6
L	13.6	**15.2**	12.8	**14.4**
S	8.8	8	8.8	10.4
C	**14.4**	13.6	12	12
X	**14.4**	12.8	12.8	12
Ku	12.8	9.6	12	9.6
K	13.6	10.4	**13.6**	10.4

The parametric analysis for a monostatic SAR (Table 3-21) shows that L band is the most suitable for all the aspects that have been investigated. P-band receives a high score for temporal decorrelation aspects but, considering that system complexity plays

a significant role in the monostatic system design, L band is the most suitable frequency for a monostatic geo-synchronous SAR.

Table 3-21. Total score, parametric analysis for a monostatic configuration

	Total Score (Applications)	Total Score (System complexity)	Total Score (Temporal decorrelation)
P (UHF)	10.5	8.25	**11.25**
L	**12**	**9.75**	**11.25**
S	8.25	7.5	8.25
C	9	7.5	7.5
X	8.25	8.25	7.5
Ku	5.25	7.5	5.25
K	6	9	6

3.5 Proposed configuration

The outcomes of the technical feasibility trade-off and of the frequency trade-off have to be matched in order to define the most suitable configuration for a geosynchronous SAR. Conclusions drawn in the sections about monostatic and bi-static systems will be used as well in order to define the most suitable system design.

L band is the most appropriate frequency due to its possible applications and its robustness to temporal decorrelation aspects.

To achieve a reasonable SNR a relatively large antenna has to be used. If the system requires a long integration time to synthesize a SAR image, phase delay effects (due mainly to ionospheric perturbations) have to be taken into account. In presence of a

perturbed ionosphere, a viable option (if the SNR is sufficiently high) is to reduce the integration time to lessen the unfavourable effect of phase delay perturbations.

At L band, an inclined geosynchronous orbit, although it allows to reduce the integration time, is not technically feasible. Antenna size and power requirements are the two major drawbacks of the active geosynchronous SAR, therefore this configuration shows significant technical complexities.

A nearly GEO orbit, that allows the use of a very long integration time (the synthetic antenna aperture is limited by the actual motion of the spacecraft) is a possible compromise to design a bi-static geosynchronous SAR system. However, the outcome of the technical feasibility trade-off shows that phase delay is a major source of concern for this configuration and this aspect has to be taken into account.

Looking forward to the cost budget, for a spacecraft in GEO, launch is a significant fraction of the cost therefore a passive bi-static configuration that does not require the generation of significant amount of power and that uses a relatively (with respect to the active monostatic configuration) smaller antenna will reduce the cost of satellite launch.

Overall project cost is also influenced by the need for new technologies to be developed. This is the case for an active monostatic configuration as large deployable antenna and power generation technologies have to be developed or improved in order to make this configuration techcnically feasible. A passive bi-static configuration does not require new techcnologies to be developed, therefore it is a more suitable candidate for a reduced cost space mission.

Following this examination, the remaining part of the present research has been focused on the L band bi-static passive configuration (originally proposed by Prati *et al.*, 1998) investigating its peculiarities and its technical challenges. Moving from these configurations at Cranfield Space Research Centre a spacecraft system design has been carried out. Further details about this project will be provided in the subsequent chapter.

The passive bi-static configuration requires an appropriate transmitter of opportunity that transmits a suitable signal with the required properties. This research assumes that such a satellite is available and does not investigate the influence of the transmitted waveform on the system design in terms of signal ambiguity function and transmitter/receiver synchronisation.

Higher frequencies (from X to K-band) allow obtaining a simpler system design but are not the optimal compromise as they suffer from target temporal decorrelation, even if relatively short (1 minute) integration times are used.

3.6 Conclusions

In this chapter, the peculiarities of the geosynchronous orbit have been discussed. The main features of monostatic and bi-static radar systems have been presented as well. The discussion carried out allowed to highlight the effect of orbit inclination on system design.

A system trade-off analysis has been completed. It has been split in two parts, a technical feasibility trade-off and a frequency trade-off. Matching the outcomes of the two analyses, an L band passive bi-static system design has been proposed as the most suitable configuration. This configuration will be presented and discussed in further details in the following chapter.

4 GeoSAR concept

The previous chapter presented the main peculiarities of both active and passive configurations. Conclusions drawn show that passive bi-static is the most appropriate configuration for a system that can be realised adopting only current technologies. Furthermore, L band has been preferred to shorter wavelengths as it is able to penetrate canopies and therefore shows a favourable behaviour with respect to temporal decorrelation.

Following the analysis of the technical complexities and challenges related to the active and passive configurations, Cranfield Space Research Centre looked into a system design of a bi-static passive SAR concept called GeoSAR. This concept has already been demonstrated in literature (Prati *et al.*, 1998). It was also the subject of a group project for Cranfield University's MSc course in Astronautics and Space Engineering for the academic year 2005/2006 (Hobbs, 2006). The group project carried out the design of a spacecraft for a geosynchronous radar capable of continuous monitoring of continental areas. The GeoSAR project shares with the present research only the baseline of the configuration therefore this chapter introduces the GeoSAR project and then moves into the analysis of system performance that has not been covered in the group project.

Section 4.1 describes briefly the GeoSAR project; section 4.2 presents system performance. An analytical derivation of SAR signal phase has been included in section 4.3. Section 4.4 presents GeoSAR geo-location budget. The following section of the chapter is dedicated to a brief presentation of a possible multi-static configuration, an area for possible developments for the GeoSAR concept.

4.1 GeoSAR - Constraints

GeoSAR is a passive bi-static SAR placed in a geosynchronous orbit with a circular ground track that reuses the L band signal generated by a transmitter of opportunity that is based in GEO as well. The main parameters that characterise the GeoSAR concept have been included in Table 4-1.

Table 4-1. GeoSAR main parameters (Hobbs, 2006).

Antenna diameter	6 m
Synthetic aperture	80 km
Integration time	8 hours
Frequency	1.5 GHz
Range Bandwidth	8 MHz
Nominal azimuth resolution	100 m
SNR	9.7 dB

To gather enough signal, the spacecraft requires large reflectors. Inflatable antennas were initially selected to minimise mass, although more recent work suggests that an alternative lightweight structure may be required to achieve the design lifetime of 15 years (Hobbs and Bruno, 2006). Figure 4-1 shows the proposed general spacecraft configuration. Each reflector corresponds to a multi-spot microstrip antenna. Performance analysis carried out in this research considers only the performances of a single spot beam.

System design follows the baseline parameters included in Table 4-2.

Table 4-2. GeoSAR constraints (Hobbs, 2006)

Mission cost budget	<€500M
Proposed launch date	≈2020
Lifetime	≈15 years
Spatial azimuth resolution	100 m
Coverage	Continental scale
Receiver frequency	L band 1.5 GHZ
Revisit time	Within 24 hours

The GeoSAR spacecraft could be realised with current technologies, however the most relevant complexities are related to signal processing. Due to the long integration time, the imaged scene (as well as the propagation medium) cannot be considered as frozen during image formation as it is assumed in LEO SAR. Variable phase delays that are due to target's fluctuations or to heterogeneities in the propagation medium have to be compensated by modifying the focussing algorithm. This problem will be addressed widely in chapters 5 and 6.

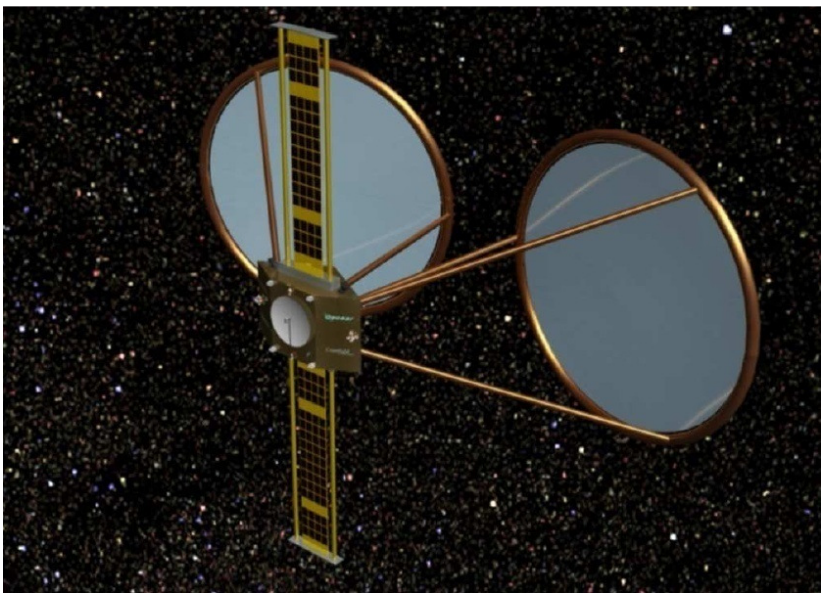

Figure 4-1. The GeoSAR spacecraft. The two large receiving antennas (6 m diameter) are visible as well as the solar arrays which rotate about their axis to stay sun-pointing (Hobbs, 2006).

4.1.1 GeoSAR orbit

Applying equations in section 3.1.2.6 under the assumption that a 80 km ground track has to be covered following a circular path in 8 hours (α=120°), the diameter of the circular track is about 92 km (projected on the ground). Therefore, satellite ground-track velocity is about 3.36 m/s.

Applying the bi-static radar equation presented in section 3.3.1 SNR comes out to be 9.7 dB.

Taking into account the altitude factor presented in section 3.1.3, the circular flight path of an orbit with such a ground track has a diameter that is A_F times the required diameter for the ground track (i.e. 603.5 km).

Orbital parameters necessary to put the spacecraft in a relative orbit with that radius are obtained using the equations presented in section 3.1.2.6 .

$$i = \tan^{-1}\left(\frac{r}{R}\right) = 0.0072 \text{ rad} = 0.41° \qquad \text{Equation 4-1}$$

In a circular relative orbit, it is also the case that $\Delta\lambda=i$, applying Equation 3-10, eccentricity is half that figure (in radians), that is 0.0036.

Table 4-3 summarises GeoSAR orbit parameters. The actual flight path, keeping in account all orbital perturbations, is not exactly circular. The dimension of the orbit (in km) along the axes x and y of the ECF reference system is given in Figure 4-2. Figure 4-3 shows the distance from the satellite to the centre of the Earth (varying with time).

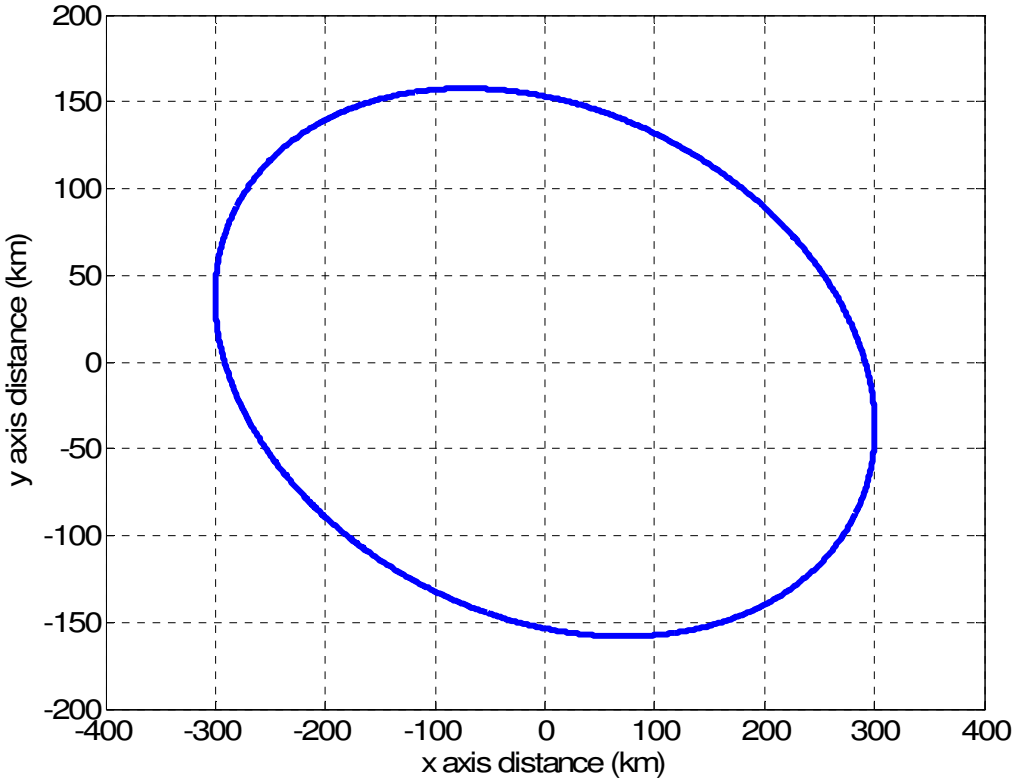

Figure 4-2. GeoSAR orbit – dimensions of the circle in km along the axes x-y in ECF reference system.

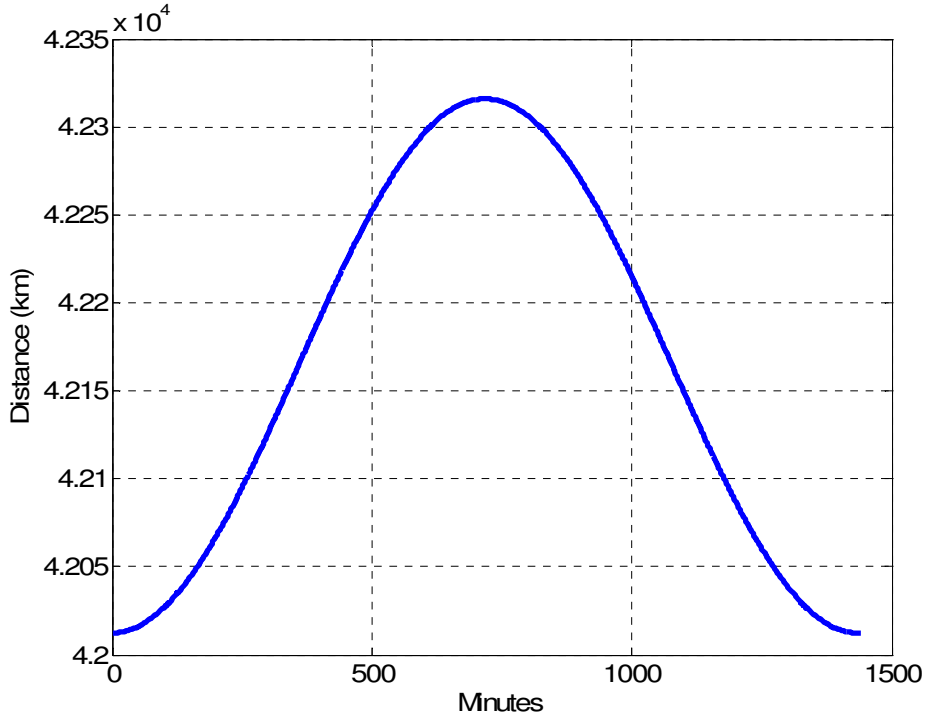

Figure 4-3. Distance of the satellite (km) from the centre of the Earth during the 24-hour period.

Table 4-3. GeoSAR orbit parameters (Jefferys, 2006)

GeoSAR orbit parameters	
Semi-major axis (km)	42164
Eccentricity	0.0036
Inclination (degrees)	0.41
Right ascension of the ascending node (degrees)	180
Argument of perigee (degrees)	90
True anomaly (degrees)	180

4.2 GeoSAR performances

GeoSAR's performance in terms of coverage and resolution are essential to evaluate the commercial potential of this system. Basic bi-static SAR relations (Willis, 1991) have to be tailored to the geosynchronous case as orbit altitude affects both ground incidence angle and squint angle. In the assumed configuration, the bi-static angle is close to the longitude separation of transmitting and receiving satellites.

The algorithm *performance.m* (in Appendix B) has been implemented in *Matlab* to estimate variations in system performance depending on the area of the Earth that is going to be imaged. GeoSAR concept main parameters have been used to derive the plots presented.

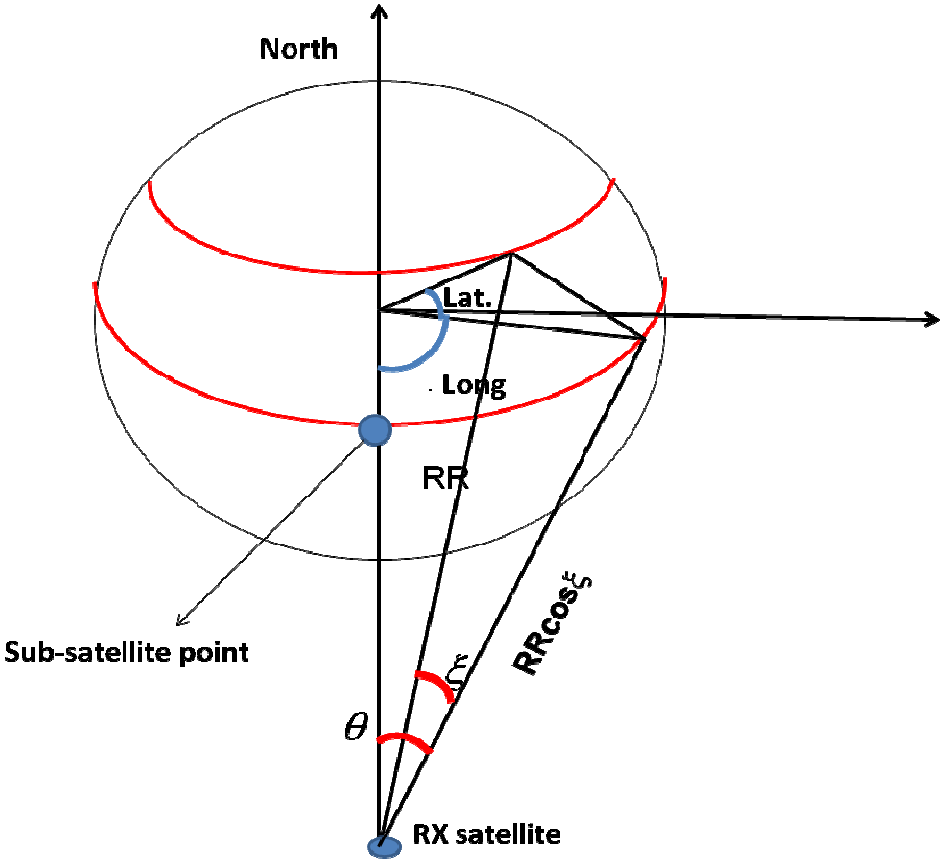

Figure 4-4. Imaging geometry from the RX satellite for a generic point on the Earth's surface.

Figure 4-4 shows the imaging geometry referred to the receiving satellite (RX), *Lat* is the latitude of the point on the Earth's surface being imaged, $\Delta long$ is the difference in longitude between the imaged area and the RX satelite and RR is the slant range.

The antenna look angle θ and the squint angle ξ are referred to the RX antenna. They are defined assuming that the transmitter is stationary and that the receiver is flying along a north-south path.

The squint angle ξ is obtained applying Equation 4-2.

$$\sin \xi = \frac{R_e \sin(Lat)}{RR} \qquad \text{Equation 4-2}$$

In Equation 4-2, R_e is the Earth's radius;
Lat is the latitude of the imaged point;
RR is the slant range from the receiver RX.

Ground squint angle ξ_g is defined in Equation 4-3 (following equations in section 0).

$$\cos \xi_g = \frac{\sin \xi}{\sin \rho} \qquad \text{Equation 4-3}$$

In Equation 4-3, ρ is 0.1518 radians as defined in section 3.1.4.

The following plots assume that the transmitting and the receiving satellites are separated by 30° in longitude (RX is placed at longitude 20°; TX is placed at longitude 50°) on the equatorial plane and that the satellite is imaging while flying along the direction north-south (i.e. its flight path has been linearised). The sub-satellite points that correspond to the positions of the transmitter and of the receiver satellites are presented in the figures as two stars on the equatorial plane.

Figure 4-5 shows contours of ground squint angle where 90° squint angle corresponds to boresight imaging.

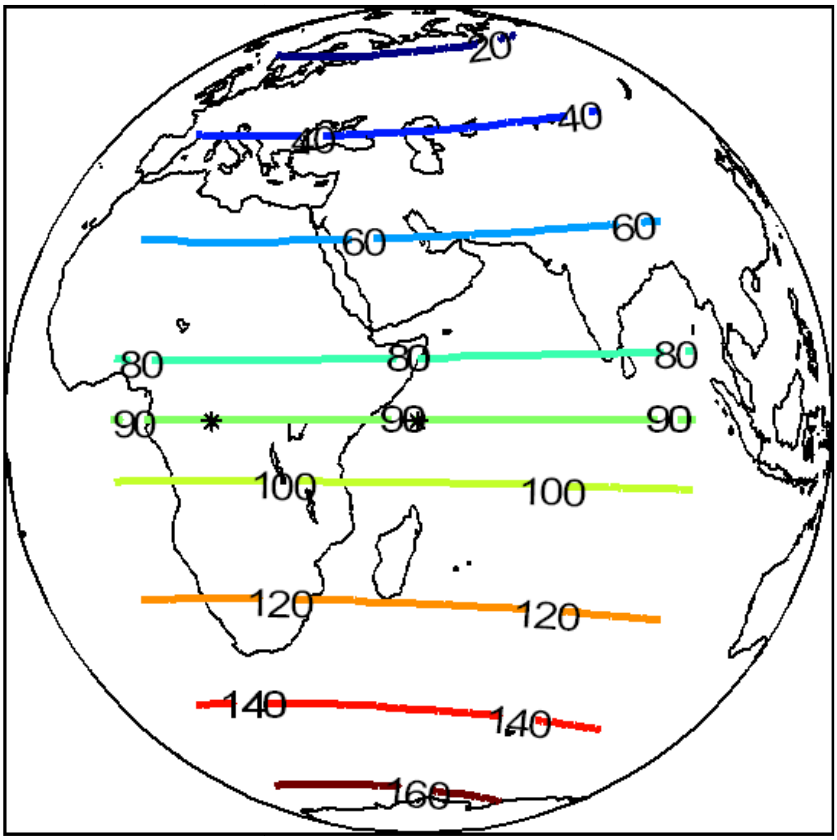

Figure 4-5. GeoSAR performances - Contours of ground squint angle (values in degrees). The two stars on the equatorial plane are the sub-satellite points relative to transmitting and receiving satellites.

Figure 4-5 shows that, considering a figure-of-eight orbit with a north-south wander (as in Prati *et al.* 1998) geographical areas with average latitude (such as Europe) have to be imaged with large squint angles (i.e. small ground squint angle). This explains why a geosynchronous orbit with a nearly circular track is more suitable to image non-equatorial zones.

Radar look angle is defined using Equation 4-4.

$$\sin\theta = \frac{R_e \sin(\Delta long)}{RR\cos\xi} \qquad \text{Equation 4-4}$$

Following equations in section 3.1.4 ground incidence angle θ_g is defined using Equation 4-5.

$$\cos\theta_g = \frac{\sin\theta}{\sin\rho} \qquad \text{Equation 4-5}$$

Figure 4-6 shows contours of the ground incidence angle or grazing angle.

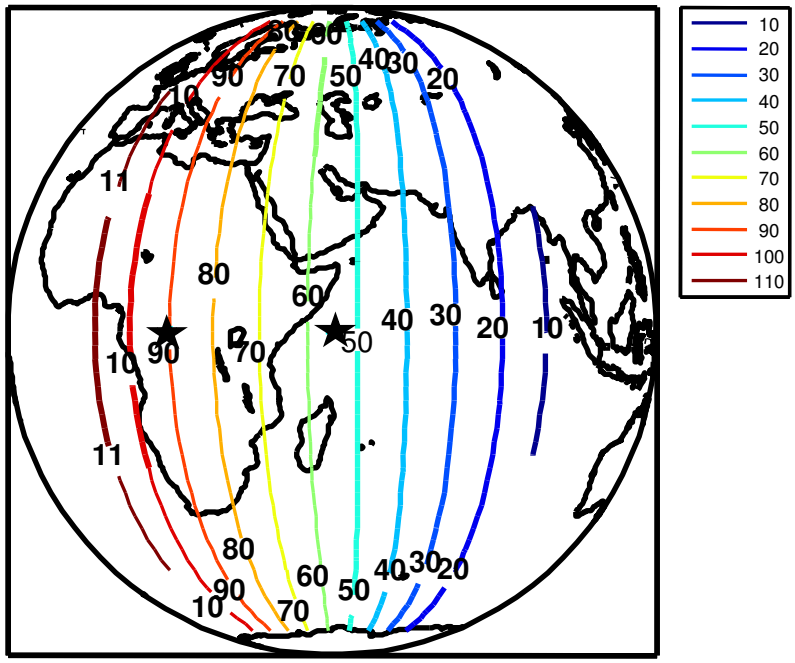

Figure 4-6. GeoSAR performances - Contours of ground incidence angle (values in degrees). The two stars on the equatorial plane are the sub-satellite points relative to the transmitting and receiving satellites.

Figure 4-7 shows the contours of azimuth ground resolution (in meters). The circles are concentric around the moving spacecraft (the receiver).

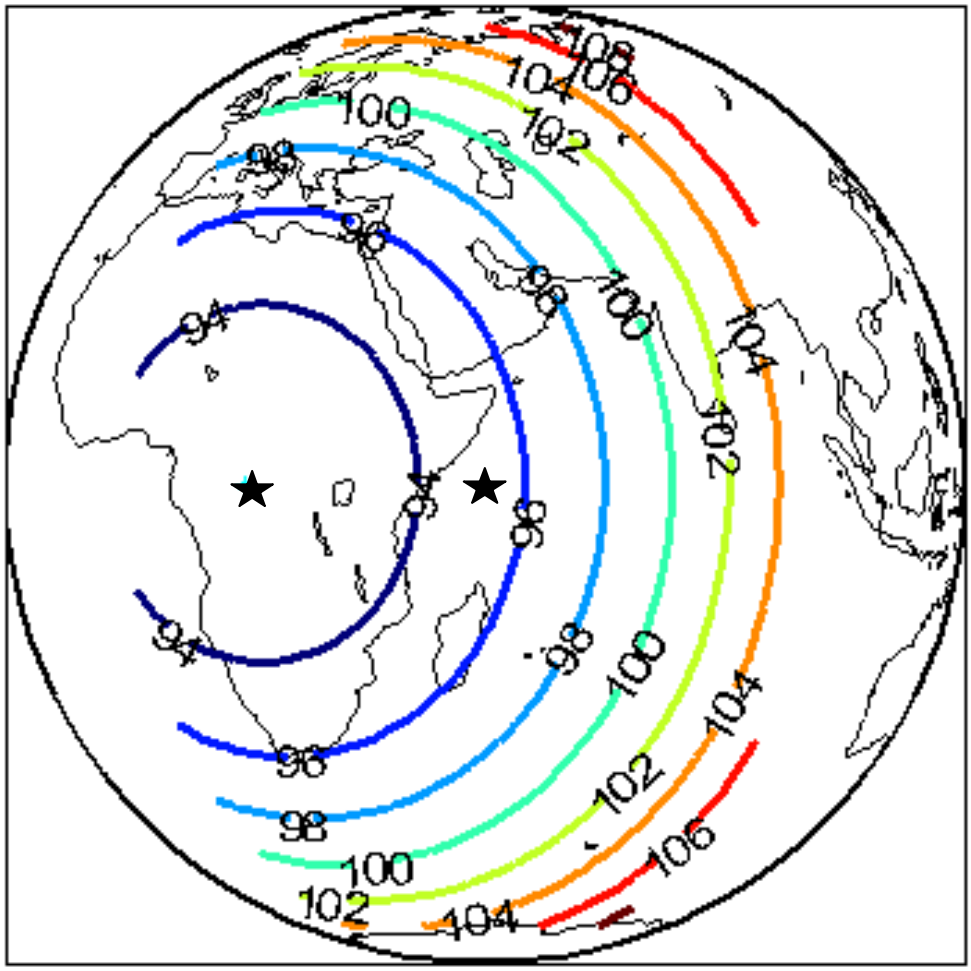

Figure 4-7. GeoSAR performances - Contours of azimuth ground resolution (values in meters). The two stars on the equatorial plane are the sub-satellite points relative to the transmitting and receiving satellites.

Figure 4-8 shows the contours of the SNR that is achieved assuming a constant power density on the Earth's surface (-171 $dBWm^{-2}Hz^{-1}$ as in Prati *et al.*, 1998). As in the previous plots, circles are concentric around the moving spacecraft (i.e. the receiver).

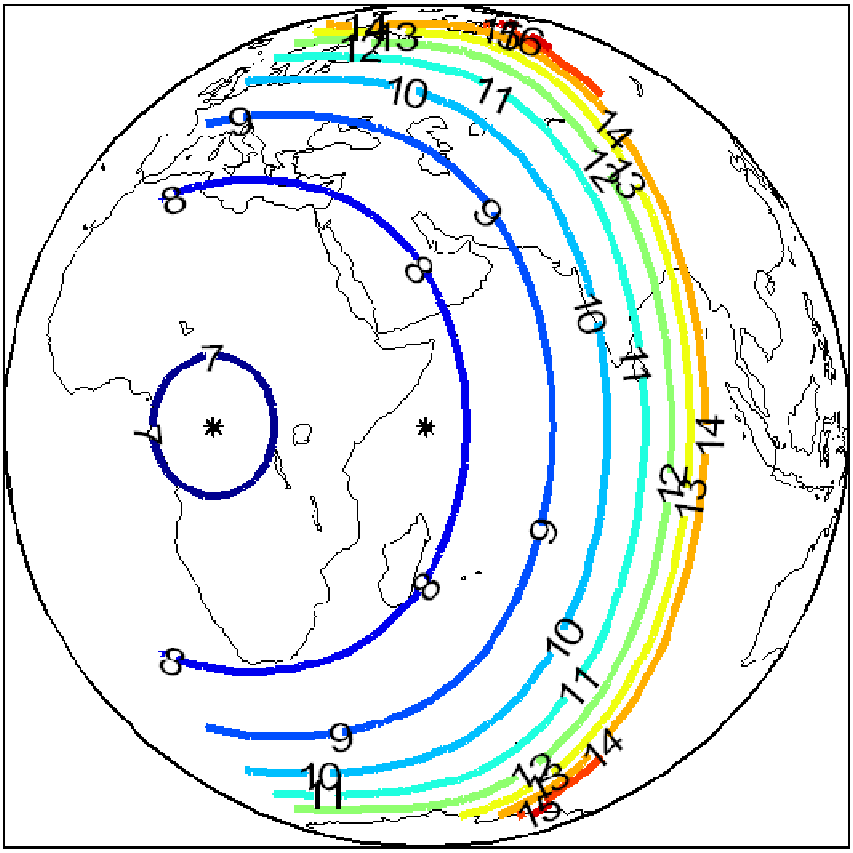

Figure 4-8. GeoSAR performances - Contours of focused SNR (values in dB). The two stars on the equatorial plane are the sub-satellite points relative to the transmitting and receiving satellites.

4.3 SAR image defocus

The effect of phase delay on SAR processing has been already discussed in the background section; moreover, a phase delay budget has been carried out within the frequency trade-off analysis. The effects of phase delays on SAR processing are an important part of the present research.

Hereafter an analytical derivation of the bi-static SAR phase will be performed in order to assess the requirements that pulse-to-pulse phase coherence poses on the knowledge of the relative and absolute position of transmitting and receiving satellites.

The outcome of this breakdown will be a requirement on the accuracy for the measurement of the satellite slant ranges and of geometrical distance ***D*** between the transmitter (TX) and the receiver (RX).

The analytical expressions for the first derivatives of the bi-static phase will allow some simple comparisons with LEO similar configurations.

4.3.1 Bi-static SAR phase

The phase detected by a bi-static system has the following expression:

$$\Phi = \frac{2\pi}{\lambda}\left(R_1 + R_2\right) = k\left(R_1 + R_2\right) \qquad \text{Equation 4-6}$$

In Equation 4-6, R_1 is the slant range from RX to the target;
R_2 is the slant range from the target to the TX.

The distance between TX and RX satellite is given by the vector **D**. $\mathbf{R_1}$ is the vector distance between the RX satellite and the target. $\mathbf{R_2}$ is the vector distance between the TX satellite and the target.

The axes of the reference system are the receiver's velocity (x-axis), nadir (z-axis) while y-axis is oriented in order to form a right-handed frame.

This analytical approach assumes that the distance R_2 is not directly measured but it is derived from the measurements of the distances R_1 and D. Therefore R_1 and D are two independent measurements while R_2 is a function of R_1 and D.

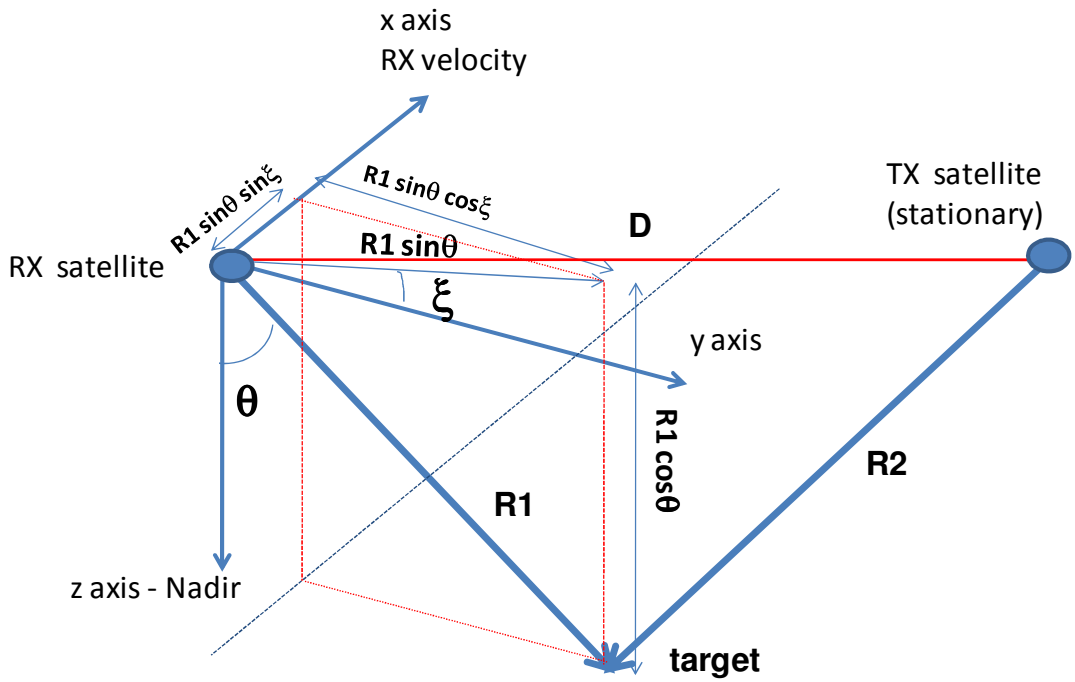

Figure 4-9. Geometry used in the calculation of the bi-static SAR phase.

The orientation of the vector $\mathbf{R_1}$ is given by the radar look angle θ and by the squint angle ξ. The angles have been specified in Figure 4-9.

Squint angle has been defined (Figure 4-9) as the angle between the y-axis and the projection of the $\mathbf{R_1}$ vector in the x-y plane.

It is important to emphasize that the above-mentioned angles are referred to the receiver radar and, due to the spherical geometry, are different from ground incidence and ground squint angles. The following equations assume that the transmitter is stationary and the vector $\mathbf{R_2}$ is determined as in Equation 4-7.

Bi-static phase (Equation 4-8) is expressed as in Equation 4-9 using Equation 4-7.

$$\mathbf{R}_2 = \mathbf{R}_1 - \mathbf{D} \qquad \text{Equation 4-7}$$

$$\Phi = k\left(R_1 + \sqrt{R_1^2 + D^2 - 2\mathbf{D}\bullet\mathbf{R}_1}\right) \qquad \text{Equation 4-8}$$

$$\Phi = k\left(R_1 + \sqrt{D^2 + R_1^2 - 2R_1\left[D_x \sin\theta\sin\xi + D_y \sin\theta\cos\xi + D_z \cos\theta\right]}\right) \qquad \text{Equation 4-9}$$

In Equation 4-9, D_x, D_y, D_z are the three components of the baseline vector **D.**

Bi-static phase will be estimated by measuring satellite slant ranges and the geometric baseline between TX and RX. Derivatives of bi-static SAR phase Φ is used to evaluate the sensitivity of the system to errors in position and attitude determination.

The following equations provide the partial derivatives of the function Φ with respect to R_1, and the three components of the vector ***D***.

$$R_2 = \sqrt{D^2 + R_1^2 - 2R_1\left[D_x \sin\theta\sin\xi + D_y \sin\theta\cos\xi + D_z\cos\theta\right]} \quad \text{Equation 4-10}$$

$$\frac{\partial\Phi}{\partial R_1} = k + \frac{2kR_1}{R_2} - \frac{2k\left(D_x \sin\theta\sin\xi + D_y \sin\theta\cos\xi + D_z\cos\theta\right)}{R_2}$$

Equation 4-11

$$\frac{\partial\Phi}{\partial D_x} = k\frac{D_x - R_1\sin\theta\sin\xi}{R_2} \quad \text{Equation 4-12}$$

$$\frac{\partial\Phi}{\partial D_y} = k\frac{D_y - R_1\sin\theta\cos\xi}{R_2} \quad \text{Equation 4-13}$$

$$\frac{\partial\Phi}{\partial D_z} = k\frac{D_z - R_1\cos\theta}{R_2} \quad \text{Equation 4-14}$$

In the previous equations, k is the radar wavenumber $2\pi/\lambda$.

Equation 4-15 provides the variance of the bi-static SAR phase σ_ϕ^2. Under the assumptions that it is influenced only by the above stated derivatives, it is expressed as a function of the variance in the measurements of the baseline and of the slant range.

$$\sigma^2_{\Phi} = \left(\frac{\partial\Phi}{\partial R_1}\right)^2 \sigma^2_{R1} + \left(\frac{\partial\Phi}{\partial D_x}\right)^2 \sigma^2_{D_x} + \left(\frac{\partial\Phi}{\partial D_y}\right)^2 \sigma^2_{D_y} + \left(\frac{\partial\Phi}{\partial D_z}\right)^2 \sigma^2_{D_z} \quad \text{Equation 4-15}$$

The derivatives of the bi-static phase presented in the present section are inversely proportional to the slant range R_2. This implies that, with respect to an analogous LEO SAR system, a GeoSAR configuration requires a less accurate orbit and baseline determination as its slant range is nearly two orders of magnitude larger with respect to a LEO system. This accuracy has to be maintained for the whole integration time as both the slant range $\mathbf{R_1}$, $\mathbf{R_2}$ and the geometrical baseline **D** are likely to change.

4.3.1.1 Effects of orbit determination accuracy

In the previous section, the derivatives of the bi-static phase Φ have been derived analytically moving from vectorial algebra. They can be used to define a requirement for orbit determinations.

According to the current design, GeoSAR will be flying along a circular ground-track. Therefore, two different cases have been worked out for north-south and for east-west motion as the vector **D** has different components along the three axes.

Table 4-4 states the values that have been used in the error analysis for the GeoSAR configuration.

Table 4-4. Parameters used in the sensitivity analysis for bi-static SAR phase.

R_1 (m)	4.00×10^7
R_2 (m)	4.00×10^7
k	25.1 (λ=0.25 m)
θ (deg)	5
ξ (deg)	5

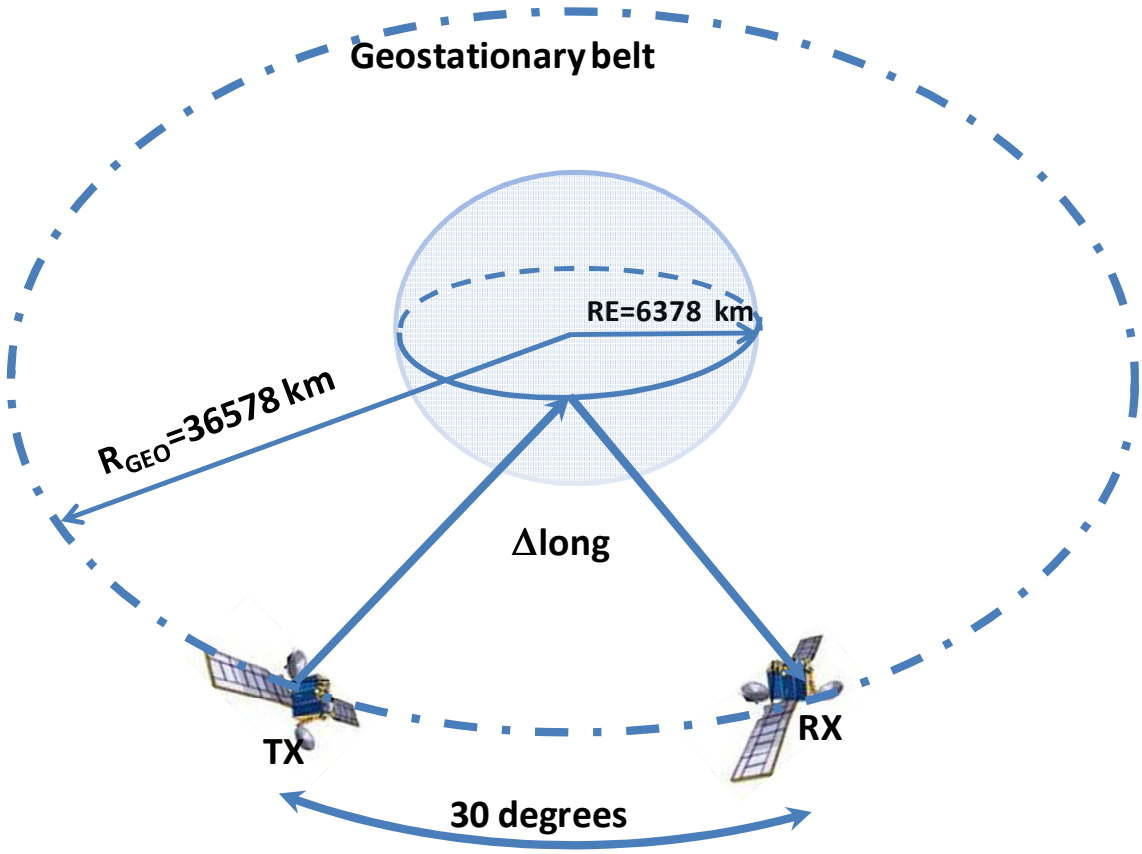

Figure 4-10. GeoSAR baseline estimation geometry

As shown in Figure 4-10, a longitude separation of 30° generates a baseline along the y-axis (north-south motion) or along the x-axis (east-west motion) of about 2×10^4 km, following Equation 4-16.

$$D_x = D_y \approx R_{GEO} \sin(\Delta Long) \qquad \text{Equation 4-16}$$

In Equation 4-16, R_{GEO} is the altitude of the geosynchronous orbit;
$\Delta Long$ is the separation in longitude between RX and TX satellites.

The remaining component of the baseline in the x-y plane is limited by the excursion of the receiver satellite (under the assumption that the TX is stationary). The component about the z-axis is given by Equation 4-17.

$$D_z = R_{GEO}\left[1 - \cos(\Delta Long)\right] \qquad \text{Equation 4-17}$$

The components of the distance vector **D** have been included in Table 4-5.

Table 4-5. Components of the vector D (in meters).

	D_x	D_y	D_z
north south motion	4.00 *x 10*^{4}	2.00 x10^7	6.00 x 10^3
east-west motion	2.00 x 10^7	4.00 x 10^4	6.00 x 10^3

The values achieved for the derivatives presented in the previous section are presented in Table 4-6.

Table 4-6. Numerical values of the derivatives (in rad/m) with λ=0.2 m.

	$\delta\phi/\delta R_1$	$\delta\phi/\delta D_x$	$\delta\phi/\delta D_y$	$\delta\phi/\delta D_z$
north south motion	26.1	-0.166	10.4	-25.0
east-west motion	27.1	12.4	-2.16	-25.0

Assuming that every derivative contributes to phase noise for 0.1 radians the requirements for baseline and slant range accuracy could be obtained. The baseline accuracy requires knowledge in the centimetre range of the relative orbit position. The accuracy required in the knowledge of the slant range and D_z could become limiting factors for the processing of GeoSAR images.

Table 4-7. Accuracies required in the knowledge of the slant range and of the D vector to achieve a 0.1 rad phase error.

	R (mm)	D_x *(mm)*	D_y *(mm)*	D_z *(mm)*
north-south motion	3.83	603	9.63	-3.99
east-west motion	3.69	8.08	-46.4	-3.99

According to Richards (2003), assuming that the errors above are modelled as Gaussian noise; the integration loss could be expressed as:

$$\left[L\right]_{dB} = -4.343\left[\sigma^2\right]_{rad} \qquad \text{Equation 4-18}$$

A phase noise of 0.1 radians implies a relatively small loss in processing gain (about 0.05 dB).

4.3.1.2 Effect of topographic height

The analysis carried out in the previous section highlights that the system requires an accurate measurement of the vectors $\mathbf{R_1}$ and $\mathbf{D}$ to achieve a correct focussing. This implies that an accurate knowledge of the topographic height of the imaged area is required for a precise processing.

The aim of this section is to find an analytical expression that relates bi-static phase to terrain topography. This issue has been tackled under the simplifying assumption that there is no squint angle and that the transmitter is stationary. As in the previous sections, it has been assumed also that the distance R_2 is not directly measured but it is derived from the measurements of the distances R_1 and D, this implies that only variations in the two variables R_1 and D are relevant to the problem.

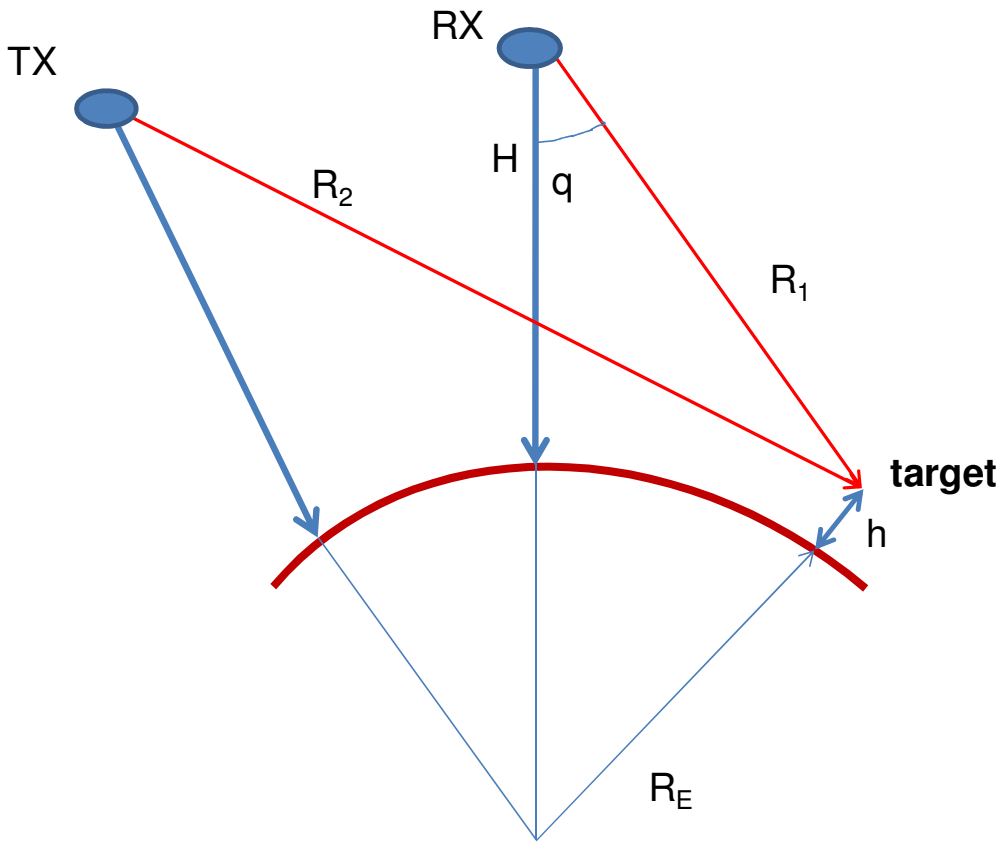

Figure 4-11. Geo-synchronous imaging geometry.

Considering GeoSAR imaging geometry presented in Figure 4-11, Equation 4-19 provides an analytical expression for topographic height taking into account a spherical Earth. In this geometry:

$$h = \sqrt{\left[\left(H + R_e\right)\cos\theta - R_1\right]^2 + \left[\left(H + R_e\right)\sin\theta\right]^2} - R_e \qquad \text{Equation 4-19}$$

In Equation 4-19, θ is the radar look angle;
H is GeoSAR altitude;
R_e is Earth radius;
R_1 is slant range from RX;
R_2 is slant range from TX;
h is topographic height.

All the derivatives of equation Equation 4-19 are obtained analytically.

$$\frac{\partial h}{\partial \theta} = \frac{R_1\left(H + R_e\right)\sin\theta}{h + R_e} \qquad \text{Equation 4-20}$$

$$\frac{\partial h}{\partial H} = \frac{H + R_e - R_1\cos\theta}{h + R_e} \qquad \text{Equation 4-21}$$

$$\frac{\partial h}{\partial R_1} = \frac{R_1 - \left(H + R_e\right)\cos\theta}{h + R_e} \qquad \text{Equation 4-22}$$

Topographic height of the target being imaged over the Earth's surface has an influence on bi-static SAR phase as it changes the slant range.

Using Equation 4-9:

$$\frac{\partial \Phi}{\partial h} = \frac{\dfrac{\partial \Phi}{\partial \theta}}{\dfrac{\partial h}{\partial \theta}} = \frac{-k\dfrac{R_1}{R_2}\left(D_x\cos\theta\sin\xi + D_y\cos\theta\cos\xi - D_z\sin\theta\right)}{\dfrac{R_1\left(H + R_e\right)\sin\theta}{h + R_e}} \qquad \text{Equation 4-23}$$

$$\frac{\partial \Phi}{\partial h} = -k\frac{\left(h + R_e\right)}{R_2\left(H + R_e\right)\sin\theta}\left(D_x\cos\theta\sin\xi + D_y\cos\theta\cos\xi - D_z\sin\theta\right) \qquad \text{Equation 4-24}$$

Equation 4-24 provides the derivative of the bi-static SAR phase with respect to the topographic height of the target. Using the parameters of the system included in Table 4-4 and Table 4-5 it is possible to obtain the results that are presented in Table 4-8.

Table 4-8. Accuracies required in the knowledge of topographic height to avoid errors in bi-static phase.

	$\delta\phi/\delta h$ (rad/m)	δh (m) ($\delta\phi$ 0.1 rad)
north-south motion	-21.6	-4.62×10^{-3}
east-west motion	-1.93	-5.19×10^{-2}

The system is extremely sensible to variation in scatterer's height that should occur during the integration time. Earth tides cause target displacements that are of the same order of magnitude of those presented in Table 4-8. Therefore, they have to be looked into in order to evaluate any eventual reduction in system performances.

4.4 Geo-location budget

Geo-location accuracy is a major driver for many applications. It represents the accuracy of a coordinate on the Earth's surface. An accurate knowledge of the geo-location budget is required for data fusion with data collected from different sources.

Space and ground segments affect the overall geo-location accuracy. As far as the space segment is concerned, contributions to the geo-location budget can come from the spacecraft or from the SAR instrument. In fact, the SAR instrument shall refer the radar raw data to the spacecraft reference system in terms of slant range accuracy and azimuth (flight line direction) accuracy.

In GeoSAR, the geo-location process depends from the measurements of the slant range from the target to the receiver and of the baseline between TX and RX satellites. This section investigated the contributions to the geo-location budget given by the receiver. The simplification is acceptable as any error contribution due to baseline measurement is considered as an error in the knowledge of receiver's position.

The accuracy of the location depends on the quality of the measurements of the following parameters of the receiver:

- position and the velocity of the satellite;
- measurement of the pulse delay time;
- knowledge of the satellite height with respect to the assumed Earth model.

The location procedure does not require any attitude information.

Ground segment impacts on the geo-location accuracy are mainly due to:

- intrinsic accuracy (tolerance) of the geo-coding algorithms;

- navigation data availability and accuracy;
- Doppler centroid estimated accuracy;
- approximate knowledge of the true local topography (DEM).

Geo-location error could be improved through image processing only if other satellite products with higher accuracy are available for the same areas. Such procedure is usually carried out through image correlation. In any case an accuracy better than that of the reference image cannot be achieved.

Next sections briefly describe how the various contributions above mentioned propagate into the geo-location budget.

4.4.1 SAR processor contribution

The target location on a reference ellipsoid is determined solving simultaneously three equations:

- range equation;
- Doppler equation;
- Earth model equation.

The range equation, for the j[th] pixel in the image, is given by Equation 4-25.

$$sr_j = sr_0 + m_r j = R \qquad \text{Equation 4-25}$$

In Equation 4-25, *j* slant range index of the pixel;
sr_0 slant range distance of the first pixel;
sr_j slant range distance of pixel with index j;
m_r slant range pixel spacing;
R is the slant range,

The Doppler equation (modified from Curlander and McDonough, 1991) is obtained imposing that $f_{DC}=0$.

$$f_{Dc} = \frac{2}{\lambda R}\left(\vec{X}_s - \vec{X}_T\right) \bullet \left(\vec{V}_s - \vec{V}_T\right) = 0 \qquad \text{Equation 4-26}$$

In Equation 4-26, f_{Dc} is the Doppler centroid frequency;
L is the radar wavelength;
X_s is the sensor position vector;
X_t is the target position vector;
V_s is the sensor velocity vector;
V_T is the target velocity vector (hereafter assumed to be zero);
R is the slant range.

4.4.2 Platform error contribution

These errors are related to the difference between the true and the estimated platform position. The key uncertainties in the model are satellite position and velocity errors. This choice is justified by the fact that these erros are usually obtained as a part of the AOCS sub.system design.

4.4.2.1 Along-track position error

An along-track position error causes an azimuth target location error Δx_1 given in Equation 4-27.

$$\Delta x_1 = \Delta R_x \frac{R_e}{H + R_e} \qquad \text{Equation 4-27}$$

In Equation 4-27, ΔR_x is the along-track satellite position error,
H is the satellite altitude,
R_e is the Earth's radius.

4.4.2.2 Across-Track Position Errors

An across-track position error causes a radial target location error Δr_1 given in Equation 4-28.

$$\Delta r_1 = \Delta R_y \frac{R_e}{H + R_e} \qquad \text{Equation 4-28}$$

In Equation 4-28, ΔR_y is the cross-track satellite position error.

4.4.2.3 Radial Position Errors

A sensor radial position error is essentially an error in the estimate of the sensor altitude H as presented in the Figure 4-12. Following equations demonstrate that radial position error causes an across-track displacement.

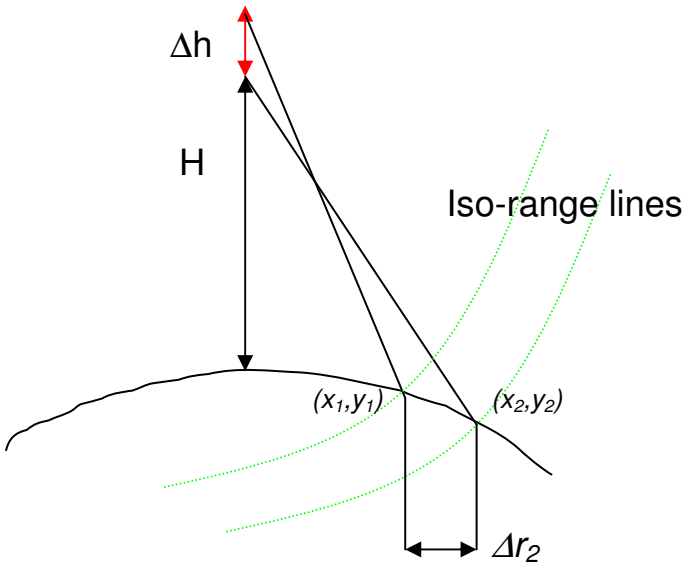

Figure 4-12. Geometry used to estimate the effect of radial error in the geo-location budget.

A target on the ground is placed on an inaccurate iso-range line due to the error in satellite altitude Δh. The two iso-range lines in Figure 4-12 intersect the Earth surface in two contact points (x_1, y_1) and (x_2, y_2). Their position can be derived solving Equation 4-29 and Equation 4-30. The reference Cartesian axes are defined in Figure 4-13.

$$\begin{cases} x_1^2 + y_1^2 = R_e^2 \\ x_1^2 + \left(y_1 - \left(R_e + H\right)\right)^2 = R^2 \end{cases}$$ Equation 4-29

$$\begin{cases} x_2^2 + y_2^2 = R_e^2 \\ x_2^2 + \left(y_2 - \left(R_e + H + \Delta h\right)\right) = R^2 \end{cases}$$ Equation 4-30

In the previous equations, R is the measured slant range.

$$y_1 = \frac{R_e + \left(R_e + H\right)^2 - R^2}{2\left(R_e + H\right)}$$ Equation 4-31

$$y_2 = \frac{R_e + \left(R_e + H + \Delta h\right)^2 - R^2}{2\left(R_e + H + \Delta h\right)}$$ Equation 4-32

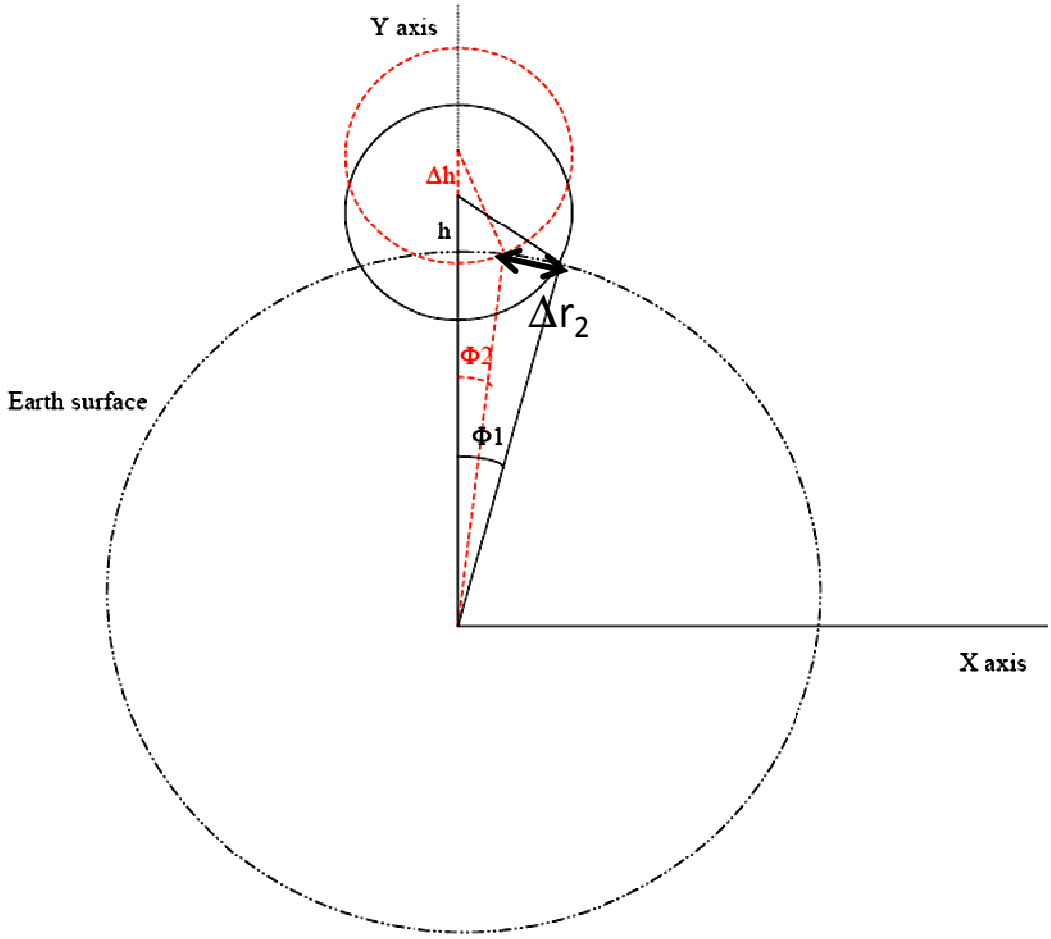

Figure 4-13. Geometry to estimate radial position error.

Therefore, considering the geometry in Figure 4-13, the ground range error Δr_2 is given in Equation 4-33.

$$\Delta r_2 = R_e\left(\Phi_1 - \Phi_2\right) = R_e\left[\operatorname{acos}\left(\frac{y_1}{R_e}\right) - \operatorname{acos}\left(\frac{y_2}{R_e}\right)\right] \qquad \text{Equation 4-33}$$

4.4.2.4 Satellite velocity error

The ground along-track positioning error Δx_3 due to an error in the estimate of satellite velocity is given by Equation 4-34.

$$\Delta x_3 = \left(\Delta V_x \sin\theta_s + \Delta V_y \sin\gamma + \Delta V_z \cos\gamma\right)\frac{v_{sc}R}{V_{st}^2} \qquad \text{Equation 4-34}$$

In Equation 4-34, ΔV_x is along-track velocity error;
ΔV_Y is cross-track velocity error;
ΔV_Z is radial velocity error;
θ_s is the squint angle measured with respect to broadside;
γ is the look angle;
v_{sc} is the ground velocity of the satellite;
V_{st} is the orbital velocity of the satellite.

The term in brackets in Equation 4-34 provides the projection of the velocity error along the orbital velocity of the satellite.

Along-track velocity error produces an error in azimuth scale (Equation 4-35).

$$k_a = \frac{\Delta V_x}{V_x} \qquad \text{Equation 4-35}$$

4.4.2.5 DEM accuracy contribution

DEM are tipically used in image processing to improve the quality of the geo-location. In particular the altitude of a given target on the Earth's surface is a key parameter to achieve a correct target location.

Topographic altitude is required to perform a precise geo-location budget. An error on the target quota within the SAR image focussing process can be translated into the effect of an altitude error on the geo-located product accuracy.

According to the figure below, the target quota error Δq is considered equivalent to a satellite altitude error.

Considering geometry expressed in Figure 4-14 and assuming that $r_1=r_2=r$ (this assumption is acceptable as slant range is about five orders of magnitutude than the error Δq itself), following equations derive the error contribution due to this cause.

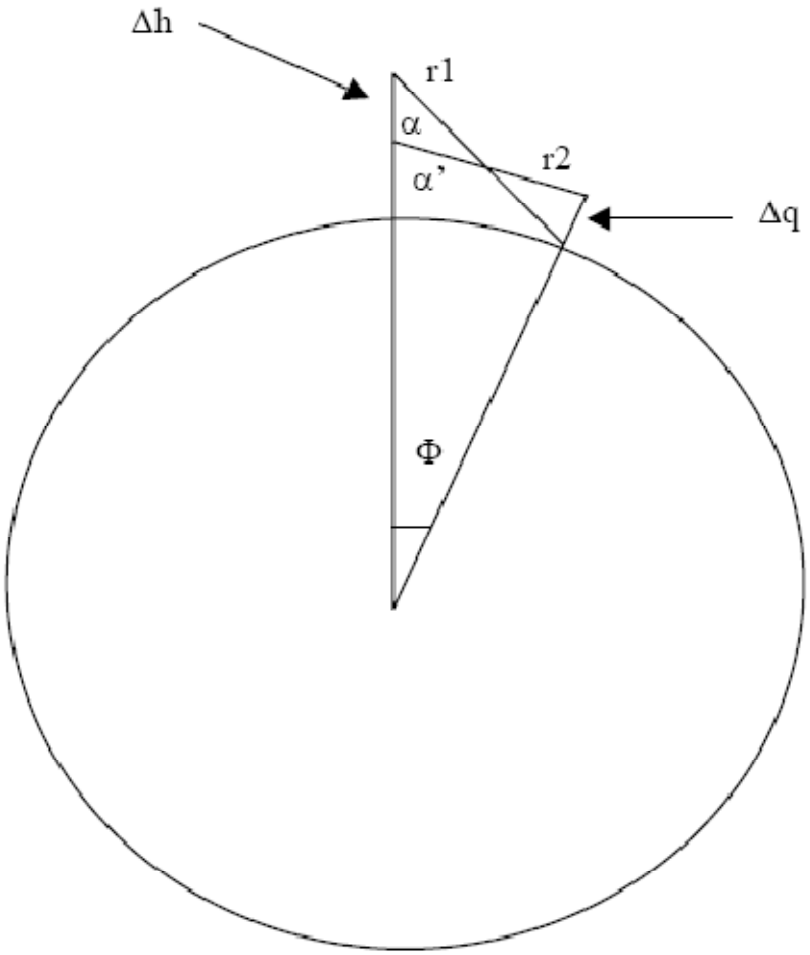

Figure 4-14. Geometry used to estimate the contribution of DEM accuracy

$$\alpha' = \arcsin\left(\frac{R+\Delta q}{R}\sin\alpha\right) \qquad \text{Equation 4-36}$$

$$\cos\Phi = 1+\frac{H}{R}-\frac{r}{R}\cos\alpha \qquad \text{Equation 4-37}$$

$$\Delta h = r\left(\cos\alpha - \cos\alpha'\right) - \Delta q\cos\Phi \qquad \text{Equation 4-38}$$

The geo-location error due to the quota shift is then computed as the geo-location error due to a corresponding satellite altitude shift.

4.4.2.6 SAR payload contribution - Datation accuracy

Echo samples datation accuracy, i.e. the knowledge of the flight time when echo data have been received, affects the along-track positioning error.

The effect of an error in the datation time is stated in terms of the effective azimuth location error (Equation 4-39).

$$\Delta x = \tau_{Da} v_{sc} \quad \text{Equation 4-39}$$

In Equation 4-39, $\tau_{Da,}$ is the datation accuracy;
v_{sc} is the ground velocity of the satellite.

4.4.2.7 Timing error - Slant range positioning error

The timing error determines the most part of the error that is estimated as the reciprocal of the minimum sampling frequency used by the SAR instrument.

Hence, an error contribution in the order of $c/2f_s$, where c is the speed of the light and f_s is the minimum SAR sampling frequency, is to be expected in the range direction.

The error affecting the impulse response function in the range plane (Δr) is considered in a within pulse basis: the time delay used in across-track calculation (range error) is given in Equation 4-40.

$$\tau_{slant} = \frac{within\ pulse\ linear\ phase\ error\ (deg)}{360} \frac{1}{Range\ bandwidth} \quad \text{Equation 4-40}$$

The resultant range error is given in Equation 4-41 (valid for bi-static configurations).

$$\Delta r = \tau_{slant} \frac{c_0}{\sin\theta} \quad \text{Equation 4-41}$$

4.4.2.8 Timing error - Along track positioning error

Timing errors referred to the IRF azimuth characteristic are defined in a pulse-to-pulse basis.

Consequently, the time delay used in azimuth calculation is given in Equation 4-42.

$$\tau_{az} = \frac{pulse\ to\ pulse\ phase\ error\ (\deg)}{360} \frac{1}{Doppler\ bandwidth}$$ Equation 4-42

To compute the effect in azimuth localisation Equation 4-43 has to be applied.

$$\Delta x = \tau_{Az} v_{sc}$$ Equation 4-43

4.4.2.9 On-board electronic delay

Error in the estimation of the on-board electronic delay (i.e. τ_e) will cause a slant range error that, reported on ground is:

$$\Delta r = \tau_e \frac{c}{2\sin\gamma}$$ Equation 4-44

In Equation 4-44, γ is the radar look angle.

Un-compensated atmospheric propagation delays will contribute as well to an across-track target displacement.

4.4.3 Geo-location budget - conclusions

In this section, a complete geo-location budget will be performed moving from the parameters included in Table 4-9.

Table 4-9. Parameters used to estimate the global geo-location budget.

Earth radius (km)	6378
Satellite altitude (km)	35786
Orbit inclination (degrees)	0
Light velocity (km/s)	300000
Satellite velocity (m/s)	19.833
Swath Velocity (m/s)	3.0
Antenna length (m)	6
Chirp bandwidth (MHz)	4
Doppler Bandwidth (Hz)	0.2
Datation accuracy (μs)*	100
Pulse to pulse linear phase error (deg)*	25
Electronic delay error (ns)*	100
Within pulse linear phase error (deg)*	25

*values assumed from previous work experience.

Table 4-10 presents the expected performances of the GeoSAR attitude and orbit determination system. These values will be used to perform the budget calculation.

Table 4-10. GeoSAR Attitude and Orbit determination system performances.

Satellite Position Error - Along track (m)	2.5
Satellite Position Error - Across track (m)	2.5
Satellite Position Error - Radial track (m)	2.5
Satellite Velocity Error - Along track (m/s)	0.01
Satellite Velocity Error - Cross track (m/s)	0.01
Satellite Velocity Error - Radial track (m/s)	0.01
DEM accuracy (km)	0.01

Table 4-11. GeoSAR imaging geometry.

	Incidence angle (degrees)				
	20.00	*25.00*	*40.00*	*50.00*	*59.50*
Off-nadir angle (deg)	2.97	3.67	5.58	6.65	7.49
Earth centre angle (deg)	17.03	21.33	34.42	43.35	52.01
Slant range (km)	36114.17	36297.32	37078.38	37780.27	38567.26
Ground Range (km)	1868.41	2320.41	3605.21	4377.86	5026.69

Table 4-11 includes the imaging geometry for the various incidence angles (degrees). Ground range is the distance across-track (in km) between the sub-satellite point and the point being imaged.

Using the data included in all the tables in this section, the final geo-location budget has been compiled. The results are included in Table 4-12.

Table 4-12. Geo-location budget.

Contributions to along-track errors	*Incidence angle (degrees)*				
	20	*25*	*40*	*50*	*59*
Satellite Position Error - Along track (m)	0.38	0.38	0.38	0.38	0.38
Satellite Position Error - Velocity error (m)	3.58	3.73	4.03	4.11	4.08
Datation accuracy (μs)	0.30	0.30	0.30	0.30	0.30
Pulse to pulse linear phase error (deg)	1.04	1.04	1.04	1.04	1.04
Orbit contribution (m)	3.60	3.75	4.05	4.13	4.10
Radar contribution (m)	1.08	1.08	1.08	1.08	1.08
Total Along track error (m)	***3.76***	***3.90***	***4.19***	***4.27***	***4.24***
Contributions to across-track errors					
Satellite Position Error - Across track (m)	0.38	0.38	0.38	0.38	0.38
Satellite Position Error - Radial (m)	7.30	5.90	3.87	3.24	2.88
Electronic delay contribution (m)	43.86	35.49	23.34	19.58	17.41
Within pulse linear phase contr. (m)	7.614	6.162	4.051	3.399	3.022
DEM contribution (m)	-7.34	4.35	34.51	57.60	88.22
Summary					
Orbit contribution (m)	7.31	5.92	3.89	3.26	2.90
DEM contribution (m)	-7.34	4.35	34.51	57.60	88.22
Radar contribution (m)	44.51	36.02	23.68	19.87	17.67
Total Across track error (m), rms	***45.70***	***36.77***	***42.04***	***61.02***	***90.02***
Total error with DEM (m), rms	***45.86***	***36.97***	***42.25***	***61.17***	***90.12***

Each line in Table 4-12 provides a contribution to the geo-location budget. The table has five columns that correspond to five different values of the ground incidence angle.

Assuming that GeoSAR has 8 MHz bandwidth, the total geo-location accuracy is within two pixels ($\Delta R_{range} \approx 25$ m).

4.5 Multi-static parasitic SAR

The background chapter provided some insights into multi-static SAR configurations. Following the introduction about multi-static configurations and specifically about the SAR train concept, the present section will present an analysis with the aim of demonstrating the potential of GeoSAR in multi-static constellations.

The SAR train concept (Aguttes, 2003; Aguttes, 2004) could be applied to GeoSAR to improve system performances. This concept has been discussed in the background chapter and two operating modes have been investigated: a first one that has random spacing between spacecrafts forming the constellation and a second operating mode that requires exact spacing in the flying formation.

Only the first operating mode (random spacing) could be applied to GeoSAR as very tight formation flying requirements cannot be met for the whole integration time.

Assuming that the SAR train is made up of $\boldsymbol{n_{sat}}$ satellites, the constellation with random spacing can achieve an improvement $\boldsymbol{n_{sat}}$ of the SNR and an improvement by $\boldsymbol{n_{sat}}$ of ambiguity protection.

4.5.1 Signal coherence

Phase variations caused by terrain topography *h* in many applications are sufficient to reduce dramatically target coherence. Aguttes (2004) gives the phase decorrelation term caused by unknown topography (Equation 4-45).

$$\varepsilon = \frac{4\pi h \omega}{6 \sin i R \lambda \sqrt{2}} \qquad \text{Equation 4-45}$$

In Equation 4-45, ε is the phase error of any of the $\boldsymbol{n_{sat}}$ signals to be focused;
ω is the width of the tube containing the trajectories of the $\boldsymbol{n_{sat}}$ SARs;
h is the error in the knowledge of the topographic altitude of the target;
i is the orbit inclination;
R is the radar slant range;
λ is the wavelength.

Equation 4-45 shows that the error is inversely related to the slant range and that a good knowledge of terrain topography is required to reduce phase error. A high altitude orbit could make this configuration feasible even though the orbit control is not extremely precise (i.e. ω) and in absence of a good knowledge of terrain height (i.e. *h*).

A comparison between GeoSAR and a conventional LEO SAR has been carried out. Table 4-13 shows the parameters that have been taken into account in the analysis.

Figure 4-15 has been plotted using Equation 4-45 and the parameters included in Table 4-13. It compares the influence of the error in the knowledge of topographic height on phase error in multi-static SAR processing. This inaccuracy is not significant in the geosynchronous case while it is important for the LEO multi-static configuration where precise SAR processing requires an accurate knowledge of topography that is not readily available especially in remote areas of the globe.

Table 4-13. Parameters used to generate the plot in Figure 4-15.

	GeoSAR	*LEO SAR*
R	40000 km	800 km
i	50 deg	50 deg
λ	0.25 m	0.25 m

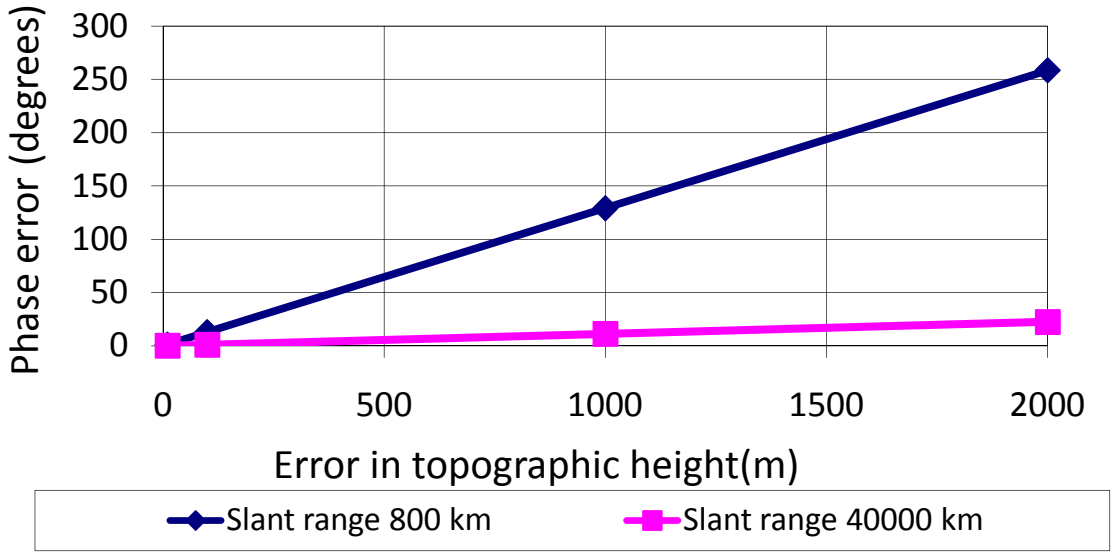

Figure 4-15. Phase error induced by an error in the knowledge of the topographic height (constant perpendicular baseline ω=100 m).

Equation 4-45 can be used as well to estimate phase errors induced by the width of the tube that contains the orbit of the n_{sat} satellites that constitute the SAR train. Using parameters included in Table 4-13 for the GeoSAR, the phase decorrelation induced by the tube width is presented in Figure 4-16.

It has to be said, however, that GeoSAR requires a very accurate knowledge of the slant range in order to avoid phase decorrelation. This aspect poses a strict requirement on the knowledge of the topography as well.

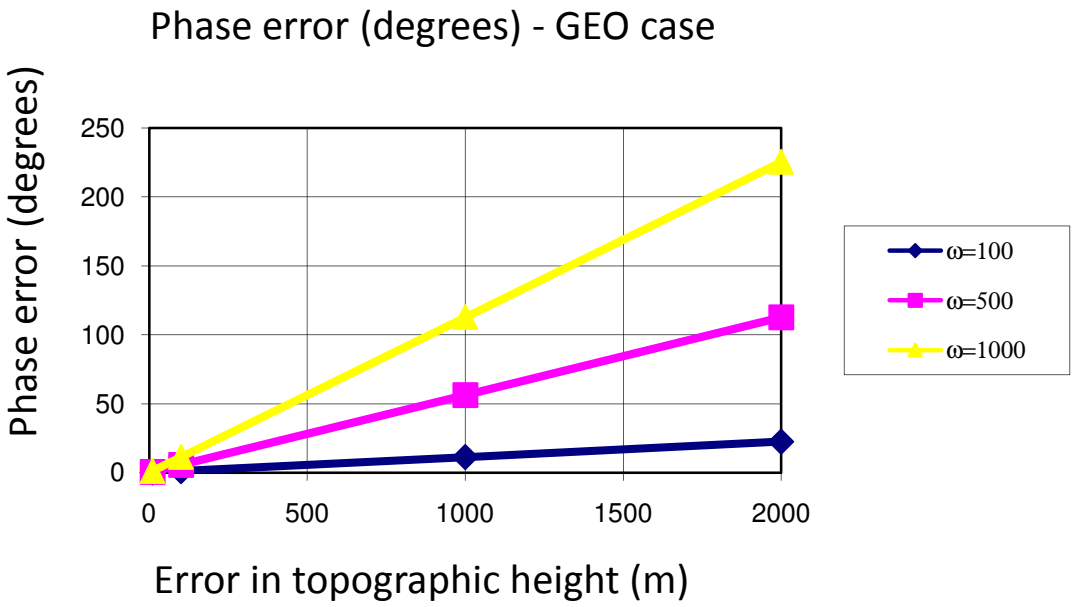

Figure 4-16. Phase error induced by the width of the tube containing the orbits of the satellites that constitute the SAR train tube width is expressed in meters.

4.6 Conclusions

The GeoSAR concept, developed at Cranfield Space Research Centre, is a system design for an L band bi-static geosynchronous SAR system. This research contributes to the development of this concept that has already been demonstrated in literature, estimating performances and investigating issues related to phase decorrelation aspects that happen during the integration time.

Performance varies with the location of the target on the globe due to the differences in slant range and viewing angles.

The analysis carried out on the bi-static SAR phase provides estimates of its sensitivity to phase delays. The expressions worked out highlight that GeoSAR, due to the large slant range and the long integration time (8 hour), is extremely sensible to phase delays, much more than any equivalent LEO configurations.

SAR image reconstruction has to take into account decorrelation effects induced by fluctuating targets and by heterogeneities in the propagation medium. This issue is not usually addressed in the literature, as it does not concern the design of LEO SARs.

The outcome of this analysis provides the rationale for the detailed analysis about decorrelation effects that will be addressed in the remaining part of this report.

A geo-location accuracy better than two pixel could be achieved without a very tight requirement on orbit determination accuracy. The most important contributions to the budget have been given by the electronic delay and by the DEM. It is well known that a good quality DEM is a major requirement to achieve a good geo-location.

5 SAR Azimuth Focussing Simulation

The aim of this chapter is to discuss the methodology and the tools that have been used in the present research to look into the issues related to GeoSAR azimuth focussing.

In order to investigate the effect of perturbations that influence the system during the integration time, an azimuth bi-static SAR simulator has been implemented. This methodology requires the preliminary definition of an appropriate dataset. The rationale that is behind the generation of simulated SAR signal backscattered is presented in section 5.1. The subsequent section 5.2 presents some aspects related to temporal decorrelation.

Section 5.3 describes the procedure carried out to generate correlated Gaussian noise, used in the simulations to generate noise sources with a given temporal correlation. Section 5.4 proposes an analytical approach to estimate the loss in coherent signal integration gain for Gaussian phase noise with limited amplitude. This methodology will be extensively applied to estimate the effect of perturbations affecting SAR signal.

The bi-static azimuth SAR simulator that has been implemented for the simulations has been presented in section 5.5. The subsequent section 5.6 summarises the different approaches that have been used in the simulations carried out.

Section 5.7 recalls the potential sources of temporal decorrelation that have been investigated in this research (Earth tides, tropospheric and ionospheric perturbations) and looks into the rationale that is behind the simulations that have been carried out.

In the relevant sections, a more specialist literature review, related to the subjects under investigation, has been included.

5.1 Statistical modelling of SAR backscatter

In order to implement a bi-static SAR simulator, SAR backscatter has been modelled following an approach that allows taking into account temporal decorrelation. The idea behind this methodology comes from previous research carried out at Cranfield Space Research Centre about the effect of wind motion on temporal coherence (Seynat, 2000).

The images of uniform surfaces have a typical noise-like aspect that is due to the phenomenon of speckle. Assuming that the total backscatter received by the antenna is the result of the summation of multiple individual scattering elements in the scattering volume, the total backscattered signal is given in Equation 5-1 (Seynat, 2000; Hobbs, 1997).

$$V = |V| e^{i\phi} = \sum_{i=1}^{n} |V_k| e^{i\phi_k} \qquad \text{Equation 5-1}$$

This summation can be compared to an interference phenomenon between individual contributions.

To take into account the changes in radar backscatter that occur during the integration time, in principle it is possible to separate the scattering contribution in two parts: a static one and a dynamic one. The static contribution is due to all the individual scatterers that do not change their position and their properties during the integration time while the dynamic contribution simulates the various sources of decorrelation in the radar backscatter.

5.1.1 Static contribution

The static contribution V_s is expressed as:

$$V_s = a e^{i\phi_s} \qquad \text{Equation 5-2}$$

If the individual scatterers are uniformly distributed in the ground resolution cell then the phase is uniformly distributed in the interval $[-\pi;+\pi]$. This implies that the real and imaginary parts of the backscatter have a Gaussian distribution. The resulting backscatter amplitude has a Rayleigh distribution with probability distribution as in Equation 5-3, where v is the mean and σ the variance of the distribution.

$$P_{|V|}(v) = \frac{2v}{\sigma} \exp\left(-\frac{v}{\sigma}\right) \qquad \text{Equation 5-3}$$

In order to evaluate phase distortions induced by temporal decorrelation heterogeneities, the dataset used for SAR azimuth focussing simulations should refer to a stable point target.

Therefore, in the simulations that have been carried out in the present research, the static component V_s will have a stable behaviour (both in amplitude and in phase).

5.1.2 Dynamic contribution

The dynamic component V_d is expressed as in Equation 5-4

$$V_d = e^{i\phi_d} \qquad \text{Equation 5-4}$$

In Equation 5-4, ϕ_d is the phase of the dynamic component specified by a probability distribution.

In Equation 5-4, a unit amplitude of the dynamic component has been assumed so that coefficient *a* in Equation 5-2 gives the relative accuracy.

The dynamic component is a multiplicative phase factor that can model phase delays induced by surface displacements or by heterogeneities in the propagation medium. Dynamic phase can be simulated with a Gaussian distribution.

5.1.3 Dataset construction

The static component V_s models the amplitude and the phase of the stable point scatterer. The dynamic contribution V_d provides an additional phase term that can be used to model phase perturbations that affect GeoSAR focussing using the phase screen approach (Greene and Moller, 1961; described in section 5.6.2).

$$V = V_s \times V_d; \qquad \text{Equation 5-5}$$

Different phenomena that affect GeoSAR focussing will be modelled varying the stochastical properties of the dynamic term V_d.

5.2 Temporal decorrelation

The SAR capability to measure the relative phase within each pulse requires coherence from pulse to pulse over the collection time needed for azimuth resolution (Carrara *et al.*, 1995). The concept of coherence in an imaging system is related to the predictability and, more in general, to the stability of phase.

The key concept in analysing coherence is the “coherence time”, the time during which the scattered signal retains the same amplitude and scattering phase (Ulaby *et al.*, 1986). The only phase shift that can occur during this time lapse is the one due to the motion of the radar. A coherence time or correlation time shorter than the actual integration time implies that the achievable azimuth resolution is smaller. If the target is completely non-coherent, the pulses collected by the radar do not sum coherently and the targets cannot be processed coherently unless the resolution is reduced (i.e., the integration time is diminished to become closer to the actual correlation time).

The long integration time of a geosynchronous SAR implies that the coherence of the imaged target has some serious implications on the determination of the radar SNR. Only a few targets could be considered so stable to preserve their coherence on time scales of about 30 minutes or even more (Prati *et al.*, 1998).

The long integration time behaves like a filter as it focuses mainly stable targets. Following the discussion provided by Prati *et al.* (1998) it is possible to investigate the effects of geosynchronous SAR parameters on target's response and clutter in order to evaluate if there are any relatively unstable scatterers that could be filtered out by the integration process for their lack of coherence.

This section recalls a simplified analytical approach described by Prati *et al.* (1998) to estimate the integration loss expected for both stable and unstable scatterers. Stable, partially stable and non-coherent scatterers have been looked into to derive an analytical expression for SNR. This method has not been applied in the present research but its rationale provides a useful background to the methodology that has been effectively applied to estimate the coherent integration loss.

5.2.1 Stable scatterer

As explained by Picardi (2000) a single scatterer stable on the terrain and that is illuminated by a chirp signal with a bandwidth *B* is focused in range by cross-correlation. This function has a peak at the scatterer location plus a random pedestal with noise. The peak to pedestal power ratio is given by Equation 5-6 (Picardi, 2000).

$$\Delta T \times B \qquad \text{Equation 5-6}$$

In Equation 5-6, ΔT is the pulse length;
B is the bandwidth of the transmitted signal.

Prati *et al.* (1998) specify that the correlation is repeated for every azimuth position of the synthetic aperture. Under the hypothesis that the scatterer is stable, the correlation peaks at the target location sum up coherently while the pedestals sum incoherently. The SNR due to any stable scatterer therefore is given by Equation 5-7.

$$SNR_1 = \Delta T \times B \times T_{obs} \times PRF \qquad \text{Equation 5-7}$$

In Equation 5-7, SNR_1 is the peak to pedestal power ratio that corresponds to a stable scatterer;
T_{int} is the integration time;
PRF is the Pulse Repetition Frequency.

The term $T_{int}xPRF$ stands for the number of coherent pulses that sum coherently during the integration time.

Thermal noise has not been included in this analysis. The SNR comes purely from signal focussing.

5.2.2 Partially coherent targets

Partially coherent targets such as water or vegetation have a finite correlation time that is usually much shorter than the integration time and larger than the pulse length. For water or dense vegetation at L band it can be considered τ=0.1 seconds (Prati *et al.*, 1998). Analogous results can be achieved even considering a longer correlation time (i.e. few seconds) that appears more likely for canopies (Seynat, 2000; Hobbs, 1997).

The correlation time or coherence time is the time lapse during which the range focussed correlation peaks sum coherently. In the whole synthetic aperture, there are a series of correlation peaks that are not related to each other. Those peaks generate a 1D pedestal in the azimuth direction. On the other hand, there is a 2D (both in range and in azimuth directions) noise pedestal given by the signals that sum-up non-coherently in range and in azimuth focussing. The SNR is given in Equation 5-8.

$$SNR = \Delta T \times B \times \tau_c \times PRF \qquad \text{Equation 5-8}$$

In Equation 5-8, τ_c is the correlation time of the target.

5.2.3 Totally non coherent targets

For a theoretical non-coherent target, the correlation time is shorter than the pulse length (taking into account the bandwidth). The output of the correlation gives only a noise pedestal both in range and in azimuth, there is no useful signal.

5.3 Correlation time (distance)

The concept of correlation time has been used in this research to estimate the temporal or spatial coherence of various noise sources.

Correlation time (or distance) has been estimated using the approach usually applied to time series. Phase variations have been modelled as a first-order Gauss-Markov process. Figure 5-1 illustrates that correlation time (or distance) ρ has been defined in terms of the variance σ^2 as the time/distance that corresponds to a value of the auto-correlation equal to 1/e σ^2 = 0.3769 σ^2.

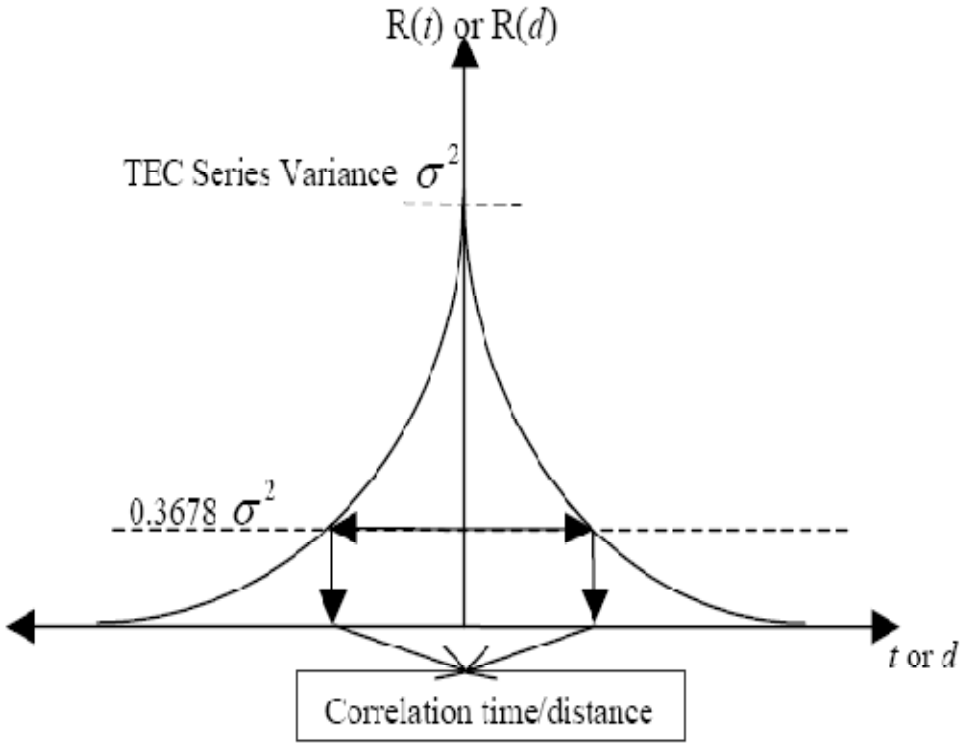

Figure 5-1. Illustration of estimating the correlation times (or distance) (El Gizawy, 2003).

The expression for the autocorrelation ρ as a function of the lag k is:

$$\rho(k) = \frac{\frac{1}{N-k}\sum_{i=1}^{N-k-1} V_i V_{i+k}^*}{\frac{1}{N}\sum_{i=1}^{N} V_i^2} \qquad \text{Equation 5-9}$$

In Equation 5-9, V is the time (or spatial) series that is being considered.

5.3.1 Gaussian filter

In the present research, an azimuth SAR processor has been implemented in Matlab to investigate the effect of temporal correlation on GeoSAR focussing. Where necessary, Gaussian correlated noise has been added to the system to investigate its effects.

Oksanen and Sariakoski (2005) describe a procedure to generate a Gaussian filter that can be implemented in order to generate correlated noise starting from white Gaussian noise. The code in Matlab that has been used to generate correlated Gaussian noise is included in Appendix B (*Gaussian_filter.m*).

The method is thoroughly described in their paper. An a priori determined spatial autocorrelation function is determined and, exploiting the properties of Gaussian distributions and convolution, uncorrelated noise is filtered as to achieve the desired autocorrelation in the form presented in Equation 5-10 (Oksanen and Sariakoski, 2005):

$$\rho(t) = e^{-\left(t^2/\tau^2\right)} \qquad \text{Equation 5-10}$$

In Equation 5-10, ρ is the correlation coefficient;
t is the time lag;
τ is a time constant that has to be tuned to set the filter response.

With respect to box filtering, the Gaussian filter actually low-passes the noises removing the desired frequencies.

Figure 5-2 shows the correlation function that corresponds to τ=3.

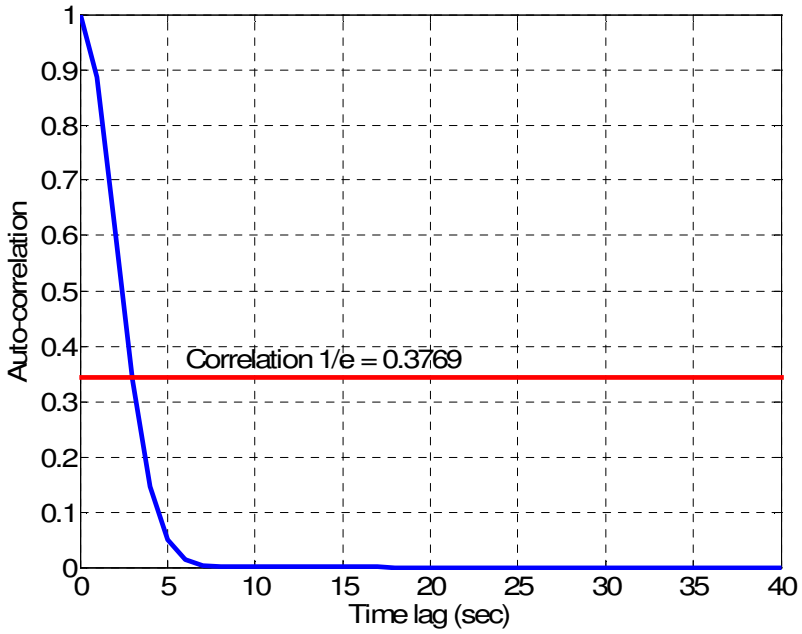

Figure 5-2. Auto-correlation function achieved with a Gaussian filter (τ= 3). The figure shows the correlation level that corresponds to correlation time (1/e = 0.3769).

Setting the coefficient τ and using Equation 5-10, it is possible to obtain the desired correlation time (i.e. time lag that corresponds to an auto-correlation 1/e). Figure 5-3 shows the auto-correlation function with correlation time 10 samples.

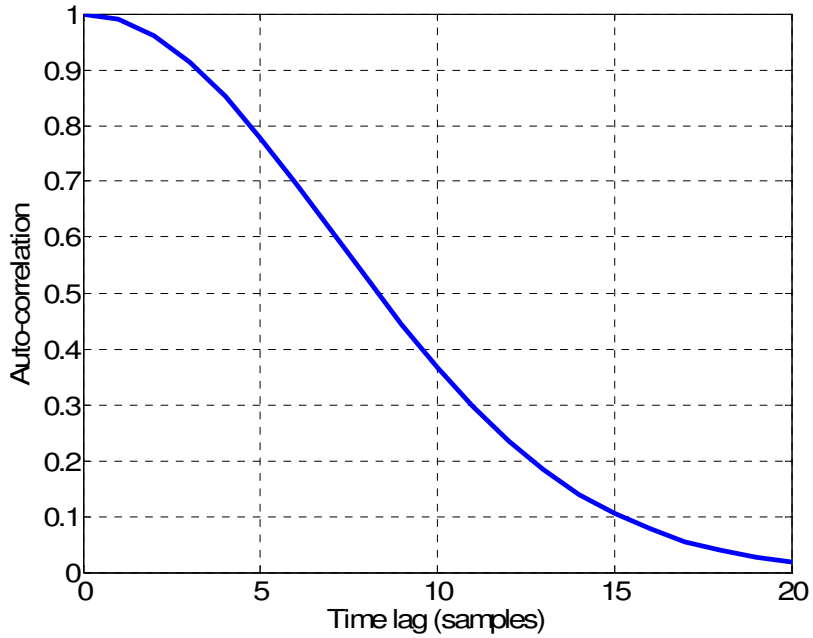

Figure 5-3. Auto-correlation function with correlation time 10 samples.

5.4 Coherent integration loss estimation

Under the assumption that heterogeneities are modelled as white Gaussian noise, Richards (2003) provides a valuable analytical derivation that might be used to estimate analytically the loss in integration gain *L* (Equation 5-11).

$$L \cong 10\log_{10}\left(e^{-\sigma^2}\right) = -4.343\sigma^2 \text{dB} \qquad \text{Equation 5-11}$$

It is applicable for small phase errors due to white noise (i.e. up to 20°) with variance σ^2 (in rad^2). When the amount of phase delay is beyond this limit, its effect on GeoSAR azimuth PSF has been evaluated by means of Monte Carlo simulations as recommended in Green and Moller (1961).

5.5 SAR azimuth processing

In order to evaluate GeoSAR's robustness to temporal decorrelation, a SAR simulator has been implemented. The code *simulator.m* has been developed in Matlab (listing in Appendix B). The code has been run mostly on a commercial laptop (Windows XP operative system). Longer simulations have been run on Cranfield University's computing grid. For validation purposes a different code (developed independently) by Hobbs (2008) has been used. This software has been developed in C (Visual C++ 5.0 environment). Only azimuth processing has been implemented for the two main reasons listed below.

- Target fluctuations and phase delays affect mainly azimuth (slow-time) processing that happens during the integration time (i.e. 8 hours).

- Due to the large number of pulses required to focus a single image, a complete SAR processor (i.e. range and azimuth) would be feasible only adopting processing farms.

The simulator is able to focus a line of scatterers; however, the most useful output of the simulator is the azimuth ambiguity function, also known in literature with the names azimuth Point Spread Function (PSF) or Impulse Response Function (IRF). It is the response of the system to a stable scatterer with unit radar cross section (in absolute terms) placed at the centre of the synthetic aperture.

The ideal azimuth ambiguity function is represented by a spike of infinitesimal width that peaks at the origin and is zero everywhere else, as illustrated in Figure 5-4. An ideal ambiguity function provides perfect resolution between neighbouring targets regardless of how close they may be with respect to each other. This will require an infinite Doppler bandwidth and therefore cannot physically exist.

Simulations run can provide GeoSAR's azimuth impulse response in the ideal (without noise) and the real (noisy) case. The comparison between the results will provide insights into the effect of temporal decorrelation.

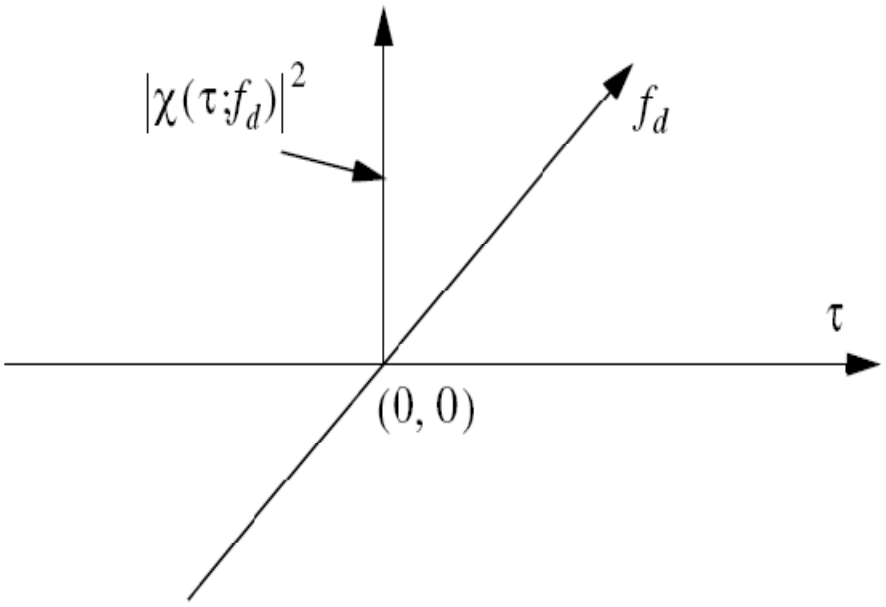

Figure 5-4. Ideal radar ambiguity function, $\chi(\tau,f_d)$ is the ambiguity function, τ is the fast-time coordinate, f_d is Doppler frequency (Mahafza, 2000).

Section 5.5.1 will present some specialist literature about SAR image processing; the subsequent section will discuss in details the structure of the simulator and its validation process.

5.5.1 Literature

Cumming and Wong (2004), Soumekh (1999) and Franceschetti and Lanari (1999) provide the three major references about SAR signal processing.

The fundamentals of SAR processing have already been discussed in the background chapter; hereafter the analytical approach described by Soumekh (1999) has been presented.

SAR focussing could be carried out in two phases: fast time (i.e. range) processing and slow-time (i.e. azimuth) processing. Even though this research dealt only with the analysis of the system azimuth PSF, in this section about literature review both the steps required for a complete SAR processing will be discussed for the sake of completeness.

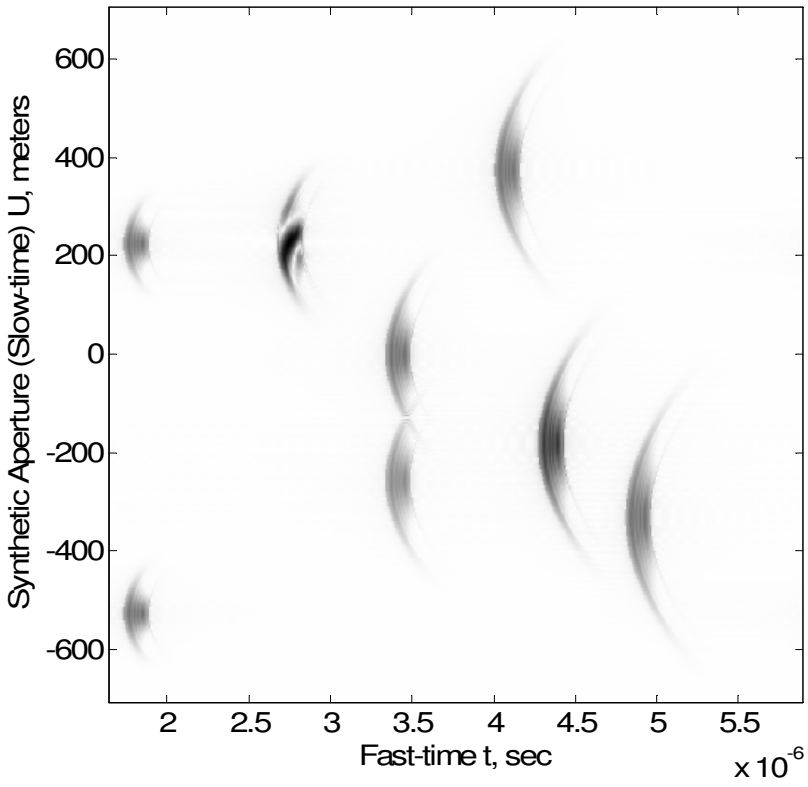

Figure 5-5. SAR raw data in the fast-time/slow-time domain (Soumekh, 1999).

5.5.1.1 Range processing

Range processing, also called fast-time processing, refer to the imaging process across-track. Figure 5-5 refers to a LEO configuration, in a geosynchronous SAR the effect of range migration is not relevant due to the size of the resolution cell (Hobbs, 2008).

Assuming that, within the range swath, there are *n* targets with backscatter σ_n at range distance x_n that are illuminated by a signal *p(t),* the received echoed signal has the following form in the time domain (Equation 5-12).

$$s(t) = \sum_n \sigma_n p\left(t - \frac{2x_n}{c}\right) \qquad \text{Equation 5-12}$$

Equation 5-12 is appropriate for a monostatic configuration. In a bi-static configuration the round-trip delay $2x_n$ has to be substituted with x_t+x_r to take into account the different slant ranges from the transmitter to the target and from the latter to the receiver.

The Fourier transform of the echoed signal (in bi-static form) is given in Equation 5-13.

$$S(\omega) = P(\omega) e^{-j\frac{(x_{tn}+x_{rn})}{c}} \qquad \text{Equation 5-13}$$

As reported in the background chapter, matched filter is one of the methods for range imaging. The output signal $s_M(t)$ is obtained from inverse Fourier transform of the convolution of the collected signal $S(\omega)$ with the reference range signal $P^*(\omega)$ (i.e. complex conjugate of $P(\omega)$).

$$s_M(t) = FT^{-1}\left[S(\omega)P^*(\omega)\right] = FT^{-1}\left[\sum_n \sigma_n \left|P(\omega)\right|^2 e^{-j\omega\frac{(x_{tn}+x_{rn})}{c}}\right] \qquad \text{Equation 5-14}$$

The range Point Spread Function (i.e. PSF) or range ambiguity function therefore is:

$$psf_r(t) = FT^{-1}\left[\left|P(\omega)\right|^2\right] \qquad \text{Equation 5-15}$$

The *PSF* clearly depends on the spectral shape of the radar signal. Franceschetti and Lanari (1999) report (Equation 5-17) the *PSF* for a chirp signal or linear frequency modulated radar signal (Equation 5-16).

$$p(t) = a(t) e^{j\beta t + j\alpha t^2} \qquad \text{Equation 5-16}$$

$$psf(x') = e^{-j\frac{2\pi}{\lambda}2x}\,\mathrm{sinc}\left[\pi\frac{c}{2B_R}(x'-x)\right] \qquad \text{Equation 5-17}$$

In Equation 5-17, B_R is the bandwidth of the chirp signal,
x' is an arbitrary range variable.

SAR range resolution, as discussed in section 2.2.1, is a function of the bandwidth of the transmitted signal (Equation 5-18).

$$\Delta R_r = \frac{c}{2B_R} \qquad \text{Equation 5-18}$$

Figure 5-6 shows the raw SAR data after fast-time processing.

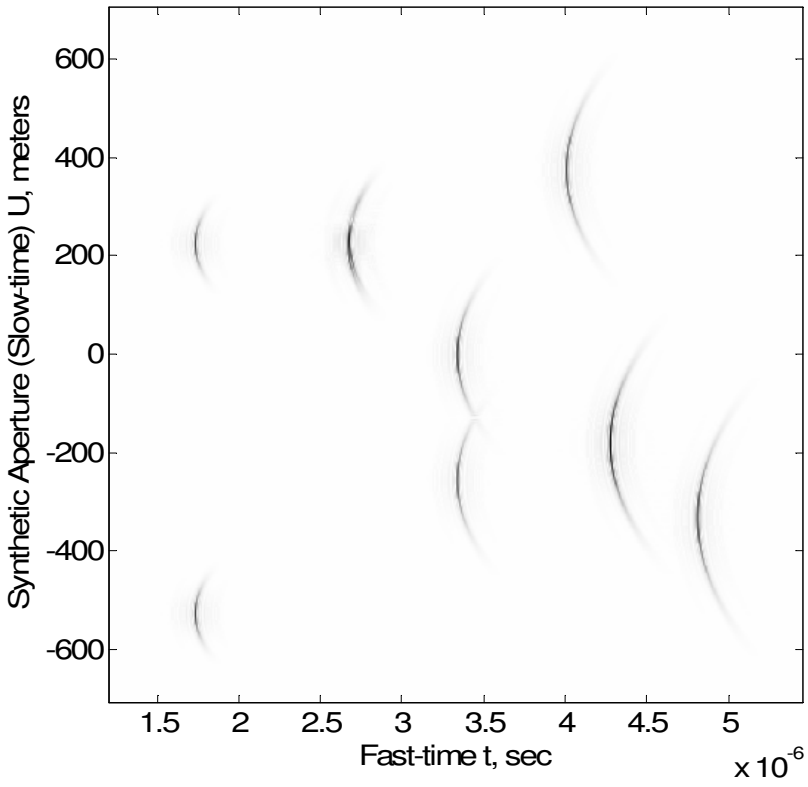

Figure 5-6. SAR data after fast-time processing (Soumekh, 1999).

5.5.1.2 Azimuth processing

Azimuth or slow-time processing is the key item in SAR processing as it allows to synthesize the synthetic aperture and to achieve a resolution that is considerably smaller compared to real aperture radars as shown in the background chapter.

It is assumed that the platform carrying the radar is moving along a straight path and is located at *(0,u),* where the coordinate u is varying with time. The measured echoed signal is presented in Equation 5-19 (for monostatic SAR).

$$s(t,u) = \sum_n \sigma_n p\left(t - \frac{2\sqrt{x_n^2 + (y_n - u)^2}}{c} \right) \qquad \text{Equation 5-19}$$

In Equation 5-19, y_n is the along-track position of the scatterer;

u is the spatial coordinate along the flight path of the antenna.

The round trip delay for the wave propagation for the i[th] target, in the monostatic case, is:

$$t_i = \frac{2\sqrt{x^2 + \left(y - u_i\right)^2}}{c} \qquad \text{Equation 5-20}$$

The above is the equation of a half hyperbola in the (*t,u*) (i.e. fast time, slow time) domain.

After fast-time matched filtering, as presented in section 5.5.1.1 , the Fourier transform of the generic SAR signal *s(t,u)* with respect to fast time is:

$$s\left(\omega, u\right) = P\left(\omega\right)\sum_n \sigma_n e^{-j2k\sqrt{x_n^2 + \left(y_n - u\right)^2}} \qquad \text{Equation 5-21}$$

In Equation 5-21, $k=\omega/c=2\pi f/c$ is the wavenumber.

The subsequent operation in SAR processing is a Fourier transformation in the slow-time (i.e. azimuth) domain:

$$FT\left[e^{-j2k\sqrt{x_n^2 + \left(y_n - u\right)^2}} \right] = e^{-j\sqrt{4k^2 - k_u^2}x_n - jk_u y_n} \qquad \text{Equation 5-22}$$

In Equation 5-22, $k_u \in [-2k;2k]$ is the synthetic aperture frequency domain.

The slow-time Fourier transform of the signal *s(ω,u)* is:

$$S\left(\omega, k_u\right) = P\left(\omega\right)\sum_n \sigma_n e^{-j\sqrt{4k^2 - k_u^2}x_n - jk_u y_n} \qquad \text{Equation 5-23}$$

The phase function in the exponential term is a linear function of the position of the target. This will be used in SAR reconstruction.

Assuming that there are *M* samples along the synthetic aperture (*u* coordinate) with sample spacing *Δu*, after Fourier transforming as in Equation 5-22 we have *M* samples *S(ω, ku)* with the following spacing:

$$\Delta k_u = \frac{2\pi}{M\,\Delta u} \qquad \text{Equation 5-24}$$

Defining two new functions k_x and k_y:

$$k_x(\omega, k_u) = \sqrt{4k^2 - k_u^2} \qquad \text{Equation 5-25}$$

$$k_y(\omega, k_u) = k_u \qquad \text{Equation 5-26}$$

If the synthetic aperture of the SAR considered is *2L,* the variable $u \in [-L; +L]$. The aspect angle interval over which a target is observable to the radar is related obviously to the size of the antenna beam width. For a planar antenna it is:

$$\phi \in [-\phi_D; \phi_D] = \left[-\frac{\lambda}{2D}; \frac{\lambda}{2D}\right] \qquad \text{Equation 5-27}$$

The k_u domain is limited by the SAR geometry:

$$k_u \in [-2k \sin\phi_D; 2k \sin\phi_D] \qquad \text{Equation 5-28}$$

In fast-time domain, the frequency ω is limited by the bandwidth of the signal.

The SAR focused signal is achieved via inverse bi-dimensional Fourier transform as shown in the diagram in Figure 5-7. The focused SAR image is shown in Figure 5-8.

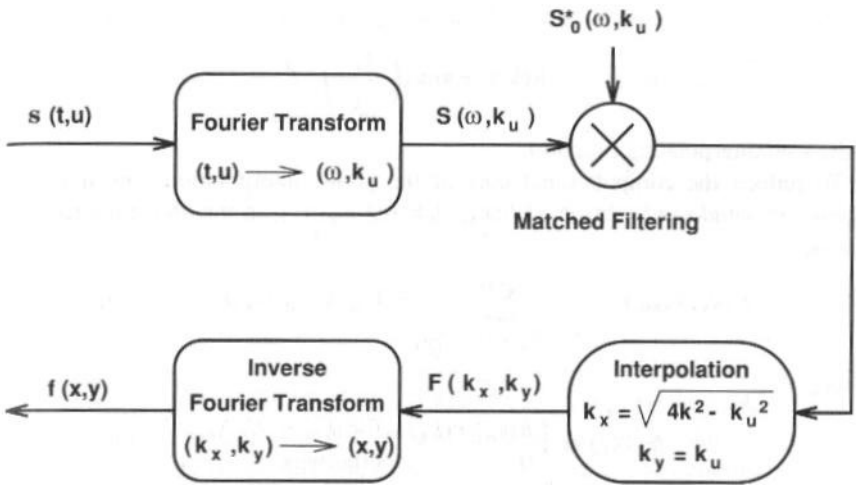

Figure 5-7. Block diagram of generic SAR digital reconstruction algorithm via spatial domain interpolation (Soumekh, 1999).

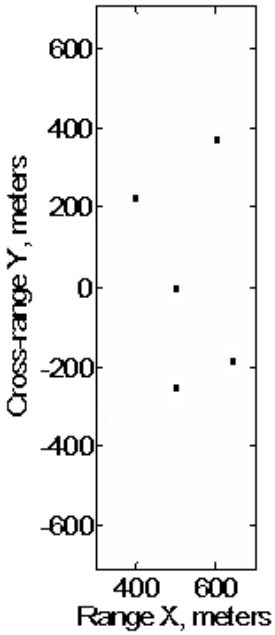

Figure 5-8. Stripmap SAR reconstruction.

5.5.2 GeoSAR bi-static azimuth processor

The main objective of this research is to investigate the effects of temporal decorrelation on GeoSAR, analysing image focussing in presence of fluctuating targets or variations in the propagation medium that induce phase delays.

An azimuth bi-static SAR processor has been implemented in Matlab following the methodology described in previous sections (the source code *simulator.m* and all the functions and subroutines that have been used are enclosed in Appendix B).

Figure 5-9 presents the flow chart with the relevant steps in GeoSAR focussing. The following sections describe in details the operations related to each of the logic steps.

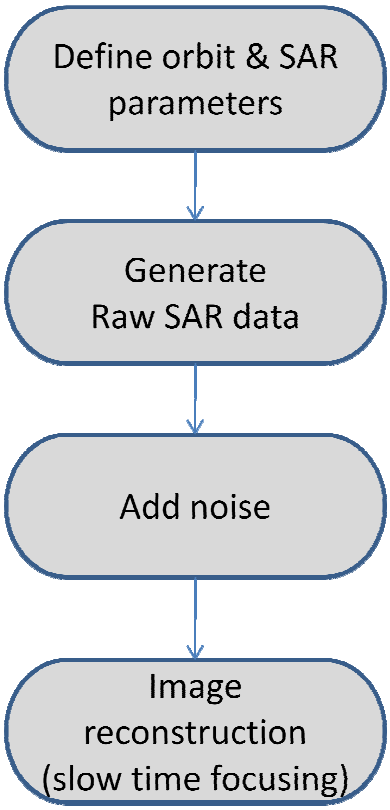

Figure 5-9. GeoSAR bi-static azimuth simulator flow chart.

Figure 5-10 describes the structure of the code *simulator.m* and the relative dependencies among the functions that implement the various functionalities in the code.

The simulator is also capable of importing/exporting raw data that could be used for validation purposes.

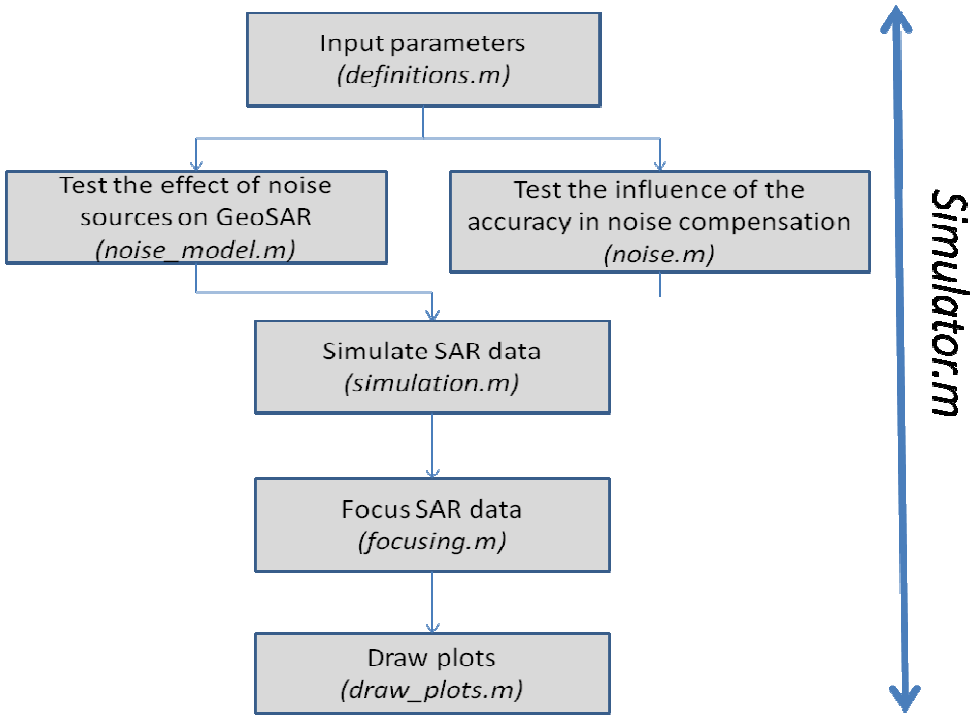

Figure 5-10. Functions included in the simulator.m code.

5.5.2.1 Define orbit and SAR parameters

Table 5-1 includes the parameters that are relevant for the simulation. The table reports a simple description of each parameter, the name of the variable inside the code and some additional information that can be useful for the comprehension of the problem.

Table 5-1. Relevant parameters in the simulation.

Description	Variable	Units	**Notes**
System properties			
Range resolution	dx	m	**To be used to determine the RCS of each scatterer.**
Grid resolution	dy	m	**To be used to determine the RCS of each scatterer. It has to be much**

Table 5-1. Relevant parameters in the simulation.

Description	Variable	Units	**Notes**
			smaller than azimuth resolution.
Number of points in the grid	n_grid	N.A.	**The grid is defined from abscissa yref0 to abscissa (ygrid+n_grid x dy).**
Number of pulses	n_pulse	N.A.	**Number of pulses along RX trajectory where SAR signal is estimated.**
Height of the satellites	h0	m	**Same height for TX and RX.**
Location of the scattering grid	ygrid0	m	**Abscissa of the first scatterer.**
Surface noise temperature	Tsurf	K	**To be used in SNR estimation.**
Frequency	fc	Hz	**Centre frequency.**
Speckle effect	Random_phase	N.A.	**Flag that activates speckle effect**
Thermal noise	Flag_ideal	N.A.	**Flag that activates thermal noise**
Transmitter			
Transmitted power	Pt	W	
Transmitter velocity	vt	m/s	**Velocity is assumed to be zero (transmitter stationary) in GeoSAR.**
Transmitter position across-track	dxt	m	**Used to locate the position of the transmitter.**
Bandwidth of the signal	nbw	Hz	
Transmitter antenna area	Atx	m^2	
Location of the transmitter	ytx0	m	**Used to locate the position of the transmitter.**

Table 5-1. Relevant parameters in the simulation.

Description	Variable	Units	**Notes**
Receiver			
Receiver velocity	v_sat	m/s	
Pulse Repetition Frequency	prf	Hz	
Antenna area	Arx	m^2	
Receiver noise figure	n	absolute	
Start of synthetic aperture	yref0	m	**Abscissa where the synthetic antenna aperture starts.**
Start of pulse reception	ypulse0	m	**Abscissa where the receiver receives the first pulse.**
Position across-track	dxt	m	

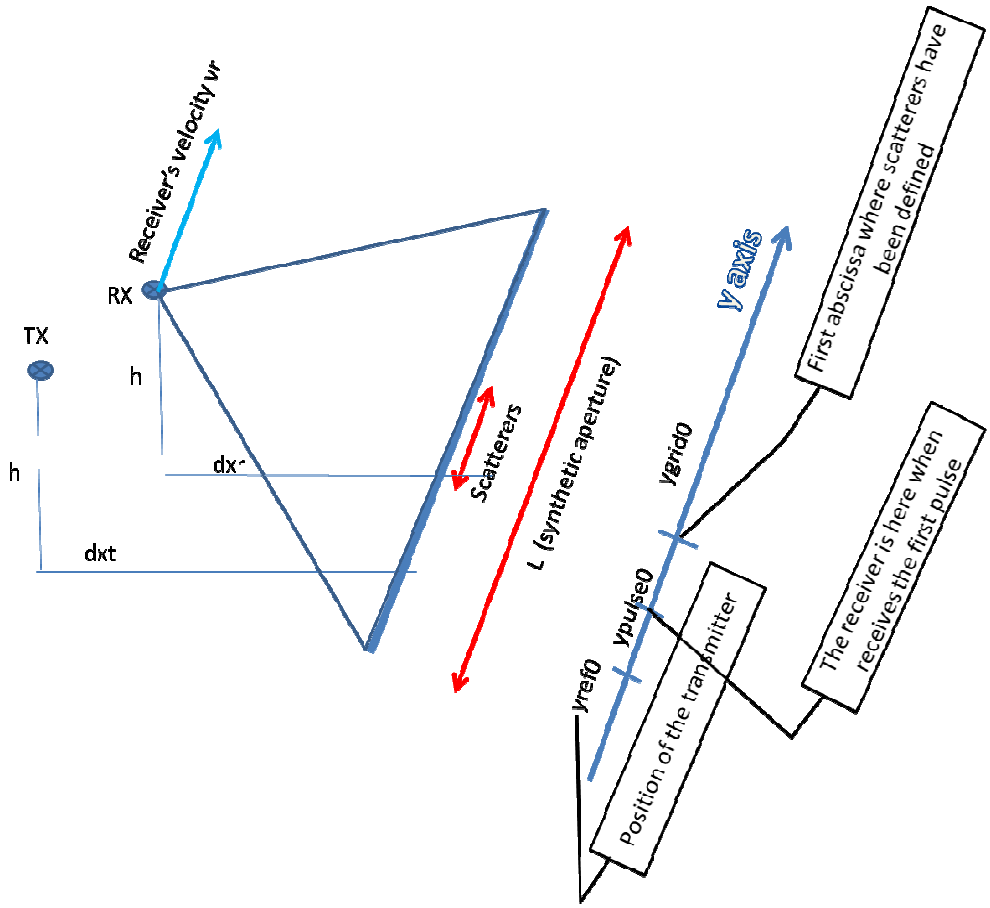

Figure 5-11. Bi-static acquisition geometry.

Figure 5-11 includes some of the variables that have been previously introduced. The simulator is able to focus targets that are located along a fixed range (i.e. across-track) coordinate. The picture shows the across-track positions of the transmitter and of the receiver (i.e. *dxt*, *dxr*), the abscissas along the *y-axis* (cross-range coordinate) of the transmitter (i.e. *yref0*), of the receiver when the first pulse is received (i.e. *ypulse0*) and the first abscissa where the scatterers have been defined (i.e. *ygrid0*)

5.5.2.2 SAR raw data generation

SAR raw data has been generated using the function *simulation.m*. In SAR imaging the real antenna has a footprint that is much larger than the azimuth resolution and contains a large number of scatterers (i.e. *n_grid* in the simulation). For any pulse that is transmitted, *n_grid* contributions (i.e. reflections coming from each scatterer that has been modelled) sum up at the receiver antenna under the assumption that they are

included in the same range gate. Figure 5-12 shows the formation of the signal coming from each pulse.

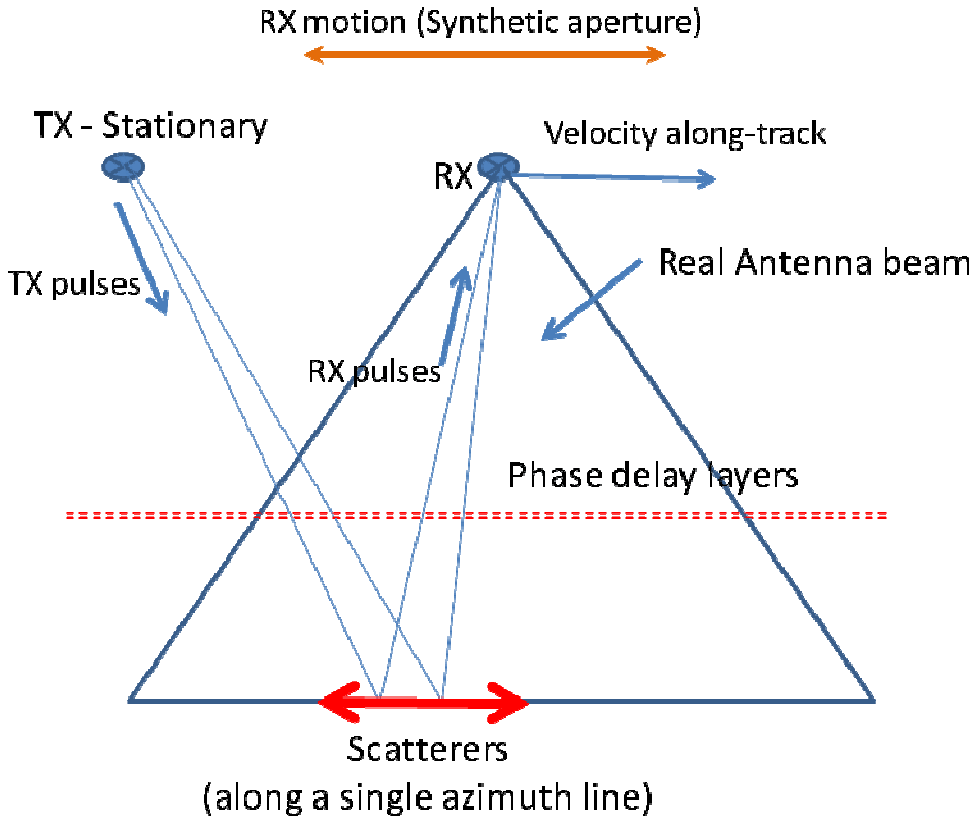

Figure 5-12. SAR raw data generation, imaging geometry.

For each pulse transmitted every (v_{sc} / PRF) seconds, the simulator performs the operations included in the following flow chart.

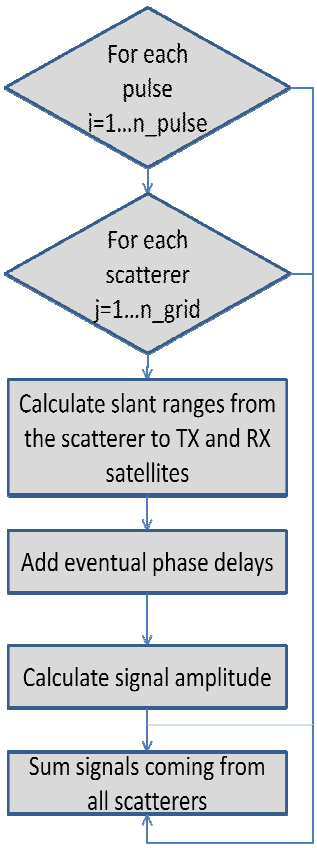

Figure 5-13. SAR raw data generation, flow chart.

The amplitude of the signal coming from each scatterer has been estimated considering a power budget. The amplitude of the received power P_R is a function of the transmitted power, the ranges from the receiver and the transmitter (R_R, R_T), the incidence angles for transmission and reception, transmitter and receiver beam gain functions (f_1, f_2) and target radar cross section σ as in Equation 5-29 (Hobbs, 2008).

$$P_R = \frac{P_T A_T}{\lambda^2 R_T^2} f_T \cos\theta_T \sigma \times \frac{A_R}{4\pi R_R^2} f_R \cos\theta_R \qquad \text{Equation 5-29}$$

In Equation 5-29,
λ is the system wavelength (m);
P_T is the transmitted power in (W);
P_R is the received power (W);
θ_T is the transmitter incidence angle;
θ_R is the receiver incidence angle;
R_R range from the receiver to the target (m);
R_T range from the transmitter to the target (m);
A_T is the transmitter antenna area (m^2);
A_R is the receiver antenna area (m^2);

σ is the radar cross section (m^2).

Radar cross section σ (Equation 5-30) has been defined taking into account the radar cross section in absolute terms σ^0 and the surface that corresponds to a single scatterer.

$$\sigma = \sigma^0 \times dxgrid \times dygrid \qquad \text{Equation 5-30}$$

The electric field strength E is proportional to the square root of the receiving power, a receiver calibration c_0 of 1 $VW^{-1/2}$ has been assumed (Hobbs, 2008).

$$E = c_0 \sqrt{P_r} \qquad \text{Equation 5-31}$$

Figure 5-14 shows the amplitude of the real part of the signal collected from a single scatterer with unit amplitude (i.e. in absolute terms) placed at abscissa y=0. The aperture length is 1068 samples. A target placed in the origin corresponds to a peak at samples 534 (i.e. 1068/2).

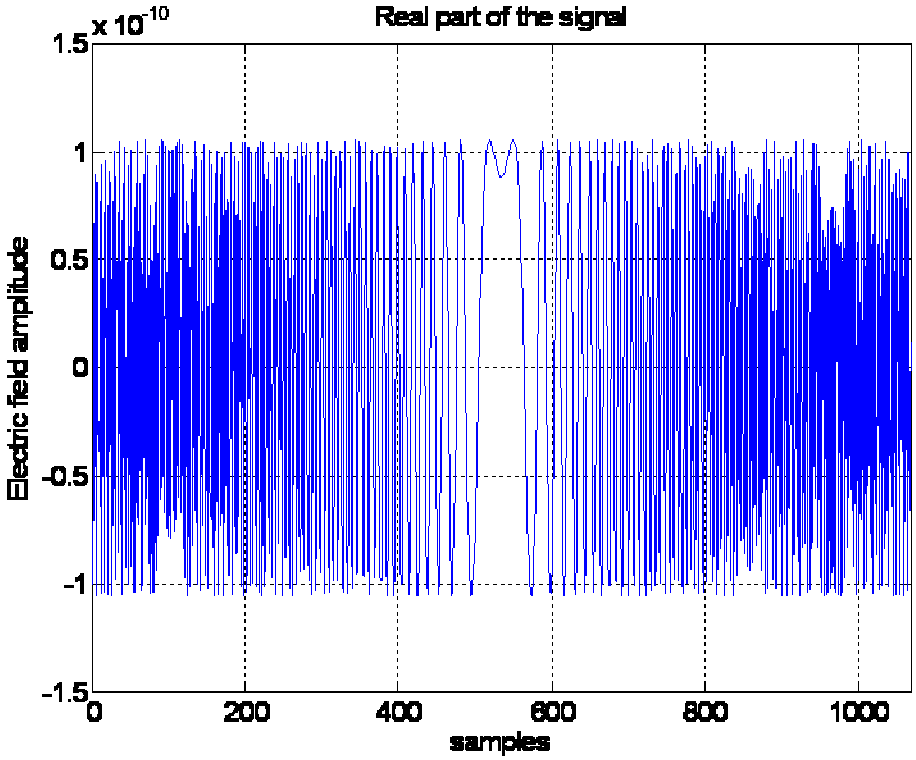

Figure 5-14. Real part of the signal corresponding to a unit amplitude backscatter target placed at abscissa y=0.

5.5.2.3 Noise generation

The different noise sources that will be added in the simulator will be described hereafter.

5.5.2.3.1 Speckle effect

To simulate speckle effect, a random phase (with uniform distribution between 0 and 2π) will be added to every pulse (both to the in-phase and to the quadrature component).

The series or random phase numbers has been obtained using the Matlab function *unifrnd*.

5.5.2.3.2 Thermal noise

The electric field due to thermal noise is given in Equation 5-32:

$$E_n = c_0\sqrt{nkTB_w} \qquad \text{Equation 5-32}$$

In Equation 5-32, n is the noise figure of the receiver (dB);
T is noise temperature of the Earth's surface (K);
k is the Boltzmann constant;
B_W is the radar bandwidth.

The electric field induced by thermal noise is given by the value presented in Equation 5-32 multiplied by a normally distributed random variable with zero mean and unit standard deviation. The random variable has been generated using the Matlab function *normrnd.*

5.5.2.3.3 Other noise sources (temporal decorrelation)

The SAR simulator will be used with two different purposes: to evaluate the effect of temporal decorrelation sources and to assess the accuracy of the models available in literature to compensate for the various noise contributions. Two different functions have been developed in Matlab.

The function *noise_model.m* has been used to model, when possible, the different noise sources that affect the system. The objective of the simulations carried out with

this approach is to understand the effects on GeoSAR focussing of potential sources of decorrelation (i.e. Earth tides, tropospheric and ionospheric noise).

The function *noise.m* has been used to simulate the effect of residual noise effects after compensation has been carried out using the available information.

5.5.2.4 Image focussing

SAR azimuth processing has been implemented in both time and Fourier domain. This allows to compare results achieved with different algorithms and to validate the code itself. The *sarsim* code (Hobbs, 2008) does not include a complete SAR processing. SAR raw data generated with the sarsim code have been imported in Matlab for validation purposes.

5.5.2.4.1 Focussing in time domain

Image focussing has been carried out in three steps:

- Correlation in time domain using the Matlab function *xcorr* that estimates the unbiased (i.e. non normalised) correlation between two vectors, the signal generated through the code *simulation.m* and the reference signal;
- Normalisation of the outcome of the correlation (i.e. divide by the number of samples involved in the correlation process).

5.5.2.4.2 Focussing in Fourier domain

Image focussing has been carried out in two steps:

- Fourier transform of the SAR raw data, $F(\omega)$;
- Fourier transform of the SAR raw data given by a unit amplitude (σ=1) at abscissa y=0, the impulse reference function $F_{ref}(\omega)$;
- Complex multiplication between $F(\omega)$ and $F_{ref}(\omega)$ as in Equation 5-33 where the operator *conj* is the complex conjugate;

$$F_{signal}(\omega) = F(\omega) \times conj\left[F_{ref}(\omega)\right] \qquad \text{Equation 5-33}$$

- Inverse Fourier transform to obtain $F_{signal}(t)$ from $F_{signal}(\omega)$.

5.5.2.5 Image normalization

The radar calibration factor (Hobbs, 2008) given in Equation 5-34 has been used to normalize the focused SAR image and get the radar cross section of the scatterers that have been inserted in the model.

$$rad\_cal = \frac{P_t A_{rx} A_{tx}}{4\pi\lambda^2 r_R^2 r_T^2} \qquad \text{Equation 5-34}$$

5.5.2.6 Distributed scatterers

The simulator is able to focus different targets with variable amplitude that are placed along an across-track line. Figure 5-15 shows a focused SAR image with scatterers with unit amplitude between abscissa y=0 m and y=156 m without the effect of speckle. The aperture length is 1068 samples. A target placed in the origin corresponds to a peak at samples 534 (i.e. 1068/2).

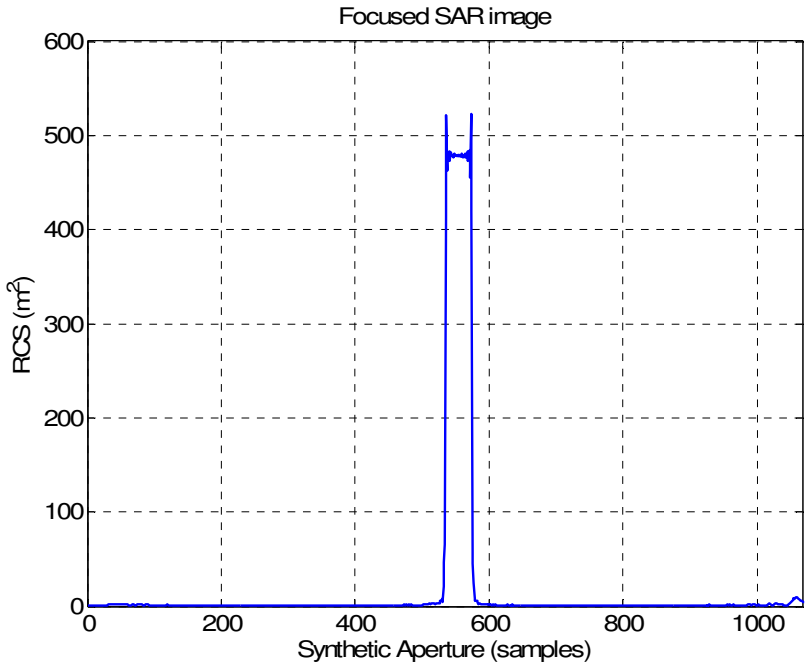

Figure 5-15. Focused SAR image with a series of unit amplitude scattered placed between abscissa y=0 and abscissa y=156 m. Speckle effect has not been introduced.

Figure 5-16 shows the focused image for the same scenario with the natural randomisation of phase added (flag *random_phase* turned on in the code). In presence of speckle effect, neighbouring targets do not in general sum up coherently; therefore, the expected amplitude peaks are lower and the background noise has a larger amplitude.

In Figure 5-15 and Figure 5-16 1300 pulses have been focused therefore the points in the synthetic aperture from zero to 232 (synthetic aperture is made up of 1068 pulses) are not focused correctly (synthetic aperture shorter than nominal). This explains the behaviour observed in presence of speckle (Figure 5-16).

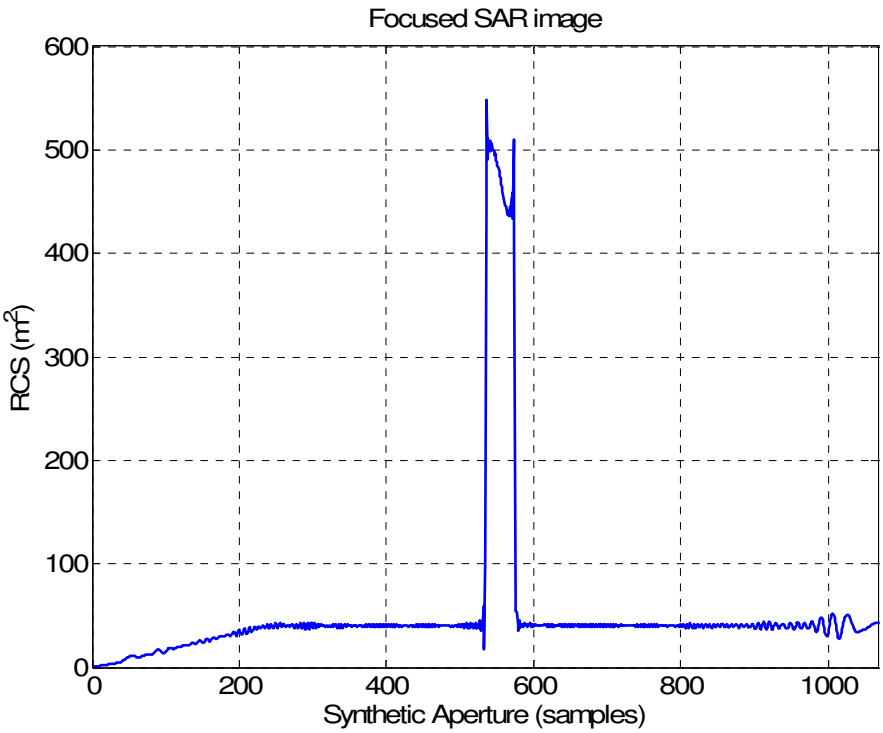

Figure 5-16. Focused SAR image with a series of unit amplitude scattered placed between abscissa y=0 and abscissa y=156 m with speckle effect.

5.5.2.7 Link budget considerations

The code has the option to include thermal noise in the system (flag *flag_ideal* turned on). This option will be used to make some considerations on the power budget and on the ground resolution of the system.

The plots that will be presented in this section have been generated assuming the following values for these relevant parameters:

- transmitter antenna size 10 m^2;
- receiver antenna size 25 m^2;
- transmitted power (EIRP) 100 kW;
- surface temperature 290 K;
- receiver noise figure 3 (absolute terms);

- system bandwidth 6 MHz.

5.5.2.8 Validation

Table 5-2 includes the list of the parameters have been used for the validation test case.

Table 5-2. Input values used in the validation test cases.

Description	Variable	Units	**Value**
System properties			
Range resolution	dx	m	**100**
Grid resolution	dy	m	**4**
Number of points in the grid	n_grid	N.A.	**201**
Number of pulses	n_pulse	N.A.	**1200**
Height of the satellites	h0	m	**$36x10^6$**
Location of the scattering grid	ygrid0	m	**-2000**
Surface noise temperature	Tsurf	K	**290**
Frequency	fc	Hz	**$1.5x10^9$**
Speckle effect	Random_phase	N.A.	**0**
Thermal noise	Flag_ideal	N.A.	**0**
Transmitter			
Transmitted power (EIRP)	Pt	W	**$100x10^5$**

Table 5-2. Input values used in the validation test cases.

Description	Variable	Units	**Value**
Transmitter velocity	vt	m/s	**0**
Transmitter position across-track	dxt	m	**$-5x10^6$**
Bandwidth of the signal	nbw	Hz	**$6x10^6$**
Transmitter antenna area	Atx	m^2	**10**
Location of the transmitter	ytx0	m	**0**
Receiver			
Receiver velocity	v_sat	m/s	**2.778**
Pulse Repetition Frequency	prf	Hz	**0.0371**
Antenna area	Arx	m^2	**25**
Receiver noise figure	n	absolute	**3**
Start of synthetic aperture	yref0	m	**$-40x10^3$**
Start of pulse reception	ypulse0	m	**$-40x10^3$**
Position across-track	dxt	m	**$5x10^6$**

The validation process includes several steps:

- The program correctly reads input parameters (visual inspection).
- The radar calibration factor agrees with the value that has been calculated with an independent Excel spreadsheet and with the output of the *sarsim* code (Hobbs, 2008).
- The peak value of the point spread function is at the correct position (sample 534 for a synthetic aperture of 1068 samples). The synthetic aperture starts at abscissa -40.000 m, therefore pulse no. 535 corresponds to an abscissa y=0 m.

- The point spread function generated with the GeoSAR simulator coincides with the one generated with the simulator *sarsim*.

The impulse response function of the system has been estimated assuming that there is a single scatterer with unit amplitude (in absolute value) at the abscissa y=0.

The impulse response function estimated with the Matlab code *simulator.m* is shown in Figure 5-17.

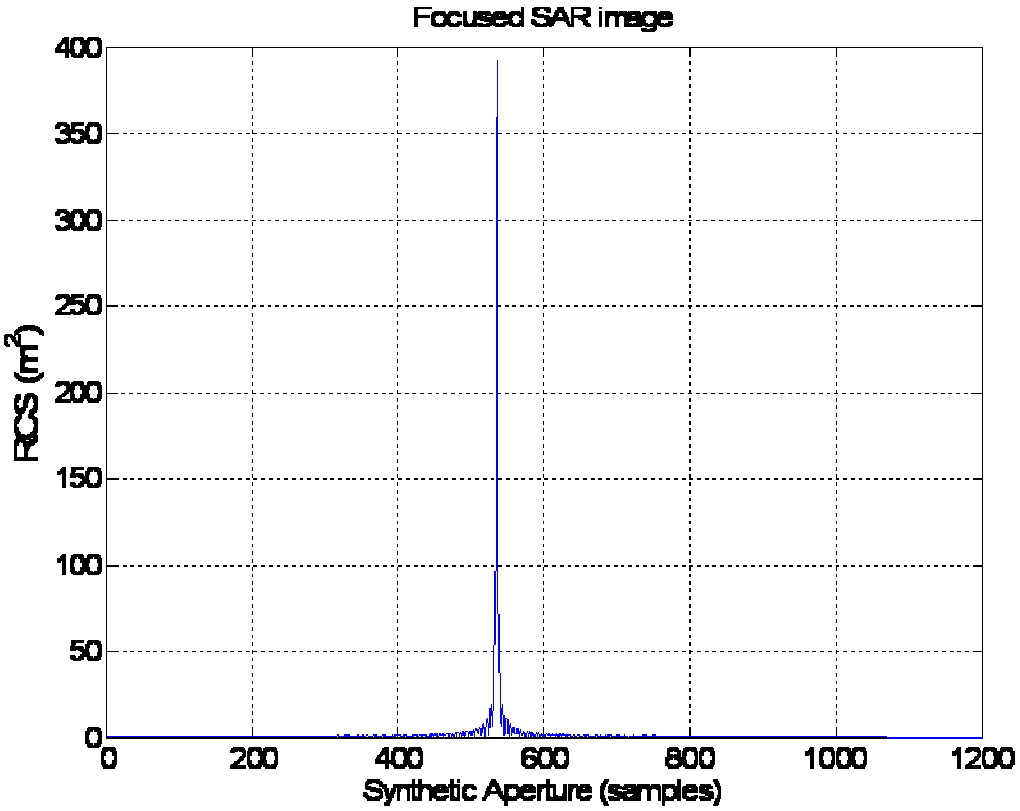

Figure 5-17. Impulse response function generated with the SAR simulator in Matlab.

The value of the peak of the radar cross section is 392.429 m^2, the initial value of σ was 400 m^2, taking into account incidence losses (0.9811), this value is correct for at least the first six figures (radar calibration factor ≈2.8501 x 10^{23}). The peak of the impulse response function is correctly located at the pulse 535 that corresponds to abscissa y=0.

The same function has been estimated using the *sarsim* function in C environment (Hobbs, 2008). Simulated SAR signal has been extracted from the output file and Fourier processing has been applied to generate the impulse response function (Figure

5-18). The value of the peak coincides with the one achieved using the Matlab code for at least the first 6 figures. The peak is located at sample 535 as in the previous case.

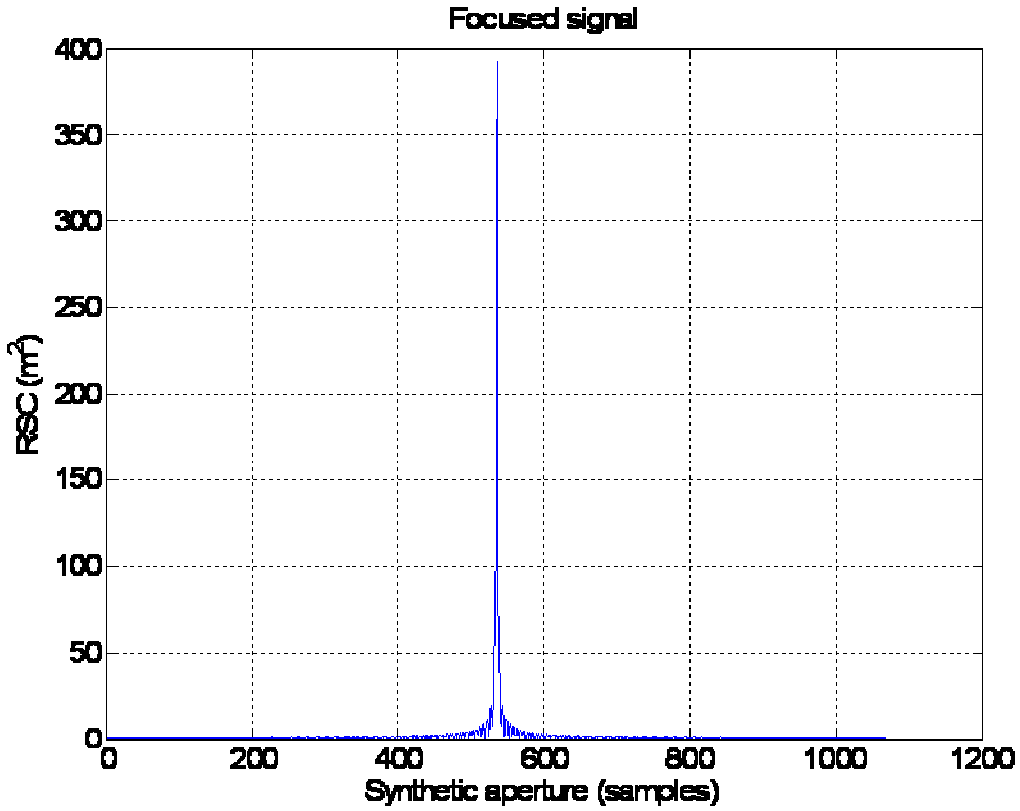

Figure 5-18. Impulse response function generated with sarsim code.

5.6 Analysis of temporal decorrelation effects - methodology

Temporal decorrelation aspects are discussed in SAR literature under the assumption that the imaged scenario, as well as the propagation medium, is frozen during the integration time. This hypothesis implies that temporal decorrelation do not hamper SAR processing. It is acceptable in conventional LEO SAR as the integration time is too short (i.e. shorter than 1 second) to allow for significant effects to take place during image formation. This assumption fails in GeoSAR due to the long integration time, therefore the sources of temporal decorrelation have to be considered as acting during image formation.

Phase disturbances acting on the system vary both in space and in time. The bi-static SAR simulator implemented in this research allows azimuth SAR focussing. Only temporal variations in phase delays that are active during the integration time will be investigated in the present research.

Phase delays obviously show spatial variations within a SAR image. GeoSAR spatial scale (with nominal azimuth ground resolution) is about 80 km in azimuth (i.e. as large as the satellite motion along-track) and 1000 km in range, therefore phenomena with similar spatial length have to be taken into account. These kinds of problems affect conventional LEO SAR as well and they have been widely studied in literature. The effect of variations within the image is usually in the form of slant range distortions or azimuth target displacement. The analysis of these geometric distortions is beyond the scope of the present research.

In SAR, the fluctuation component of the phase $\Delta\phi_b$ is twice as large as the phase in the one-way path $\Delta\phi_m$ (Equation 5-35).

$$\Delta\phi_b = 2\Delta\phi_m \qquad \text{Equation 5-35}$$

Accordingly, the variance of the phase $\sigma^2_{\phi b}$, will be four times the variance of the phase in the single-way path $\sigma^2_{\phi m}$ (Equation 5-36).

$$\sigma^2_{\phi b} = 4\sigma^2_{\phi m} \qquad \text{Equation 5-36}$$

A complete simulation of temporal decorrelation effects requires a SAR simulator that is able to focus both in range and in azimuth. This requires a significant computational effort and it is an area of further research.

It has to be said that this simplification does not affect the scope of the present research, as slant range variations are smaller than 1 pixel.

To investigate their effect on GeoSAR, all noise sources have been traced back to phase noise that affects the system during the integration time. This section presents the two different methodologies that have been used in the present research: the analytical approach and the phase screen approach.

5.6.1 Clutter rejection analytical derivation

An analytical derivation of the amount of clutter that enters the main lobe of the synthetic antenna has been carried out in order to estimate the effect of phase noise. Generic noise sources have been modelled as a first-order Gauss-Markov process with given temporal correlation. The output of the calculation is the fraction of clutter generated by phase fluctuations that enters the main lobe of the antenna.

This analytical derivation allows understanding the parameters that play a significant role in temporal decorrelation and allows making some comments on the peculiarities of GeoSAR with respect to conventional LEO systems.

5.6.2 Phase screen approach

Greene and Moller (1961) and Gray *et al.* (2000) suggest a quite simple way to simulate the effects of heterogeneities that cause temporal decorrelation and to evaluate the effects of signal fluctuations that happen during the integration time. The aim is to simulate these effects as a phase screen that has to be placed above the background scenario being imaged.

The azimuth SAR processor that has been developed during the research with the methodology described in the previous sections has been used to compare results with and without the phase screen.

The aim of this research is to assess the degradation in the GeoSAR's azimuth Point Spread Function (PSF) caused by these perturbations.

5.7 Temporal decorrelation sources

In this section, some considerations about the three major phase noise sources have been included. The focus is on the assumptions made for every perturbation that has been taken into account.

5.7.1 Earth tides

Four major contributions to site displacements that refer to the Earth tide phenomenon have been identified:

- solid Earth tide;
- ocean loading displacement;
- pole tide;
- atmospheric loading.

As mentioned in the background chapter (section 2.10 , displacements introduced by Earth tides vary smoothly therefore the spatial distribution of phase delays within a single image could be neglected (Milbert, 2002). Only temporal variations for a single scatterer have to be taken into account.

Solid Earth tide is the major contributor to site displacement as its period is about 12 hours and its amplitude is comparable with the wavelength of the radar signal. Analytical models currently available (McCarthy and Petit, 2004) allow determining the displacement with an accuracy of about 1 mm.

Ocean loading vertical displacement is much less significant (few centimetres) and it could be modelled with an accuracy that is about +/- 3 mm (McCarthy, 1992) given an ocean tidal motion table. Its contribution therefore cannot be neglected in this analysis.

Pole tide, the contribution due to Earth rotation, has a period close to 12 months. Its contribution in the time scale of a GeoSAR image is negligible.

Atmospheric loading could be neglected, as it requires variations of about 20 hPa to be significant (McCarthy and Petit, 2004). Such variations are quite unusual at GeoSAR spatial and temporal scales.

In conclusion, only the effects of solid Earth and ocean loading tides have to be taken into account when considering temporal decorrelation. Simulations have been carried out with the phase screen approach super-posing to the imaged scene a phase layer that introduces the residual uncertainty of the models (i.e. the residual phase delay due to uncompensated Earth tidal noise). Although the residual phase is spatially and temporally correlated, it has been modelled as a white Gaussian variable with zero mean and standard deviation equal to the 1 σ accuracy of the model. Neglecting noise correlation is a conservative assumption.

The effect of Earth tides on GeoSAR focussing becomes nearly negligible after proper phase delay compensation; a more accurate modelling is not required.

5.7.2 Tropospheric effects

Three main contributions related to tropospheric delay can be identified:

- dry delay;
- wet delay;
- liquid delay.

As presented in the background chapter, some published models in literature allow predicting tropospheric delay with known accuracy (section 2.11.2).

5.7.2.1 Tropospheric spatial and temporal decorrelation

GeoSAR ground resolution is about two orders of magnitude larger than a conventional LEO SAR satellite. The analytical models (presented in the literature review) that are applied to predict tropospheric delays, show an accurate behaviour in large scale tropospheric delay estimation but, on the other hand, fail in presence of very small scale perturbations. GeoSAR's ground resolution clearly low-pass filters small-scale perturbations therefore the accuracy of tropospheric models is sufficient to compensate for tropospheric phase delay.

5.7.2.2 Tropospheric phase delay modelling

Tropospheric phase delay temporal and spatial correlations derive from the smooth variation of all meteorological parameters.

In the present research, tropospheric phase delay will be modelled and subtracted from the SAR collected signal prior to SAR focussing. After this preliminary step, GeoSAR is affected by a residual phase delay that could be modelled as a white Gaussian stochastical variable with zero mean and standard deviation equal to the 1σ accuracy of the tropospheric model. This is a conservative assumption with respect to considering the effects of temporal and spatial correlations. A more accurate modelling is not required due to the good accuracy of the models that are currently available.

The effects of tropospheric variations have been investigated using the phase screen approach (Greene and Moller, 1961). Following this methodology, residual tropospheric phase delay has been introduced in the model as a phase screen over the SAR image that varies during the integration time following a white Gaussian distribution.

5.7.3 Ionospheric effects

Quegan and Lamont (1986) provide a very clear description of the effects of ionospheric path delay variations within a SAR image. "*Irregularities in the propagation medium can cause fluctuations in the phase, amplitude and polarisation vector of a signal. These errors can be split into two terms, the first a mean value across the synthetic aperture, and the second a fluctuating component. The mean amplitude and polarisation errors cause an overall power loss in the synthetic aperture gain pattern, whilst the fluctuating components may cause severe distortions, leading to degradations in many aspects of the image quality.*"

The analysis carried out in the present research is focused on the distortions caused by fluctuating components of the ionosphere.

Many papers in literature (Quegan and Lamont, 1986; Ishimaru *et al.* 1999; Mattar and Gray, 2002; Xu *et al.* 2004; Meyer *et al.*, 2006; Lejeune and Warnant, 2008) provide insights into the effect of TEC variations on SAR images. Their analysis is limited to conventional LEO satellites therefore ionospheric temporal variation during image formation is not taken into account as the integration time is very short (i.e. about 1 second). Ionospheric spatial variations affect image formation well; the image is focused collecting signal coming from the same resolution cell but piercing different zones of the ionospheric layer.

Ionospheric delays can vary with high temporal and spatial frequency. A preliminary review about ionospheric temporal and spatial correlation is required to assess the assumptions that will be made when simulating ionospheric effects on the GeoSAR system.

The accuracy of TEC measurements currently available is usually about 1-2 TECU, about one order of magnitude larger than the accuracy required in TEC measurements for coherent GeoSAR azimuth processing (as it will be discussed in Chapter 6). This implies that it is not possible to calculate accurate statistics of TEC distributions and therefore it is not possible to simulate, starting from real measurements, the effects of ionosphere on GeoSAR focusing.

5.7.3.1 Ionospheric spatial correlation

Quegan and Lamont (1986) report two different stochastical models that describe spatial fluctuations of ionospheric phase delay. They provide an autocorrelation function that can be used to investigate ionospheric effect on a given SAR system.

GeoSAR has a synthetic aperture of about 80 km with respect to a ground target and flies at an altitude of about 36000 km. Assuming that the ionosphere is a thin layer at an altitude of about 400 km, signals coming from a scatterer during the whole integration time pierce the ionosphere along a line that is about 6 km long.

Table 5-3 provides the comparison between the numbers involved in GeoSAR and the figures obtained for conventional monostatic LEO SAR (L and C band).

Table 5-3. Synthetic apertures projected on an ionospheric layer (400 km altitude) for different SAR systems (antenna length 10 m for LEO satellites) (modified from Quegan and Lamont, 1986).

	Altitude	Wavelength	Synthetic aperture	Synthetic Aperture at the ionospheric altitude
GeoSAR L band	≈35000 km	0.20 m	80 km	6 km
C band LEO	800 km	0.05 m	4 km	2 km
L band LEO	800 km	0.20 m	16 km	8 km

The autocorrelation function presented by Quegan and Lamont (1986) for severe ionospheric disturbances has a correlation length of about 2 km. The projection of the synthetic aperture on the ionospheric layer (assumed a thin layer at 400 km altitude) is about 6 km long for GeoSAR. Quegan and Lamont (1986) state that, in these circumstances, a system is likely to suffer substantial phase delays during the integration time.

Ishimaru *et al.* (1999) presents an analysis with numerical examples of ionospheric effects. Figure 5-19 is relevant to the present research as it shows the coherent integration length at 400 km versus frequency for different TEC values and different levels of TEC variance. The figure confirms the results provided by Quegan and Lamont (1986), under the assumption of a frozen ionosphere, ionospheric spatial variations within the synthetic aperture cause correlated phase delays.

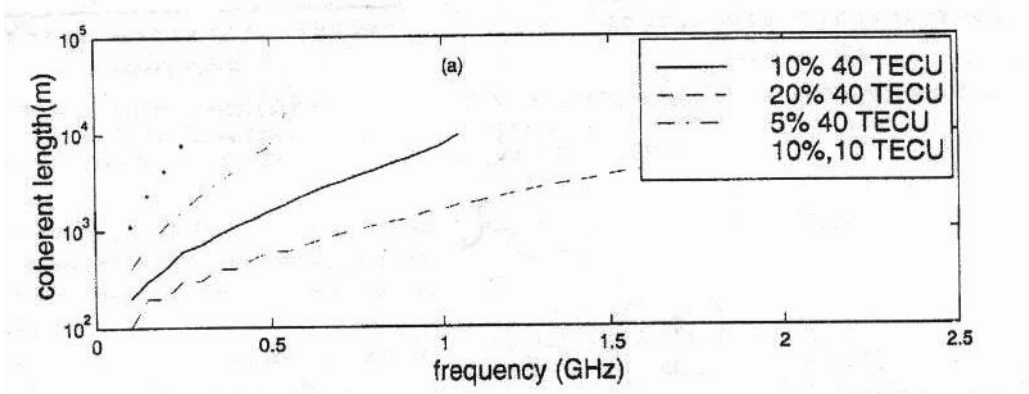

Figure 5-19. Coherent length versus frequency for different TEC at an altitude of 400 km (Ishimaru *et al.*, 1999).

More recent work by Xu *et al.* (2008) provide a plot of the correlation distance for SAR signal at an altitude of 600 km, channel bandwidth 10 MHz, with a TEC variance of 10% of the mean value. The values are consistent with those already presented.

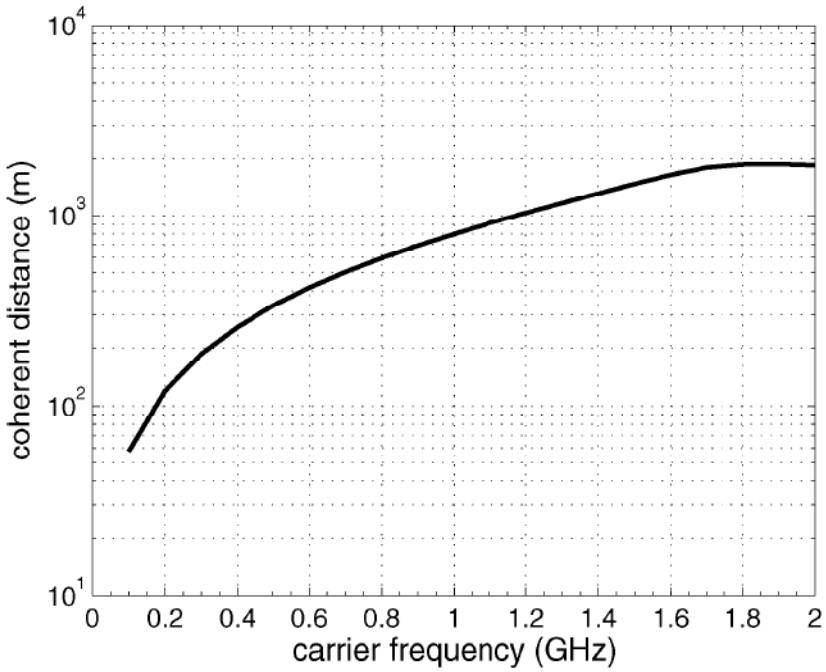

Figure 5-20. Ionospheric effects on the azimuthal coherence distance of SAR signal, TEC variance 10 % of the mean value.(Xu *et al.*, 2008)

5.7.3.2 Ionospheric temporal correlation

El Gizawy (2003) in his work on ionosphere monitoring using GPS measurements analysed a set of ionospheric time series (1 hour long, 30 seconds sampling) in order to look into ionospheric correlation time and distances.

This piece of work is valuable to the present analysis as it presents results relative to different ionospheric states. Ionospheric activity has been classified in three classes:

- high ionospheric activity (geomagnetic index K >7) (see section 2.12.4.4);
- medium ionospheric activity (geomagnetic index 3 < K < 6);
- low ionospheric activity (geomagnetic index K<3).

As presented in Figure 5-21 during quiet ionosphere, TEC variation is extremely smooth and its derivative is nearly zero. On the contrary, during high ionospheric activity levels, TEC variations in the short period can be significant and cannot be neglected.

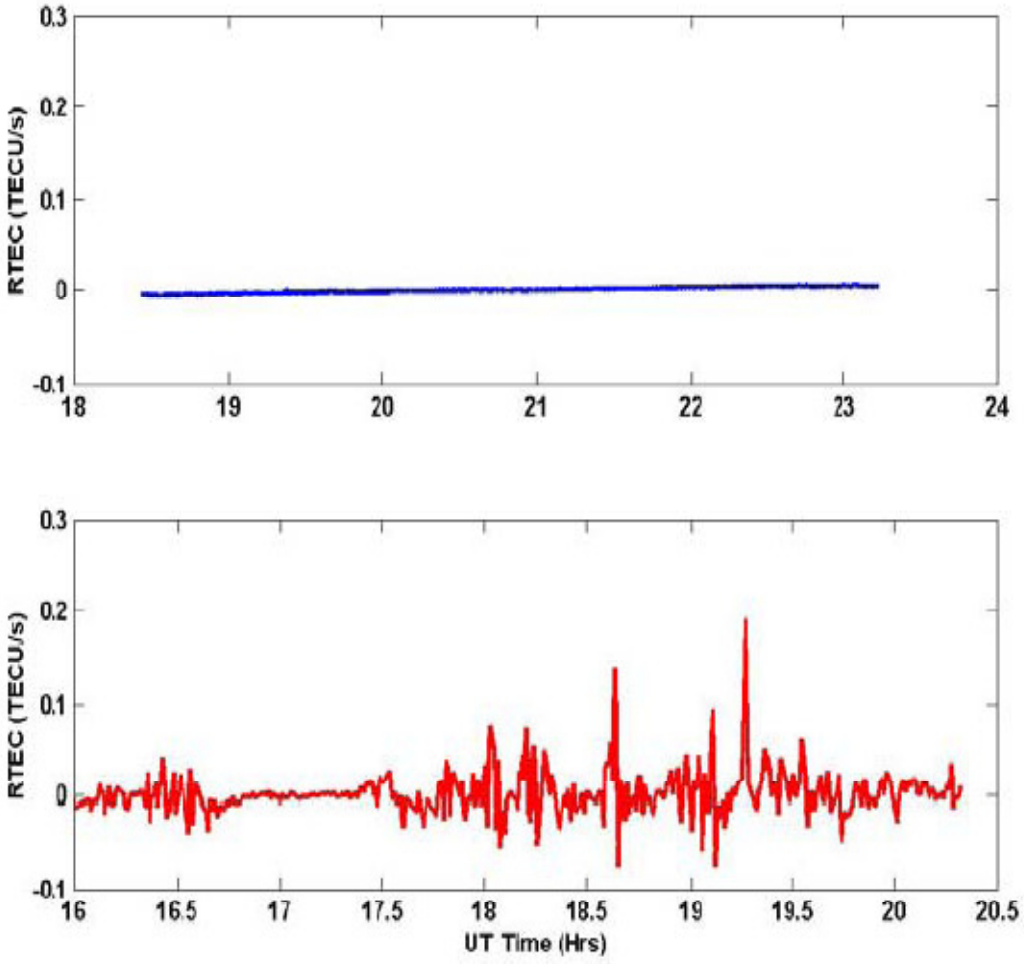

Figure 5-21. Derivative of TEC time series for PRN 17 during quiet ionosphere on day 154 of the year 2000 (upper panel), and high ionospheric activity on day 197 of the year 2000 (lower panel) at Yellowknife, northwest Territories (El Gizawy, 2003).

Analysing a large number of 1-hour time series, correlation time goes from about 300 seconds (high latitude and strong ionospheric activity) to 800 seconds in a quiet ionosphere (El Gizawy, 2003). It has to be said that results suffer from the limited duration of the series taken into account.

Spectre dataset (Crespon *et al.*, 2007) provide TEC measurements with a very good temporal sampling, i.e. 30 seconds. Although the limited accuracy of the dataset dows not allow to estimate TEC statistics, Fourier analysis can be applied to evaluate its power spectrum. The aim of this analysis is to evaluate quantitatively the amount of information that is actually lost using a different dataset with a longer sampling interval. The same approach has been used in this research to assess the effect of temporal sampling on soil moisture measurements.

The power spectral density of ionospheric phase delay has been integrated with respect to frequency to evaluate the distribution of integral signal power. A measurement system with 1-hour sampling interval (frequency 1 cycle/hour) is able to collect more than 90% of the information content of the signal while this value decreases rapidly for longer sampling intervals.

Figure 5-22 presents the normalised integral of ionospheric VTEC power spectral density. Plotted data refer to 24 December 2004. The power spectral density fluctuates, depending from location over Europe (i.e. latitude and longitude), within the two lines in the figure.

Figure 5-23 presents the autocorrelation function for VTEC time series collected over Europe on 24 December 2004. Depending from location, there is a difference in the correlation length of about 400 samples.

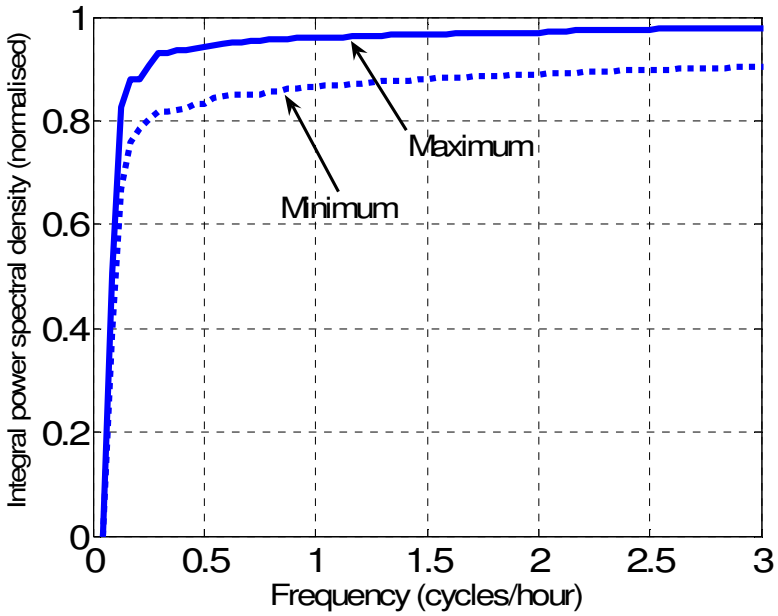

Figure 5-22. Normalised integral of the ionospheric VTEC power spectral density. Ionospheric TEC data from spectre database relative to 24 December 2004. Depending from latitude/longitude the curve is within the boundaries given by the solid and the dotted lines.

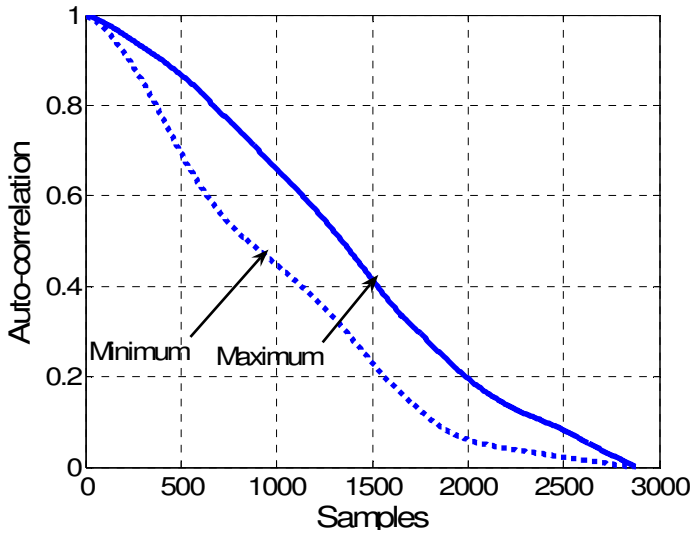

Figure 5-23. Autocorrelation function of the ionospheric VTEC. Data from *spectre* database relative to 24 December 2004. Depending from latitude/longitude the curve is within the boundaries given by the solid and the dotted lines.

Results are clearly influenced by the temporal sampling of the dataset available that filters out all high frequency components generated by ionospheric noise.

5.7.3.3 Ionospheric noise modelling

Literature currently available does not investigate the effect of ionospheric heterogeneities on SAR image focussing as current SAR systems have been designed with a very short integration time (i.e. about 1 second) and this implies that ionospheric temporal fluctuations can be neglected.

Considering GeoSAR integration time and synthetic aperture length, ionosphere is not likely to be coherent for the whole integration time and synthetic aperture length is expected to be longer than ionospheric correlation distance. Therefore, significant ionospheric effects are expected.

Ionospheric spatial variations affect the azimuth PSF as different pulses that contribute to synthesize the synthetic aperture pierce the ionospheric layer at different locations. The azimuth SAR processor that has been developed in the present research does not allow taking into account this process. However, this simplification is acceptable as GeoSAR synthetic aperture length is shorter than the ionospheric correlation distance therefore decorrelation induced by ionospheric spatial heterogeneities is a second order effect with respect to temporal variations.

GeoSAR peculiarities require an accurate assessment of the coherent integration loss that is caused by ionospheric temporal variations. Ionospheric phase delays show strong variability and models currently available do not allow for a precise modelling and compensation. This implies that residual variations have to be modelled taking into account temporal correlation without further simplifications. A first-order Gauss Markov process with given correlation time has been used for the purpose in the phase screen approach.

5.8 Conclusions

The present chapter analyses the methodology proposed to investigate temporal decorrelation effects that hamper GeoSAR's images.

An approach to model the backscatter of a fluctuating target has been presented following the dissertation of Seynat (2000) and Hobbs (1997).

An azimuth SAR simulator has been implemented in order to assess the effect of various sources of temporal decorrelation. Two main issues have been addressed: the amount of clutter that the long integration time allows to reject, and the effect of phase delays (Earth tides, tropospheric and ionospheric delays) that are modelled with a phase screen approach.

Earth tides, tropospheric and ionospheric effects have been addressed separately. The models used to simulate their phase delay contribution have been described, justifying the assumptions made.

Earth tides and tropospheric residual phase delay after phase compensation have been modelled as white Gaussian noise. This assumption does not take into account temporal correlation, however their influence can be compensated with proper noise modelling therefore this conservative assumption is acceptable.

Ionospheric phase delay has a significant influence on GeoSAR imaging. The models available do not allow an accurate compensation therefore, in this case, temporal decorrelation might not be neglected. Residual noise has been modelled as a first order Gauss-Markov process.

6 Presentation of results

In the chapter about methodology, the algorithm used to perform slow-time processing of GeoSAR data has been described. The discussion about temporal decorrelation showed that there are two main issues related to the long integration time: GeoSAR's capability to reject clutter induced by fluctuating targets and the effect of perturbations on GeoSAR's azimuth PSF.

In this chapter, the outputs of the simulations carried out will be presented and some preliminary conclusions will be drawn.

Section 6.1 introduces an analytical derivation to look into GeoSAR's capability to reject clutter. Sections 6.2, 6.3 and 6.4 deals respectively with Earth tides, tropospheric and ionospheric propagation. Section 6.5 draws some preliminary conclusions.

6.1 Analytical approach – effect of phase noise

GeoSAR's integration time allows the system to reject clutter induced by unstable scatterers or by heterogeneities in the propagation medium. This aspect can be modelled analytically. Any disturbance such as the motion of the scatterer along the line of sight or the variation of the phase delay due to heterogeneities in the propagation medium is modelled as a first order Gauss-Markov process with a given correlation function.

This approach has been worked out following some suggestions included in a personal communication from Prof. Rocca (Politecnico di Milano, Italy).

Considering a scatterer at a position y=0 on the ground, any phase disturbance is equivalent to a target displacement $d(t)$. Under the assumption that the displacement happen along the bisector of the bi-static angle the variation in bi-static slant range is $2x(t)$ (neglecting the angle $\delta\theta$) as shown in Figure 6-1. This hypothesis allows simplifying the math of the problem without losing generality.

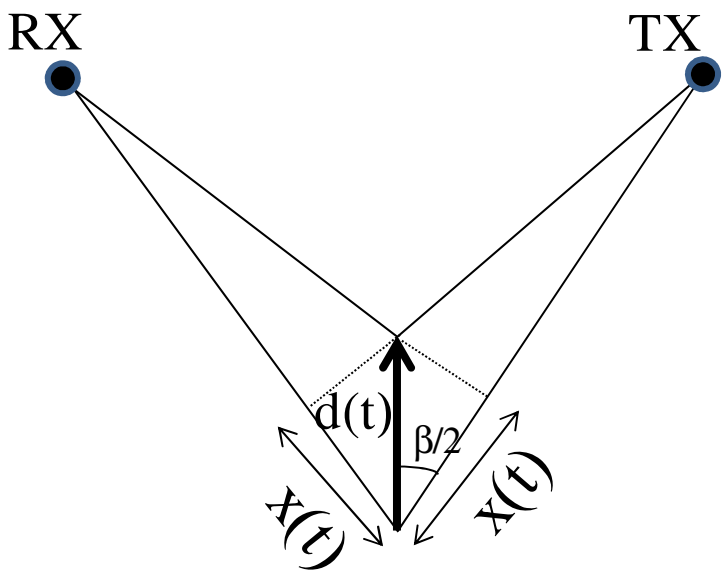

Figure 6-1.Bi-static slant range variation caused by a target displacement along the bi-sector of the bi-static angle β.

Fluctuations in the bi-static slant range are modelled as a stochastical variable with a correlation function $\rho_x(\tau)$ (Equation 6-1).

$$\rho_x(\tau) = \sigma_x^2 e^{-\frac{|\tau|}{\tau_0}} \qquad \text{Equation 6-1}$$

In Equation 6-1, σ_x^2 is the noise variance of the function *x(t)*;
τ_0 is the correlation time.

Variations in the bi-static slant range *x(t)* are equivalent to variations in the bi-static phase collected by the receiver antenna ϕ_b(t) (Equation 6-2). This implies that both variations induced by unstable scatterers and by heterogeneities in the propagation medium are tackled through the same analytical approach.

$$\phi_b(t) = \frac{2\pi}{\lambda}\left[2x(t)\right] \qquad \text{Equation 6-2}$$

In Equation 6-2, ϕ_b is the bi-static phase.

Equation 6-3 gives the SAR echo coming from the considered scatterer:

$$r(t) = Ae^{j\frac{4\pi}{\lambda}x(t)} = Ae^{j\phi_b(t)} \qquad \text{Equation 6-3}$$

Assuming that the transmitter is stationary, the bi-static slant range varies only due to the velocity of the receiver and the along-track coordinate of the scatterer. The receiver flies along its path with a velocity *v* parallel to the y-axis.

In Figure 6-2, β is the bi-static angle;
h is the altitude of the satellites, both transmitter and receiver;
the TX is at coordinates (0,-B, h) in the reference system ξ, η, ζ at time t=0;
the RX is at coordinates (0,B, h) in the reference system ξ, η, ζ at time t=0;
v is the receiver's velocity vector;
R_R is the RX slant range at time t=0;
R_T is the TX slant range at time t=0.

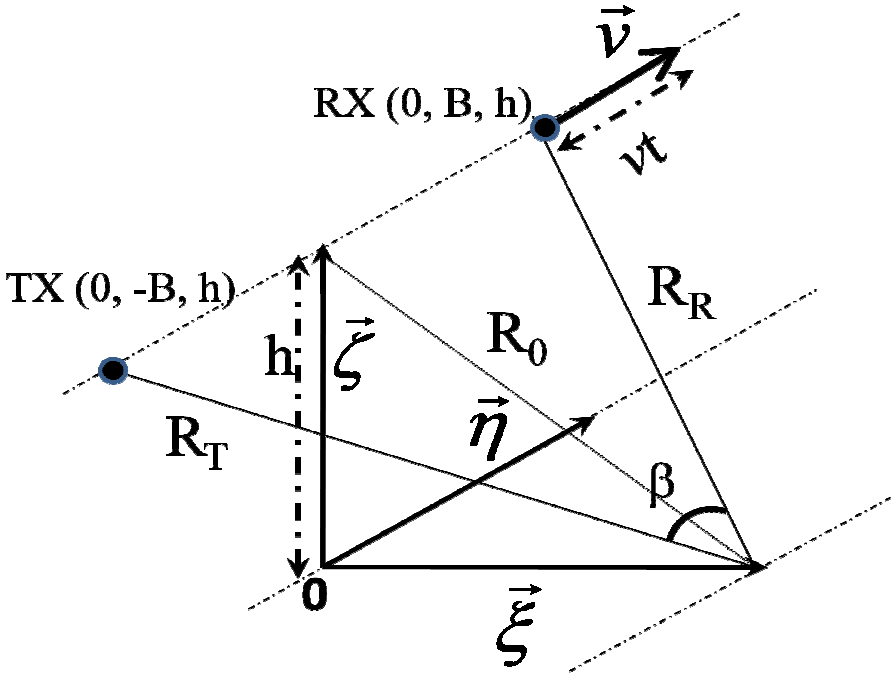

Figure 6-2. Geometry used for bi-static slant range calculation.

The bi-static slant range (varying with time and with the position *y* of the scatterer along-track) is given in Equation 6-4. This function does not include target displacement *x(t)* that will be included in the calculations afterwards.

$$D(t,y)=\sqrt{R_0^2+(B+y)^2}+\sqrt{R_0^2+(B+vt-y)^2} \qquad \text{Equation 6-4}$$

In Equation 6-4, *y* is the position of the scatterer along-track.

Expanding in a Taylor series the function *D(t,y)* and neglecting terms with higher order:

$$\Delta(t,y)=D(t,y)-D(t,0)=\left.\frac{\partial D(t,y)}{\partial y}\right|_{y=0} y \qquad \text{Equation 6-5}$$

$$\frac{\partial D(t,y)}{\partial y}=\frac{2y+2B}{2\sqrt{R_0^2+(B+y)^2}}+\frac{2y-2B-2vt}{2\sqrt{R_0^2+(B+vt-y)^2}} \qquad \text{Equation 6-6}$$

$$\left.\frac{\partial D(t,y)}{\partial y}\right|_{y=0} y=\frac{By}{\sqrt{R_0^2+B^2}}+\frac{-By-vty}{\sqrt{R_0^2+(B+vt)^2}} \qquad \text{Equation 6-7}$$

$$\left.\frac{\partial D(t,y)}{\partial y}\right|_{y=0} y=\frac{By}{R_R}+\frac{-By-vty}{\sqrt{R_0^2+(B+vt)^2}} \qquad \text{Equation 6-8}$$

$$\left.\frac{\partial D(t,y)}{\partial y}\right|_{y=0} y\approx \sin\tfrac{\beta}{2}\, y+\frac{-R_R\sin\frac{\beta}{2}\, y-vty}{R_R\sqrt{1+\frac{v^2t^2}{R_R^2}+\frac{2vtB}{R_R^2}}} \qquad \text{Equation 6-9}$$

Typical values for GeoSAR geometry are R_R=40000 km, *vt*<40km (half the synthetic aperture). This allows to assume that $v^2t^2/R_R^2<<1$:

$$D(t,y)-D(t,0)=y\sin\tfrac{\beta}{2}-\frac{By+vty}{R_R\sqrt{1+\frac{v^2t^2}{R_R^2}+\frac{2Bvt}{R_R^2}}}\approx-\frac{vty}{R_R}\cos^2\frac{\beta}{2} \qquad \text{Equation 6-10}$$

The image focused at abscissa *y*, neglecting target displacement, is given in the following equation. The contribution due to target displacement *x(t)* is given by the function *r(t).*

$$r(t)=Ae^{j\frac{4\pi}{\lambda}x(t)} \qquad \text{Equation 6-11}$$

$$w(y) = \int_{-T/2}^{T/2} r(t) e^{jk\Delta(t,y)} dt \qquad \text{Equation 6-12}$$

$$k = \frac{2\pi}{\lambda};\ k' = k\frac{y}{R_R}\cos^2\left(\frac{\beta}{2}\right) \qquad \text{Equation 6-13}$$

$$jk\Delta(t,y) = jk'vt \qquad \text{Equation 6-14}$$

Within the mentioned assumptions, considering the SAR echo coming from the scatterer in Equation 6-3 and following subsequent equations, the mean square value of the image focused is given in the following equations:

$$q = E\left[w(y)w^*(y)\right] = E\left(\int_{t_1=-T/2}^{T/2} r(t_1) e^{jk\Delta(t_1,y)} dt_1 \int_{t_2=-T/2}^{T/2} r(t_2) e^{jk\Delta(t_2,y)} dt_2\right) \qquad \text{Equation 6-15}$$

$$q = A^2 E\left(\int_{t_1=-T/2}^{T/2}\int_{t_2=-T/2}^{T/2} e^{j2k(x(t_1)-x(t_2))}\, e^{jk'vt_1}\, e^{-jk'vt_2}\, dt_1\, dt_2\right) \qquad \text{Equation 6-16}$$

$$q = A^2 \int_{t_1=-T/2}^{T/2}\int_{t_2=-T/2}^{T/2} E\left[e^{j2k[x(t_1)-x(t_1+\tau)]}\right] e^{-jk'vt_1}\, dt_1\, d\tau \qquad \text{Equation 6-17}$$

In previous equations, T is the integration time;
$x(t)$ is the target displacement.

The expected value depends only on τ and not on the time t_1. Equation 6-18 has been derived by Richards (2003) considering a random signal ϕ_n.

$$E\left(e^{j\phi_n}\right) = e^{-\sigma_\phi^2/2} \qquad \text{Equation 6-18}$$

The variance of the target motion is given in Equation 6-19.

$$\sigma_{\Delta x}^2 = \sigma_x^2 + \sigma_x^2 - 2\rho_x \qquad \text{Equation 6-19}$$

Taking into account Equation 6-1, the induced phase error and its variance are given in Equation 6-20 and Equation 6-21.

$$\delta\phi = 2k\delta\Delta x = \frac{4\pi}{\lambda}\left[x(t+\tau) - x(t)\right] \qquad \text{Equation 6-20}$$

$$\sigma_\phi^2 = (2k)^2 \sigma_{\Delta x}^2 = (2k)^2 2\sigma_x^2 \left(1 - e^{-\frac{|\tau|}{\tau_0}}\right) \approx \frac{8k^2\sigma_x^2|\tau|}{\tau_0}$$ Equation 6-21

The integral in Equation 6-17 is expressed as:

$$q = A^2 \int_{t_1=-T/2}^{T/2} \int_{\tau=-T/2-t_1}^{T/2-t_1} e^{-\sigma_\phi^2/2}\, e^{-jk'v\tau}\, d\tau\, dt_1$$ Equation 6-22

$$q = A^2 \int_{t_1=-T/2}^{T/2} \int_{\tau=-T/2-t_1}^{T/2-t_1} e^{-4k^2\sigma_x^2|\tau|/\tau_0}\, e^{-jk'v\tau}\, d\tau\, dt_1$$ Equation 6-23

It is solved using the standard integral and the assumptions in the following equations.

$$I = \int_{-\infty}^{+\infty} e^{-|a|t} e^{jbt} dt = \frac{2a}{a^2 + b^2}$$ Equation 6-24

$$a = \frac{4k^2\sigma_x^2}{\tau_0}$$ Equation 6-25

$$b = -k'v = -\frac{kyv\cos^2\left(\beta/2\right)}{R_R} = \frac{\tau_0}{2k^2\sigma_x^2} \frac{1}{1 + \left(y/y_0\right)^2}$$ Equation 6-26

$$y_0 = \frac{8\pi\sigma_x^2 R_R}{\lambda v \tau_0 \cos^2\left(\beta/2\right)}$$ Equation 6-27

Therefore, the mean square value of the image focused is given in Equation 6-28:

$$q = \frac{A^2 T \tau_0}{2k^2\sigma_x^2} \frac{1}{1 + \left(y/y_0\right)^2}$$ Equation 6-28

The entire energy of the reflection is spread over a space interval with approximate diameter $2y_0$ (Equation 6-27).

The backscatter from a moving target could be considered as noise with respect to the signal collected from stable scatterers.

The key point is that $2y_0$, (the approximate diameter of the reflection spread, i.e. the zone where the energy reflected by the scatterer is spread), could be much larger than

the pixel size therefore noise is filtered out by the system during SAR processing as it does not enter the main lobe of the synthetic antenna. This is understandable since the Doppler frequency range is extended by the frequency modulation effect due to the scatterer's motion.

Therefore, Equation 6-28 is used to understand the effects of temporal correlated noise on GeoSAR focussing.

Whenever y_0 is wider than the antenna footprint, only clutter noise inside the antenna footprint has to be considered.

In a bi-static SAR azimuth resolution (Willis, 1991) is expressed as:

$$\Delta R_{az} = \frac{\lambda R}{v_{sc}} \frac{1}{T_{obs} \cos \beta/2} = \frac{\lambda R}{L_A} \frac{1}{\cos \beta/2} \qquad \text{Equation 6-29}$$

The fraction of clutter that affects a pixel is proportional to the factor p given in Equation 6-30.

$$p = \frac{y_0}{\Delta R_{az}} = \frac{L_A}{v\tau_0 \cos \beta/2} \frac{\sigma_\phi^2}{2\pi} \qquad \text{Equation 6-30}$$

Equation 6-30 shows that the fraction of clutter is proportional to phase noise variance σ_ϕ^2 and to the ratio between the length of the synthetic aperture L_A and the actual integration aperture $v\tau_0$.

6.1.1 Comparison with LEO SAR

The long integration time is the main peculiarity of the GeoSAR configuration. A typical LEO orbit such as ERS 1/2 or ENVISAT has an integration time of less than one second.

For a LEO SAR, considering Equation 6-30, there are only a few targets that are unstable during such a short time lapse therefore the clutter induced by fluctuating targets such as canopies is well inside the synthetic antenna main lobe.

GeoSAR is virtually able to filter out target that shows a short correlation time, as an example it can image the soil filtering out the canopies. This is a clear advantage for many applications such as SAR interferometry or soil moisture monitoring.

6.2 Earth tides

Earth tides affect both the position of a target on the Earth's surface and the orbit determination accuracy of orbiting satellites. In the following sections, both the issues have been tackled.

The models described in section 2.10 provide in output a local displacement that is referred to a local topocentric reference frame north, east, Up. SAR systems are sensible to slant range variations therefore a coordinate transformation (Maral and Bousquet, 1998; Bate *et al.*, 1971) would be required to obtain the projection of the displacement on the relevant direction.

The aim of this research is to evaluate the overall effect induced by Earth tides; hence the analysis has been carried out under the worst case assumption that the absolute value of the displacement is converted in bi-static phase delay without considering its spatial orientation (Equation 6-31). This corresponds to the hypothesis that the displacement induced by Earth tides is directed towards the bisector of the bi-static angle.

$$\phi = \frac{4\pi}{\lambda} x \qquad \text{Equation 6-31}$$

In Equation 6-31, ϕ is the resultant bi-static SAR phase;
x is the displacement induced by Earth tides.

6.2.1 Earth tide effects on orbit determination accuracy

IERS recommendations are currently taken into account in every accurate spacecraft orbit determination algorithm. Kudryatsev (2002) describes an analytical procedure to estimate the accuracy of a satellite in a MEO orbit (similar to GLONASS). Applying the prescriptions included in McCarthy (1996), an accuracy of about 1-2 cm was demonstrated. Sharoo and Visser (1998), in their discussion about ERS precise orbit determination procedure, included IERS recommendations as well.

The effects of Earth tides are usually taken into account in common procedures to determine the orbit of a spacecraft. Therefore, Earth tides' effects on orbit determination accuracy could be neglected.

6.2.2 Solid Earth tide effects - simulations

According, to McCarthy and Petit (2004), solid Earth tidal displacements could be modelled with accuracy better than 1 millimetre.

Milbert (2002) provides a FORTRAN compiled code that implements the models described in IERS Technical Note n°32. The output for a given location is presented in Appendix D.

Figure 6-3 presents the absolute value of the displacement induced by solid Earth tidal motion.

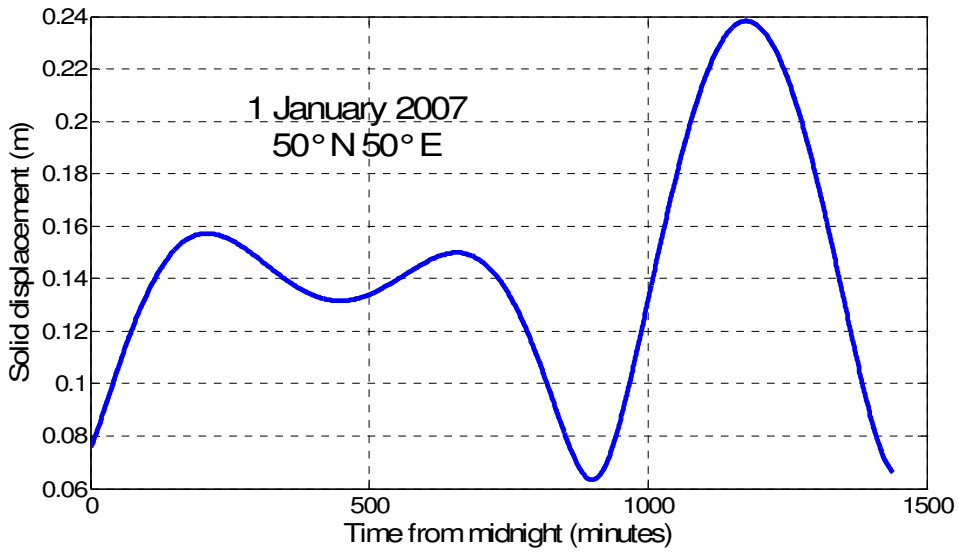

Figure 6-3. Solid Earth displacement output of the *solid.exe* executable.

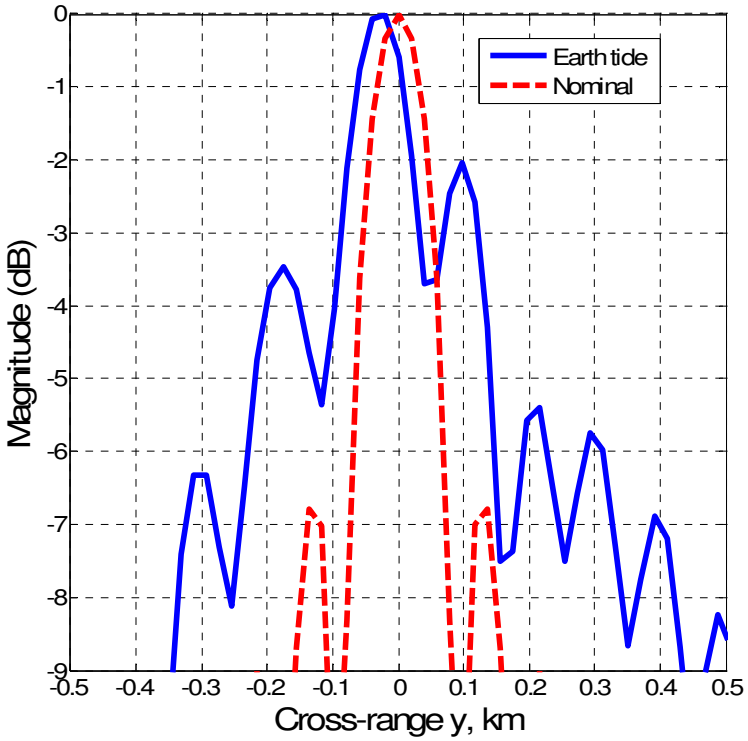

Figure 6-4. Comparison between the azimuth PSF obtained in the nominal case where Earth tidal motion has been completely compensated (dotted line) and the azimuth PSF obtained if the uncompensated solid Earth tide is taken into account (solid line).

Figure 6-4 presents the azimuth PSF obtained focussing a single pixel along the azimuth direction adding the phase delay induced by the displacement plotted in Figure 6-3 according to Equation 6-31.

The solid line is the output of a simulation where the displacement induced by Earth tidal motion has not been compensated while the dotted line is the noiseless case where the effect of the Earth tidal displacement has been completely compensated. The latter case corresponds to the nominal case when the target is stationary with respect to the radar and the azimuth PSF along the synthetic aperture is a *sinc* function.

The linear trend in the solid Earth displacement introduces an azimuth displacement of the target. The level of the side-lobes is increased as well (i.e. 5 dB).

6.2.3 Solid Earth tides - accuracy

According to McCarthy and Petit (2004), the models presented in IERS Technical Note n° 32 allow to model solid Earth tidal displacements with accuracy better than 1 mm.

The figures presented in the previous section show that a proper focussing of a GeoSAR image requires an accurate compensation of solid Earth tides. To estimate the residual coherent integration loss after solid Earth tide compensation, the error in the knowledge of solid Earth displacement is modelled as a Gaussian random noise with zero mean and standard deviation 1 mm. As specified in section 5.7.1 about methodology, this conservative assumption neglects any temporal correlation in the residual error and considers the accuracy in the measurement of Earth tidal displacements as the standard deviation of the white Gaussian noise distribution. When referring to slant range delay, this effect has to be multiplied by a factor 2 as the displacement affects both transmitted and received signal.

Richards (2003) provides an analytical formulation, valid under the assumption that phase noise is relatively small (i.e. < 20° ≈ 0.35 rad 1σ) and that a large number N of pulses are integrated.

$$[L]_{dB} = -4.343\left[\sigma^2\right]_{rad} \qquad \text{Equation 6-32}$$

In Equation 6-32, L is the integration loss;
σ is the standard deviation of Gaussian phase noise

1 mm site displacement corresponds to a phase delay (1 mm x 2) /λ x 2 π= 0.06 rad. This case is well within the boundaries included by Richards (2003) for this methodology. The resultant integration loss in dB is about 0.01 dB.

A simple Monte Carlo simulation has been implemented to have a second estimate of the coherent integration loss. 1000 Monte Carlo trials have been averaged and compared with the noiseless case where solid Earth tide effect had been completely compensated. Results in Figure 6-5 show that the two lines are indistinguishable.

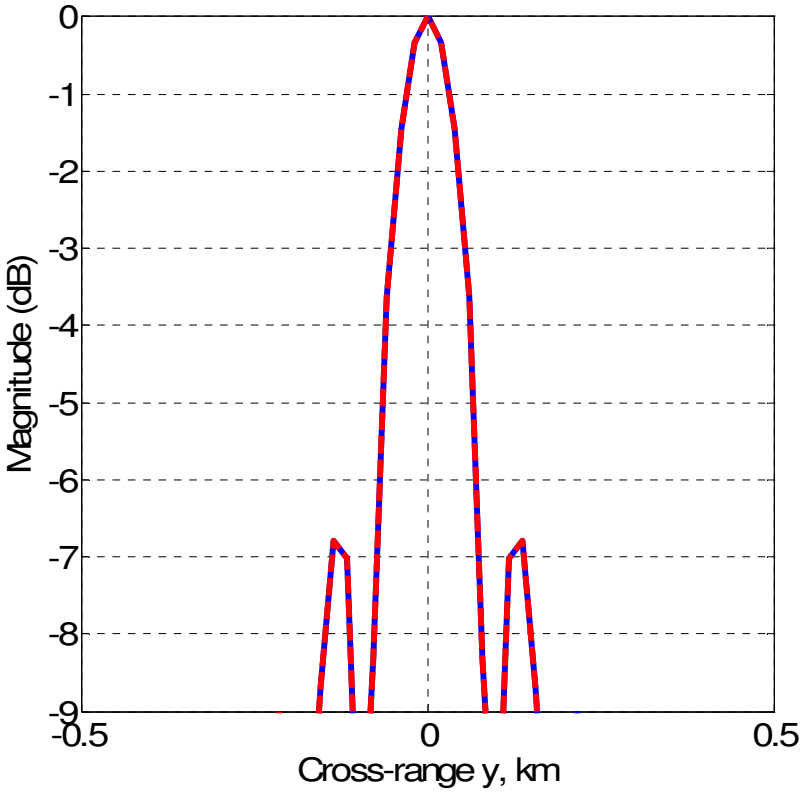

Figure 6-5. (Dotted line) Azimuth PSF in presence of a Gaussian noise (zero mean standard deviation 1 mm). The solid line is the nominal case (solid Earth tide exactly compensated). The two lines are not distinguishable.

6.2.4 Ocean loading effects - simulation

As mentioned in the background chapter, ocean loading effects are estimated considering a given ocean tide model and integrating a Green's function. The global effect of ocean loading can be estimated if the amplitude and the phase angles of each partial tide are known.

Ocean loading tables (as presented in appendix D) provide both amplitude A_i and phase φ_i for each of the 11 partial tides considered (semi-diurnal, diurnal and long period). They are available from ocean tide loading providers (Scherneck, 2006). Their temporal variation is a function of the longitude of the lunar node. McCarthy and Petit (2004) refer to available sub-routines to calculate the temporal variation of ocean tide loading.

The analysis of one ocean loading table shows that the effect of semi-diurnal tides is about one order of magnitude larger with respect to long-term tides.

In order to estimate the effect of uncompensated ocean loading a simplified procedure is implemented adding a target displacement with a 12-hour sinusoidal variation and 1 cm amplitude.

Results presented in Figure 6-6 show clearly that a target displacement with this order of magnitude could not be neglected in SAR focussing.

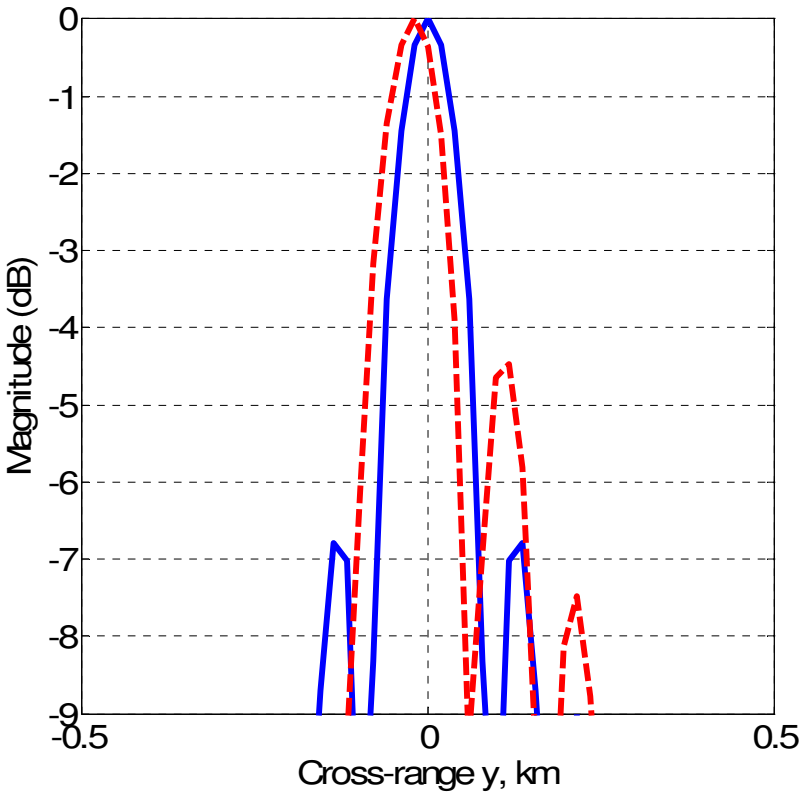

Figure 6-6. Comparison between the azimuth PSF obtained in the nominal case where ocean loading deformation has been completely compensated (solid line) and the azimuth PSF obtained if the ocean loading deformation, a sinusoidal wave with 1 cm amplitude has not been balanced (dotted line).

6.2.5 Ocean loading effects - accuracy

Yi *et al.* (2002) report that, according to McCarthy (1992), vertical displacements are accurate within +/- 3 mm. The effect of this displacement is modelled with the same approach followed for solid Earth tides (section 6.2.3).

Applying the analytical procedure described by Richards (2003), assuming that the residual ocean loading error can be modelled as white phase noise with zero mean, the standard deviation that corresponds to 3 mm site displacement is (3 mm x 2) /λ x 2 π= 0.18 rad. This case is well within the boundaries included by Richards (2003) for this methodology. The resultant integration loss in dB is about 0.15 dB.

6.2.6 Pole tide and atmospheric loading

Pole tide generates a fluctuation that can be up to 25 mm. As shown in section 2.10.4.3 , the period is about 12 months so site displacements induced during the 8-hour integration time might be neglected.

Atmospheric loading could be neglected as it requires variations of about 20 hPa to be significant (McCarthy and Petit, 2004). Such variations are quite unusual at GeoSAR spatial and temporal scales.

6.3 Tropospheric delay

Tropospheric delay modifies the length of the slant range from the satellites (i.e. both transmitter and receiver) to scatterers on the Earth's surface.

6.3.1 Assumptions

Simulations have been carried out under the following assumptions:

a. Tropospheric effects are considered on both TX and RX signals.
b. Tropospheric delays on both TX and RX rays are identical.

Assumption a. derives from the fact that tropospheric phase delay affects the path length of both transmitting and receiving signal therefore tropospheric delay has to be added twice to each pulse.

Assumption b. simplifies the approach to tropospheric delay simulations but introduces an error in the modelling. Dry and wet delay components have to be analysed

separately. Troposphere is concentrated below the tropopause at an altitude that is about 10 km, considering a bi-static angle of 30° (difference in longitude between transmitter and receiver); signals coming from the transmitter and going back to the receiver pierce the troposphere at a distance of about 5 km.

Referring to hydrostatic delay, both transmitted and received signals suffer from a similar tropospheric dry delay, as there are not large pressure variations on such small spatial scales.

The same consideration is not valid when investigating wet and liquid delay as variations in water vapour and cloud cover can happen with very large spatial frequency. It has to be said however that, looking forward to an operative GeoSAR tropospheric delay correction, some models that allow a 3D water vapour mapping and a consequent very accurate tropospheric error modelling are currently under development (Zhu *et al.*, 2007).

The solution proposed in this project to compensate tropospheric wet delay considers a spatial averaging to reduce noise variance. This averages out high frequency fluctuations thus making this assumption acceptable.

6.3.2 Effect of turbulence

Tropospheric variations within the SAR image are due mainly to turbulence. Hanssen (2001) specified that, using Kolmogorov's turbulence theory, the inner scale of the process is in the order of 10 m. According to Hall *et al.* (1996), the outer scale of turbulence is about 100 m. Considering that nominal azimuth resolution for GeoSAR is 100 m, it is straightforward to assume that turbulence effects are averaged inside a single azimuth resolution cell. Moreover, considering that turbulence is not going to be steady throughout the whole integration time, its variations can be traced back to the analysis that considers only variations of the atmosphere during the integration time.

According to Hall *et al.* (1996) "*the largest amplitude fluctuations observed in the aperture plane of the antenna are produced by eddies with scale size of the order of the Fresnel zone. For antenna aperture larger than the Fresnel zone, the fluctuations area spatially averaged by the antenna: this results in an apparent loss of antenna gain*".

In conclusion, turbulence effects are averaged out from the large antenna beam-width and from the long integration time. Therefore, the most significant aspect to deal with is the effect of tropospheric variations on a stable scatterer during the integration time, the effect of turbulence can be neglected.

Jakowatz and Wahl (2006) demonstrated that the auto-focus procedure Phase Gradient Algorithm (PGA) is able to estimate and correct phase delay caused by tropospheric phase noise in SAR images.

6.3.3 Tropospheric variations during the integration time

Tropospheric effects during the integration time will be investigated analysing hydrostatic, wet and liquid delay. Whenever possible an analytical evaluation of the coherent integration loss has been carried out. If the phase noise is too large to allow an analytical solution, Monte Carlo runs have been implemented in Matlab. Tropospheric noise has been added to the system following the phase screen approach.

6.3.3.1 Hydrostatic delay

Hydrostatic delay could be modelled with an accuracy of about 1 mm if accurate measurements of static pressure (better than 0.4 hPa) are available (Hanssen, 2001). The residual delay is modelled as a Gaussian variable with zero mean and standard deviation equal to the *rms* error. This is a conservative assumption, as it does not take into account any temporal correlation.

Phase delays are smaller than 20° therefore the coherent integration loss induced by un-modelled hydrostatic delay can be predicted with the same methodology previously used in this research (Richards, 2003). Following the procedure presented in section 6.2.3, the coherent integration loss is about 0.01 dB.

6.3.3.2 Liquid delay

Hall *et al.* (1996) listed the liquid water content W of clouds that has been reported in Table 6-1.

Although some physical properties of water are dependent from temperature, refractivity index can be approximated to within 1% with the expression (Hanssen, 2001) already discussed in section 2.11.2.5 (Equation 6-33).

$$N = 1.45W \qquad \text{Equation 6-33}$$

Table 6-1. Liquid water content in clouds (Hall *et al.* 1996, Hanssen, 2001).

Type of cloud	Liquid water content [g/m^3]	Slant delay [mm/km]
Stratiform clouds	0.05 – 0.25	0.1-0.4
Small cumulus clouds	0.5	0.7
Cumulus congestus and cumulonimbus	0.5-2.0	0.7-3.1
Ice clouds	<0.1	<0.1

The liquid delay is significant only for cumulus type of clouds that have a large extent in vertical (i.e. a few km), and relatively small horizontal extent. In this case the liquid delay can be up to 5 mm but, due to its limited spatial extent, their effect can be neglected in GeoSAR focussing that affects an area about 1000 km large across-track.

For other clouds, the effect is of the order of 1 mm (Hanssen, 2001). Considering the limited spatial scale their effect can be neglected in GeoSAR.

6.3.3.3 Wet delay

The wet delay induced by the concentration of water vapour in the atmosphere can be referred to the precipitable water vapour (PWV) that is defined as (Hanssen, 2001):

$$PWV = \frac{1}{\rho_l}\int \rho_v dh \qquad \text{Equation 6-34}$$

In Equation 6-34, ρ_l is the density of liquid water
ρ_v is the density of water vapour.

Bevis *et al.* (1994) provide a simplified expression to relate zenith wet delay to PWV:

$$\delta_{wet} = \Pi^{-1} PWV \qquad \text{Equation 6-35}$$

Where Π is a dimensionless constant of proportionality that is about 0.15 (Bevis *et al.* 1994).

PWV has a quite strong spatial variability (< 50 km) (Hanssen, 2001). In presence of a network of GPS stations, PWV can be obtained with a very good accuracy (1.5 mm) therefore this delay can be removed (Li, 2004).

In the absence of external measurements of local water vapour partial pressure, the only applicable wet delay model (MOPS, 1998) has an error of about 5 cm.

Multi-looking 10 range cells, the accuracy is reduced by the factor $10^{0.5} \approx 3.16$.

Assuming a Gaussian noise with zero mean and standard deviation 5/3.16=1.58 cm the azimuth PSF is presented in the following figure where 1000 Monte Carlo trials have been averaged and compared with the noiseless case where tropospheric effects had been completely compensated (Figure 6-7).

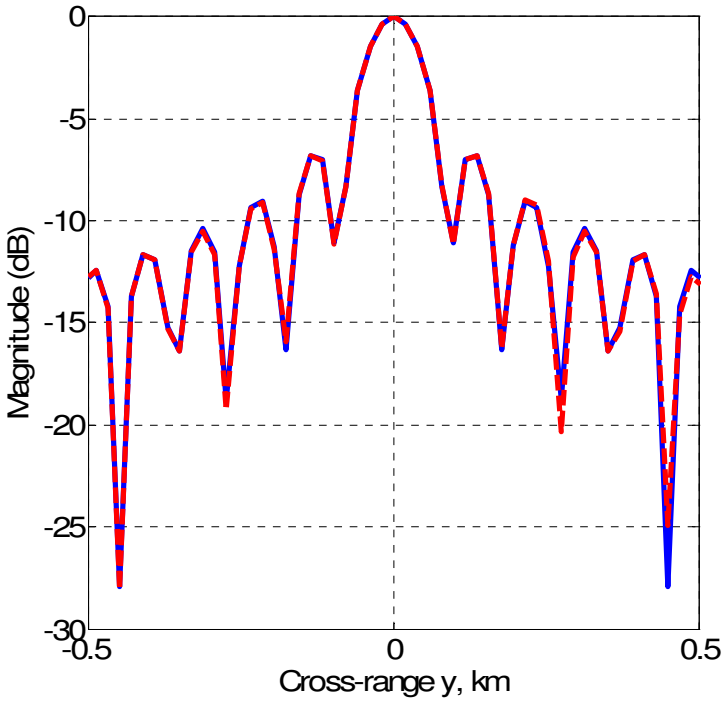

Figure 6-7. Azimuth PSF in presence of uncompensated tropospheric wet delay with standard deviation 1.58 cm (dotted line) and nominal azimuth PSF where tropospheric delay effects have been properly compensated (solid line). In the noisy case, 1000 Monte Carlo trials have been averaged. The two lines are nearly undistinguishable.

Averaging along the across-track direction is a strict requirement as a standard deviation of 5 cm gives the results presented in Figure 6-8 (1000 Monte Carlo trials averaged).

Holley *et al.* (2008) and Zhu *et al.* (2007) describe a procedure for advanced meteorological modelling that, starting from the knowledge of the orography, land use, vegetation and using other meteorological observations, develops a 3D map atmospheric map of the area of interest with 300 m spatial sampling and 10 second temporal sampling. At the moment, this is not an operative tool but, due to its excellent accuracy, it could be used in the future to completely compensate tropospheric wet delay. Results of this approach have been compared with MERIS data and showed a promising 1.6 mm *rms* residual wet delay.

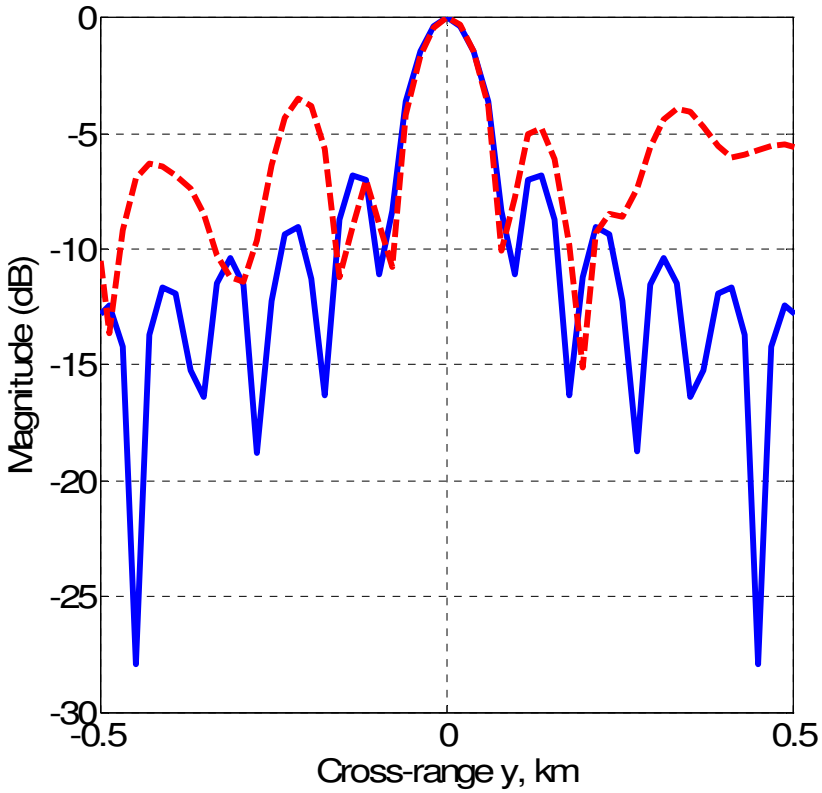

Figure 6-8. Azimuth PSF in presence of uncompensated tropospheric wet delay with standard deviation 5 cm (dotted line) and nominal azimuth PSF where tropospheric delay effects have been properly compensated (solid line). In the noisy case, 1000 Monte Carlo trials have been averaged.

6.3.4 Tropospheric delay – conclusions

To take into account tropospheric hydrostatic delay an accurate measurement of static pressure (0.4 hPa) is enough to reduce practically to zero its effects.

Liquid delay can practically be neglected due to its extremely high spatial frequency variations, when compared to SAR images.

Wet delay could be compensated using a relatively simple model (MOPS, 1998) that does not require *in situ* measurements to predict relative humidity. A spatial averaging across-track is required in order to reduce the standard deviation of the measurement noise.

Advanced atmospheric modelling could provide very accurate 3D modelling of the atmosphere on a local scale. Such approach, still in a development phase, allows to reduce significantly any residual wet delay effect on GeoSAR processing.

Tropospheric variations within the SAR image due to turbulence can be neglected as they are averaged out in the focussing of a resolution cell as they take place on spatial scale of about 10 m (nominal azimuth resolution 100 m).

Residual phase noise could be estimated and corrected applying auto-focus procedures as shown by Jakowatz and Wahl (2006).

6.4 Ionospheric delay

Ionospheric heterogeneities modify the length of the slant range from the satellites (i.e. both transmitter and receiver) to scatterers on the Earth's surface. Due to the complexity and the relevance of the argument, ionospheric effects require a detailed analysis.

6.4.1 Ionospheric effects on GeoSAR images

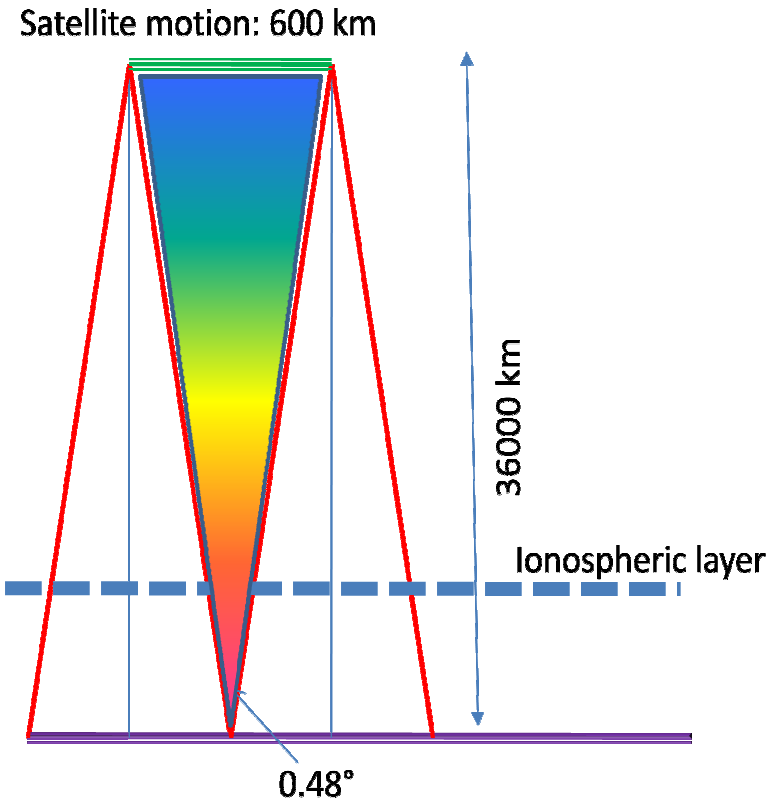

Figure 6-9. GeoSAR acquisition (equivalent flat Earth geometry). Ionospheric layer (400 km altitude) pierce points are inside a triangle with apex angle 0.48°. A 80-km synthetic aperture corresponds to a satellite motion of about 600 km (due to the altitude factor) in a Cartesian geometry.

GeoSAR has an 8-hour integration time, on such time scale, ionosphere varies significantly both in space and in time, therefore temporal variations have to be combined with spatial variations. Figure 6-9 shows the acquisition geometry assuming a flat Earth. The synthetic aperture is only 80 km, it corresponds to a satellite motion of about 600 km (due to the altitude factor) in a Cartesian geometry. Signals coming from a single scatterer pierce ionosphere along a line that is about 6 km long.

In a LEO SAR only spatial ionospheric variations have to be taken into account as integration time is about one second. GeoSAR is clearly different and TEC variations have to be considered using appropriate TEC measurements. Four different issues have to be tackled:

a. TEC varies for each pulse along-track within the footprint;
b. TEC varies for each pulse across-track within the footprint;

c. TEC varies along-track from pulse to pulse;
d. TEC varies across-track from pulse to pulse.

Issue a. considers TEC heterogeneities that will be averaged within the antenna footprint. Phase delay compensation requires TEC measurements that could be carried out applying methodologies such as split-spectrum approach. However, in presence of strong TEC variations, any correction leaves a residual phase delay due to heterogeneities within the footprint. Such variations cannot be measured with GeoSAR.

Issue b. has to be taken into account in fast-time processing. TEC heterogeneities introduce geometric distortions in range processing and in the geo-location procedure. This issue has been widely described in literature, as it is also a concern for LEO SAR (Meyer *et al.*, 2006) it has been discussed in section 6.4.8.

Issue c. includes all the complexities related to GeoSAR ionospheric delay compensation. Slow-time processing is performed integrating pulses that have been corrected using TEC measurements averaged within the antenna footprint (in order to remove pulse-to-pulse phase delay). This is an operational limitation to GeoSAR as, in presence of strong ionospheric decorrelation, the system will not be able to focus any data. In the above-mentioned cases, a more complex signal processing technique has to be used. This issue can be studied with the simulator developed in the present research and will be discussed in this report.

Issue d. takes into account temporal TEC variations that occur during the integration time. Their effect on fast-time processing implies mostly geometric distortions.

6.4.2 Ionospheric phase delay - simulations

Slow-time azimuth processing is clearly influenced by ionospheric variable phase delays. Precise ionospheric delay information is available neither from GeoSAR nor from other sensors. Simulations carried out investigate issues related to pulse-to-pulse varying phase delays. The aim of the simulations carried out is to evaluate the amount of degradation in GeoSAR performances induced by TEC variations that affect along-track (i.e. azimuth) focussing during the integration time (issue c. presented in section 6.4.1). In order to isolate the problem and limit the number of independent variables, TEC variations within the antenna footprint (issues a. and b. presented in section 6.4.1) as well as pulse-to-pulse variations across-track (issues d. presented in section 6.4.1) have been neglected in the present research.

6.4.2.1 Methodology

The analytical approach (Richards, 2003) is viable only for very small perturbations therefore a Monte Carlo simulation (1000 runs) was implemented in Matlab to investigate the effect of larger perturbations on the azimuth PSF.

Different scenarios have been analysed in order to understand the limitations of the system. Phase delays have been added to the noiseless bi-static SAR phase history of a single stable scatterer (i.e. to generate the azimuth PSF). Ionospheric noise has been initially added to the system throughout the whole integration time to evaluate the robustness of the system. The simplicity of this approach allows drawing some valuable conclusions in the design of GeoSAR. TEC noise has been simulated according to the following models:

- linear trend through the synthetic aperture (section 6.4.3);
- TEC sinusoidal variation (section 6.4.4);
- Gaussian random noise (section 6.4.5);
- Gaussian correlated noise (section 6.4.6).

A subsequent set of simulations has been carried out applying more realistic phase disturbances that affect the system only during a fraction of the integration time, following the behaviour of TID (section 6.4.7).

6.4.2.2 Assumptions

Simulations have been carried out under the following assumptions:

a. Ionospheric effects are considered on both TX and RX signals.
b. Ionospheric delays on both TX and RX rays are identical.

Assumption a. is obvious as the system is bi-static and ionospheric heterogeneities affect both the transmitted and received signal.

Assumption b. implies a simplification in the model. Ionosphere is considered as a single layer at 400 km altitude. If transmitter and receiver are both at GEO altitude and there is a 30° separation in longitude, the distance between the two piercing point on the ionospheric layer is about 200 km. TEC value affecting GeoSAR is actually the sum of the electrons along the path from the transmitter to the scatterer and from the latter to the receiver. This assumption is verified for a quiet ionosphere while fails in presence of strong disturbances.

6.4.3 Linearly varying TEC

The aim of this section is to evaluate the effect (on the azimuth PSF) of a TEC distribution linearly varying during the integration time.

6.4.3.1 Analytical derivation

Given a certain phase change (one-way) there is a resultant change in the observed frequency (Equation 6-36).

$$df_D = \frac{1}{2\pi}\frac{d\varphi}{dt} \qquad \text{Equation 6-36}$$

In Equation 6-36, df_D is a Doppler frequency variation;
$d\varphi$ is the ionospheric phase variation.

The azimuth shift that is related to the change in Doppler frequency is evaluated considering the full amount of Doppler bandwidth and the along-track antenna footprint.

A variation of about 1 TECU (for a stable scatterer) during the integration time causes a $\Delta\varphi$ of about 2π radians (f=1.5GHz).

$$\frac{d\varphi}{dt} = \frac{\Delta\varphi}{T_{obs}} = \frac{2\pi}{T_{obs}}\left[rad/sec\right] = \frac{1}{T_{obs}}\left[Hz\right] = \frac{1}{8\times 3600} = 3.47\times 10^{-5}\,Hz \qquad \text{Equation 6-37}$$

The above expression provides the variations in Doppler for a one-way propagation and a ramp of 1 TECU. To obtain the azimuth displacement induced by this factor, Doppler Bandwidth B_D has to be taken into account.

$$B_D = \frac{v_{sc}{}^2 T_{\text{int}}}{\lambda R_0}\sin^2\theta_{squint} \qquad \text{Equation 6-38}$$

For the GeoSAR configuration (v_{sc}=3.36 m/s, T_{int}=28800 sec, imaging at boresight, R_0=40000 km) B_D is equal to 0.0406Hz.

The relative Doppler bandwidth error is about 0.000854. The footprint of the antenna is about 80 km thus the along track displacement is about 68 meters. Bearing in mind the effect of the mapping function, a 50° ground incidence angle implies that the azimuth displacement is about 106 m.

Following the assumption that the TX signal suffers the same ionospheric delay as the RX signal, the relative azimuth displacement has to be doubled, i.e. 212 m for a 1 TECU ionospheric TEC variation.

6.4.3.2 Numerical simulation

Ionospheric contribution has been introduced in SAR focussing as a phase ramp varying linearly throughout the aperture. Initial TEC has been set to 50 TECU. In 8 hours (i.e. the integration time) TEC increases linearly.

$$TEC_i = TEC_0 + \frac{\Delta TEC}{T_{obs}/PRI}\,\text{Pulse Number} \qquad \text{Equation 6-39}$$

In Equation 6-39, TEC_i is the TEC value for the i^{th} pulse;
TEC_0 is the initial TEC value (i.e. 50 TECU);
PRI is the pulse repetition interval (i.e. 30 sec to take into account azimuth pre-summing);
T_{int} is the integration time (i.e. 8 hours);
ΔTEC is the amplitude of the TEC ramp.

Table 6-2. Azimuth displacement for a given TEC ramp (ΔTEC).

ΔTEC	Azimuth displacement
1 TECU**	220 m
5 TECU	1200 m
10 TECU	2500 m

**Note that 1 TECU is the typical accuracy of TEC measurements currently available.

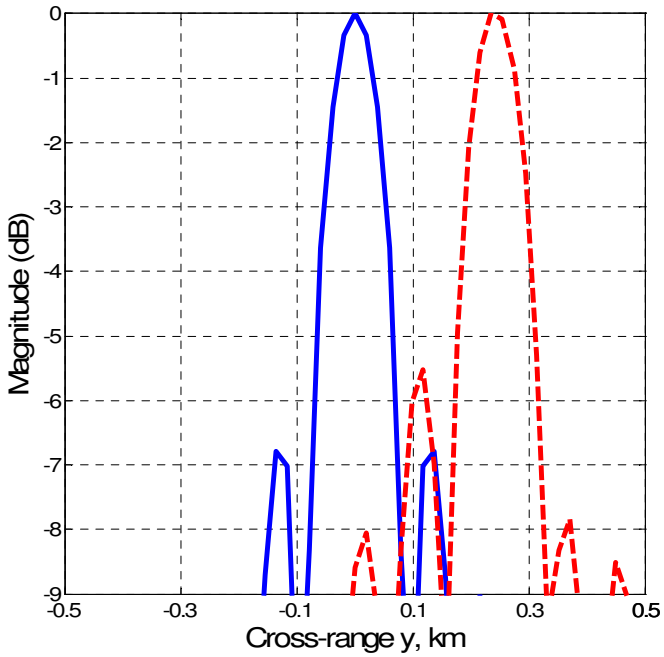

Figure 6-10. (Dotted line) Azimuth PSF in presence of ionosphere (ΔTEC variation 1 TECU). Azimuth displacement is about 220 m. The solid line is the nominal case (no ionosphere).

Figure 6-10 compares the azimuth PSF in the ideal noise-less case (solid line) and in presence of a linear TEC variation (dotted line). An ionospheric phase ramp during the integration time does not cause any significant reduction in azimuth resolution.

Numerical simulations carried out in Matlab confirm the azimuth displacement estimated analytically. This is a further validation of the code that has been implemented to focus GeoSAR data.

6.4.4 TEC sinusoidal variation

Ionospheric TEC has a nearly sinusoidal variation with a period that is roughly about 24 hours (section 2.12). A simulation dataset has been built assuming a sinusoidal TEC variation during the integration time. Equation 6-40 presents the chosen TEC distribution.

$$TEC_i = TEC_0 + \Delta TEC \sin\left(\frac{2\pi}{Period}\mathrm{PRI}\times Pulse\ number\right) \quad \text{Equation 6-40}$$

In Equation 6-40, TEC_i is the TEC value for the i^{th} pulse;
TEC_0 is the initial *TEC* value (i.e. 50 TECU);
PRI is the pulse repetition interval (i.e. 30 sec to take into account azimuth pre-summing);
Period is the period of the sinusoidal wave (i.e. 24 hours);
ΔTEC is the amplitude of the sinusoidal variation; daily variations depend from ionospheric activity but can be considered in the order of 20 TECU.

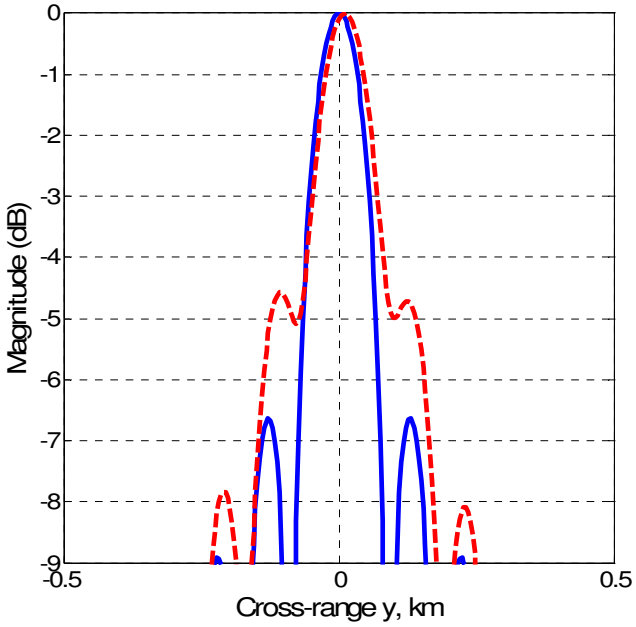

Figure 6-11. Azimuth PSF in presence of ionosphere (ΔTEC amplitude 0.1 TECU, sinusoidal variation). The solid line is the nominal case (no ionosphere).

As in the previous plot, Figure 6-11 compares the azimuth PSF in the ideal noise-less case (solid line) and in presence of a sinusoidal TEC variation (dotted line). Noise that has been added causes a significant increase in the level of side-lobes and an azimuth displacement.

Simulations carried out using a sinusoidal TEC variation (with amplitude ΔTEC of 0.1 TECU) showed that even a small ionospheric variation during the integration time requires phase compensation to allow for SAR image focussing.

6.4.5 Gaussian noise

Results presented in previous sections show clearly that ionospheric TEC variations that happen during the integration time could not be neglected in the SAR focussing process.

To focus a target, an accurate knowledge of ionospheric TEC is required. To estimate the accuracy required in TEC modelling, a Gaussian white noise has been superposed to the actual TEC (*Spectre* dataset) to evaluate the loss in SNR and in azimuth resolution. Figure 6-12 shows the two test cases that have been compared.

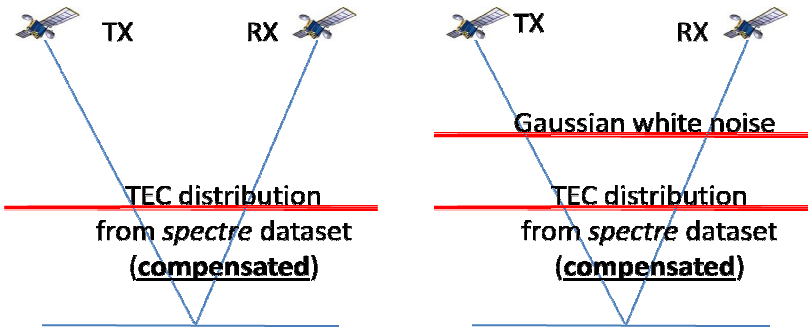

Figure 6-12. The two cases that have been compared to evaluate the accuracy in TEC modelling.

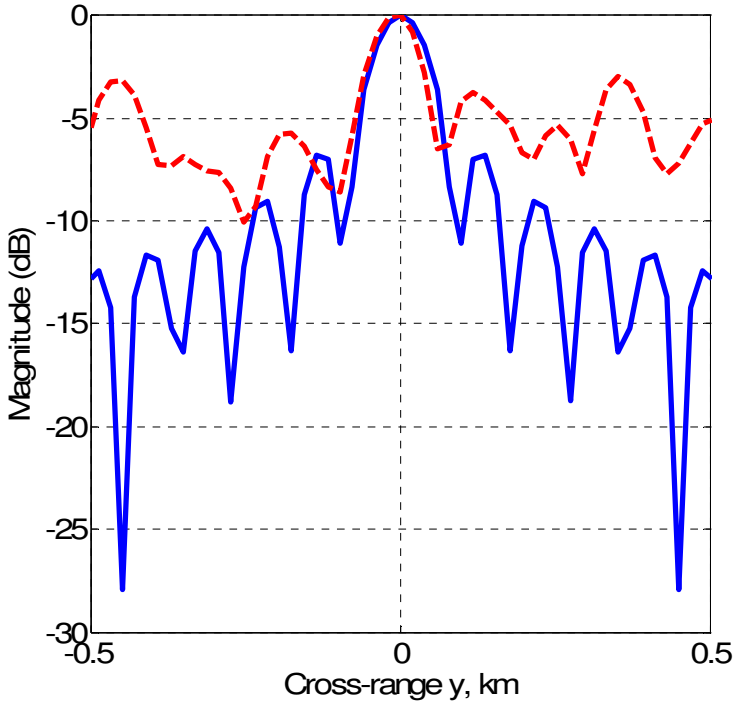

Figure 6-13. (Dotted line) Azimuth PSF in presence of a Gaussian noise added to the exact TEC (zero mean standard deviation 0.2 TECU), 1000 Monte Carlo trials have been averaged. The solid line is the nominal case (ionosphere exactly compensated).

To obtain statistically significant results, 1000 Monte-Carlo trials have been averaged. Figure 6-13 shows the comparison between the azimuth PSF achieved in presence of ionospheric effects exactly compensated (solid line) and the system response worked out in presence of an uncompensated ionosphere (Gaussian random noise with zero mean, standard deviation 0.2 TECU).

An exact estimate of the coherent integration loss cannot be performed using the methodology proposed by Richards (2003) as phase noise is larger than 20 degrees.

A standard deviation of 0.2 TECU in the knowledge of ionospheric TEC (assuming a residual phase delay modelled as white Gaussian noise) is marginally acceptable for imaging purposes. Figure 6-14 shows the results of the same analysis when carried out in presence of a smaller noise level (i.e. zero mean, standard deviation 0.1 TECU).

From the analysis of Figure 6-15, it can be drawn that ionospheric phase delay has to be known with accuracy better than 0.2 TECU. It has to be said that this level of accuracy in TEC estimates cannot be achieved with any of the methodologies currently available for ionospheric TEC measurements.

However ionospheric noise has a certain degree of spatial and temporal correlation (sections 5.7.3.1 and 5.7.3.2), therefore more significant indications about system limitations induced by ionospheric noise will be given in the following section when the effects of correlated Gaussian noise will be looked into.

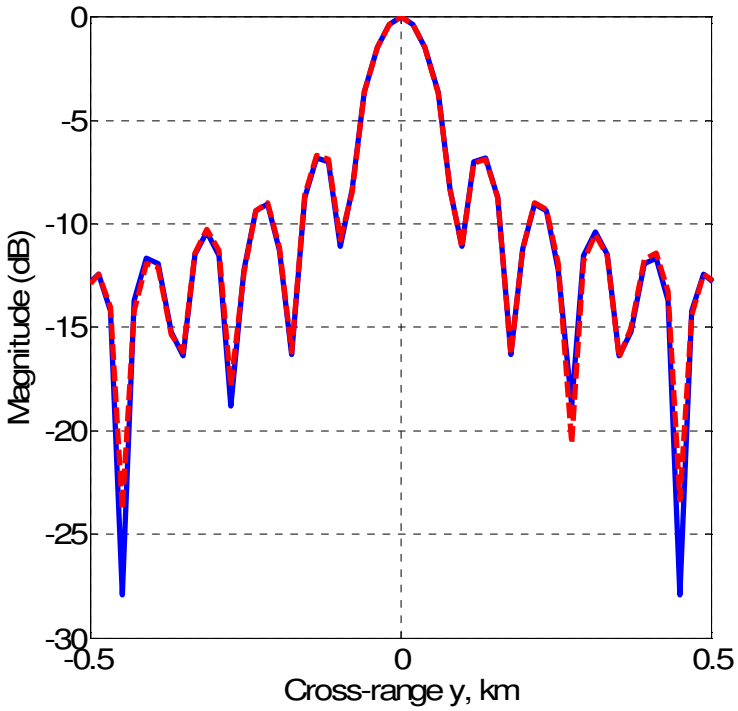

Figure 6-14. (Dotted line) Azimuth PSF in presence of a Gaussian noise (zero mean standard deviation 0.1 TECU), 1000 Monte Carlo trials have been averaged. The solid line is the nominal case (ionosphere exactly compensated).

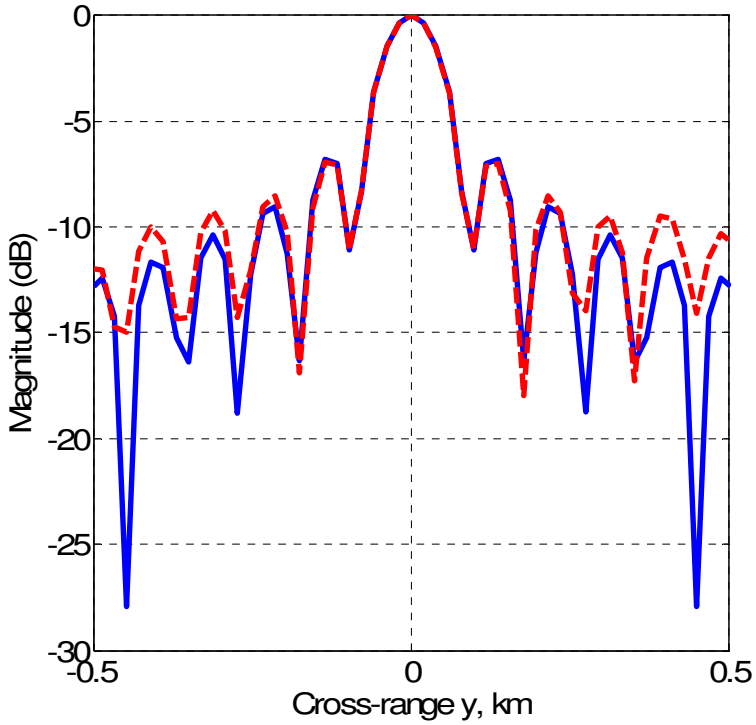

Figure 6-15. (Dotted line) Azimuth PSF in presence of a Gaussian noise (zero mean standard deviation 0.15 TECU), 2000 Monte Carlo trials have been averaged. The solid line is the nominal case (ionosphere exactly compensated).

6.4.6 Correlated Gaussian noise

In this section the effect of ionospheric delay modelled as correlated Gaussian noise will be investigated.

6.4.6.1 Gaussian filter

Oksanen and Sariakoski (2005) describe a procedure to generate a Gaussian filter that is implemented in order to generate correlated noise starting from white Gaussian noise.

The method is thoroughly described in their paper. An a priori determined spatial autocorrelation function is determined and, exploiting the properties of Gaussian distributions and convolution, uncorrelated noise is filtered to achieve the desired

autocorrelation in the form presented in Equation 6-41 (Oksanen and Sariakoski, 2005):

$$\rho(t) = e^{-A\left(t^2/\tau^2\right)} \qquad \text{Equation 6-41}$$

In Equation 6-41, ρ is the correlation coefficient;
A is a coefficient that has to be tuned in order to achieve the desired correlation function;
t is the time lag;
τ is a time constant that has to be tuned to set the filter response.

With respect to box filtering, the Gaussian filter low-passes noise removing high frequencies.

6.4.6.2 Correlated Gaussian noise – simulations

Previous simulations showed that a small amount of uncorrelated noise is sufficient to hamper completely azimuth focussing. As discussed thoroughly in chapter 5, ionospheric TEC is correlated both in space and in time, therefore correlated Gaussian noise is a more realistic model.

In the following simulations, noise is the residual ionospheric phase delay contribution after compensation. Figure 6-12 in section 6.4.5 shows the test cases that have been compared.

Figure 6-16 depicts the behaviour of the system in presence of correlated noise. The blue line is the ideal azimuth PSF (when ionospheric noise has been completely accounted for); the red line is the output in presence of correlated ionospheric noise (5 samples correlation time, noise with zero mean and standard deviation 0.15 TECU); the green line is the output in presence of correlated ionospheric noise (10 samples correlation time, noise with zero mean and standard deviation 0.15 TECU). Figure 6-17 plots the same datasets used in Figure 6-16 on a different spatial scale. Each sample corresponds to 36 second integration time therefore 5 samples correlation time is about 3 minutes and 10 samples is about 6 minutes.

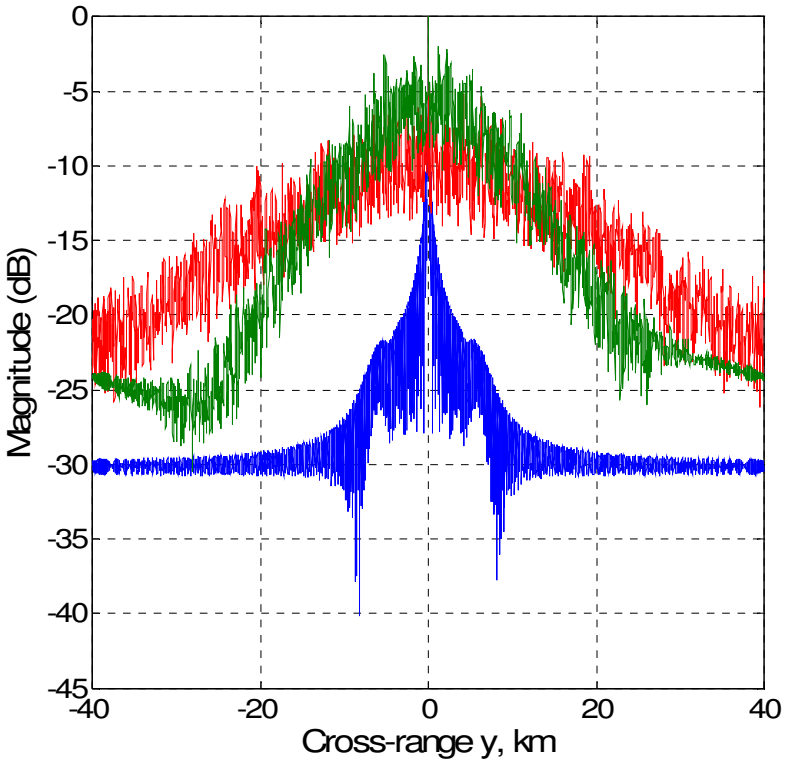

Figure 6-16. Azimuth PSF in presence of correlated Gaussian noise. Blue line is the ideal (noiseless case); the red line is the output in presence of correlated ionospheric noise (5 samples correlation time, noise with zero mean and standard deviation 0.15 TECU), the green line is the output in presence of correlated ionospheric noise (10 samples correlation time, noise with zero mean and standard deviation 0.15 TECU).

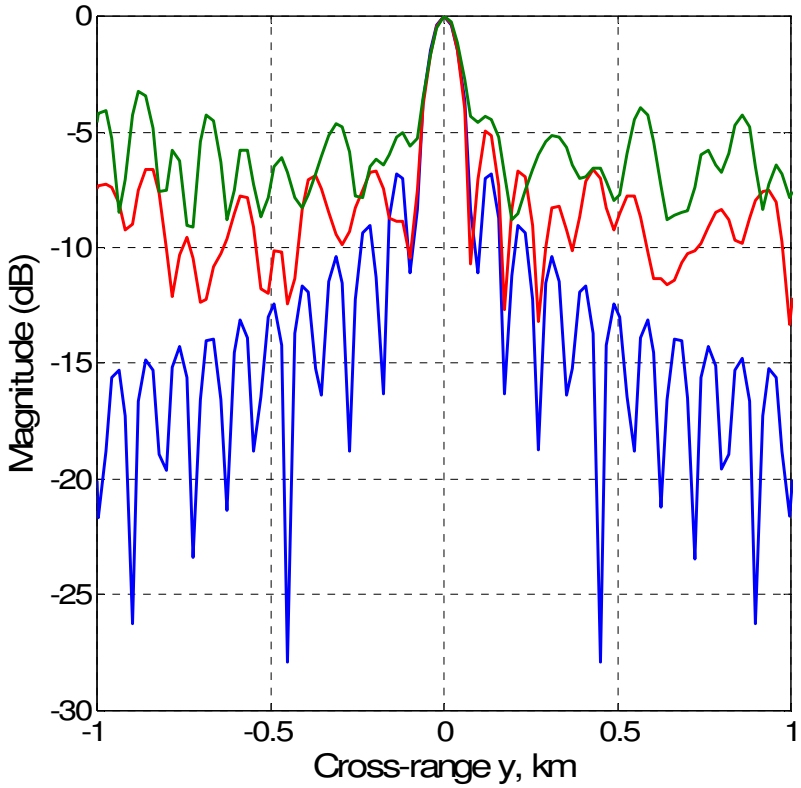

Figure 6-17. Expanded view of Figure 6-16.

Figure 6-18 shows that the main lobe of the azimuth PSF becomes narrow in presence of a longer correlation as the picture shows the variations in the PSF due to various ionospheric coherent lengths (the amplitude of the disturbance is constant to 0.3 TECU for all the datasets).

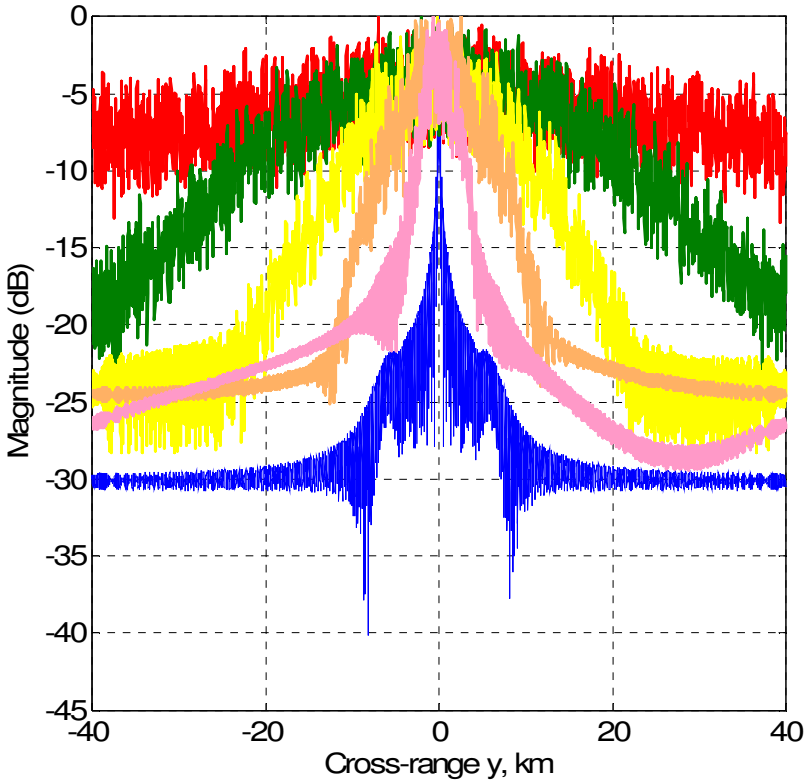

Figure 6-18. Azimuth PSF in presence of correlated Gaussian noise with zero mean and standard deviation 0.3 TECU. The blue line is the ideal (noiseless case); the other lines have an increasing correlation length (i.e. red - 5 samples, green – 10 samples, yellow – 20 samples, orange - 40 samples, pink – 80 samples).

Figure 6-19 shows the azimuth PSF of the system in presence of residual ionospheric noise with a very long correlation time (i.e. 100 samples that correspond to a coherent length of about 1 hour) and large standard deviation (0.5 TECU and 1.0 TECU). In presence of correlated noise, the main lobe is still identifiable in the azimuth PSF even if azimuth resolution is severely degraded.

Figure 6-20 shows the azimuth PSF in presence of correlated Gaussian noise with different correlation time, the solid line refers to a 2-hour correlation time, the dotted line refers to a 1-hour correlation time.

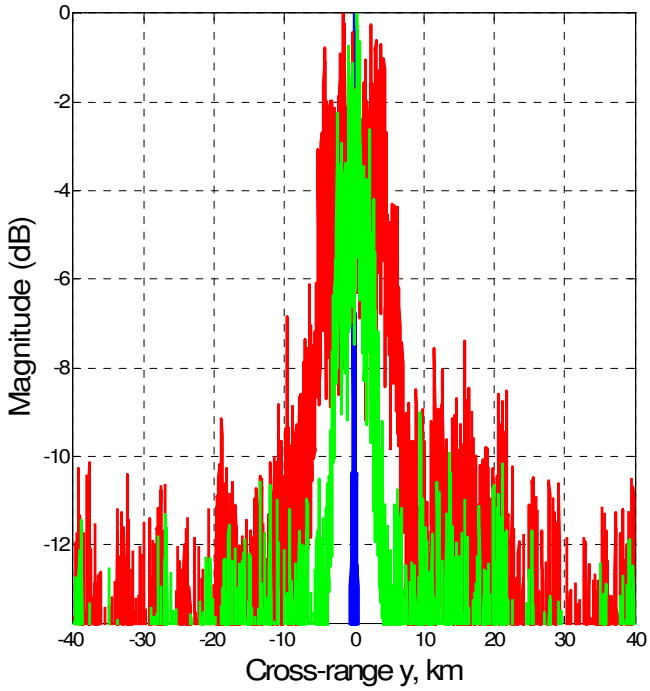

Figure 6-19. Azimuth PSF in presence of correlated Gaussian noise. The blue line is the ideal (noiseless case); the red line has been obtained adding noise with correlation time 1 hour and standard deviation 1.0 TECU; the green line has been obtained adding noise with correlation time 1 hour and standard deviation 0.5 TECU.

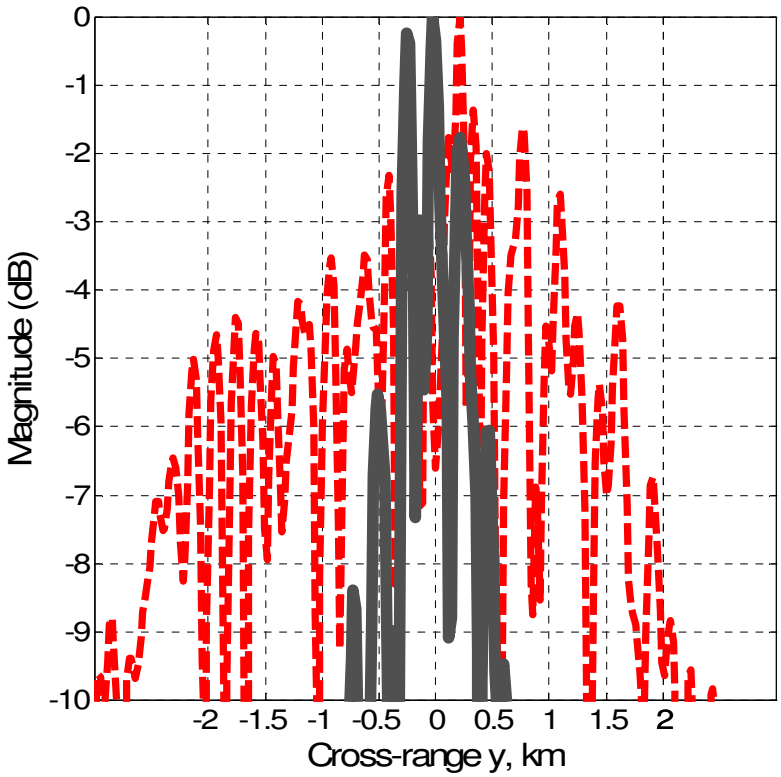

Figure 6-20. Azimuth PSF in presence of correlated Gaussian noise with zero mean and standard deviation 0.4 TECU: 2-hour correlation time (solid line), 1-hour correlation time (dotted line).

6.4.7 TID simulations

Simulations presented in previous sections moved from the assumption that ionospheric noise affects GeoSAR during the whole integration time. However, a more realistic test case takes into account that the long integration time allows the system to filter out short-term disturbances even if their amplitude is quite large.

Assuming that ionospheric scintillations are affecting SAR signal for two hours (25% of the integration time) the system is able to cope with large amplitude noise. Figure 6-21 shows the effects of white (uncorrelated) Gaussian noise with amplitude of 1 TECU that affects the system for two hours (solid line) and for three hours (dotted line).

Figure 6-22 shows the azimuth PSF main lobe in presence of disturbances (2 TECU amplitude) with different durations.

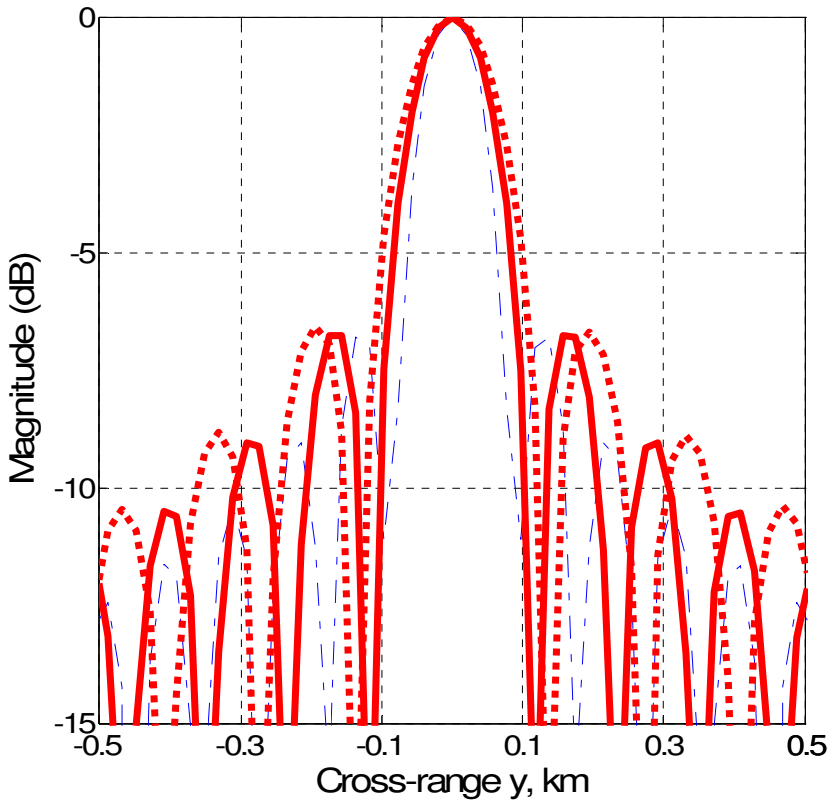

Figure 6-21. Azimuth PSF in presence of uncorrelated Gaussian noise with 1 TECU standard deviation. The simulated TID affects the system for two hours (solid line) of for three hours (dotted line).

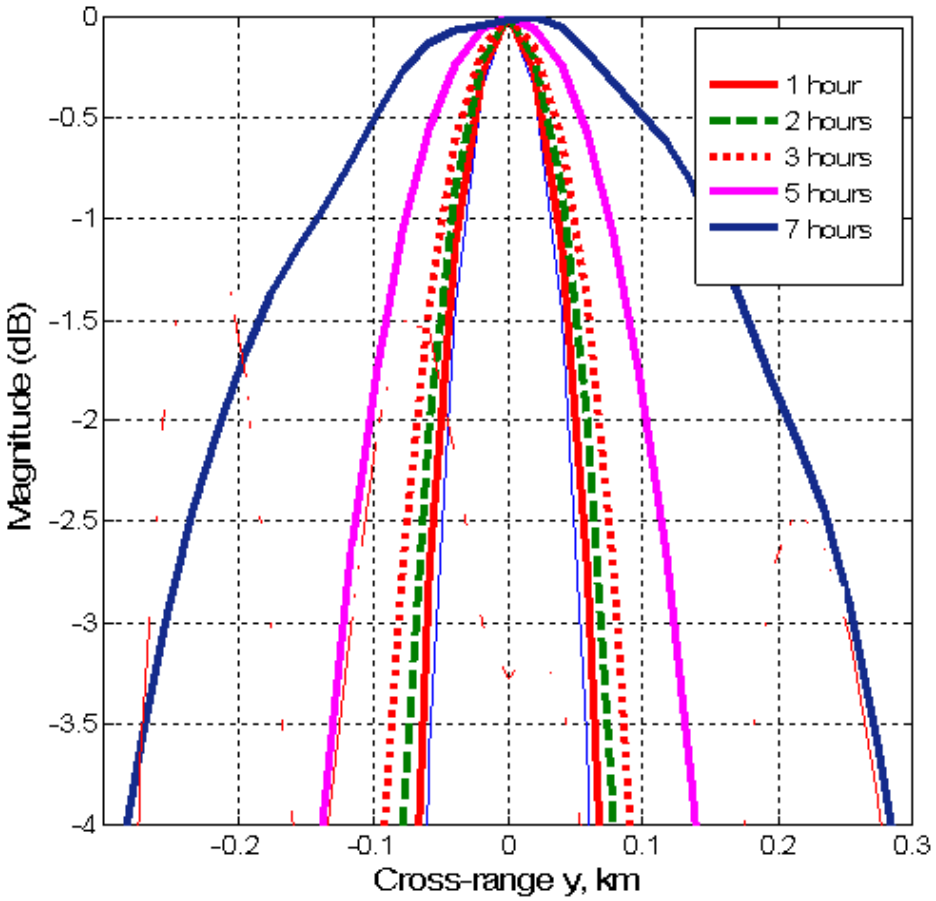

Figure 6-22. Azimuth PSF in presence of disturbances that affect azimuth SAR focussing for a limited fraction of the integration time.

In presence of ionospheric perturbations that affect image processing for a period shorter than the integration time, there is a progressive decrease in azimuth resolution that is equivalent to a reduced integration time (i.e. and a reduced synthetic aperture).

The resolution achieved when the undisturbed integration time is a fraction f of the full period is 1/f that of the nominal system, i.e. 2 hr disturbance (undisturbed period, 6 hr, is 3/4 of 8 hr) increases the PSF width by a factor 4/3.

Figure 6-23 shows the same dataset presented in Figure 6-22 focussing only on perturbations with shorter duration (i.e. 2 hours and 4 hours).

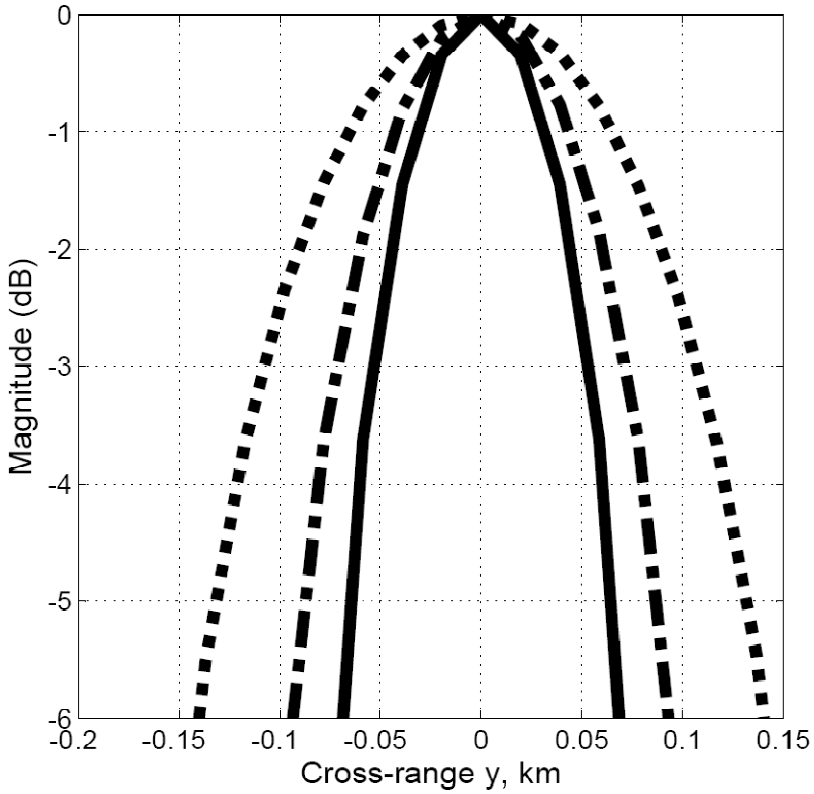

Figure 6-23. Main lobe of the azimuth PSF in presence of white Gaussian noise with zero mean and standard deviation 2.0 TECU affecting the system for various time intervals: nominal noiseless case (solid line), 2-hour disturbances (dash-dotted line) and 4-hour disturbances (dotted line).

6.4.8 Across-track distortions

Issue b. in section 6.4.1 was addressing across-track ionospheric phase delay variations within the antenna footprint during the integration time.

GeoSAR pulses have to be corrected to take into account ionospheric phase delays using an average TEC. It is obvious that this value will be accurate only for a limited number of pixels in the footprint.

As mentioned in the section about ionospheric effects on SAR images, an error in TEC measurement corresponds to a ranging error according to the Equation 6-42 here reminded (Curlander and McDonough, 1991).

$$\Delta r = \frac{c_0 \Delta \tau}{2 \sin \theta}$$ Equation 6-42

In Equation 6-42, θ is the ground incidence angle (i.e. 50°);
Δr is the ranging error;
$\Delta \tau$ is the slant delay error.

A TEC variation of 1 TECU generates a group delay of about one wavelength (i.e. 0.66 ns delay). The effect on range displacement is therefore negligible.

6.4.9 TEC measurement with GeoSAR

This section investigates the potential of GeoSAR in ionospheric TEC measurements. This is a potential field of application for the system itself as TEC data on large scale is valuable information for many various scientific and engineering applications (i.e. GPS correction and integrity, volcanology, seismology, satellite communications, space weather).

6.4.9.1 Rationale

The aim of this section is to determine the accuracy that can be achieved in TEC measurements. The methodology presented hereafter has been already applied to estimate ionospheric contribution for GPS applications.

The NASA JPL concept GESS (NASA JPL, 2003) describes the GPS-like methodology to use a split-spectrum approach to determine ionospheric TEC. This methodology is currently applied in satellite radar altimetry (Monaldo, 1993) as well as in GPS navigation. This approach will be evaluated as well in the GeoSAR configuration in order to obtain, in post-processing, accurate TEC measurements.

Determine TEC accurately is a strong operational requirement and has some implications on GeoSAR system design:

- The system has to operate on two different frequencies in order to estimate ionospheric slant delay.
- The spacing between the two frequencies is essential to improve the performance of TEC measuring.
- A large range bandwidth (i.e. about 8 MHz) is required in order to improve the efficiency of the algorithm.
- Many TEC measurements have to be averaged to reduce the uncertainty on TEC determination.

For any given system with a long integration time, there is a level of ionospheric perturbation that will impair completely SAR image focussing. In this case, a different operational mode has to be engaged reducing the integration time (i.e. reducing resolution as well).

6.4.9.2 Dual frequency systems

Assuming that the system is working with two separate frequencies *F1* and *F2*, as range measurements are affected by ionosphere, the measurements at the two frequencies will differ. Neglecting other error sources:

$$R_{F1} = R + \delta i_{F1}$$
$$R_{F2} = R + \delta i_{F2}$$

Equation 6-43

In Equation 6-43, R is the actual slant range;
R_{F1} is the range measured at the frequency F1;
R_{F2} is the range measured at the frequency F2;
δi_{f1} is the ionospheric correction at the frequency F1;
δi_{f2} is the ionospheric correction at the frequency F2.

Using equations presented in the background chapter, ionospheric delays at the two frequencies are expressed as:

$$\delta i_{F1} = -\frac{40.28}{f_{F1}^2} TEC$$
$$\delta i_{F2} = -\frac{40.28}{f_{F2}^2} TEC$$

Equation 6-44

In Equation 6-44, δi_{F1}, δi_{F2} are ionospheric zenith delay is expressed in *m*,
f_1 and f_2 are frequencies in *Hz*;
TEC is measured in *electrons/m*^{2}.

Combining Equation 6-43 and Equation 6-44:

$$R_{F2} - R_{F1} = \delta i_{F2} - \delta i_{F1}$$
$$R_{F2} - R_{F1} = 40.28\ TEC \left(\frac{1}{f_{F1}^2} - \frac{1}{f_{F2}^2} \right)$$
$$TEC = \frac{R_{F2} - R_{F1}}{40.28} \frac{f_{F1}^2 f_{F2}^2}{f_{F2}^2 - f_{F1}^2}$$

Equation 6-45

From Equation 6-45, standard deviation of TEC is derived, assuming that noise is normally distributed and that the two measurements are independent:

$$\sigma_{TEC} = K \sigma_{range} \sqrt{2} \qquad \text{Equation 6-46}$$

$$K = \frac{1}{40.28} \frac{f_{F1}^2 f_{F2}^2}{f_{F2}^2 - f_{F1}^2} \qquad \text{Equation 6-47}$$

The values provided in literature about the GESS concept (NASA JPL, 2003) will be used to validate Equation 6-46. In this system *F1*=1255 MHz; *F2*=1325 MHz therefore the constant *K* is 3.8 x10^{17} e^-/m^3. If TEC (Equation 6-46) is expressed in TECU, *K* is about *38* e^-/m^3.

Applying Equation 6-46, GESS single pulse measurement (zenith delay) is 1074 TECU. It could be improved through spatial averaging.

$$\left[\sigma_{TEC}\right]_{\text{N cell}} = \frac{\left[\sigma_{TEC}\right]_{\text{1 cell}}}{\sqrt{N}} \qquad \text{Equation 6-48}$$

In Equation 6-48, $[\sigma_{TEC}]_{Ncell}$ is the standard deviation achieved averaging N samples;
$[\sigma_{TEC}]_{1cell}$ is the standard deviation achieved without averaging;
N is the number of samples being averaged.

In GESS project (NASA JPL, 2003), range resolution is 15 m therefore σ_{range} could be set equal to 15 m. Average azimuth resolution is 10 m. Averaging the range offset data over areas about 200 km^2 (20 km x 10 km) σ_{TEC} is reduced up to 0.57 TECU.

$$\left[\sigma_{TEC}\right]_{\text{N cell}} = 38 \frac{\sigma_{range}\sqrt{2}}{\sqrt{2000 \cdot 1000}} \simeq 0.57 \text{ TECU} \qquad \text{Equation 6-49}$$

This value corresponds to the value 0.5 TECU provided in NASA JPL (2003). These results validate the procedure to estimate σ_{TEC} that will be hereafter applied to GeoSAR.

6.4.9.3 GeoSAR implementation

For GeoSAR it is essential to estimate TEC variations during the integration time to evaluate the appropriate phase correction that has to be applied to each pulse prior to SAR focussing.

Assuming a split-spectrum approach, two different channels are recorded by the receiver separated by 100 MHz, (i.e. 1500 MHz and 1600 MHz).

The parameter *K* presented in Equation 6-47 becomes equal to 46 e^-/m^3.

While GESS system uses a split-spectrum approach in order to improve the accuracy of its interferometric products, GeoSAR requires TEC information to process the SAR image. Therefore, only range cells are averaged in order to improve the accuracy in TEC measuring.

Range resolution is about 40 m for a 4 MHz bandwidth signal, therefore σ_{range} could be set equal to 40 m.

For GeoSAR the single pulse measurement (zenith delay) σ_{TEC} is estimated using Equation 6-49. This pulse-to-pulse TEC accuracy is achieved.

$$\sigma_{TEC} = 46\sigma_{range}\sqrt{2} \cong 2602\ TECU \qquad \text{Equation 6-50}$$

This value can be improved through averaging many different pulses or modifying some of the system parameters.

6.4.9.4 GeoSAR – possible configurations

The design parameters that can be modified in order to improve this performance are:

- distance between the two parts of the split-spectrum;
- range resolution (i.e. SAR signal bandwidth).

A second option, that requires a complete re-design of the system, includes an additional C or X band antenna that receives another signal transmitted from a different system. In this case, the distance between the frequencies used for the purpose is so large that the factor *K* (Equation 6-47) decreases significantly. This design increases the complexity (and the cost) of the GeoSAR satellite and is not viable as this is a low-cost concept.

6.4.9.4.1 Distance between the two parts of the split-spectrum

The distance between the two parts of the spectrum cannot be too large, as the radar has to reuse different channels of the same transmitting system. Increasing the spectrum distance to 150 MHz, (10% relative bandwidth at 1.5 GHz) allows improving the accuracy in TEC determination.

6.4.9.4.2 Range Bandwidth

Increasing the bandwidth of the SAR signal is the easiest way to improve σ_{TEC}. Doubling the bandwidth of the signal allows to halve the range resolution.

Increasing the bandwidth of the system increases the complexity of the TX satellite and reduces the number of possible transmitters of opportunity.

6.4.9.4.3 Proposed GeoSAR design

In order to achieve a higher accuracy in TEC determination, it is possible to use two different 8 MHz channels of an L band transmitting system. The two channels have to be spaced of about 150 MHz.

Assuming that f_1=1.5 GHz and f_2=1.65 GHz, the parameter *K* is equal to 1.61×10^{17} e^-/m^3. If TEC is expressed in TECU *K* is about *32* e^-/m^3. Range resolution is about 20 m (due to the 8 MHz signal bandwidth) therefore σ_{range}=20 m. σ_{TEC} is averaged over the whole antenna footprint (1500 km) for a single pulse.

$$\sigma_{TEC} = 32\sigma_{range}\sqrt{2} \cong 905 \; TECU \qquad \text{Equation 6-51}$$

To reduce further σ_{TEC} many different pulses can be averaged. The averaging window (in space and in time) should be limited to time and length scales over which ionospheric delay is constant.

Ionospheric delay is spatially correlated therefore many different range measurements can be averaged. Assuming a 50° ground incidence angle a 20 m slant range cell corresponds to a ground range cell of about 30 m. A 20 km size spatial window (ground range) allows to average about 660 pulses.

Ionosphere is not likely to be stable for time lengths longer than about 2 hour. Reducing the integration time to 2 hours, the ground resolution along-track is about 400 m.

Averaging the range offset data over areas about 400 km^2 (20 km x 20 km) data coming from about 660 range cells and 40 azimuth cells are averaged. Applying Equation 6-48 σ_{TEC} is reduced up to 5.6 TECU. This estimate is available every 2 hours.

Averaging on larger spatial scales (100 km in range and 20 km in azimuth) σ_{TEC} is reduced up to 2.4 TECU (averaging about 3330 range cells and 40 azimuth cells) with a temporal sampling of 2 hours.

In presence of a quiet ionosphere the accuracy of this measurements are improved as measurements are averaged on a longer time (or spatial) scale.

GPS networks allow to measure ionospheric TEC using a network of GPS receivers on the ground and a complex post-processing that takes into account ionospheric models. Those systems have an accuracy of about 1-2 TECU with temporal sampling up to 30 seconds (Crespon *et al.*, 2007). The order of magnitude of spatial resolution is about 100 km. It has to be said that GPS does not require an extremely accurate ionospheric monitoring as slant range error of few centimetres (1 TECU is about 20 cm) are widely acceptable for positioning purposes.

GeoSAR is able to provide TEC measurements with accuracy comparable with GPS networks without using any ground equipment. Its performances are enhanced with auto-focus algorithms and ionospheric models to improve this figure. This is an area where further research is required.

6.4.10 GeoSAR processing

Ionospheric phase delay is a major source of concern for GeoSAR image processing. Some algorithms could be applied to solve this problem. This is an area where further work is necessary.

6.4.10.1 Ionospheric turbulence

According to Belcher (2008) SAR focussing is more sensible to ionospheric turbulence than to the absolute level of TEC as signal de-focus is caused by heterogeneities in the propagation medium.

Ionospheric turbulence is measured by the parameter C_kL (Belcher, 2008), the coherent length in the ionosphere for various frequencies and values of C_kL is given in Figure 6-24.

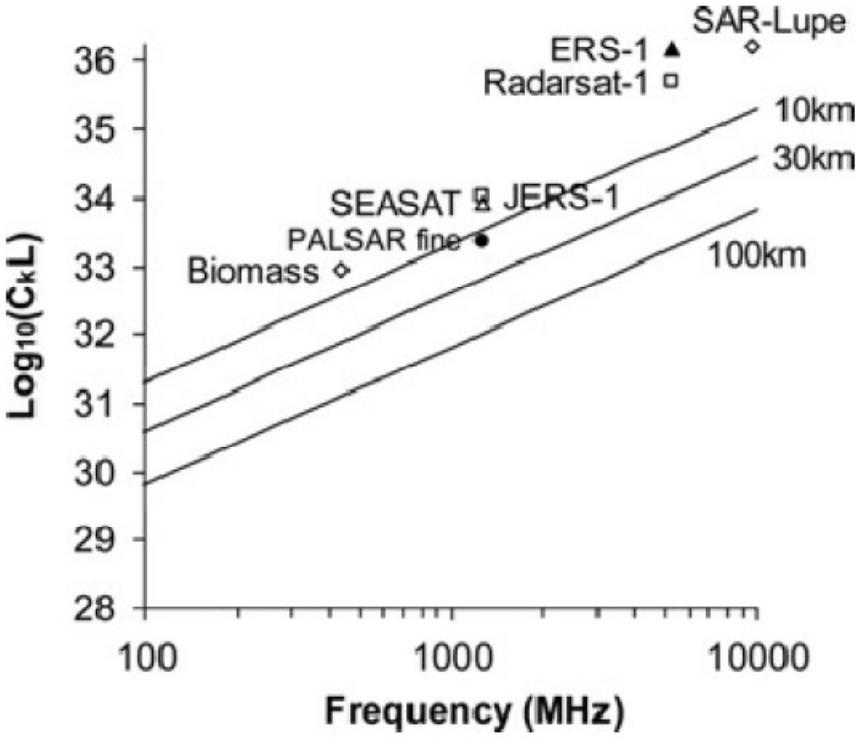

Figure 6-24. Maximum value of C_kL for several different coherence lengths (Belcher, 2008). The plot shows the relative position of some existing SAR systems.

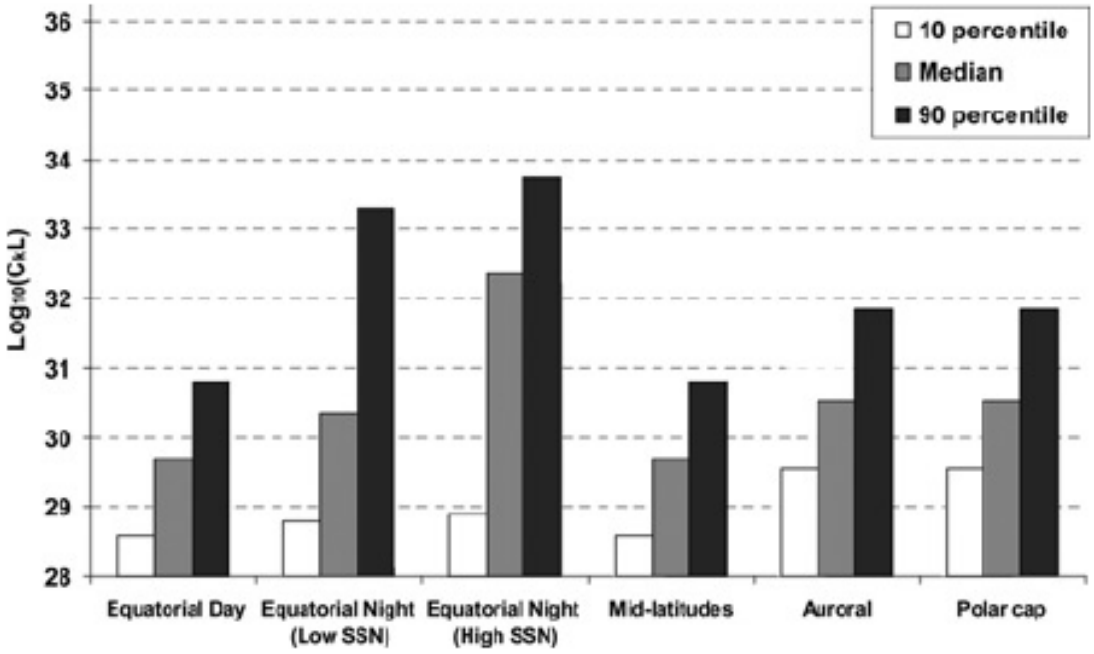

Figure 6-25. Typical values of C_kL (Belcher, 2008).

Figure 6-25 shows some statistics for the value of the ionospheric turbulence parameter. Comparing this graph with information provided in Figure 6-24, ionospheric coherent length will be shorter than 100 km (i.e. shorter than GeoSAR synthetic aperture) only in correspondence with the equatorial night (high sun spot number).

Although the absolute TEC value is higher during day-time, the level of turbulence is higher during the night. Therefore imaging during the day is preferable to reduce the effects of ionospheric phase delay.

It has to be said that the analysis provided by Belcher (2008) takes into account only spatial variations in the ionosphere as it is assumes that ionosphere is stationary during the whole integration time. A more complete analysis referred to GeoSAR should include ionospheric temporal variations as well.

6.4.10.2 Reversionary mode – Reduced integration time

In presence of strong ionospheric perturbations that affect the whole integration time, nominal GeoSAR performances could not be achieved. In these cases, the system can engage a reversionary mode with reduced integration time and degraded performances. This should overcome this problem.

This operational mode could be used as well to image targets with a shorter revisit time where nominal azimuth resolution is not required. This approach could be used to tackle TID phenomena that affect ionosphere for a limited amount of time.

6.4.10.2.1 Synthetic antenna aperture 8 km

In this case, the synthetic antenna aperture has been reduced by a factor 10. The integration time has been reduced as well by the same factor.

Figure 6-26 shows the azimuth PSF that is obtained focussing a single target super posing a phase fluctuation with a standard deviation 0.5 TECU. The correlation length of the Gaussian noise is 20 samples (i.e. about 10 minutes). The main lobe of the PSF is clearly identifiable, this shows the effectiveness of this methodology.

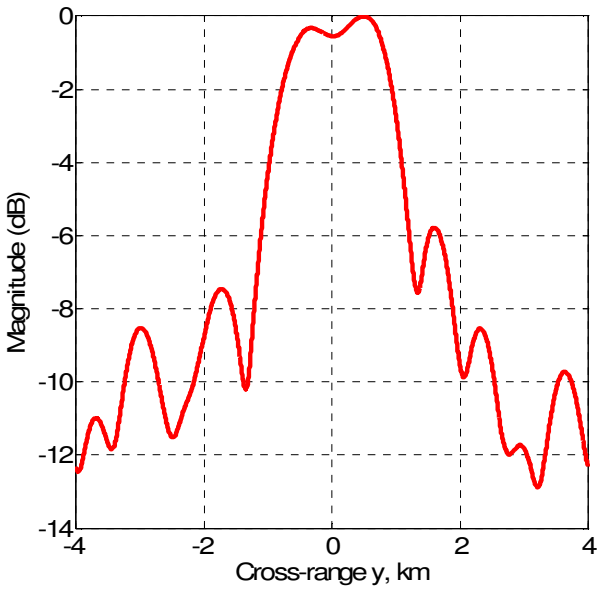

Figure 6-26. Azimuth PSF in presence of correlated Gaussian noise with zero mean and standard deviation 0.5 TECU and correlation length 20 samples. The synthetic antenna aperture has been reduced by a factor 10 to 8 km.

6.4.10.3 Autofocus of SAR imagery

The previous sections demonstrate how ionosphere induces phase delays that can cause a significant degradation in SAR imagery. Section 6.4.10.2 showed that, reducing the integration time, the system is able to cope with large amplitude phase delays. In principle, reducing the integration time up to ionosphere correlation time, the

best azimuth resolution could be achieved with an initial estimate of TEC variations. Applying an iterative procedure, the estimates of ionospheric TEC could be improved and consequently the integration time could be increased to get a better azimuth resolution. This is clearly an area for further work.

A nonparametric phase error correction scheme developed at Sandia National Laboratories some years ago (Jakowatz *et al.*, 1989), the Phase Gradient Autofocus Algorithm (PGA), has been demonstrated to produce good estimates for phase errors of arbitrary structure. This algorithm proved to be effective in contrasting high frequency noise sources.

Xu *et al.* (2004) point out that this phase error removal scheme is iso-planatic, i.e. "*it works on an area that is smaller than the decorrelation length of the phase error projected onto the target plane*" (Jakowatz *et al.*, 1989). This condition comes from the need for phase error to be space-invariant inside the imaged scene. When decorrelation length becomes shorter, it will be impractical to remove phase errors from the whole image; however, the PGA procedure could be applied to sub-images.

Belcher (2008), as discussed in section 2.12.3, showed that an auto-focus procedure could be applied to estimate and correct ionospheric phase delays. Figure 6-27 shows that the accuracy achievable with auto-focus techniques is proportional to the SNCR (dB) of the system.

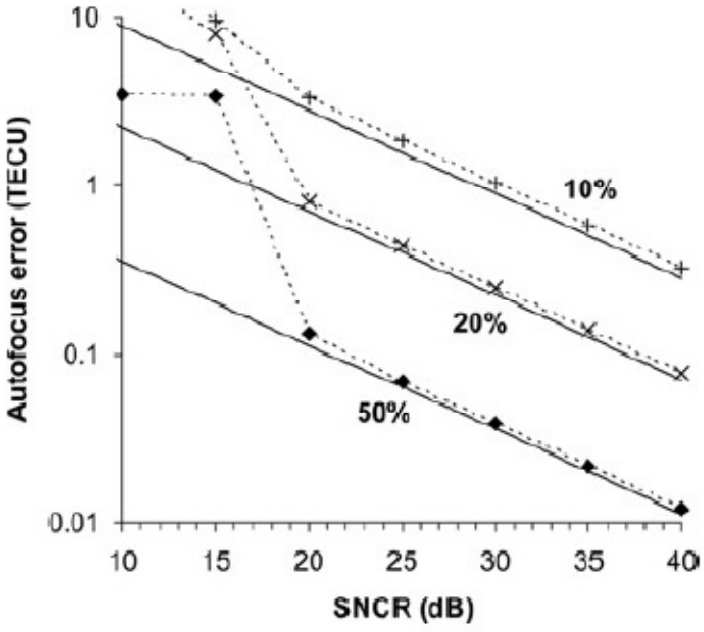

Figure 6-27. Autofocus *rms* error for a centre frequency of 500 MHz and a variety of percentage bandwidths. Solid lines represent the theory and the markers the simulation results (Belcher, 2008)

6.4.10.4 Short Time Fourier Transform (STFT) processing

Ionospheric noise enlarges the Doppler spectrum of the received signal. In such a scenario time-frequency transforms could be applied to achieve a better SNR. As signals backscattered by various targets are not overlapped in time, a STFT algorithm is likely to provide a SNR improvement (Chen and Ling, 2002) with respect to conventional range-Doppler SAR processing. To avoid decorrelation, the sampling period of the transform should be shorter than ionospheric correlation time. An exact prediction of the expected SNR improvement requires a precise characterization of ionospheric propagation spectral properties.

6.4.10.5 Sub-aperture focussing

During strong ionospheric perturbations that affect the whole integration time, nominal GeoSAR performance cannot be achievable. In this case, applying sub-aperture focussing (Chen and Ling, 2002), the full aperture is broken into a sequence of short apertures, for each sub-aperture, a low-resolution but well-focused image is formed. Thus, by coherently combining the corrected sub-aperture images, the resolution of the image can be subsequently improved.

6.4.11 Ionospheric delay – conclusions

Ionospheric phase delay is the major source of temporal decorrelation for the GeoSAR system. Simulations carried out show that the system requires an accurate knowledge of TEC variations in order to focus an image with nominal resolution.

Ionospheric residual (after compensation) phase noise with amplitude larger than 0.2 TECU (assuming that noise has a white Gaussian distribution) impairs image formation. The effects of correlated residual noise are less important but nominal azimuth resolution cannot be achieved,

The system is able to cope with disturbances such as TID with duration shorter than the integration time that however reduce azimuth resolution.

GeoSAR could be used to measure ionospheric TEC with accuracy comparable to systems that are currently used (GPS networks). Those measurements could be used to compensate ionospheric phase delays.

Iterative auto-focus algorithms such as Phase Gradient Autofocus (Jakowatz *et al.*, 1989) or sub-aperture focussing could be applied to achieve a better TEC estimate and consequently more accurate phase delay compensation.

SAR imaging is more susceptible to ionospheric turbulence than to the absolute value of TEC. The level of turbulence is usually higher during the night than during daytime. This implies that imaging during the day is preferable to reduce the detrimental effect of ionospheric heterogeneities.

6.5 Conclusions

The analysis carried out for the GeoSAR configuration stated that the issues related to temporal decorrelation are the most relevant technical complexities. Due to the 8-hour integration time, unstable scatterers and instabilities in the propagation medium have to be taken into account in SAR image processing. This problem is usually not addressed in SAR literature as conventional LEO SAR images are focused under the assumption that both the scene and the atmosphere are frozen during the integration time.

An azimuth SAR processor has been implemented in Matlab in order to simulate the effect of various decorrelation sources on the azimuth Point Spread Function (PSF).

A detailed analysis has been provided for the three major sources of decorrelation that have been identified: Earth tides, tropospheric delay and ionospheric delay. All the terms need to be compensated to avoid substantial degradation in GeoSAR imaging. Following sub-sections provide a summary of results presented earlier in this chapter.

6.5.1 Analytical approach – effect of correlated phase noise

Assuming that phase noise due to target's fluctuation or to variable phase delays are modelled as a first-order Gauss-Markov process, an analytical expression that estimates the fraction of clutter that enters the synthetic antenna main lobe has been derived.

This relation allows to compare different noise sources and shows that unstable scatterers (with a wider Doppler bandwidth) are filtered out in GeoSAR image processing, thus reducing the integrated SNR. This is another advantage of azimuth pre-summing that further reduces the processed azimuth bandwidth and contributes to filter out unstable targets.

6.5.2 Earth tides

Only solid Earth tides and ocean loading contribute significantly to site displacements on GeoSAR's temporal and spatial scales. They are modelled with an accuracy that is respectively 1 mm and 3 mm. Their residual error (after phase compensation) causes a small reduction in the coherent integration gain that can be neglected.

6.5.3 Tropospheric propagation

Tropospheric propagation delay is made up of three different contributions: dry delay, wet delay and liquid delay.

Dry delay is modelled with a very good accuracy if macroscopic meteorological parameters at the ground level (i.e. static pressure and temperature) are known. Its residual phase delay can be neglected.

Tropospheric wet delay has complex temporal and spatial variations that are due to turbulence and water vapour distribution. An accurate modelling requires the use of complex numerical meteorological models together with information about orography and land use. Models based only on ground measurements do not provide a very good accuracy; however, they simplify the image processing and they allow coping with tropospheric wet delay with a reasonable coherent integration loss.

Liquid delay can be neglected due to its negligible effects on GeoSAR.

6.5.4 Ionospheric propagation

Ionospheric phase delay is the most significant perturbation that affects GeoSAR focussing. The present research presented a set of simulations carried out in order to investigate their effect on GeoSAR imaging.

Ionospheric perturbations affecting the system for the whole integration time can interfere severely with SAR processing even if they show modest amplitude (TEC fluctuations modelled as Gaussian noise with zero mean and standard deviation of about 0.2 TECU). If ionospheric noise has a large temporal correlation time, the system is more robust to interference. In any circumstances, the system can operate in a reversionary mode reducing the integration time (and the synthetic aperture) to reduce noise influence on the system.

Ionospheric disturbances that happen for a period shorter than the integration time can be tolerated by the system even if they show large amplitude (i.e. geomagnetic storms

with TEC fluctuations of 1-2 TECU). In these cases, the system filters out ionospheric noise worsening azimuth resolution.

An iterative auto-focus procedure that processes data with progressively longer integration time (starting from ionospheric decorrelation time) can be used to achieve the best possible ground azimuth resolution and to extract very valuable information about temporal ionospheric variations.

Imaging during day-time when the level of turbulence in the ionosphere is lower is an alternative approach to tackle ionospheric noise.

6.5.5 TEC measurements

GeoSAR, applying the split-spectrum approach, is able to measure TEC with accuracy (2.4 TECU with 2 hour sampling) comparable with other systems currently available such as GPS networks. Post-processing that exploits autofocus techniques and ionospheric models can provide even better results.

In presence of strong ionospheric perturbations that happen during the whole integration time, the system is not able to compensate phase delays, nevertheless frequent TEC measurements over a relatively large area can provide useful information to study and monitor the ionosphere.

In quite ionospheric conditions, TEC measurements can be used to remove residual ionospheric delays from SAR signal on a pulse-to-pulse basis. Temporal sampling of the measurements has to be tuned according to the level of ionospheric perturbation. A more perturbed ionosphere requires a shorter sampling to take into account its temporal variations.

In any circumstances, GeoSAR is able to provide TEC measurements that can be used to monitor the ionosphere on a national scale. The TEC measurements carried out while imaging can be used in differential interferometry to remove artefacts generated by uncompensated ionospheric phase delays.

7 Applications

One of the aims of the present research is to investigate possible fields of applications for the GeoSAR concept.

The 24-hour revisit time allows the system to take one image every 12 hours. Repeat-pass interferometry and soil moisture measurements are candidate applications for GeoSAR. Section 7.1 discusses the relevant issues related to bi-static SAR interferometry. Section 7.2 is focused on GeoSAR's potential in monitoring soil moisture.

7.1 Bi-static SAR interferometry

SAR interferometry (InSAR) is certainly one of GeoSAR's main fields of application. The basic GeoSAR system is made up of a transmitter of opportunity placed in a geostationary orbit and of a receiver in a geosynchronous orbit. Using a single receiver only repeat-pass interferometry can be performed.

Hereafter the transmitter is assumed to be stationary (i.e. in GEO) and does not provide any contribution to the formation of the geometrical baseline. A more realistic case would require the exact knowledge of the transmitter's motion and its resultant contribution to the baseline.

In literature, geometrical baseline is usually defined as the distance between two acquisition points under the assumption that image formation is instantaneous. In GeoSAR, the receiver is flying along a curved path during the integration time and image formation cannot be considered instantaneous.

Interferometric processing is based on the assumption that the geometric baseline is constant during acquisitions (this is equivalent to considering parallel flight paths). GeoSAR acquires interferometric couples with variable geometrical baseline. This adds additional complexity to interferogram generation, expecially to the process of interferogram flattening (Ferretti *et al.,* 2007). This section assumes that this problem could be tackled prior to interferogram generation taking into account a pulse-to-pulse phase correction.

In the rest of this section an average geometrical baseline has been considered assuming that the receiving satellite is imaging flying along a straight path.

The relevance of geometrical baseline in SAR interferometry has been discussed in section 2.5.2. In that section the concept of critical geometrical baseline has been introduced as well.

Geometrical calculations have to be carried out in a Cartesian geometry (i.e. neglecting Earth curvature) that takes into account the altitude factor (Zebker and Villasenor, 1992; Hanssen, 2001). Therefore, the diameter of the GeoSAR's circular flight path is about 600 km (that corresponds to a 92 km diameter ground track).

Depending on the temporal baseline, two different geometries have to be considered, as there will be different expected baselines:

- The receiving satellite is imaging the same area from a slightly different point of view with a 24 hour (+ n days) temporal baseline. In this case, the across-track displacement is due only to orbit perturbations. Hereafter this geometry will be called *1-day interferometry* (Figure 7-1). This configuration is relevant for disaster response.

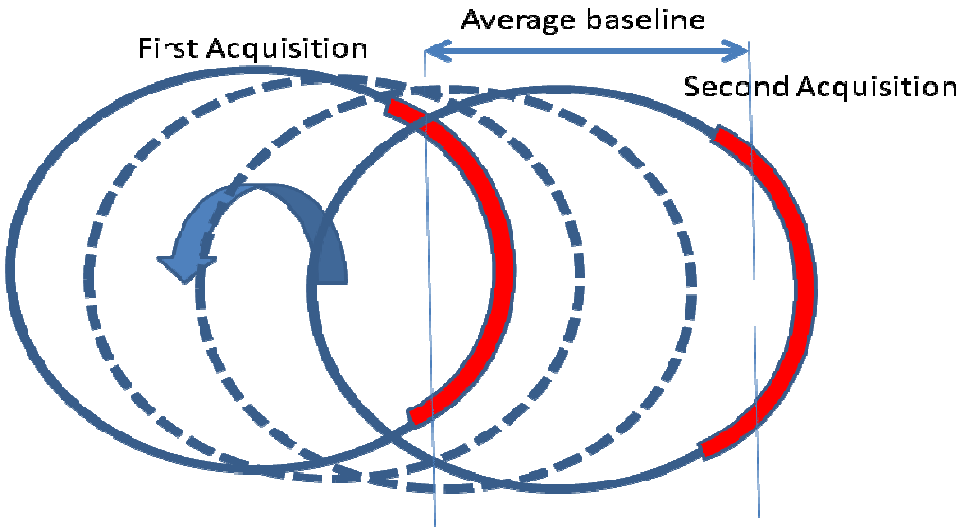

Figure 7-1. 1-day interferometry: relative geometry of the two acquisitions.

- The receiving satellite is imaging the same area from a slightly different point of view with a 12 hour (+ n days) temporal baseline. In this case, the across-track displacement is due to the different positions of the satellite along the circular orbit (≈600 km diameter). Hereafter this case will be called *12-hour interferometry* (Figure 7-2). This configuration is relevant for topographic applications.

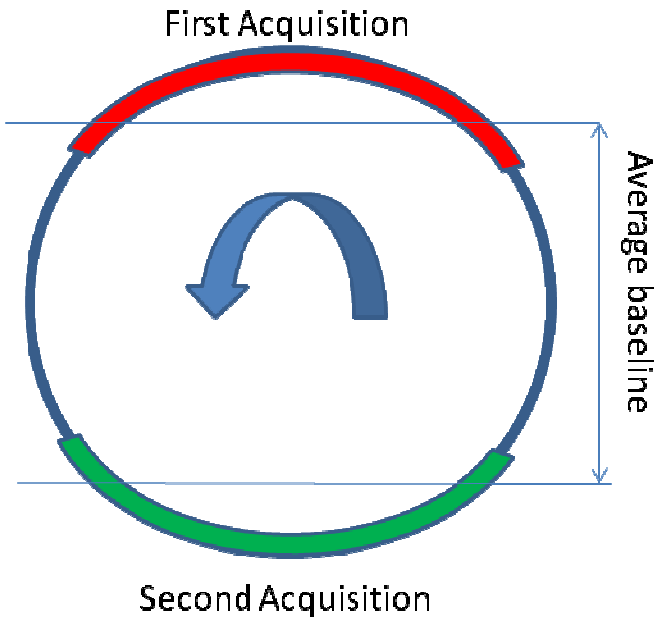

Figure 7-2. 12-hour interferometry: relative geometry of the two acquisitions

A correct prediction of InSAR performances requires a precise definition of the different contributions to the interferometric phase and to the geometrical baseline. Interferometric decorrelation issues have to be discussed as well.

The following issues have been tackled hereafter:

- bi-static interferometric phase;
- bi-static baseline estimation;
- decorrelation effects.

7.1.1 Bi-static interferometric phase

An interferometric couple is made up of two different images, for each of them both transmitter and receiver contribute to the bi-static interferometric phase. To derive its value, signals collected by the system at different epochs (i.e. $S_1(P)$, $S_2(P)$) have to be taken into account.

Signal received by the receiver (RX) from the scatterer P at time t_1 is:

$$S_1(P) = u(t-\tau_1)e^{-j\omega(t-\tau_1)}e^{j\varphi_s(P)} \qquad \text{Equation 7-1}$$

Signal received by the receiver (RX) from the scatterer P at time t_2, $S_1(P)$ is:

$$S_2(P) = u(t-\tau_2)\, e^{-j\omega(t-\tau_2)} e^{j\varphi_s(P)}$$ Equation 7-2

In previous equations, *u(t)* is the transmitted pulse;
$\varphi_s(P)$ is the phase corresponding to the scatterer P.
τ_1 and τ_2 are the range gates that correspond to the position of the scatterer P.

$$\tau_1 = \frac{r_{1,1}(P) + r_{2,1}(P)}{c}$$ Equation 7-3

$$\tau_2 = \frac{r_{1,2}(P) + r_{2,2}(P)}{c}$$ Equation 7-4

In Equation 7-3, $r_{1,1}$ is the distance from TX satellites to point P at the epoch t_1;
$r_{2,1}$ is the distance from RX satellites to point P at the epoch t_1.

In Equation 7-4, $r_{1,2}$ is the distance from TX satellites to point P at the epoch t_2;
$r_{2,2}$ is the distance from RX satellites to point P at the epoch t_2.

Given the signal collected by GeoSAR at two different epochs, interferometric phase φ is estimated via complex multiplication (Equation 7-5 and Equation 7-6).

$$\varphi = \omega_0(\tau_2 - \tau_1) = \omega_0\left[\frac{r_{1,2}(P) + r_{2,2}(P)}{c} - \frac{r_{1,1}(P) + r_{2,1}(P)}{c}\right] = \frac{\omega_0}{c}\left[\left(r_{1,2}(P) - r_{1,1}(P)\right) + \left(r_{2,2}(P) - r_{2,1}(P)\right)\right]$$
Equation 7-5

$$\varphi = \frac{\omega_0}{c}\left[\left(r_{1,2}(P) - r_{1,1}(P)\right) + \left(r_{2,2}(P) - r_{2,1}(P)\right)\right]$$ Equation 7-6

Interferometric phase for the pixel P is referred usually to a reference point (O in the following equation) in the interferogram:

$$\varphi = \frac{\omega_0}{c}\left[\left(r_{1,2}(P) - r_{1,1}(P)\right) - \left(r_{1,2}(O) - r_{1,1}(O)\right) + \left(r_{2,2}(P) - r_{2,1}(P)\right) - \left(r_{2,2}(O) - r_{2,1}(O)\right)\right]$$
Equation 7-7

The above expressions show clearly that, in the bi-static case, there are two separate contributions to interferometric phase that could be traced back to TX and RX satellites.

7.1.2 Baseline due to orbit perturbations (1-day interferometry)

Repeat-pass SAR interferometry requires two acquisitions at two different epochs; the imaging geometry will differ between the two images due to occasional orbit manoeuvres or to orbit perturbations.

Both TX and RX satellites are flying along a nearly geostationary orbit. The flight path about the geostationary position can be linearised. The parameters that have to be taken into account to model the motion of the spacecrafts are:

- ΔR, difference in altitude from the typical geostationary altitude (42164.2 km)
- e, residual orbit eccentricity
- i, residual orbit inclination.

Calculations carried out to estimate the different contributions to interferometric baseline are based on the following assumptions:

- As far as orbit perturbations are concerned, temporal baseline is equal to one or more sidereal days. This implies that all perturbations with a period of a sidereal day can be neglected.
- The baseline is the geometric distance between the acquisition points of the two considered images. It takes into account both TX and RX satellites.
- Geometrical baselines have been calculated assuming an “average” position of the satellites during the integration time.
- Only across-track interferometry has been considered.
- Baseline has been expressed in the form (B_h, B_v) that is directly related to orbit perturbations: B_h, the horizontal baseline, is equivalent to an across-track orbit difference while B_v, the vertical baseline, is equivalent to a radial difference.
- The previous assumptions imply that inclinations of the orbits of the satellites do not change.
- For every satellite, the first acquisition of each interferometric couple has been considered as the reference to calculate interferometric phase.
- According to ITU (1988) the longitudinal station-keeping requirement for a spacecraft in GEO is ±0.1° (about 73,5 km).

Moving from the horizontal and the vertical baselines (B_h, B_v), it is possible to calculate the parallel and the perpendicular components of the baseline through Equation 7-8 (Hanssen, 2001) that takes into account the antenna look angle θ_{look}.

$$\begin{cases} B_{\parallel} = B_h \sin\theta_{look} - B_V \cos\theta_{look} \\ B_{\perp} = B_h \cos\theta_{look} + B_V \sin\theta_{look} \end{cases}$$

Equation 7-8

A satellite placed in a non-ideal geostationary orbit such as GeoSAR is flying along a geosynchronous orbit with a non-zero eccentricity and inclination. Its altitude is generally not exactly equal to 42164.2 km (GEO orbit altitude).

Cazzani *et al.* (2000) provide some linearised equations to estimate longitude, latitude and altitude of a geosynchronous satellite assuming that its orbit is not perfectly geostationary and there are residual eccentricity (*e*) and inclination (*i*). Satellite altitude is as well slightly different (δR) from the GEO one. These equations are derived from Kepler's equations neglecting second order terms.

$$\begin{cases} r = R_{GEO} + \delta R - R_{GEO} e \cos\left[\omega_T (t - t_0)\right] \\ long - long_0 = 2e\left(\frac{180}{\pi}\right)\sin\left[\omega_T (t - t_0)\right] - \frac{3}{2}\frac{\delta R}{R_{GEO}}\left[\omega_T (t - t_0)\right] \\ lat = i \sin\left[\omega_T (t - t_0)\right] \end{cases}$$ Equation 7-9

In Equation 7-9, *r, lat and long* describe the position of the satellite;
$long_0$ is the initial longitude of the satellite;
ω_T is the Earth's angular velocity;
R_{GEO} is the altitude of GEO orbit.

7.1.2.1 Altitude contribution

In Equation 7-9 there is only one component of the motion that is not harmonic. Considering a 24-hour temporal baseline (1-day interferometry) there is only a term in the longitude equation that contributes to form the geometric baseline.

$$long - long_0 = -\frac{3}{2}\frac{\delta R}{R_{GEO}}\left[\omega_T (t - t_0)\right]$$
$$\omega_T = \frac{2\pi}{T}$$ Equation 7-10

In Equation 7-10, *T* is the period of revolution of the satellite that is equal to a sidereal day.

$$B_h = \Delta long\big|_{rad} R_{GEO} = -\frac{3}{2}\frac{\delta R}{R_{GEO}}\left[\frac{2\pi}{T}T\right]R_{GEO}\frac{\pi}{180} = -\frac{3}{2}\delta R 2\pi\frac{\pi}{180}$$ Equation 7-11

Both transmitter and receiver satellites have to be taken into account in the formation of the geometrical baseline.

Assuming in Equation 7-11 a δR (i.e. difference from the geostationary altitude) of about 2 km for both the satellites, the equivalent B_h after 24 hours is about 656 meters. This value for δR has been chosen in order to avoid relevant longitude displacements that would require frequent orbit control maneuvers.

7.1.2.2 Other perturbations

Assuming that the system is imaging while flying following a North-South path, perturbations that affect the satellite along this axis can be neglected as they are equivalent to an along-track displacement. The same conclusion can be drawn considering a satellite imaging while flying in the East-West direction.

The most significant perturbation that affects the East-West motion of satellites flying along a geosynchronous orbit is the longitude drift due to the anomalies in the Earth gravitational field. It causes a linear drift that could be estimated assuming a constant acceleration towards the stability points. The longitudes of stable points are 75.1°E or 254.7°E.

$$\frac{d^2 long}{dt^2} = -0.00168 \sin\left[2\left(long - long_s\right)\right] \left[\frac{\text{deg}}{\text{day}^2}\right] \qquad \text{Equation 7-12}$$

As we are interested in the relative motion between the orbits of the transmitter and the receiver, the longitude to be used in the calculation is practically equal to the bi-static angle.

For a 30° longitude separation between TX satellite and the stable point the acceleration term is:

$$\frac{d^2 long}{dt^2} = -0.00145 \text{ deg/day}^2 \qquad \text{Equation 7-13}$$

The longitudinal drift could be expressed as:

$$\Delta long = \frac{1}{2} \frac{dlong^2}{dt^2} t^2; \qquad \text{Equation 7-14}$$

That is equal to 0.00073° after 1 day. This longitude separation causes a 537 m drift. Note that the station keeping requirement for satellites in GEO is ±0.1° degrees (about 75 km).

7.1.2.3 Orbit determination accuracy

Orbit determination accuracy for both TX and RX satellites (first and second acquisition point) brings an unknown contribution to the geometrical baseline (Equation 7-15 and Equation 7-16) that is equivalent to an uncompensated phase delay. The along track position error could be neglected as it is corrected during the co-registration phase. The remaining error terms, across-track and radial error, cause an additional uncertainty to baseline estimation.

$$B_{h.noise} = \sqrt{\sigma^2{}_{a,1,1} + \sigma^2{}_{a,2,1} + \sigma^2{}_{a,1,2} + \sigma^2{}_{a,2,2}} \qquad \text{Equation 7-15}$$

In Equation 7-15, $\sigma_{a,1,1}$ is the across-track error for the first satellite and the first pass;
$\sigma_{a,2,1}$ is the across-track error for the second satellite and the first pass;
$\sigma_{a,1,2}$ is the across-track error for the first satellite and the second pass;
$\sigma_{a,2,2}$ is the across-track error for the first satellite and the first pass.

$$B_{v.noise} = \sqrt{\sigma^2{}_{r,1,1} + \sigma^2{}_{r,2,1} + \sigma^2{}_{r,1,2} + \sigma^2{}_{r,2,2}} \qquad \text{Equation 7-16}$$

In Equation 7-16, $\sigma_{r,1,1}$ is the radial error for the first satellite and the first pass;
$\sigma_{r,2,1}$ is the radial error for the second satellite and the first pass;
$\sigma_{r,1,2}$ is the radial error for the first satellite and the second pass;
$\sigma_{r,2,2}$ is the radial error for the first satellite and the first pass.

7.1.2.4 Perpendicular and parallel baseline

The relative geometry between the two acquisitions has been presented in Figure 7-1. The different circles are the various orbits followed by the spacecraft; they are displaced due to orbit perturbations.

The previous sections presented the various terms that contribute to the formation of an across-track displacement of a GeoSAR satellite during the time lapse between the acquisitions of the two images that constitute an interferometric couple.

The GeoSAR spacecraft will be flying along an orbit with a nearly circular ground-track in order to be able to form a synthetic aperture both in north-south and in east-west direction.

While flying along the north-south direction the longitudinal drift between TX and RX satellites is equivalent to an across-track displacement. While flying along the east-west direction the longitudinal drift due to orbit perturbations corresponds to an along-track displacement, therefore it does not contribute to the formation of the interferometric geometrical baseline.

Orbit perturbations described in the previous sections provide the horizontal and vertical components of the baseline. It is possible to retrieve the components of the parallel and perpendicular baseline applying Equation 7-8.

The perpendicular baseline is proportional to the factor $sin\theta_{look}$, therefore within the field of view of the antenna it could vary according to the look angle. This variation, although relevant, does not change the order of magnitude of the baseline length and does not change the conclusions that will be drawn.

Values for the perpendicular baseline in Table 7-1 are significantly smaller than the critical baseline (see section 7.1.4).

Table 7-1. Geometrical baseline due to orbital elements and longitudinal displacements. The satellite is imaging while flying along a north-south track. All the values are expressed in meters. Each line refers to a given temporal baseline.

Temporal baseline	δR (m) (TX)	δR(m) (RX)	Longitudinal Displacement TX (m)	Longitudinal Displacement RX (m)	θ_{look}	B_h (m)	B_v (m)	$B_\parallel$ (m)	$B_\perp$ (m)
1 day	2000	2000	537	537	5°	1731	0	150	1725
2 days	2000	2000	1074	1074	5°	3463	0	301	3450
3 days	2000	2000	1611	1611	5°	5194	0	452	5175

7.1.3 Perpendicular and parallel baseline (12 hour interferometry)

In the 12-hour interferometry (Figure 7-2) there is an across-track displacement because the system is imaging while it is flying at two opposite sides of the circular trajectory.

The across-track displacement, the horizontal baseline B_h between the two acquisitions, is at least the chord subtended by a 60° angle, ≈315 km. We can assume that there is no vertical baseline; therefore, the perpendicular baseline is about 300 km (5° look angle). This value is about half the value of the critical perpendicular baseline (see section 7.1.4).

7.1.4 Critical perpendicular baseline

The concept of critical perpendicular baseline will be defined in the monostatic case. As specified in previous sections, in a bi-static configuration both transmitter and receiver contribute to the formation of the baseline therefore in the bi-static case the critical perpendicular baseline has a different expression.

The concept of critical perpendicular baseline is very important to predict performances that could be achieved via SAR interferometry. The following equations describe the analytical derivation of the critical baseline for a monostatic configuration.

7.1.4.1 Monostatic case

Figure 7-3 shows the geometry that has been considered to analyse the problem.

In Figure 7-3,

B is the geometric baseline;
B_n is the perpendicular baseline;
θ is the radar incidence angle (different from the radar look angle in the GEOSAR case due to spherical Earth geometry);
α is the slope of the terrain imaged;
ρ is the slant range;
R_e is the Earth's radius (6378 km).

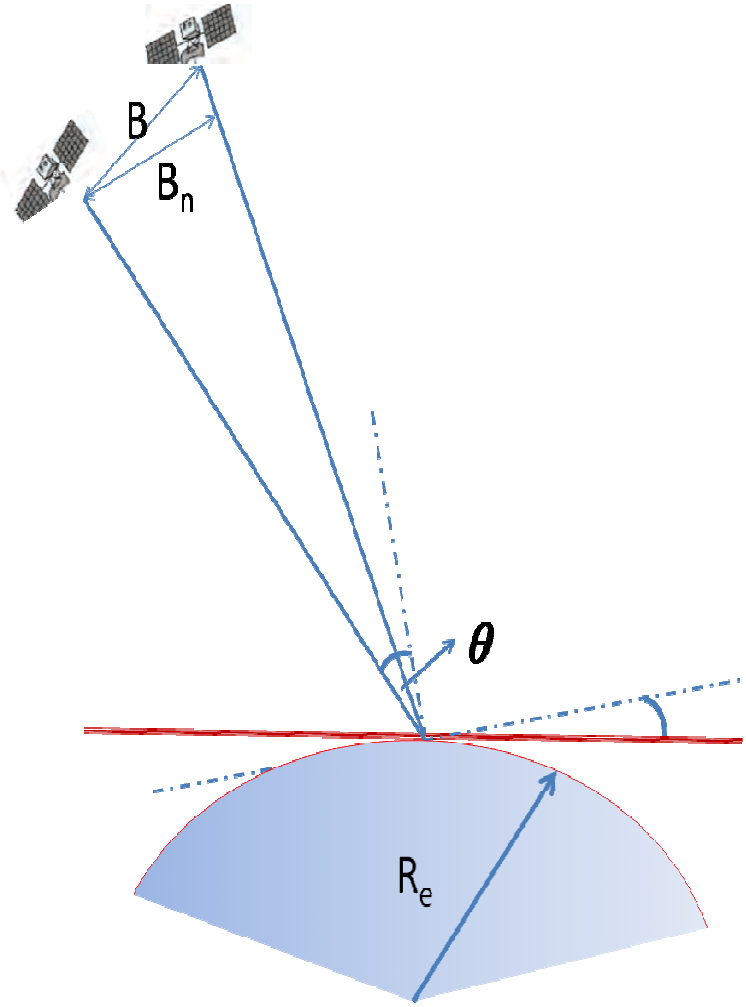

Figure 7-3. Monostatic SAR interferometry. Geometry of the problem.

$$\frac{\partial \varphi}{\partial \rho} = -\frac{4\pi}{\lambda} B \cos(\theta - \alpha) \frac{\partial \theta}{\partial \rho}$$ Equation 7-17

In Equation 7-17, φ is the interferometric phase;
remaining symbols have the same meaning as in Figure 7-3.

$$b = R_e + h$$ Equation 7-18

$$\cos\theta = \frac{b^2 + \rho^2 - R_e^2}{2b\rho}$$ Equation 7-19

$$\frac{\partial\varphi}{\partial\rho}=-\frac{4\pi}{\lambda\rho}B\frac{\cos(\theta-\alpha)}{\sin\theta}\left(\cos\theta-\frac{\rho}{h}\right)$$ Equation 7-20

The critical perpendicular baseline (assuming that the slope of the terrain α is zero) is the value that satisfies the expression in Equation 7-21.

$$\frac{\partial\varphi}{\partial\rho}=-\frac{4\pi}{\lambda\rho}\frac{B_{\perp}}{\tan\theta}+\frac{4\pi}{\lambda b}\frac{B_{\perp}}{\sin\theta}\leq\frac{2\pi}{\Delta R_{range}}$$ Equation 7-21

In Equation 7-21, ΔR_{range} is the slant range resolution.

$$\Delta R_{range}=\frac{c\tau}{2}=\frac{c}{2B_w}$$ Equation 7-22

In Equation 7-22, B_w is the bandwidth of the radar signal.

$$B_{\perp crit}=\frac{2\pi}{\frac{c\tau}{2}}\frac{1}{4\pi\left(\frac{1}{\lambda\sin\theta b}-\frac{\cos\theta}{\lambda\sin\theta\rho}\right)}=\frac{\lambda\sin\theta}{c\tau\left(\frac{1}{b}-\frac{\cos\theta}{\rho}\right)}=\frac{\lambda b\rho\sin\theta}{c\tau(\rho-b\cos\theta)}=\frac{B_w\lambda b\rho\sin\theta}{c(\rho-b\cos\theta)}$$ Equation 7-23

$$B_{\perp crit}=\frac{B_w\lambda b\rho\sin\theta}{c(\rho-b\cos\theta)}=\frac{B_w\lambda(R_e+h)\rho\sin\theta}{c\left[\rho-(R_e+h)\cos\theta\right]}$$ Equation 7-24

Considering a system in a geosynchronous orbit (h=36000 km; ρ=40000 km) with a ground incidence angle (i.e. θ) of 50°, Equation 7-24 can be expressed grouping all geometrical parameters in a single term.

$$B_{\perp crit}=B_w\lambda\frac{(R_e+h)\rho\sin\theta}{c\left[\rho-(R_e+h)\cos\theta\right]}=B_w\lambda\times0.3392[\mathrm{s}]$$ Equation 7-25

Assuming an L band (λ=0.20 m) system with 8 MHz bandwidth, 50° incidence angle the critical perpendicular baseline is equal to ≈542 km. For a longer wavelength (λ=0.25 m), the critical baseline would increase up to ≈678 km.

Equation 7-23 is a general expression that takes into account satellite altitude. In literature a simplified expression (Equation 7-26) is commonly used referring to LEO satellites (under the assumption that $\rho<<(R_e+h)$, where ρ is slant range and h is satellite altitude) (Hanssen, 2001).

$$B_{\perp crit\_monostatic}=\frac{\lambda B_w\rho\tan\theta}{c}$$ Equation 7-26

7.1.4.2 Bi-static case

In the bi-static case, the phase contribution due to a single satellite is only $2\pi/\lambda$ therefore the bi-static critical baseline is given in Equation 7-27.

$$\frac{\partial \varphi}{\partial \rho} = \left[-\frac{2\pi}{\lambda} B_{transmitter} \cos(\theta - \alpha) - \frac{2\pi}{\lambda} B_{receiver} \cos(\theta - \alpha) \right] \frac{\partial \theta}{\partial \rho} \quad \text{Equation 7-27}$$

Under the assumption that the look angle and the orbit altitude are equal for both transmitter and receiver (acceptable in the GeoSAR concept), it is possible to obtain a simplified expression for the bi-static critical perpendicular baseline (neglecting the slope of the terrain α).

$$B_{\perp crit\_bistatic} = B_{\perp transm} + B_{\perp receiver} = B_w \frac{\lambda \rho (R_e + h) \sin\theta}{c\left[\rho - (R_e + h)\cos\theta\right]} \quad \text{Equation 7-28}$$

The critical perpendicular baseline for each of the satellites is equal to half the baseline allowed for a monostatic SAR. Under the assumption that the transmitter is stationary, the critical baseline is half the value expected for a monostatic SAR.

The expression for the critical bi-static baseline is identical to that provided in Equation 7-25.

7.1.5 Interferometric noise – Decorrelation

Given the system configuration and the estimates made for the geometrical baseline in sections 7.1.2.4 and 7.1.3), it is possible to evaluate the various noise sources that affect interferometric products. The output of this analysis is essential to evaluate possible filed of applications for SAR interferometry from a geosynchronous orbit.

7.1.5.1 Thermal noise

Thermal noise effects are represented by SNR. They could be evaluated looking at the specific SNR that could be achieved on the specific type of terrain. Considering a SNR of about 9 dB, following the investigations of Just and Bamler (1994) the expression for coherence loss induced by thermal noise is:

$$\rho_{thermal} = \frac{1}{1 + SNR^{-1}} = 0.89 \quad \text{Equation 7-29}$$

According to Just and Bamler (1994) the variance of SAR phase in rad^2 is:

$$\sigma^2{}_{\Psi} = \frac{1-\rho_{thermal}{}^2}{2\rho_{thermal}{}^2} = 0.134 \text{ rad}^2 \qquad \text{Equation 7-30}$$

The variance of interferometric phase in rad^2 is (interferometric phase is relative to a pixel in the image):

$$\sigma_{\varphi}{}^2 = 2\sigma_{\Psi}{}^2 \text{ rad}^2 \qquad \text{Equation 7-31}$$

$$\sigma^2{}_{\Psi} = \frac{1-\rho_{thermal}{}^2}{\rho_{thermal}{}^2} = 0.268 \text{ rad}^2 \qquad \text{Equation 7-32}$$

$$\sigma_{\varphi} = 0.52 \text{ rad} \qquad \text{Equation 7-33}$$

Interferometric phase noise in degrees is φ=29.8°. Such statistical phase noise can be reduced by interferogram multi-looking if a loss of geometric resolution can be accepted.

Applying multi-look, it is possible to reduce the effect of thermal phase noise at the expense of resolution. Averaging 20 independent looks, the variance of thermal noise becomes:

$$\sigma_{\varphi,N} = \frac{\sigma_{\varphi,1}}{\sqrt{N_L}} = 0.11 \text{ rad} \qquad \text{Equation 7-34}$$

After multi-looking, interferometric thermal error is only 6.3°.

7.1.5.2 Height ambiguity

Section 7.1.2.4 provides a budget for the geometrical baseline. Rodriguez and Martin (1992) provide an expression that, for repeat pass interferometry, allows estimating the expected error in topographic phase given the error in interferometric phase. Height ambiguity is the error that corresponds to a 2π phase variation.

$$\delta H = -\frac{\lambda\rho\left(h+R_e\right)\sin\theta}{R_e\left(B_{\perp transm}+B_{\perp receiver}\right)}\frac{\delta\varphi}{2\pi} \qquad \text{Equation 7-35}$$

In Equation 7-35, δH is height variation;
φ is the interferometric phase;

h is the altitude of the satellites (i.e. ≈36000 km);
ρ is the slant range (i.e. ≈40000 km);
λ is the radar wavelength (0.2 m);
θ is the radar ground incidence angle (i.e. 50°).

Height ambiguity is influenced by the altitude factor A_F that is usually neglected in LEO SAR literature. Equation 7-35, under the assumption that $h<<R_e$ assumes the expression in Equation 7-36 (Hanssen, 2001).

$$\delta H = -\frac{\lambda \rho \sin\theta}{\left(B_{\perp transm} + B_{\perp receiver}\right) 2\pi} \frac{\delta\varphi}{2\pi} \qquad \text{Equation 7-36}$$

Following Equation 7-35, height ambiguity is expressed in equation Equation 7-37.

$$Height\ ambiguity = \frac{\lambda \rho \left(h + R_e\right) \sin\theta}{R_e \left(B_{\perp transm} + B_{\perp receiver}\right)} = \frac{\lambda \rho \left(h + R_e\right) \sin\theta}{R_e B_{\perp}} \qquad \text{Equation 7-37}$$

Table 7-2 shows the values of the height ambiguity for different values of the perpendicular baseline (due to both transmitter and receiver satellites). The same table includes also the expected error in topographic height due to thermal noise only for both 1-day and 12-hour interferometry following the analysis about thermal noise included in section 7.1.5.1 .

Table 7-2. Error in topographic height due to thermal noise – SNR 9 dB.

$B_{\perp}$(m)	Height ambiguity (m)	δh (m) single look	δh (m) 20 looks
3000	12154	1006	212
5000	7292	603	127
7000	5208	431	91
10000	3646	301	63
300 km (12 hour interferometry)	121	10	2

7.1.6 Topographic height and perpendicular baseline

Using a different approach, height sensitivity with respect to perpendicular baseline could be worked out.

$$H = \frac{\lambda\rho\left(R_e + h\right)\sin\theta}{2\pi R_e\left(B_{\perp transm} + B_{\perp receiver}\right)}\varphi = \frac{\lambda\rho\left(R_e + h\right)\sin\theta}{2\pi R_e B_\perp}\varphi \qquad \text{Equation 7-38}$$

$$\frac{\delta H}{\delta B_\perp} = \frac{-\lambda\rho\left(R_e + h\right)\varphi\sin\theta}{R_e B_\perp^{\,2}} \qquad \text{Equation 7-39}$$

The system parameters used to estimate topographic height sensitivity are presented in Table 7-3. Under this assumption the derivative $dH/dB_\perp$ is equal to *-1.02*.

Table 7-3. Values used to estimate the sensitivity of topographic height to perpendicular baseline variations.

ρ *(m)*	4.00 $^{X\ 10+07}$
h (m)	3.58 $^{X\ 10+07}$
H (m)	1000
R_e *(m)*	6.38x 10^6
B_{perp} *(m)*	5.00 x 10^3
θ *(deg)*	50
φ *(rad)*	π

It is important to mention that a very tight requirement on the knowledge of TX and RX satellite position is given by SAR focussing needs. Therefore, the need for a very precise knowledge of the baseline is driven by SAR focussing requirements.

7.1.6.1 Geometric correlation

Neglecting misregistration between the two SAR images constituting the interferometric couple, geometric correlation is given by Equation 7-40 (Zebker and Villasenor, 1992; Hanssen, 2001).

$$\rho_{spatial} = 1 - \frac{B_\perp}{B_{\perp critical}} \qquad \text{Equation 7-40}$$

In Equation 7-40, $B_{\perp}$ is the perpendicular baseline,
$B_{\perp critical}$ is the critical perpendicular baseline.

Considering the expression of the critical baseline given in Equation 7-25, geometric correlation is given in Equation 7-41.

$$\rho_{spatial} = B_{\perp crit} = 1 - \frac{B_{\perp} c\left[\rho - \left(R_e + h\right)\cos\theta\right]}{B_w \lambda \left(R_e + h\right)\rho \sin\theta} = 1 - \frac{2\Delta R_{range} B_{\perp}\left[\rho - \left(R_e + h\right)\cos\theta\right]}{\lambda\left(R_e + h\right)\rho\sin\theta} \quad \text{Equation 7-41}$$

$$\rho_{spatial} = 1 - \frac{2\Delta R_{range} B_{\perp}}{\lambda} \frac{\left[\rho - \left(R_e + h\right)\cos\theta\right]}{\rho\left(R_e + h\right)\sin\theta} = 1 - \frac{B_{\perp}}{B_w \lambda} \frac{c\left[\rho - \left(R_e + h\right)\cos\theta\right]}{\rho\left(R_e + h\right)\sin\theta} \quad \text{Equation 7-42}$$

Due to the large slant range and to the relatively short perpendicular baseline, the spatial decorrelation term is negligible for the 1-day interferometry.

The 12-hour interferometry exploits a quite large geometrical baseline (≈300 km) therefore there is a significant geometrical decorrelation (i.e. geometrical correlation ≈0.45).

Equation 7-43 introduces the concept of interferometric correlation (Zebker and Villasenor, 1992), taking into account only thermal and spatial correlation:

$$\rho = \rho_{thermal}\rho_{spatial} = \frac{1}{1 + SNR^{-1}}\rho_{spatial} \quad \text{Equation 7-43}$$

The expression for interferometric phase variance can be expressed using the Cramer-Rao bound (Hanssen, 2001).

$$\sigma_{\varphi}^2 = \frac{1}{2N_L}\frac{1-\rho^2}{\rho^2} = \frac{\left(1 + SNR^{-1}\right)^2 - \rho_{spatial}^2}{2N_L\rho_{spatial}^2} \quad \text{Equation 7-44}$$

In Equation 7-44, N_L is the number of independent looks.

The expression for topographic height accuracy derived from Equation 7-35 can be modified in order to provide topographic height standard deviation:

$$\sigma_h = \frac{\lambda\rho\left(R_e + h\right)\sin\theta}{2\pi R_e\left(B_{\perp transm} + B_{\perp receiver}\right)} \frac{\sqrt{\left(1 + SNR^{-1}\right)^2 - \rho_{spatial}^2}}{\sqrt{N_L}\rho_{spatial}} \quad \text{Equation 7-45}$$

Using Equation 7-45 it is possible to retrieve a new form for the standard deviation of topographic height that takes into account the decorrelation effect induced by the

perpendicular baseline. Table 7-4 and Table 7-5 provide the results achieved assuming that the radar ground incidence angle θ is 50° and the number of looks is 20.

Table 7-4. 1-day interferometry: values expected for the standard deviation of the topographic height taking into account thermal noise and geometric decorrelation. Height ambiguity is 13504 m, $B_\perp$ is 3 km and B_w is 8 MHz.

SNR (dB)	$\rho_{thermal}\,\rho_{spatial}$	σ_h *(m)*
7.0	0.83	229
8.0	0.86	203
9.0	0.88	180
10.0	0.90	160

Table 7-5. 12-hour interferometry: values expected for the standard deviation of the topographic height taking into account thermal noise and geometric decorrelation. Height ambiguity is 135 m, $B_\perp$ is ≈300 km and B_w is 8 MHz.

SNR (dB)	$\rho_{thermal}\,\rho_{spatial}$	σ_h *(m)*
7.00	0.39	8.4
8.00	0.38	8.1
9.00	0.37	7.8
10.00	0.36	7.6

Table 7-4 shows that 24-hour interferometry configuration can be applied for differential interferometry as the short baseline (keeping the geometrical correlation close to 1) makes the system extremely sensible to phase variations.

Table 7-5 shows that 12-hour interferometry, due to the large geometrical baseline, is well suited to topographic applications although the large geometrical baseline causes a significant spatial decorrelation.

7.1.6.2 Volumetric decorrelation

The contribution of volumetric decorrelation (1-γ_{vol}) depends on imaging geometry too. It could be neglected if Equation 7-46 is satisfied (Gatelli *et al.*, 1994). This condition is easily achieved for a geosynchronous orbit therefore volumetric decorrelation can be neglected.

$$|\Delta z| << \left| \frac{\lambda h \tan\theta}{2B_{\perp}} \right| \qquad \text{Equation 7-46}$$

In Equation 7-46, Δz is the height difference between the scatterers in the same resolution cell;
h is the satellite altitude;
$B_{\perp}$ is the perpendicular baseline;
θ is the ground incidence angle.

7.1.7 Bi-static SAR interferometry – summary

Two different configurations for SAR interferometry have been investigated.In the first one, the receiving satellite is imaging the same area from a slightly different point of view with a 24 hour (+ n days) temporal baseline. In this case, the across-track displacement is due only to orbit perturbations. In the second configuration, the receiving satellite is imaging the same area from a slightly different point of view with a 12 hour (+ n days) temporal baseline. In this case, the across-track displacement is due to the different positions of the satellite along the circular orbit (≈600 km diameter).

For both configurations the critical baseline has been estimated. Results show that 12-hour interferometry is suitable for topographic applications while 24-hour geometry is suitable to differential interferometry.

Various sources of decorrelation such as thermal noise or geometric and volumetric decorrelation have been looked into.

7.2 Other applications

The very short revisit time is the main advantage of GeoSAR therefore applications that require frequent passes apper as the most suitable to GeoSAR. Among them disaster response and soil moisture measurements have been considered the most relevant.

7.2.1 Rationale

Hobbs (2009) discusses the issues related to the measurement of a dynamic process. Assuming that a system is able to take a measurement every Δ seconds and that a measurement requires *s* seconds, the system is able to measure signals (i.e. phenomena) with frequencies lower than $1/\Delta$ Hz while frequencies between $1/\Delta$ and $1/s$ Hz become uncertainty that affects the measurement process (Figure 7-4).

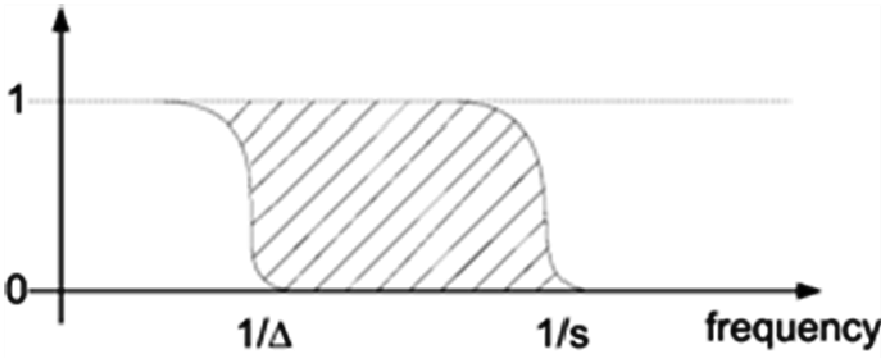

Figure 7-4. Signal bandwidth filtered by a measurement system. Δ is the sampling period and s is the measurement time (Hobbs, 2009).

LEO systems are characterised by a very short integration time *s* and by a long revisit time Δ. This implies that physical phenomena that are characterised by high frequency variations can be measured with poor accuracy. GeoSAR, on the other hand, filters out high frequency contributions (due to the relatively long integration time) but allows a very short revisit time; therefore it is suitable to measure phenomena that require frequent sampling.

7.3 Disaster response

Madsen (2001), NASA JPL (2004) considered a geosynchronous SAR as the most appropriate solution to monitor earthquakes and to provide fast-response to natural disasters. GeoSAR, besides having a 24-hour revisit time, has 1/3 of the globe in its field of regard. A constellation of 4 satellites would therefore allow nearly global coverage.

7.4 Soil moisture measurements

Soil moisture is an important parameter for agriculture and natural vegetation, but has proved to be difficult to measure accurately by Earth observation. GeoSAR could be

exploited to monitor effectively soil moisture in a way that is not viable with current satellite systems.

7.4.1 Measurement accuracy

Experiment data have been analysed to investigate the effect of the revisit time on the accuracy of soil moisture measurements. Hourly soil moisture data (Figure 7-5) from the Sevilleta experiment (Muldavin, 2004) were analysed to study the effect of changing the measurement repeat period on the accuracy of soil moisture estimates. The power spectral density of the signal has been integrated with respect to frequency to evaluate the distribution of integral signal power (Figure 7-6). A measurement system with 1-day revisit time is able to collect more than 55% of the information content of the signal while this value decreases to about 20% if the revisit time becomes 35 days.

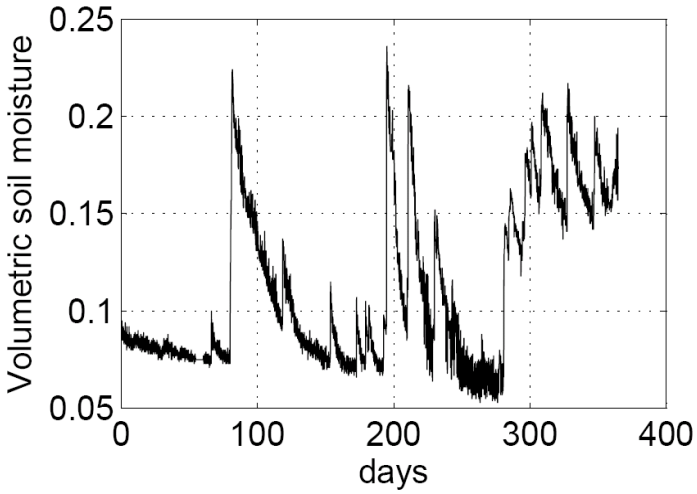

Figure 7-5. Hourly average volumetric soil moisture from the Sevilleta experiment (Muldavin, 2004).

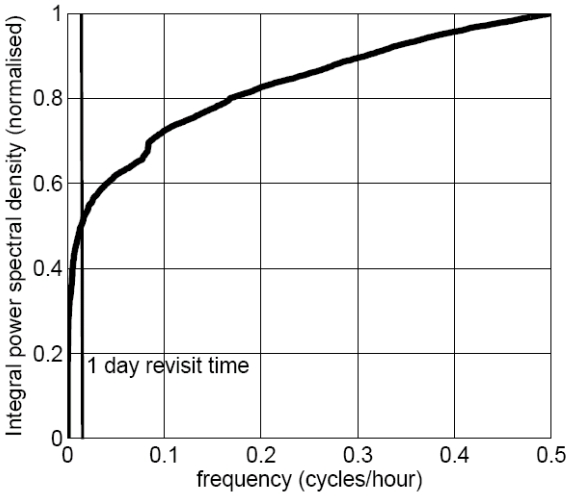

Figure 7-6. Normalised integral of the soil moisture power spectral density. The vertical line in the plot corresponds to 1-day revisit time.

Although the model is simple and is clearly influenced by the dataset used in the calculation, there is a clear indication from the results that measurements of soil moisture separated by more than a few days cannot give an accurate estimate of the average soil moisture. Since there are seasonal and geographical variations of soil moisture time dependence, appropriate measurement strategies will vary with these parameters.

These results suggest that a measurement system, which is capable of daily measurements such as GeoSAR, has the necessary temporal resolution to capture the true variation of soil moisture, where measurements with a repeat period of a week or more are likely to miss much significant variation.

Another aspect of GeoSAR's capability is that when changes of soil moisture and soil roughness occur on different timescales it should be possible to separate their effects on radar backscatter.

The first evidence of interferometric phase variations due to soil moisture was provided using L band SEASAT data (Gabriel *et al.* 1989). A technique to extract soil moisture information from SAR images using both intensity and phase information has been proposed using multi-temporal repeat-pass SAR images (Lu and Meyer, 2002). This approach is based on the assumption that only changes in surface roughness cause variations in the scattering phase and that local soil moisture variations influence only scattering amplitude. This method allows the discrimination between changes in soil roughness that affect interferometric coherence and soil moisture variations that concern only backscatter magnitude.

The main weakness of this approach is that soil moisture contribution to scattering phase cannot be neglected as it affects soil swelling as well as radar penetration depth

(Nolan and Fatland, 2003). To overcome this constraint soil moisture induced phase variations have to be identified. This could be done taking into account that changes in soil moisture and in soil roughness occur on different timescales. GeoSAR's revisit time could be exploited to separate soil moisture effects as they can be modelled taking into account their temporal correlation.

Interferometric phase can be expressed as the sum of different components (Equation 7-47).

$$\varphi = \varphi_t + \varphi_d + \varphi_a + \varphi_n \qquad \text{Equation 7-47}$$

In Equation 7-47, φ_t is the topographic phase contribution;
φ_d takes into account ground subsidences,
φ_a is the atmospheric phase delay;
φ_n is the generic phase noise term that includes all the noise sources that cannot be modelled accurately.

The last term can be specialized to include the phase term related to soil moisture explicitly as it can act as either signal or noise (Equation 7-48).

$$\varphi_n = \varphi_{soil\ moisture} + \varphi_{other\ sources} \qquad \text{Equation 7-48}$$

A parameter *K* that measures the change in radar backscatter between the two images of the interferometric couple can be used for soil moisture information retrieval (Nolan and Fatland, 2003). It has to be averaged over a window including *N* pixels (Equation 7-49).

$$K = \frac{\sum_{i=1}^{N} \left| \sigma_{1i}^{0} \right|}{\sum_{i=1}^{N} \left| \sigma_{2i}^{0} \right|} \qquad \text{Equation 7-49}$$

Soil moisture affects both radar backscatter magnitude and phase, therefore a joint analysis of residual phase noise (Equation 7-48) and of magnitude variations (Equation 7-49) could provide a way of retrieving soil moisture information from SAR interferometry in areas that are not strongly affected by temporal decorrelation (i.e. bare soil or sparsely vegetated areas).

A 12-hour revisit time is particularly suitable to monitor soil moisture variations. Permanent Scatterer (PS) interferometry (Ferretti *et al.* 2001; Ferretti *et al.* 2003) can be effectively applied on frequent interferograms. Moving from the PS approach it is possible to obtain an interferogram that is not biased by ground deformation and atmospheric phase delays. This product could therefore be used to filter out a soil moisture contribution that can be discriminated bearing in mind that it is temporally

correlated and that the residual phase contribution is related to a change in backscatter magnitude.

7.5 Conclusions

This sections draws the conclusion about GeoSAR's possible applications.

7.5.1 GeoSAR interferometry

Considering the 24-hour revisit time interferometry is the most obvious field of application for GeoSAR.

Two different geometries are obtained if the two images are taken when the spacecraft is at the opposite sides of its flight path with 180° difference in the argument of perigee (12-hour baseline interferometry) or when the satellite is at the same position along its orbit but there is a displacement induced by orbit perturbations (1 day baseline interferometry).

In 1-day interferometry, geometric baseline is caused by orbit perturbations or by deliberate orbit manoeuvres. The amount of displacement of the spacecraft is limited by station keeping issues that usually limit in longitude the east-west wander of the spacecraft. Due to the large slant range, the perpendicular baseline is usually very small (about 5 km) compared to the critical baseline (about 600 km). This implies that this configuration is well suited for differential interferometry. In 12-hour geometry the baseline is about 300 km. Although this configuration shows a significant geometric decorrelation (i.e. about 0.4), the significant geometric baseline could be exploited for topographic applications.

7.5.2 Disaster response and soil moisture

Disaster response is an application that requires a very short revisit time and therefore is well suited to GeoSAR. A geosynchronous satellite, moreover, has 1/3 of the globe in its field of regard.

Soil moisture measurements as well will strongly benefit from GeoSAR's 24-hour revisit time. The analysis of 1-hour sampled experimental data showed that measuring soil moisture with 1-day revisit time allows users to reconstruct effectively its temporal variations.

8 Conclusions and further work

Relevant conclusions and follow-on areas for the present research have already been included in the relevant chapters.

This chapter will provide a synthesis of the research (section 8.1) and then will focus on the main findings and conclusions (section 8.2). They have been grouped in accordance to the objective that they meet. Section 8.3 summarises the areas of further work that have been identified.

8.1 Overall discussion

This report presents research undertaken at the Cranfield University Space Research Centre (SRC) from October 2003 to September 2009. The work focuses on the development and analysis of a geosynchronous SAR concept.

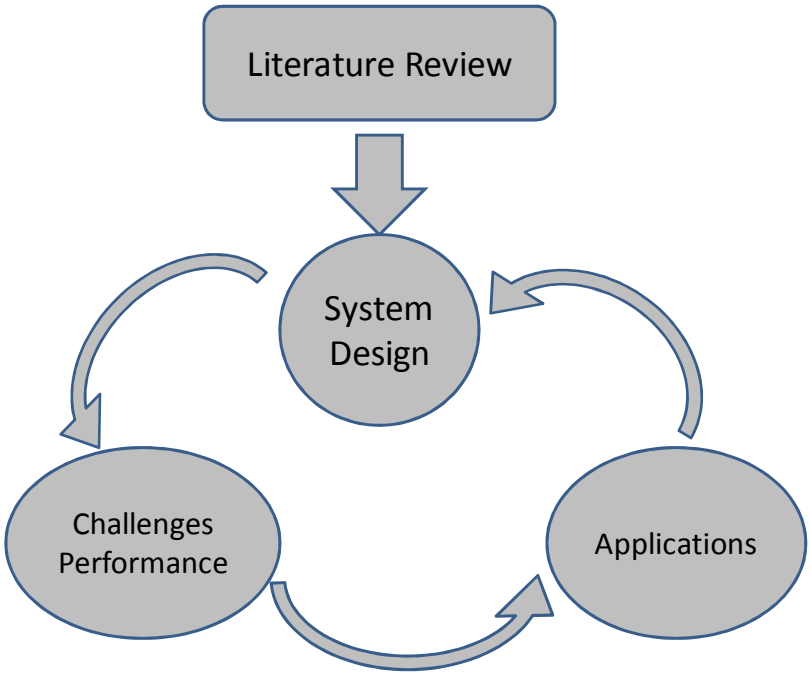

Figure 8-1. Overall research logical flow.

The aim of the research is to "*propose a geosynchronous SAR configuration, analyse quantitatively its performances and its limitations focussing on possible fields of applications"*. To tackle this problem, three main objectives have been identified.

1) Investigate both active and passive geosynchronous SAR configurations to choose a suitable system design.

2) Analyse technical challenges and predict quantitatively system performances.

3) Investigate possible fields of applications.

Figure 8-1 shows the logical flow of the research. Moving from literature review, a system design has been developed with the aim of selecting the most suitable configuration. The design proposed has been looked into in order to investigate performances and technical challenges. Particular emphasis has been given to issues related to image formation. Relevant potential applications for the system design under discussion have been investigated.

During the research, the logical process described above has been run iteratively to adapt the system design to requirements driven by applications and by technical feasibility.

Geo-synchronous SAR concept dates back to late 70s (Tomiyasu, 1978; Tomiyasu and Pacelli, 1983), however more substantial work about a possible system design has been provided by Prati *et al.* (1998) for a passive bi-static configuration, and by Madsen *et al.* (2001) for an active configuration. None of these papers however discuss in details the main technical challenges of the concepts developed.

System design explored both active and passive configurations in order to unveil their advantages and their complexities. A complete frequency trade-off has been carried out in order to justify the selection of the radar frequency. L band has been identified as the most suitable frequency for both configurations in order to tackle problems related to temporal decorrelation.

A passive bi-static configuration has been preferred to an active monostatic, as the latter requires a very large antenna and a significant transmitted power that prevents this system to be practically realised with current technologies. On the other hand a bi-static passive system is considered as a potential low budget mission (financial budget <100 M€).

Moving from this analysis GeoSAR, a concept for a geosynchronous bi-static passive SAR, has been developed at Cranfield Space Research Centre. This satellite reuses the L band signal transmitted by any transmitter of opportunity that can be in GEO as well. The spacecraft, with a 6 m diameter circular antenna, flies along a geosynchronous orbit with a circular ground-track (about 92 km radius) to achieve a nominal 100 m resolution, collecting signal during the 8-hour integration time. Applications have been the major drivers in the final orbit selection. A circular ground-track orbit allows two different imaging geometries for SAR interferometry (i.e. 12-hour and 1-day interferometry) that are suitable respectively for topographic mapping and differential interferometry. Moreover, the geosynchronous circular orbit, with respect to the figure-of-eight one, allows imaging while flying both in the North-South and in the

East-West directions. In this way, it is possible to image with nominal resolution in the whole antenna footprint.

GeoSAR's main peculiarity is the 8-hour integration time required to achieve an azimuth resolution of about 100 m. Signal phase coherence over such timescale is a significant challenge and some decorrelation aspects, usually neglected in conventional LEO SAR (i.e. Earth tides, tropospheric noise and ionospheric noise), have to be taken into account. An azimuth SAR processor has been implemented in Matlab in order to simulate the effects of various decorrelation sources on the azimuth Point Spread Function (PSF). In the present research, the analysis has been limited to three main sources of decorrelation: Earth tides, tropospheric delay and ionospheric delay.

Earth tides and tropospheric delay models available in literature allow the system to be able, in post-processing, to cope with their induced variable phase delays. Ionospheric phase delays, due to their temporal and spatial variability, cannot be properly compensated by applying analytical models. A split-spectrum approach could be used to estimate ionospheric TEC while imaging; however, although GeoSAR allows to measure TEC with a good accuracy (accuracy 2,4 TECU, 2 hour sampling), in presence of strong ionospheric heterogeneities system performances can be seriously affected.

A focussing procedure that iteratively increases the integration time (starting from ionospheric decorrelation time) could be used to achieve the best possible ground azimuth resolution and to extract very valuable information about temporal ionospheric variations. Imaging during the day when the level of ionospheric turbulence is lower is an alternative approach to tackle ionospheric noise. Temporal decorrelation aspects clearly reduce the spectrum of possible applications. Due to ionospheric perturbations, GeoSAR could not be able to provide in all circumstance its nominal resolution although coarser resolution implies more frequent imaging.

Repeat-pass interferometry is the most obvious field of application for GeoSAR. Differential interferometry could be carried out with good performances as orbit perturbations do not allow for the formation of a significant geometrical baseline (1-day interferometry). Imaging from opposite sides of the circular ground-track can be used for repeat-pass interferometry to have a large geometrical baseline and the shortest temporal baseline (i.e. 12-hour interferometry). Soil moisture monitoring has been identified as one of the most promising fields of applications for the system.

The present research provides a better understanding of the technical complexities that lay behind a geo-synchronous SAR and their implications on possible future practical implementation of this concept. The analysis about temporal decorrelation aspects and their implications on SAR systems that require a long integration time has an high degree of novelty; phase errors induced by Earth tidal motion, in particular, have never been tackled in previous SAR literature as well.

The geometrical model implemented to provide an analytical expression for the bi-static phase shows that relative position between transmitter and receiver has to be known with millimetre accuracy. This will pose a strict requirement on AOCS sub-systems of both satellites involved, thus increasing the complexity of the receiving satellite and limiting the number of potential transmitters of opportunity.

These problems have not been tackled in any previous research and unveil some difficulties that could increase the complexity of an eventual GeoSAR mission.

Looking towards a more advanced stage of GeoSAR's system design, the above-mentioned problems have to be taken into account as they increase the technical risk of the project. In particular, orbit accuracy requirements and ionospheric phase delay correction algorithms have to be carefully taken into account.

Some risk reduction technology demonstration programs, eventually carried on-board of existing platforms, are the best programmatic options to acquire some information in the above-mentioned grey areas. This solution could be adopted to collect some experimental data and demonstrate the technical feasibility of the concept. A demonstrator could be a cost-effective solution to test the ability, with dedicated SAR processing algorithms, to achieve image formation and tackle limitations imposed by orbit determination accuracy and temporal decorrelation.

To investigate all issues related to ionospheric decorrelation aspects, a technological demonstrator should be developed at L-band although it might require a large antenna that could prevent this system from being a secondary payload on another satellite. Having said that, an experiment to test GeoSAR processing algorithms could be developed at shorter wavelengths (up to K band) to reduce the mass budget of the experiment. In this case, as emphasised in the trade-off analysis, tropospheric noise could be the main decorrelation source of this system; however, this experiment could be relevant in terms of developing auto-focus algorithms and testing the capability to form a SAR image from space over a long integration time. With the aim of reducing technical risk associated to such a technology demonstrator, the receiver could be carried on-board the transmitting satellite; in this way all complexities related to precise relative orbit position between transmitter and receiver could be removed.

The application of auto-focus algorithms is likely to provide products with a ground resolution proportional to the correlation time of phase noise affecting the image. Therefore, GeoSAR's possible fields of applications depend from the capability of coping with temporal decorrelation issues. A technology demonstrator focused on temporal decorrelation aspects could be relevant to define the expected quality of GeoSAR's products and to clearly identify scientific drivers that could be used to justify the need for the development of a geosynchronous SAR concept.

In conclusion, having discussed the potential of the concept and its main drawbacks, only after a proper demonstration about the technological capability of coping with all image formation issues, the system will be mature for a potential dedicated mission.

8.2 Statements of conclusions

The conclusions will be grouped hereafter according to the objective they refer to.

8.2.1 Objective 01: System design

Active monostatic and passive bi-static geosynchronous SAR configurations have been looked into. Both the concepts have been demonstrated in literature.

An active configuration has to fly on a highly inclined geosynchronous orbit to allow for a significant synthetic aperture. It has a relatively short integration time (minutes) and therefore temporal decorrelation aspects are not as relevant as in the passive bi-static. Antenna size and power requirements are the two major drawbacks of the active geosynchronous SAR; therefore, this configuration does not appear feasible in the short term due to its costs and to its technical complexities.

A passive bi-static configuration does not require new technologies to be developed and can be proposed as a candidate for a low-cost space mission. The major driver in the system design is the amount of power provided by the transmitter of opportunity being used. To collect enough signal power it has to fly along a low inclination geosynchronous orbit. The oscillation of the spacecraft along its path has to be shorter that the achievable synthetic aperture in order to achieve a long integration time (i.e. 8 hour). Due to this limitation, the length of the satellite motion drives azimuth resolution.

A system design trade-off has been carried out in order to determine the most suitable configuration in terms of frequency and integration time. A technical feasibility trade-off has been completed to investigate the effects of phase delay and of the link budget at various frequencies (from P to K band) employing different integration times (from 1 minute to 8 hours). Following this study a frequency trade-off allowed to determine that L band is the most suitable frequency for its robustness to temporal decorrelation.

Matching the outcomes of the two trade-off analysis, a passive bi-static L band configuration has been proposed as the most suitable configuration. Moving from this approach a spacecraft system design has been carried out at Cranfield Space Research Centre. A circular ground-track orbit has been preferred to a figure-of-eight orbit as it allows to image with the same resolution both when flying along the north-south and the east-west portion of the trajectory. The passive bi-static configuration requires an appropriate transmitter of opportunity that transmits a suitable signal with the required properties. This research assumes that such a satellite is available and does not investigate the influence of the transmitted waveform on the system design.

8.2.2 Objective 02: System technical complexities

The analysis carried out for the GeoSAR configuration stated that the issues related to temporal decorrelation are the most relevant technical complexities. Due to the 8-hour integration time, unstable scatterers and instabilities in the propagation medium have to be taken into account in SAR image processing. This problem is usually not addressed in SAR literature as conventional LEO SAR images are focused under the assumption that both the scene and the atmosphere are frozen during the integration time.

An azimuth SAR processor has been implemented in Matlab in order to simulate the effect of various decorrelation sources on the azimuth Point Spread Function (PSF).

Phase fluctuations increase system Doppler bandwidth and therefore, in presence of fluctuating phase delays, a portion of the reflected energy does not affect the main lobe of the synthetic aperture. An analytical expression has been proposed in order to estimate the amount of clutter that the system is able to reject, given its variance and its correlation time.

A more detailed analysis has been provided for the three main sources of decorrelation that have been identified: Earth tides, tropospheric delay and ionospheric delay. All the terms need to be compensated to avoid substantial degradation in GeoSAR imaging.

Earth tides can be accurately modelled and their residual error can be neglected. Only solid Earth tides and ocean loading contribute significantly to site displacements on GeoSAR's temporal and spatial scales.

Tropospheric dry propagation delay can be modelled with a very good accuracy if synoptic meteorological parameters (i.e. static pressure and temperature) are known. Tropospheric wet delay has complex temporal and spatial variations that are due to turbulence and water vapour distribution. An accurate modelling requires the use of complex numerical meteorological models together with information about orography and land use. Analytical model available in literature do not guarantee the same level of accuracy; however, they allow coping with tropospheric wet delay with an acceptable coherent integration loss (about 1 dB).

Ionospheric phase delays, due to their temporal and spatial variability, cannot be properly compensated by applying analytical models. Real TEC measurements (30 second sampling) from the *spectre* dataset have been used in the analysis. Some data about temporal and spatial ionospheric decorrelation have been derived. A split-spectrum approach can be used to estimate ionospheric TEC while imaging. With this technique, GeoSAR allows to measure TEC with a good accuracy (accuracy 2.4 TECU, 2 hour sampling). The system is able to cope with disturbances that happen only for a fraction of the integration time while, in presence of strong ionospheric heterogeneities, its performances can be seriously affected.

An iterative focussing procedure that processes data with progressively longer integration time (starting from ionospheric decorrelation time) can be used to achieve the best possible ground azimuth resolution and to extract very valuable information about temporal ionospheric variations. Imaging during the day when the level of ionospheric turbulence is lower is an alternative approach to tackle ionospheric noise.

8.2.3 Objective 03: Possible fields of applications

GeoSAR's applications can benefit from its very short revisit time, as the system is in principle able to image any area in its field of view once every 12 hours.

Due to the long integration time, only stable scatterers will be imaged with a significant SNR. L band is able to penetrate the canopies and reach the soil surface providing significant benefits to InSAR processing.

Differential interferometry can be carried out with good performances as orbit perturbations do not allow for the formation of a significant geometrical baseline. Imaging from opposite sides of the circular ground-track can be used for repeat-pass interferometry to shorten the temporal baseline (i.e.12-hour) and achieve a larger geometrical baseline (i.e. 300 km).

Disaster response is well suited to GeoSAR as it can benefif from the short revisit-time and the wide field of regard.

Soil moisture monitoring has been identified as one of the most promising fields of applications for the system. Measuring soil moisture with 1-day revisit time allows collecting a significant amount of information about its variations.

8.3 Further work

Overall, the analysis has revealed a number of areas for further investigation and research. They have been grouped in four areas: multi-static configurations, spacecraft system design, signal processing and ionospheric monitoring.

- Multi-static configuration

The analysis carried about multi-static configurations showed that the geosynchronous orbit is particularly suitable to multi-static operations. With respect to a LEO constellation, large slant range allows for a larger tolerance in the knowledge of the topography of the imaged terrain.

The SAR train concept (Aguttes, 2003; Aguttes, 2004) can be applied to GeoSAR to make a multi-static configuration with improved system performances. This concept

has been discussed in the background chapter and two operating modes have been investigated: a first one that has random spacing between the spacecraft forming the constellation and a second one that requires exact spacing in the flying formation. Only the first operating mode (random spacing) can be applied to GeoSAR as very tight formation flying requirements cannot be met for the whole integration time.

Spread-spectrum waveforms have an unambiguous ambiguity function therefore could allow for a multi-static constellation with relaxed formation flying constraints.

- GeoSAR spacecraft design

The AOCS and the ground segment could benefit from the analysis that has been carried out about bi-static SAR phase and its sensitivity to the measurements of the transmitter-receiver baseline. The geo-location budget provides further information that can be used to define a performance requirement for the AOCS sub-system.

- Signal processing

GeoSAR synthetic antenna formation poses many challenges that require further research activities. In all configurations proposed, spacecraft flies along a curved path; therefore, a dedicated algorithm should be developed to obtain synthetic aperture focusing for non-linear trajectories.

The bi-static proposed configuration requires a non-cooperative transmitter. Looking forward to a possible co-operative mission, the most appropriate waveform for GeoSAR should be defined in order to set the specifications for a transmitter that could eventually be deployed for the purpose on a GEO spacecraft.

The simulator implemented in the present research is dealing only with azimuth SAR processing. GeoSAR's data processor can be modified to include fast-time (i.e. range) processing. This would allow to simulate the effect of spatial heterogeneities.

The effect of variable phase delays is the main issue in GeoSAR image formation. A more advanced system design requires the evaluation of the performances of auto-focus algorithms such as Phase Gradient Algorithm and Short Time Fourier Transforming in estimating variable phase delays due to ionospheric and tropospheric perturbations.

- Ionospheric monitoring

TEC measurements collected with GeoSAR, with appropriate post-processing, can be used to provide accurate TEC maps on a national base without the need of any ground equipment (such as GPS networks). GeoSAR could measure TEC with accuracy better than systems that are currently used (GPS networks).

Accurate TEC measurements can be a potential outcome of innovative GeoSAR data processing that refines iteratively (with the aim of compensating phase delays) TEC distributions.

- Interferometry

GeoSAR is flying along a curved path therefore, to generate an interferogram, trajectories of the two passes have to be linearised to obtain a geometry with a constant baseline throughout the whole integration time. This increases the complexity of interferogram generation and introduces a further source of decorrelation as this process introduces some residual phase delay.

References

1. Agrawal, B. N. 1986. Design of Geosynchronous Spacecraft. New York: Prentice-Hall.

2. Aguttes, J. P., inventor. 2003. Formations orientées le long du trajet du satellites SAR. CNES, assignee. European Patent Office EP 1369704 A01.

3. Aguttes, J. P., 2004. The SAR Train concept: Required antenna area distributed over N smaller satellites, Increase of performance by N. Paper Nr.IAC-04-B.2.09 presented at 55th International Astronautical Conference, Vancouver (Canada)

4. Anderson, D. and Fuller-Rowell T. 1999. Space environment topics: the ionosphere. Citing Internet resources (www document) [http://sec.noaa.gov]. *Last accessed* August 2007.

5. Anderson, P. R. and Bartamian L. 2008. Growth trends in communication satellites and the impact on satellite system architecture. 26th International Communications Satellite Systems Conference (ICSSC), San Diego USA, 10-12 June 2008; AIAA 2008-5440.

6. Askne, J. and Nordius H. 1987. Estimation of tropospheric delay for microwaves from surface weather data. Radio Science 22: 379-86.

7. Bamler, R. and Eineder M. 2005. Accuracy of differential shift estimation by correlation and split-bandwidth interferometry for wideband and Delta-k SAR systems. IEEE Transactions on Geoscience and Remote Sensing Letters 2, no. 2: 151-5.

8. Barber, B. C. 1985. Theory of digital imaging from orbital synthetic aperture radar. International Journal of Remote Sensing 6, no. 7: 1009-57.

9. Bate, R. R. Mueller D. D. and White J. E. 1971. Fundamental of astrodynamics. New York: Dover Publications, Inc.

10. Belcher, D. P. 2008. Theoretical limits on SAR imposed by the ionosphere. IET Radar, Sonar and Navigation 2, no. 6: 435-48.

11. Bevis, M. Businger S. and Chiswell S. 1994. GPS Meteorology: mapping zenith wet delays onto precipitable water. Journal of Applied Meteorology 33: 379-86.

12. Bevis, M. Chiswell S. Businger S. Herring T. A. and Bock Y. 1996. Estimating

wet tropospheric delays using numerical weather analysis and predictions. Radio Science 31 , no. 3: 477-87.

13. Bevis, M. Businger S. Herring T. A. Rocken C. Anthes R. A. Ware R. H. 1992. GPS Meteorology: Remote Sensing of Atmospheric Water Vapor Using the Global Positioning System. Journal of Geophysical Research 97, no. D14: 15787-801.

14. Bilitza, D. 2001. International Reference Ionosphere 2000. Radio Science 36, no. 2: 261-75.

15. Bohem, J., Kouba, J. and Schuh, H. 2008. Forecast Vienna Mapping Functions 1 for real-time analysis of space geodetic observations, Journal of geodesy. Note: available on line at [www.springerlink.com].

16. Brosche, P. and Schuh A. 1998. Tides and Earth rotation. Surveys in Geophysics 19: 417-30.

17. Bruno, D. Hobbs S. and Ottavianelli G. 2006. Geosynchronous Synthetic Aperture Radar: concept design, properties and possible applications. Acta Astronautica 59: 149 – 156.

18. Carrara, W. G. R. S. Goodman R. M. Majewski. 1995. Spotlight Synthetic Aperture Radar. Northwood: Artech House.

19. Cazzani, L. Colasanti C. Leva D. Nesti G. Prati D. Rocca F. and Tarchi D. 2000. A Ground-based parasitic SAR experiment. IEEE Transactions on Geoscience and Remote Sensing 38, no. 5: 2132-41.

20. Chen, V. C. and Ling, H. 2002. Time-frequency transforms for radar imaging and signal analysis, Boston USA: Artech House.

21. Cherniakov, M. 2008. Bistatic Radar Emerging technology. New York: John Wiley and sons.

22. Closa, J. 1998. The influence of orbit precision in the quality of ERS SAR interferometric data. ESA, Technical Report ES-TN-APP-APM-JC01. Note: available on line at [http://envisat.esa.int/rootcollection/sysutil/orbites.html].

23. Crespon, F. Jeansou E. Helbert J. Moreaux G. Lognonné P. and Godet and Garcia P. R. 2007. SPECTRE (www.noveltis.fr/spectre): a web service for ionospheric products. Proceedings, 1st Colloquium Scientific and Fundamental Aspects of the Galileo Programme, Toulouse, France, October, 2007. Note: available on line at [http://www.noveltis.fr/spectre/interface/pdf/ProceedingGalileo2007_SPECTRE.pdf]

24. Cumming, F. and Wong F. 2005. Digital Processing of SAR data. Northwood,

USA: Artech House.

25. Curie, A. and Brown M. A. 1992. Wide swath SAR. IEE Proceedings-F 139, no. 2: 122-35.

26. Curlander, J. C McDonough R. N. 1991. Synthetic aperture radar - Systems and signal processing (Book) . New York: John Wiley and sons.

27. Davis J. L., Herring T. A. Shapiro I. I. Rogers A. E. E. and Elgered G. 1985. Geodesy by radio interferometry: effects of atmospheric modelling errors on estimates of baseline length. Radio Science 20, no. 6: 1593–1607.

28. Egbert, G. D. and Erofeeva, S.Y. 2002. Efficient inverse modeling of barotropic ocean tides, Journal Atmospheric Oceanic Technology, 19(2), 183-204

29. El-Gizawy. M. L. 2003. Development of an Ionosphere Monitoring Technique Using GPS Measurements for High Latitude GPS Users. Calgary, UCGE Reports Number 20171. Citing Internet resources (www document) [http://www.geomatics.ucalgary.ca/ links/GradTheses.html]. *Last access* April 2007

30. Elder, K. J. 2002. The detection and measurement of landfill subsidence using SAR interferometry. MSc Thesis academic year 2001/2002, Cranfield University.

31. Elgered, G. Davis J. L. Herring T. A. and Shapiro I. I. 1991. Geodesy by Radio Interferometry: Water Vapor Radiometry for Estimation of Wet Delay. Journal of Geophysical Research 96, no. B4: 6541-55.

32. ESA ENVISAT. 2006. RA2/MWR Products User Guide. Citing Internet resources (www document) [http://envisat.esa.int/handbooks/ra2-mwr/CNTR2-7-1-13.htm]. *Last access* January 2007.

33. Ferretti, A. Monti-Guarnieri A. Prati C. Rocca F. and Massonet D. 2007. InSAR Principles: Guidelines for SAR Interferometry Processing and Interpretation. Nordwijk, The Nederlands: ESA, TM-19.

34. Ferretti, A. Prati C. and Rocca F. 2001. Permanent Scatterers in SAR Interferometry. IEEE Transactions on Geoscience and Remote Sensing 39, no. 8: 8-20.

35. Ferretti, A. Prati C. and Rocca F. 2003. Process for radar measurements of the movement of city areas and land sliding zones. Patent no.US6583651.

36. Franceschetti, G. and Lanari R. 1999. Synthetic Aperture Radar Processing. Boca Raton: CRC Press.

37. Franceschetti, G. and Schirinzi G. 1990. A SAR processor based on two-dimensional FFT codes. IEEE Transactions on Aerospace and Electronic Systems 26, no. 2: 356-66.

38. Franceschetti, G. Migliaccio M. and Riccio D. 1995. SAR simulation, an overview. IEEE Transactions on Geoscience and Remote Sensing: 2283-5.

39. Franceschetti, G., Migliaccio, M., Riccio, D., and Schirinzi, G. 1992. SARAS: A synthetic aperture radar (SAR) raw signal simulator. IEEE Transactions on Geoscience and Remote Sensing 30, no. 1: 110-22.

40. Gabriel A. K. , Goldstein R. and Zebker H. A. 1989. Mapping small elevation changes over large areas: Differential radar interferometry. Journal of Geophysical Research 94: 9183-91.

41. Gatelli, F. Monti Guarnieri, A. Parizzi, F., Pasquali, P. Prati C. and Rocca F. 1994. The wavenumber shift in SAR interferometry. IEEE Transactions on Geoscience and Remote Sensing 32, no. 4: 855-65.

42. Ghiglia, D. C. and Pritt M. D. 1998. Two-dimensional phase unwrapping: theory, algorithms and software. New York: John Wiley and sons, Inc.

43. Graham, L. C. 1974. Synthetic interferometer radar for topographic mapping. Proceedings of the IEEE 31, no. 1: 180-91.

44. Gray, A. L. Mattar K. E. and Sofko G. 2000. Influence of ionospheric electron density fluctuations on satellite radar interferometry. Geophysical Research Letters 27, no. 10: 1451-4.

45. Greene, C. A. and Moller R. T. 1961. The effect of normally distributed random phase errors on synthetic array gain aperture. IEEE Transactions on Military Electronics: 130-9.

46. Griffiths, H.D., Baker, C.J., Ghaleb, H., Ramakrishnan, R. and Willman, E. 2003. Measurement and analysis of ambiguity functions of off-air signals for passive coherent location. Electronics Letters, Vol.39, No.13, pp1005-1007.

47. Hall, M. P. M. Barclay L. W. and Hewitt M. T. 1996. Propagation of radio waves. London: The Institution of Electrical Engineers.

48. Hanssen, R. F. 2001. Radar interferometry: Data Interpretation and error analysis. Dordrecht: Kluwer academic publishers.

49. Hartl, P. Nahvi M. J. Rieger S. Wiesbeck W. Scivier M. S. Corr D. G. Sieber A. J. 1986. Simulation of synthetic aperture radar data products. Proceedings of the SAR Applications Workshops 16-18 September 1986, Frascati (Italy).

50. Hensley S., Rodriguez E. Siqueira P. Chapin E. Michel T. and Simard M. 2003. Vegetation Parameters using TOPSAR and GeoSAR Sensors. POLINSAR 2003, 14-16 January 2003, Frascati, (ITA).

51. Hobbs, S. E. 2009. A Measurement physics view of Earth observation, RSPSoc annual Meeting, Leicester, UK, September 2009.

52. Hobbs, S. E. 2008. Sarsim SAR simulator, Technical note. Cranfield: Cranfield University, *unpublished material*.

53. Hobbs, S. E. 2002. SAR interferometry, Technical note. Cranfield: Cranfield University. *unpublished material*.

54. Hobbs, S. E., 1997. Weather Effect on SAR backscatter for agricultural surfaces. Fringe 96 Workshop, ERS SAR interferometry: ESA SP-406, pagg. 179-88.

55. Hobbs, S. E. Bruno D. 2006. Quantifying Micrometeoroid Impacts on Large Space Structures to Assess Attitude Disturbance and Surface Damage: GeoSAR Case Study. 7th DCSS Conference Proceedings, July 2006, Greenwich (UK).

56. Holley, R. Wadge G. and Zhu M. 2008. New insights into the nature and effects of the water vapour field on InSAR measurements over Etna. Proceedings of FRINGE 2007 Workshop, ESA Special Publication SP-649.

57. Ifadis, I. 1986. Göteborg, Sweden: School of Electrical and Computer Engineering, Chalmers University of Technology, Technical Report no. 38L.

58. Ishimaru, A. Kuga Y. and Liu J. 1999. Ionospheric effects on synthetic aperture radar at 100 MHz to 2 GHz. Radio Science 34, no. 1: 257-68.

59. ITU. 1988. Handbook Satellite Communications, fixed-satellite service. International Telecommunication Union, Geneva (Switzerland).

60. ITU. 2003. Characteristics of precipitation for propagation modelling, Recommendation ITU-R P.837-4, ITU-R P Series, ITU-R, Int. Telecomm. Union, Geneva Switzerland.

61. Jakowatz, C. V. Eichel P. H. and Ghiglia D. C. 1989. Autofocus of SAR imagery degraded by ionospheric-induced phase errors. Millimeter Wave and Synthetic Aperture Radar (SPIE Proc. Vol 1101) pp. 46-52.

62. Jakowatz, C. V., Wahl, D. E. 2006. Correction of propagation-induced defocus effects in certain spotlight-mode SAR collections. Algorithms for synthetic aperture radar imagery. Conference no. 13, 17-20 April, 2006, Kissimmee, Florida, USA, vol. 6237, pp. 62370I.1-62370I.6.

63. Jefferys, S. 2006. GDP report: GeoSAR mission analysis. Cranfield: Cranfield Space Research Centre.

64. Just, D. and Bamler R. 1994. Phase statistics of interferograms with applications to synthetic aperture radar. Applied Optics 33, no. 20: 4361-8.

65. Knight, P. A. 1997. SAR interaction modeling software, contract MRC ref. 122.0, Backscatter software user guide. GEC Marconi Research Centre, Space Division, Avionics Laboratory, Tech. Report Ref. Y/BD/970283/BA402.

66. Konno, H. Pullen S. Luo M. and Enge P. 2005. Analysis of Ionosphere Gradient Using Japan GEONET Data. ION NTM 2005, January 24-26, 2005 San Diego CA, USA.

67. Koo, V. C., Lim T. S. and Chuah, H. T. 2005. A Comparison of Autofocus Algorithms for SAR Imagery. Progress In Electromagnetics Research Symposium 2005, Hangzhou, China, August 22-26: 16-19.

68. Kudryatvsev, S. 2002. Precision analytical calculation of Geodynamical effects on satellite motion. Celestial Mechanics and Dynamical Astronomy 82: 301-16.

69. Lee, C. 2003. Satellite radar imaging from geosynchronous orbit. MSc Thesis academic year 2002/2003, Cranfield University.

70. Leick, A. 2004. GPS Satellite Surveying. New York: Wiley and Sons.

71. Lejeune, S. and Warnant R. 2008. A novel method for the quantitative assessment of the ionosphere effect on high accuracy GNSS applications, which require ambiguity resolution. Journal of Atmospheric and Solar-Terrestrial Physics. 70, no. 6, pp. 889-900.

72. Li, F. K. and Goldstein R. M. 1987. Studies of multibaseline spaceborne interferometric synthetic aperture radar. International Geoscience and Remote Sensing Symposium : 1545-50.

73. Li, Z. 2004. Production of Regional 1 km × 1 km Water Vapor Fields through the Integration of GPS and MODIS Data. ION GNSS 2004, 21-24 September 2004, Long Beach CA, USA.

74. Lillesand, T. M. and Kiefer R. F. 2000. Remote sensing and image interpretation. New York: John Wiley and sons.

75. Lisi, M. 2006. The Role of Satellites in Network Centric “Welfare” Systems: a European Perspective. 24th International Communications Satellite Systems Conference (ICSSC), San Diego USA, 11-14 June 2006; AIAA 2006-5390.

76. Lu, Z. and Meyer D. J. 2002. Study of high SAR backscattering caused by an increase of soil moisture over a sparsely vegetated area: implications for characteristics of backscattering. International Journal of Remote Sensing 23, no. 6: 1063-74.

77. Madsen, S. N. Edelstein W. Di Domenico L. and Labreque J. 2001. A Geosynchronous Synthetic Aperture Radar for Tectonic Mapping, Disaster Management and Measurement of Vegetation and Soil Moisture. IGARSS July 9-13 2001 Sidney.

78. Mahafza, B. R. 2000. Radar system design using Matlab. New York: CRC press.

79. Maral, G. and Bousquet M. 1998. Satellite Communications Systems. New York: John Wiley and sons.

80. Martin M. and Kilberg, S. 2003. Techsat 2001 and revolutionizing space missions using microsatellites. 12th Annual AIAA/USU Conference On Small Satellites, Logan, USA, 31 August-1 September 199801 September 1998. AIAA Paper SSC-1-3. Note: available on line at [http://www.interfacecontrol.com/papers/TechSat21MicroSats.pdf]

81. Massonnet D. 2001. The interferometric cartwheel: a constellation of passive satellites to produce radar images to be coherently combined. International Journal of Remote Sensing 22, no. 18: 2413-30.

82. Mattar, K. E. Gray A. L. 2002. Reducing ionospheric electron density errors in satellite radar interferometry applications. Canadian Journal of Remote Sensing 28 , no. 4: 593-600.

83. McCarthy, D. 1992. International Earth Rotation and Reference Systems Service (IERS), Technical note n°13. Note: available on line at: [http://www.iers.org/MainDisp.csl?pid=46-25772].

84. McCarthy, D. 1996. International Earth Rotation and Reference Systems Service (IERS), Technical note n°21. Note: available on line at [http://www.iers.org/MainDisp.csl?pid=46-25772].

85. McCarthy, D. Petit G. 2004. International Earth Rotation and Reference Systems Service (IERS), Technical note n°32. Note: available on line at [http://www.iers.org/MainDisp.csl?pid=46-25772].

86. McGraw, G. *et al.* 2000. Development of the LAAS Accuracy Models. ION GPS 2000, September 19-22, 2000, Salt Lake City, USA, pp. 1-12.

87. Mendes, V. B. and Langley R. B. 1998. Tropospheric Zenith Delay Prediction Accuracy for Airborne GPS High-Precision Positioning. Proceedings of The

Institute of Navigation 54th Annual Meeting, pp. 337-47.

88. Meyer, F. Bamler R. Jakowski N. and Fritz T. 2006. The Potential of Broadband L band SAR Systems for Small Scale Ionospheric TEC Mapping. IEEE Transactions on Geoscience and Remote Sensing Letters.

89. Milbert, D. 2002. Solid Earth tide. Citing Internet resources (www document) [http://mywebpages.comcast.net/ dmilbert/softs/]. *Last access* January 2007.

90. Monaldo, F. 1993. TOPEX Ionospheric Height Correction Precision Estimated from Prelaunch Test Results. IEEE Transactions on Geoscience and Remote Sensing 31, no. 2: 371-5.

91. MOPS. 1998. MOPS (1998) Minimum operational performance standards for Global Positioning System/wide area augmentation system airborne equipment. Technical report. Document No. RTCA/DO-229A, June 8, 1998, prepared by SC-159.

92. Muldavin, E. 2004. Sevilleta LTER Fertilizer NPP Study Dataset Albuquerque,NM. Sevilleta Long Term Ecological Research Site Database: SEV155. Citing Internet resources (www document) [http://sev.lternet.edu/project_details.php?id=SEV155]. *Last access* December 2006.

93. NASA JPL. 2003. Global Earthquake Satellite System, a 20 year plan to enable earthquake prediction. Citing Internet resources (www document) [http://solidearth.jpl.nasa.gov/gess.html]. *Last access* January 2008.

94. NASA JPL. 2005. Pole tide. Citing Internet resources (www document) [http://podaac.jpl.nasa.gov/altimeter_ocean_pathfinder/html/pole_tide.html]. *Last access* January 2007.

95. Nava, B. Radicella S. M. Leitinger R. and Coisson P. 2007. Use of total electron content data to analyze ionosphere electron density gradients. Advances in Space Research 39: 1292-7.

96. Niell, A. E. 2000. Improved atmospheric mapping functions for VLBI and GPS. Earth Planets Space 52: 699–702.

97. NOAA SEC. 2005. NOAA Space Weather Scales. Citing Internet resources (www document) [http://www.sec.noaa.gov/NOAAscales/]. *Last access* August 2007.

98. Nolan M. and Fatland D. R. 2003. Penetration Depth as a DinSAR Observable and Proxy for Soil Moisture. IEEE Transactions on Geoscience and Remote Sensing 41, no. 3: 532-9.

99. Oksanen, J. and Sariakoski T. 2005. Error propagation analysis of DEM-based drainage basin delineation. International Journal of Remote Sensing 26, no. 14: 3085-102.

100. Ottavianelli, G. 2007. Synthetic aperture radar for landfill monitoring. Cranfield University PhD Thesis. Academic year 2006/2007.

101. Picardi, G. 2000. Elaborazione del segnale Radar: Metodologie ed applicazioni. Rome: Franco Angeli. Notes: Title translated: Radar signal processing: methods and applications.

102. Poole, I. 2002. Understanding solar indices. QST. (September 2002):38-40.

103. Prati, C. Rocca F. Giancola D. and Monti Guarneri A. 1998. Passive Geosynchronous SAR system reusing backscattered digital audio broadcasting signals, IEEE Transactions on Geoscience and Remote Sensing. 36, no. 6: 1973-6.

104. Quegan, S. and Lamont J. 1986. Ionospheric and tropospheric effects on synthetic aperture radar signals. International Journal of Remote Sensing 7, no. 4: 525-39.

105. Rees, W. G. 2001. Physical principles of remote sensing. Cambridge: Cambridge University Press.

106. Richards, M. A. 2003. Coherent integration loss due to Gaussian phase noise. IEEE Signal Processing Letters 10, no. 7: 208-10.

107. Rocca, F. 2006, personal communication.

108. Rodriguez, E. and Martin J. M. 1992. Theory and design of interferometric synthetic aperture radars. IEE Proceedings F, Radar and Signal Processing 139, no. 2: 147-59.

109. Rupert, S. 1998. Netcdf to IDL import function. Citing Internet resources (www document) [http://cheas.psu.edu/data/people/ricciuto/iss2/cdf2idl.pro]. *Last access* January 2008.

110. Sandwell, D. T. 2002. SAR image formation: ERS SAR processor coded in Matlab. Citing Internet resources (www document) [http://topex.ucsd.edu/insar/sar_image_formation.pdf]. *Last access* January 2008.

111. Scherneck, H. G. 2006. Ocean tide loading provider. Citing Internet resources (www document) [http://geodac.fc.up.pt/loading/index.html]. *Last access* January 2007.

112. Scherneck, H. G. 1991. A Parameterized Solid Earth Tide Model and Ocean Tide Loading Effects for Global Geodetic Baseline Measurements. Geophys. J. Int., no. 106: 677-94.

113. Schuler, T. 2001. On ground based GPS Tropospheric delay estimation. PhD Thesis, Universität der Bundeswehr München.

114. Schwäbisch, M. and Siegmund R. 2002. Study on concepts for radar interferometry from satellites for ocean (and land) applications. Citing Internet resources (www document) [http://www.ifm.uni-hamburg.de/~wwwrs/project_koriolis.htm]. Last access April 2007.

115. Seynat, C. 2000. Quantification of the effect of wind driven wheat motion on SAR interferometric coherence. PhD Thesis, Cranfield University.

116. Sharoo, R. and Visser P. 1998. Precise orbit determination and gravity field improvement for ERS satellites. Journal of Geophysical Research 103, no. C4: 8113-227.

117. Skolnik, M. J. 1990. Radar Handbook. Boston: McGraw Hill.

118. Snider, J. B. 2000. Temporal Variability of Precipitable Water Vapor in the north Atlantic. IEEE Transactions on Geoscience and Remote Sensing 38, no. 3: 1489-91.

119. Solaas, G.A., 1994. ERS-1 Interferometric Baseline Algorithm Verification, ESA report ES-TN-DPE-OM-GS02

120. Soumekh, M. 1999. Synthetic Aperture Radar Signal processing with Matlab algorithms . New York: Wiley and sons.

121. Tarayre, H. and Massonet D. 1996. Atmospheric propagation heterogeneities revealed by ERS-1 interferometry. Geophysical Research Letters 23, no. 9: 989-92.

122. Tomiyasu, K. 1978. Synthetic Aperture Radar in Geosynchronous Orbit. Antennas and Propagation Society International Symposium 16: 42-5.

123. Tomiyasu, K. and Pacelli J. L. 1983. Synthetic Aperture Radar Imaging from an Inclined Geosynchronous Orbit. IEEE Transactions on Geoscience and Remote Sensing GE-21(3): 324-9.

124. Treuhaft, R. N. Lanyi G. E. 1987. The effect of the dynamic wet troposphere on radio interferometric measurements. Radio Science 22: 251-65.

125. Tsugawa, T. 2006. Travelling ionospheric disturbances observed by GPS networks; MWA-LFD Meeting, November, 2006. Citing Internet resources

(www document) [http://www.haystack.mit.edu/ast/arrays/mwa/Meetings/SHI%20workshop%201Nov06/tsugawa/TIDs_observed_by_GPS_network.pdf]. *Last access* August 2007.

126. Ulaby, F. T. Moore R. K. and Fung A. K. 1986. Microwave remote sensing: Active and Passive. Massachusetts: Artech House.

127. Vergnolle, M., Bouin, M.N., Morel, L., Masson, F. Durand, S., Nicolas, J. Melachroinos, S. A. 2008. Geophysical Journal International, 173(2), pp. 444-458.

128. Wiley, C. A., inventor. 1954. Pulsed Doppler Radar Methods and apparatus. United States Patent no. 3196436.

129. Williams, S. Bock Y. and Fang P. 1998. Integrated satellite interferometry: tropospheric noise, GPS estimates and implications for interferometric synthetic aperture radar products. Journal of Geophysical Research 103(B11), no. 27: 051-27,067.

130. Willis, N. 1991. Bi-static Radar. Boston: Artech House.

131. Xiao, N. and Xia Y. 2003. Researches in China on the effects of tides on Earth rotation. Celestial Mechanics and Dynamical Astronomy 87: 3-12.

132. Xing Mengdao, Li Zhenfang Bao Zheng Liao Guisheng. 2004. Doppler ambiguity resolving in distributed microsatellites radar imaging. IEEE Aerospace Conference Proceedings : 1936-44.

133. Xu, Z. Wu J. and Wu Z. 2008. Potential effects of the ionosphere on space-based SAR imaging. IEEE Transactions on Antennas and Propagation 56, no. 7: 1968-75.

134. Yi, D. Minster B. and Bentley C. 2000. The effect of ocean tidal loading on satellite altimetry over Antarctica. Antarctic Science 12, no. 1: 119-24.

135. Zebker, H. A. and Goldstein R. M. 1986. Topographic mapping from interferometry synthetic aperture radar observations. Journal of Geophysical Research 91, no. B5: 4993-9.

136. Zebker H. A. and Villasenor, J. 1992. Decorrelation in interferometric radar echoes . IEEE Transactions on Geoscience and Remote Sensing 30, no. 5: 950-9.

137. Zhenfang Li, Hogyang Wang Tao Su and Zeng Bao. 2005. Generation of wide swath and high-resolution SAR images from multichannel small spaceborne SAR systems. IEEE Transactions on Geoscience and Remote Sensing Letters 2, no. 1: 82-6.

138. Zheng-Wen Xu, Jian Wu and Zhen-Sen Wu. 2004. A survey of ionospheric effects on space-based radar. Waves in Random Media 14: 189-273.

139. Zhu, M. Wadge G. Holley R. James I. Clark O. Wang C. Woodage M. 2007. High-Resolution Forecast Models of Water Vapor Over Mountains: Comparison With MERIS and Meteosat Data. IEEE Transactions on Geoscience and Remote Sensing Letters 4, no. 3: 401-5.

Appendix A – Digital processing: mathematical preliminaries

Barber (1995) and Picardi (2000) are two thorough references that provide a solid background in digital processing. Their work has been extensively used in this Appendix.

1. Fourier Transform

Considering a function of time *f(t)*, its Fourier transform *F(ω)* is:

$$F(\omega) = \int_{-\infty}^{+\infty} f(t) e^{-j\omega t} dt \qquad \text{Equation A-1}$$

The inverse Fourier transform is:

$$f(t) = \frac{1}{2\pi} \int_{-\infty}^{+\infty} F(\omega) \exp(i\omega t) d\omega \qquad \text{Equation A-2}$$

If *f(t)* is real valued then:

$$F^*(\omega) = F(-\omega) \qquad \text{Equation A-3}$$

if *f(t)* is imaginary valued then:

$$F^*(\omega) = -F(-\omega) \qquad \text{Equation A-4}$$

In Equation B-4, the asterisk indicates complex conjugate.

2. The analytic signal

Let *f(t)* be a purely real function while *g(t)* is a purely imaginary function. If *g(t)* is such that for *ω>0 G(ω)=F(ω)* then the Fourier transform of the sum *f(t)+g(t)* is

$$F(\omega) + G(\omega) = \begin{cases} 2F(\omega) & \text{for } \omega > 0 \\ O & \text{for } \omega < 0 \end{cases} \qquad \text{Equation A-5}$$

It is possible to associate a complex signal *z(t)* to every real signal *f(t)*:

$$f(t) \longleftrightarrow z(t) = \frac{1}{2\pi} \int_{-\infty}^{+\infty} 2F(\omega) e^{j\omega t} d\omega \qquad \text{Equation A-6}$$

The complex function *z(t)* can be expressed as:

$$z(t) = f(t) + jg(t) \qquad \text{Equation A-7}$$

Equation A-6 defines *g(t)* as the Hilbert transform of the function *f(t)*, thus:

$$z(t) = f(t) + j\hat{f}(t) \qquad \text{Equation A-8}$$

"*If we have a real-valued function such as a(t)cosϕ(t), writing it as a(t)exp(jϕ(t)) gives the analytic signal with a single sided spectrum"* (Barber, 1985). The main advantage that results from using an analytic signal is the simplification of the waveform analysis.

3. Discrete Fourier Transform

The Discrete Fourier Transform is analogous to the continue transforms.

$$F(l) = \sum_{k=0}^{N-1} f(k) \exp\left(-\frac{j2\pi kl}{N}\right) \qquad \text{Equation A-9}$$

$$f(k) = \sum_{l=0}^{N-1} F(l) \exp\left(\frac{j2\pi kl}{N}\right) \qquad \text{Equation A-10}$$

The expressions Equation A-9 and Equation A-10 can be regarded as a mapping of the sequence *f(k)* onto the sequence *F(l)* (Barber, 1985).

Usually a temporal continuous function f(t) has a finite length and it is sampled at intervals Δt so that its length $T=N\Delta t$. The spectrum is periodically repeated with frequency f_s where $f_s=1/T$. To sample the function correctly it is required that there are not any frequencies higher than $f_s/2$ because both the positive and negative frequencies have to be sampled.

The advantage of using an analytic signal (instead of only its real part) becomes clearer when considering the sampling frequency required sampling correctly a continuous signal. As the analytic signal has only the positive half of the spectrum, it can be sampled at $f_s/2$ without ambiguities.

4. The discrete convolution theorem

The convolution between two discrete signals is expressed in Equation A-11.

$$g(k) = \frac{1}{N} \sum_{m=0}^{N-1} f(m) h(k-m)$$ Equation A-11

Even in the discrete case, the convolution in the time domain corresponds to a multiplication in the frequency domain:

$$G(l) = F(l) H(l)$$ Equation A-12

Appendix B – Matlab and IDL Routines

This section presents the Matlab and IDL routines developed by the author during the research.

List of Matlab and IDL routines:

1- performances.m;

2- Gaussian_filter.m;

3- Fourier transform functions;

4- Simulator.m;

5- Definitions.m;

6- Focussing.m;

7- Draw_plots.m;

8- Slant_range.m;

9- Impulse_response.m;

10- Cdf2idl.pro.

Flowcharts are used when necessary to clarify the routine structure. An explanation of the shapes used in the flowcharts follows.

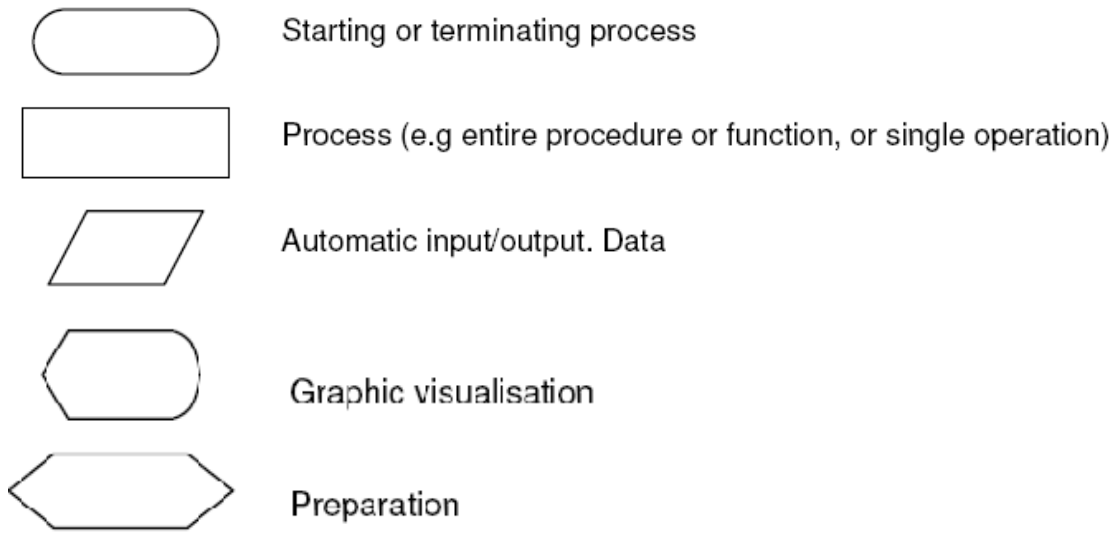

1. Performances.m

This Matlab program implements the bi-static SAR equations presented by Willis (1991) and provides performance plots for GeoSAR configurations. The algorithm uses widely the Matlab Mapping Toolbox, a powerful instrument to place spatial information on a geo-spatial reference frame.

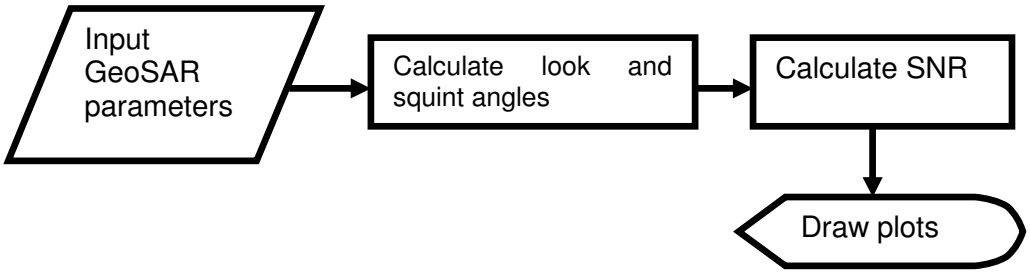


```
%   FILE NAME
%   performances.m
%   version 1.0

%   AUTHOR
%   Cranfield University - Davide Bruno

%   DESCRIPTION
%   this file estimates bi-static SAR performances applying
%   equations provided in literature by Willis (1991) among the
    others.
%   To generate plots the code requires Matlab Mapping Toolbox

%   INPUT
%   GeoSAR parameters

%   OUTPUT
%   Performance plots

%   EXTERNAL FUNCTIONS
%   not required

%   VALIDATION
%   The file has been validated with manual calculation of some values
    for
%   each equation applied.
%   SNR calculation was further validated using the parameters imposed
%   by Prati et al. (1998)
```

```
%

%   FILE STRUCTURE
%   1- Define GeoSAR parameters
%   2- Define constants and geo-graphic parameters for plots
%   3- Calculate look and squint angles
%   4- Calculate SNR
%   5- Final plots

clear

%%%%%%%%%%%%%%%%%    GEOSAR PARAMETERS   %%%%%%%%%%%%%
V=3.3;                          % velocity receiver in m/sec
RX_D=6;                   %receiving antenna diameter (meters)
Presuming_time=30;%presuming time in seconds to be used to estimate
azimuth swath
Power_TX=-171         %power density on the ground in dB
Tobs=8*3660;             % lenght of the coherent observation time, in
hours *3600 to get seconds

r_geo = (6.378 + 35.786)*1E6;    % geostationary orbit radius / m
r_surf = 6.378E6;                % Earth's mean radius / m
EIRP= 50;                        %EIRP in dB
lambda=0.25;                     %wavelength in meters
L= 10*log10(100) ;               % Target size, meters and then dB
Ar=10*log10(pi*RX_D^2/4) ;       % receiver antenna size, meters^2 and
then dB
s_nought=-18;                    % normalised backscatter coefficient
of the target, dB
k=10*log10(1.38e-23);            %Boltzmann constant
Ts=10*log10(290);                % noise temperature, K that takes into
accoun the noise figure
B=10*log10(1/Tobs);               % bandwidth to be used in noise
estimation in dB for noise calculation
F=7;                             % Noise figure
Band_signal=8e6;                 %Channel signal bandwidth

Noise_power=k+B+Ts+F;            %Noise power calculation N=KxTsxB
 %%%%%%%%%%%%%%%%%%%%%%%% GEOSPATIAL PARAMETERS   %%%%%%%%%%

radian = 180.0/pi;          % one radian in degrees
tiny = 0.001; %small number, so that FIX doesn't truncate 1.9999 to 1

RX_lon = 20.0;        %longitude of RX satellite/ deg
RX_lat = 0.0;         %latitude of RX satellite / deg
TX_lat  = 0.0;        %latitude of TX satellite / deg
TX_lon = 50.0;        %longitude of TX satellite / deg

lat_min   = -70.0;       % minimum latitude value / deg
lat_max   = 70.0;        % maximum latitude value / deg
lat_step  =  2.5;        % increment in latitude value / deg
```

```
lon_min  = 0.0;         % minimum longitude value / deg
lon_max  = 90.0;        % maximum longitude value / deg
lon_step =  2.0;        % increment in longitude value / deg

% define the number of samples in the geospatial grid
N_lat   = round(1 + (lat_max-lat_min)/lat_step + tiny);
N_lon  = round(1 + (lon_max-lon_min)/lon_step + tiny);

% define the vectors with latitude and longitude values
lat_vector = (1:N_lat)*lat_step + lat_min;
lon_vector = (1:N_lon)*lon_step + lon_min;

a = [RX_lon/radian, RX_lat, r_geo]; % Position of the RX
b = [TX_lon/radian, TX_lat/radian, r_geo]; % Postition of the TX

%[x,y,z] = sph2cart(THETA,PHI,R) is the syntax of this coordinate
%transformation
% x towards greenwich;
% z towards north
% y orthogonal

%position of sub-satellite point
[sub_sat_x,sub_sat_y, sub_sat_z] = sph2cart(TX_lon/radian,
TX_lat/radian, r_surf);
sub_sat=[sub_sat_x,sub_sat_y, sub_sat_z];

sat_lon = [RX_lon, TX_lon];
sat_lat = [RX_lat, TX_lat];
%%%%%%%%%%%%%%%%%%%%%%%%%%%%%%%%%%%%%%%%%%%%%%%%%%%%%%%%%%%%%%%%%%%
%position of receiver s/c
[RX_rect_x, RX_rect_y, RX_rect_z] = sph2cart(RX_lon/radian,
RX_lat/radian, r_geo);
RX_rect=[RX_rect_x,RX_rect_y, RX_rect_z];
%vector TX from origin to tx
RX=(RX_rect(1)*RX_rect(1)+RX_rect(2)*RX_rect(2)+RX_rect(3)*RX_rect(3))
^0.5;

%position of transmitter s/c
[TX_rect_x, TX_rect_y, TX_rect_z] = sph2cart(TX_lon/radian,
TX_lat/radian, r_geo);
TX_rect=[TX_rect_x, TX_rect_y, TX_rect_z];

%vector RX from origin to rx
TX=(TX_rect(1)*TX_rect(1)+TX_rect(2)*TX_rect(2)+TX_rect(3)*TX_rect(3))
^0.5;
i_lat = 1; %index for latitude
for latitude = lat_min+lat_step:lat_step:lat_max+lat_step

    i_long = 1; %index for longitude
```

```
    for longitude = lon_min+lon_step:lon_step:lon_max+lon_step
            %position of the point on the surface
            [r_rect_x, r_rect_y, r_rect_z] = sph2cart(longitude/radian,
            latitude/radian, r_surf);
            %define a new vector for the point on the surface of given
            lat/lon
            r_rect=[r_rect_x, r_rect_y, r_rect_z];

           % distance from the receiver to the point on the surface
           dr_RX = RX_rect-r_rect;
     RR = (dr_RX(1)*dr_RX(1)+dr_RX(2)*dr_RX(2)+dr_RX(3)*dr_RX(3))^0.5;

           % distance from the transmitter to the point on the surface
           dr_TX = TX_rect-r_rect;
       RT = dr_TX(1)*dr_TX(1)+dr_TX(2)*dr_TX(2)+dr_TX(3)*dr_TX(3))^0.5;

           R_TOT = RT+RR; %total slant range RT+RR

           % assign the slant range to a point on the surface
           sr(i_long,i_lat) = R_TOT;

           squint(i_long,i_lat)=asin(r_surf*sin(latitude/radian)/RR);

      look_angle(i_long,i_lat)=asin(r_surf*sin(longitude/radian-
      RX_lon/radian)/(RR*cos(squint(i_long,i_lat))));


      squint_ground(i_long,i_lat)=(acos(sin(squint(i_long,i_lat))/sin(
      0.1518)));  %to estimate squint angle
                  %squint angle is defined that it is 90° at boresight


      ground_angle(i_long,i_lat)=(acos(sin(look_angle(i_long,i_lat))/s
      in(0.1518))); % grazing angle
                  %ground incidence angle is 90-grazing angle
                  % this is the scalar product between RR and RT to
                  estimate bistatic angle

scalare=dr_RX(1)*dr_TX(1)+dr_RX(2)*dr_TX(2)+dr_RX(3)*dr_TX(3);
           beta(i_long,i_lat)=(acos(scalare/(RT*RR))); % beta is the
           bistatic angle

           %this gate has been added to impose a limitation on the
           acceptable incidence
           %angle and the maximum squint angle.

           if ground_angle(i_long,i_lat)<70/57.3  |
           squint_ground(i_long,i_lat)<20/57.3
           |ground_angle(i_long,i_lat)>40/57.3
```

```
                    c=3e8;

Slant_range_res(i_long,i_lat)=c/((2*Band_signal)*cos(beta(i_long,i_lat
)/2)^2);

Ground_range_res(i_long,i_lat)=Slant_range_res(i_long,i_lat)/sin(groun
d_angle(i_long,i_lat)); %ground angle is the grazing angle

% calculate the dimensions of the ground swath as a function of the
grazing
% angle and of the squint angle.

Azimuth_swath(i_long,i_lat)=(lambda/(V*Presuming_time))*RR/sin(squint_
ground(i_long,i_lat));

azimuth_res(i_long,i_lat)=Azimuth_swath(i_long,i_lat)*(Presuming_time/
Tobs);

piR2_dB=10*log10(1/(4*pi*((RR)^2))); %to be used in SNR calculations

Band_signal_dB=10*log10(Band_signal); %to be used in SNR calculations

SNR_focused(i_long,i_lat)=Power_TX+Band_signal_dB+piR2_dB+10*log10(azi
muth_res(i_long,i_lat))+10*log10(Ground_range_res(i_long,i_lat))+Ar+s_
nought-Noise_power;

 %to verify conditions imposed by Prati et al. uncomment this
                    %RR=36e6;

%SNR_focused(i_long,i_lat)=Power_TX+Band_signal_dB+piR2_dB+10*log10(12
0)+10*log10(75)+10*log10(20)+s_nought-Noise_power;
                    %
end

      i_long = i_long + 1;
      %lon + long_step to update the position in matrices
         end
     i_lat = i_lat+1;  %lat + lat_step
 end

figure(1)
title('Contours of constant slant range')
load coast
whos
axesm('ortho','origin',[0 50])
framem;
plotm(lat, long,'k')
[c,h]=contourm(lat_vector, lon_vector,
sr','LineWidth',2);clabelm(c,h,'FontSize',16)
%plot the two satellites
plotm(RX_lat, RX_lon,'-c*')
```

```
plotm(TX_lat, TX_lon,'-c*')


figure(2)
title('Contours of constant ground squint angle
(degrees)','FontSize',16)
load coast
whos
axesm('ortho','origin',[0 50])
framem;
plotm(lat, long,'k')
v=[20.40.60.80.90.100.120.140.160]; % levels of the contour lines
[c,h]=contourm(lat_vector, lon_vector,
(squint_ground*57.3)',v,'LineWidth',2);clabelm(c,h,'FontSize',16)
clegendm(c,h,-1)
% plot the two satellites
plotm(RX_lat, RX_lon,'-c*')
plotm(TX_lat, TX_lon,'-c*')


figure(3)
title('Contours of constant ground incidence angle
(degrees)','FontSize',16)
%the ground incidence angle is 90° at nadir
load coast
whos
axesm('ortho','origin',[0 50])
framem;
plotm(lat, long,'k')
[c,h]=contourm(lat_vector, lon_vector,
rad2deg(ground_angle)','LineWidth',2);clabelm(c,h,'FontSize',16)
clegendm(c,h,-1)
% plot the two satellites
plotm(RX_lat, RX_lon,'-c*')
plotm(TX_lat, TX_lon,'-c*')


figure(4)
title('Contours of ground resolution','FontSize',16)
load coast
whos
axesm('ortho','origin',[0 50])
framem;
plotm(lat, long,'k')
%v=[ 30, 40, 60,  80,  100, 120, 140, 160];
[c,h]= contourm(lat_vector, lon_vector,
(Ground_range_res)','Linewidth',2);clabelm(c,h,'FontSize',16)
clegendm(c,h,-1)
% plot the two satellites
plotm(RX_lat, RX_lon,'-c*')
plotm(TX_lat, TX_lon,'-c*')
```

```
figure(6)
title('Contours of focused SNR (dB)','FontSize',16)
load coast
grid
whos
axesm('ortho','origin',[0 50])
framem;
plotm(lat, long,'k')
%v=[7,8,9,10.11.12]
[c,h]=contourm(lat_vector, lon_vector,
(SNR_focused)','Linewidth',2);clabelm(c,h,'FontSize',16)
clegendm(c,h,-1)
%plot the two satellites
plotm(RX_lat, RX_lon,'-c*')
plotm(TX_lat, TX_lon,'-c*')
```

2. Gaussian_filter.m

This Matlab function implements the filtering algorithm described by (Oksanen and Sarjakoski, 2005).

```
function E = gaussian_filter(raster,X,Y,r)
% PURPOSE: apply a gaussian convolution filter on a raster (gaussian
data)
% ------------------------------------------------------------------
% USAGE: E = gaussian_filter(raster,X,Y,r)
% where: [raster] is the raster to apply filter to
%        [X] and [Y] are the coordinate vectors of [raster]
%        [r] is the (correlation) range of the error in units defined
by
%            the cellsize in X/Y
%
% returns matrix [E] of size [raster] = X * Y
% ------------------------------------------------------------------
% EXAMPLE: E = gaussian_filter(randn(100.100),[1:100],[1:100],5);
%
% NOTES: This approach only works for equidistant matrices (same
cellsize in
%        X and Y direction is only valid for matrices of values that
are the
%        result of a Gaussian process!
% Based on the approach of spatial moving averages according to
% Oksanen and Sarjakoski 2005:
%
http://taylorandfrancis.metapress.com/openurl.asp?genre=article&id=doi
:10.1080/01431160500057947
%
% Felix Hebeler, Geography Dept., University Zurich, March 2006.
```

```
if nargin < 4
    error('This function needs 4 input parameters
(inputraster,X,Y,range)');
end

%% Parameters
w=abs(X(1.2)-X(1.1)); %spacing of grid in the convolution (resolution
of DEM, as in the paper)
if w~=abs(Y(1.2)-Y(1.1))
    error('This approach only works for equidistant matrices (same
cellsize in X and Y direction)!')
end
r=(r/w)*w;
%R = Matrix of correlation coefficents
%W = weight kernel

E = raster; % input raster used instead of random generated white
noise error.
% only valid if the raster values are results of gaussian process

%% correlation coefficients matrix R
m=(2*((2*r)/w))+1; % dimension of matrix R

%% Gaussian autocorrelation function
% p(h)=exp(-3*(h^2/r^2)); %p(h) is the correlation coefficient of the
DEM
% error at lag h and range r.
R = euklid_dist(m,m,w,w); % get euklid distance weight matrix & apply
cellspacing w
R = exp( -3*( (R.^2) ./ (r^2) ) ); % apply corr coeff  as in paper

%% Scaling matrix R
C = real(sqrtm(R.^2)); % this gives complex numbers, but close to 0,
so ignore

%% using s
s=sum(C(:).^2);
s = 1/sqrt(s);

%% getting kernel W
W=s.*C;

%% do convolution filtering
E=conv2(E,W,'same');
```

3. Fourier transform functions

Forward and inverse Fast Fourier Transformations have been widely used in performing SAR azimuth focussing. The following functions exploits commands that are already available in the Matlab Toolbox for FFT and FFT $^{-1}$.

```
% Forward FFT w.r.t. the first variable %

function fs=ftx(s);
 fs=fftshift(fft(fftshift(s)));

% Forward FFT w.r.t. the second variable %
function fs=fty(s);
 fs=fftshift(fft(fftshift(s.'))).';

% Inverse FFT w.r.t. the first variable %
function s=iftx(fs);
 s=fftshift(ifft(fftshift(fs)));

% Inverse FFT w.r.t. the second variable %

function s=ifty(fs);
 s=fftshift(ifft(fftshift(fs.'))).';
```

4. simulator.m

This Matlab program implements the bi-static SAR azimuth processing . The flow chart of this routine has been described in Chapter 5 where validation was included as well.

```
%   Cranfield University - Davide Bruno

%   DESCRIPTION
%   this is the executable file that calls all the subroutines
%
%   EXTERNAL FUNCTIONS
%   noise_model.m   This function is used to generate a noise series
%                    according to a given model
%   noise.m        This function generates a series of n_pulse samples
%                  according to a given statistical distribution


definitions  %input parameters

% Function noise_model (solid, ocean, tropospheric, ionospheric,
% n_pulse,lambda) estimates the phase delay due to the various noise
```

```
% sources considered. If the flag is turned on the noise source is
added
% to the series of samples.

%phase_noise=noise_model(0.1.0.0,n_pulse, lambda);
%Comment out if noise
% function has to be called

% Function noise (solid, ocean, tropospheric, ionospheric,
% n_pulse,lambda) estimates the phase delay due to the various noise
% sources considered (after noise compensation). It is equivalent to
the residual
% phase noise that affect GeoSAR focussing. If the flag is turned on
the
% the correspondent noise source is added to the series of samples.

phase_noise=noise(1.0.0,0,n_pulse, lambda);
%Comment out if noise_model
% function has to be
% called

simulation %generate SAR signal
focussing    %bi-static SAR processing
draw_plots  %output
```

5. definitions.m

This Matlab program provides the required input information to the bi-static SAR simulator. This function is called within the code *simulator.m*.

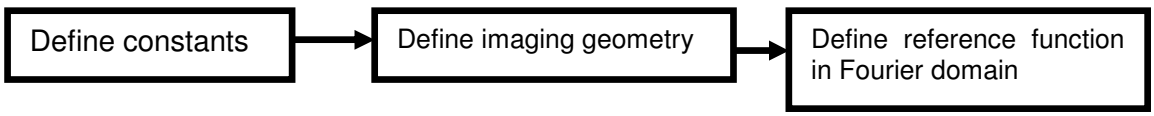


```
% Cranfield University - Davide Bruno
% 15 june 2008 version 02
% the code has been checked and commented to avoid duplications

% v.01 24 May 2008
% the code has been restructured to allow for better checking and
% validation

%%%%%%%%%%%%%%%%%%%%%%%%%%%%%%%%%%%%%%%%%%%%%%%%%%%%%%%%%%%%%%%%%%%
% PROGRAM STRUCTURE
% 1- define constants
% 2- define imaging geometry
% 3- define reference function in Fourier domain (removed in version
02)
```

```
%%%%%%%%%%%%%%%%%%%%%%%%%%%%%%%%%%%%%%%%%%%%%%%%%%%%%%%%%%
clear;
clc;
%colormap(gray(256))

%%%%%%%%%%%%%%%%%%%%%%%%%%%%%%%%%%%%%%%%%%%%%%%%%%%%%%%
%               DEFINITIONS
%
%%%%%%%%%%%%%%%%%%%%%%%%%%%%%%%%%%%%%%%%%%%%%%%%%%%%%%%
% define the constants that will be used in the code
TECU=1E16;      %Total Electron Content Unit
kb=1.38E-23;    %Boltzmann constant
cj=sqrt(-1);    %imaginary unit
pi2=2*pi;       %6.28


%%%%%%%%%%%%%%%%%%%%%%%%%%%%%%%%%%%%%%%%%%%%%%%%%%%%%%%%%%%%%%%%%%%%%
 %             Main simulation parameters
%%%%%%%%%%%%%%%%%%%%%%%%%%%%%%%%%%%%%%%%%%%%%%%%%%%%%%%%%%%%%%%%%%%%
c=3e8;              % propagation speed
fc=1.5e9;           % frequency
lambda=c/fc;        % Wavelength
k=pi2/lambda;       % Wavenumber
Xc=3.6e7;           % Range distance to centre of target area
Re=6378e3;          % Earth radius
alt_factor=((Re+Xc)/Re); %altitude factor, required to use LEO formula
                         % in GeoSAR case
antenna=6;      %Antenna diameter 6 m lambda 0.2 m
L=80000/2;      % synthetic aperture is 2*L
%range resolution / m dxgrid
dxgrid=100.0;
% grid resolution along track / m dygrid
dygrid=400.0;
% number of points along the grid to discretize surface backscatter
n_grid
n_grid=201;
% number of points along the satellite track at which signal is
calculated n_pulse_sig
n_pulse=1300;
% height / m of satellite above targets ho
h0=3.6E7;
% y / m value of start of surface discretization grid
ygrid0=-2000.0;
% transmitter antenna effective area / m2 Atx
Atx=10.0;
% radar effective transmitter power / W
Pt=1.0E5;
% receiver bandwidth / Hz (based on 1-way range resolution for Tx)
BW=6.0E6;
% receiver noise figure (absolute, not dB)
nf=3.0;
% surface noise temperature / K (nominal = 290 K)
```

```
Tsurf=290.0;
% receiver antenna effective area / m2
Arx=25.0;
% Omega_t Antenna solid angle
Omega_t=lambda^2/Atx;
%c1 constant used to calculate signal power/phasor
c1=sqrt(Pt*Arx/(4*pi*Omega_t));
%sigma_En
sigma_En=((nf*kb*Tsurf*BW)/2)^0.5;
% TX beam factor
Tx_beam=1.0;
 % RX beam factor
Rx_beam=1.0;
% for non-ideal noisy case
sigma_En = (nf*kb*Tsurf*BW/2)^0.5;
% radar pulse repetition frequency / Hz
prf=0.0371;
% y value of transmitter position / m
ytx0=0;%10e6;
% y value of transmitter velocity / m s-1
v_Tx=0.0;
% across-track displacement of Rx from target grid / m
dxr=5.0E6;
% across-track displacement of Rx from target grid / m
dxt=-5.0E6;

% receiver satellite velocity / ms-1
vsat=2.7778;
vTx=0; %velocity transmitter
% set flag to add random phase to grid cells as for natural surface
rand_phase=0; %to add randomization phase set to true
% set false if model is to run in ideal, noise-less case
flag_ideal=0;

% % spatial period of sigma 0 variation / m
% 2000
% % minimum value of sigma 0
% 0.05
% % maximum value of sigma 0
% 0.10
% % value of constant sigma0 assumed across the grid for model 2
% 0.10
% % height of layer 1 / m (~ionosphere)
% 4.0e5
% % height of layer 0 / m (~troposphere)
% 1.0e3
% start of synthetic aperture
yref0=-4.0E4;

% position of impulse response point target / m
yimpulse=0.0;
ypulse0=-4.0E4; %start of radar pulse reception
```

```
dphi_r = (( lambda)/(  Arx )^0.5);   % receiver antenna along-track
beamwidth / rad
dypulse =  vsat/( prf);                      % step in satellite
position between pulses

%n_pulse_ref = floor(  2*L /  dypulse);  % number of points in the
synthetic aperture
i_ref0 = ( ( yref0- ypulse0)/ dypulse);
rTx(1) =  dxt;   % Tx x coordinate
rTx(2) =  ytx0;  % Tx y coordinate
rTx(3) =  h0;    % Tx z coordinate
rRx(1) =  dxr;       % Rx x coordinate
rRx(2) = 0.0;                    % Rx y coordinate (to define perp
distance from origin to Rx track)
rRx(3) =  h0;        % Rx z coordinate
rp(1) = 0.0;         % coordinate origin, x coord
rp(2) = 0.0;         % coordinate origin, y coord
rp(3) = 0.0;         % coordinate origin, z coord
rR0 = slant_range ( rp, rRx );   % range from origin to receiver track
rT0 = slant_range ( rp, rTx );   % range from origin to transmitter

int_time=28800; %integration time is 8 hours (constraint)
du=(lambda/(2*L))*Xc; % there is only a factor 2 as this relation is
valid only for bistatic SAR

DY=du;  %Azimuth Resolution for bistatic SAR
du=du/1.2;                          %guard band
m=2*ceil(L/du);                      % pixels across the synth aperture

n_pulse_ref=m; % this is the number of pulses that constitute the
synthetic aperture
```

6. Simulation.m

This Matlab program generates SAR signal data. This function is called within the code *simulator.m*.

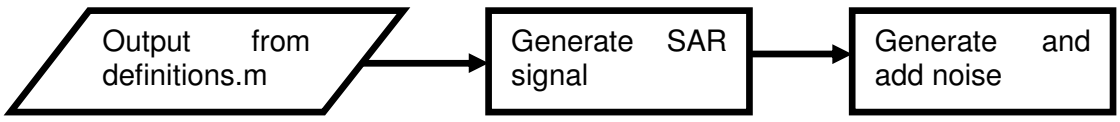


```
% Cranfield University - Davide Bruno
% Version 4 generated 24 june 08

%   DESCRIPTION
%   this is the subrountine that generates SAR signal
```

```
%
%   EXTERNAL FUNCTIONS
%   slant_range.m   Estimates the scalar product between two vectors

%  INPUT
%  requires to be executed after the routine definitions
%  includes the definition of the grid of n_grid scattereres

%  OUTPUT
%  vector signal (1, n_pulse) with the SAR signal Data
%  vector signal_ref (1, n_pulseref) with the impulse reference
   function

%   NOTE
%   has to be modified anytime the scatterers need to be modified

% Structure of the program

% 1. vectors to be initialised (define number of pulses)
% 2. SAR signal reference function
% 3. SAR signal generation
% 4. Add speckle effect
% 5. Add thermal noise


%%%%%%%%%%%%%%%%%%%%%%%%%%%%%%%%%%%%%%%%%%%%%%%%%%%%%%%%%%%%%%%%
%%%%%          DEFINITION AND INITIALISATION      %%%%%%%
%%%%%%%%%%%%%%%%%%%%%%%%%%%%%%%%%%%%%%%%%%%%%%%%%%%%%%%%%%%%%%%%

%n_pulse=1168
% the number of pulses has to be larger than the number of pulses in
the
% reference signal in order to sinthesize the full aperture on the
whole
% grid where the scatterers are located
%n_grid=201; % define the number of points in the grid
            % for every point in the grid there is a contribution that
            % has to be added to every pulse transmitted by the TX

signal=zeros(1,n_pulse);          %Measured Echoed Signal initialise
signal_ref=zeros(1,n_pulse_ref);           % reference signal
(n_pulse_ref samples)
real_signal(1:n_pulse)=0;         % real part of the signal
imag_signal(1:n_pulse)=0;         % imag part of the signal
real_ref(1:n_pulse_ref)=0;                 % real part of the
reference signal
imag_ref(1:n_pulse_ref)=0;                 % imag part of the
reference signal

% add speckle
```

```
if(rand_phase)==1
    random_phase=unifrnd(0.2*pi,1,n_grid);
    %random_phase has to be added to any scatterer (n_grid values)
else
   random_phase=zeros(1,n_grid); %no speckle effetc
end

%add thermal noise
if(flag_ideal)==1
    random_real=normrnd(0,.1.1,n_grid);
    random_imag=normrnd(0,.1.1,n_grid);
    %random_phase has to be added to any scatterer (n_grid values)
else
   random_real=zeros(1,n_grid); %no thermal noise
   random_imag=zeros(1,n_grid); %no thermal noise
end
%%%%%%%%%%%%%%%%%%%%%%%%%%%%%%%%%%%%%%%%%%%%%%%%%%%
%
%      GEOMETRIC PARAMETERS
%
%%%%%%%%%%%%%%%%%%%%%%%%%%%%%%%%%%%%%%%%%%%%%%%%%%%

% define the grid
yn=(-dypulse*100):dypulse:(dypulse*100); % vector defining the cross-
range position of the scatterers

% Simplifications
% cos_tht and cos_thr are considered constant for the whole synth
apert.
% Range_Rx and Range_Tx are assumed equal and constant for the whole
S.A.

    rTx(1) =  dxt;    % Tx x coordinate
    rTx(2) =  ytx0;   % Tx y coordinate
    rTx(3) =  h0;     % Tx z coordinate

    rp(1) = 0.0;      % scattering point x coordinate (constant)
    rp(2) = 0.0;      % temporarily set rp to origin to calculate Tx
slant range from origin
    rp(3) = 0.0;      % scattering point z coordinate (constant)
     % slant range from Tx to origin

    rT0 = slant_range(rp,rTx);

    for icomp=1:3
        et0(icomp) = -rTx(icomp)/rT0;     % et0[] is unit vector from
Tx to origin (i.e. the beam axis)
        etp(icomp) = et0(icomp);          % copy et0[] to etp[] = unit
vector from Tx to scatterer
    end
```

```
    rRx(1) =  dxr;       % Rx x coordinate
    rRx(2) = 0.0;                    % temporarily set Rx y coord to 0
to define er0[]
    rRx(3) =  h0;        % Rx z coordinate
    rR0 = (rRx(1)*rRx(1) + rRx(3)*rRx(3))^0.5;   % slant range from
line of scatterers to Rx trajectory
    for icomp=1:3
        er0(icomp) = -rRx(icomp)/rR0;    % er0[] is unit vector along
Rx beam; y component is 0
        erp(icomp) = er0(icomp);         % copy er0[] to erp[] = unit
vector from Rx to scatterer
    end

%%%%%%%%%%%%%%%%%%%%%%%%%%%%%%%%%%%%%%%%%%%%%%%%%%%%
%       REFERENCE SIGNAL
%%%%%%%%%%%%%%%%%%%%%%%%%%%%%%%%%%%%%%%%%%%%%%%%%%%%
sigma0(1:n_grid)=0;
sigma0(101)=1;
sigma=sigma0*dxgrid*dygrid;

for ipulse=1:n_pulse_ref
   %for igrid=1:n_grid

    t_rx = ipulse *  prf;    % calculates time (at Rx) after reception
of 0th (=1st) pulse
    %calculate receiver position
    rRx(1) = dxr;       % Rx x coordinate
    rRx(2) = (ypulse0) + ipulse*(dypulse);  % Rx y coordinate
    rRx(3) = h0;        % Rx z coordinate
    %calculate transmitter position
    rTx(1) = dxt;       % Tx x coordinate
    rTx(2) = (ytx0) ;   % Tx y coordinate
    rTx(3) = h0;        % Tx z coordinate

    rp(2)=0; %only for reference signal
    rT = slant_range(rp, rTx);
    rR = slant_range(rp, rRx);

    etp(3) = -(rTx(3)-rp(3))/rT;     % update local cos(incidence
angle) for grid cell
    erp(3) = -(rRx(3)-rp(3))/rR;

    cos_tht = -etp(3);   % cos(angle from surface normal to Tx) = dot
product of -etp and (0.0.1)
    cos_thr = -erp(3);   % cos(angle from surface normal to Rx) = dot
product of -erp and (0.0.1)

 n_cycle = (rT + rR)/( lambda);

 phi=2*pi*(ceil(n_cycle)-n_cycle);%size [SA]
```

```
    % it is a vector with n_pulse components, one for each pulse
 amp=
sqrt(Pt*Arx/(4*pi*Omega_t)*cos_tht*cos_thr*Tx_beam*Rx_beam*dxgrid*dygr
id)/(rT*rR);%amplitude factor %size [SA]

 real_ref(ipulse)=real_ref(ipulse)+amp.*cos(phi);
 imag_ref(ipulse)=imag_ref(ipulse)+amp.*sin(phi);

  % end % end loop over n_grid

end % end loop over the pulses in the reference function

signal_ref=real_ref+cj*imag_ref;

%%%%%%%%%%%%%%%%%%%%%%%%%%%%%%%%%%%%%%%%%%%%%%%%%%%%
%      END-  Reference signal generation
%%%%%%%%%%%%%%%%%%%%%%%%%%%%%%%%%%%%%%%%%%%%%%%%%%%%

%%%%%%%%%%%%%%%%%%%%%%%%%%%%%%%%%%%%%%%%%%%%%%%%%%%%
%      START-  Signal generation
%%%%%%%%%%%%%%%%%%%%%%%%%%%%%%%%%%%%%%%%%%%%%%%%%%%%

% call to the function noise that estimates phase noise.
% noise (solid earth tides, ocean loading, tropospheric noise,
ionospheric noise, m)
% phase_noise varies for any pixel over the grid (n_grid samples)


% define the location of the scatterers over the grid
sigma0(1:n_grid)=0;
%sigma0(191)=1;
sigma0(101)=1;
sigma=sigma0*dxgrid*dygrid;

for ipulse=1:n_pulse  %loop over the pulses transmitted by theTX

    for igrid=1:n_grid     % loop over the scatterers

    t_rx = ipulse *  prf;    % calculates time (at Rx) after reception
of 0th (=1st) pulse
    %calculate receiver position
    rRx(1) = dxr;       % Rx x coordinate
    rRx(2) = (ypulse0) + ipulse*(dypulse);  % Rx y coordinate
    rRx(3) = h0;        % Rx z coordinate
    %calculate transmitter position
    rTx(1) = dxt;       % Tx x coordinate
    rTx(2) = (ytx0) ;   % Tx y coordinate
    rTx(3) = h0;        % Tx z coordinate
```

```
    rp(2)=yn(igrid); % the location of the scatterer is defined in the
                     %vector yn
    rT = slant_range(rp, rTx);
    rR= slant_range(rp, rRx);

    etp(3) = -(rTx(3)-rp(3))/rT;     % update local cos(incidence
angle) for grid cell
    erp(3) = -(rRx(3)-rp(3))/rR;

    cos_tht = -etp(3);
    % cos(angle from surface normal to Tx) = dot product of -etp
and(0.0.1)
    cos_thr = -erp(3);
    % cos(angle from surface normal to Rx) = dot product of -erp
and(0.0.1)

    n_cycle = (rT + rR)/(lambda);

    phi=2*pi*(ceil(n_cycle)-n_cycle);%size [SA]
    phi=phi+phase_noise(ipulse);
    % it is a vector with 1068 components, one for each pulse
        if abs((abs(abs(yref0)+(yn(igrid)))-ipulse*dypulse))<(L)
            amp=
sqrt(Pt*Arx/(4*pi*Omega_t)*cos_tht*cos_thr*Tx_beam*Rx_beam*sigma(igrid
))/(rT*rR);%modified amplitude factor %size [SA]
            sigma_En=(nf*kb*Tsurf*BW)^0.5/2;
        else
            amp=0;
          end

  %for each point of the grid, a vector with amplitude for every pulse
                if(rand_phase)==1

real_signal(ipulse)=real_signal(ipulse)+amp*cos(phi)+amp*cos(random_ph
ase(igrid)); %vector with 1068 elements

imag_signal(ipulse)=imag_signal(ipulse)+amp*sin(phi)+amp*sin(random_ph
ase(igrid));
                else
                real_signal(ipulse)=real_signal(ipulse)+amp*cos(phi);
                imag_signal(ipulse)=imag_signal(ipulse)+amp*sin(phi);
                end

                if (flag_ideal==1) %true for noisy case

real_signal(ipulse)=real_signal(ipulse)+sigma_En*(random_real(igrid));

imag_signal(ipulse)=imag_signal(ipulse)+sigma_En*(random_imag(igrid));
                end
```

```
 end% for igrid
%
real_signal(ipulse)=real_signal(ipulse)+amp*cos(phase_noise(ipulse));
%
imag_signal(ipulse)=imag_signal(ipulse)+amp*sin(phase_noise(ipulse));
end %for n_pulse

% signal is n_pulse long and includes the signal transmitted by every
% scatterer over the grid.
signal= signal+ real_signal+cj*imag_signal;

%%%%%%%%%%%%%%%%%%%%%%%%%%%%%%%%%%%%%%%%%%%%%%%%%%%%
%      END  Signal generation
%%%%%%%%%%%%%%%%%%%%%%%%%%%%%%%%%%%%%%%%%%%%%%%%%%%%
```

7. focussing.m

This Matlab program focuses SAR signal according to the procedure described in section 5.5.2.4 . This routine has to be called within the code *simulator.m*.

```
%%%%%%%%%%%%%%%%%%%%%%%%%%%%%%%%%%%%%%%%%%%%%%%%%%%%
%      START  SAR focussing
%%%%%%%%%%%%%%%%%%%%%%%%%%%%%%%%%%%%%%%%%%%%%%%%%%%%

%radar calibration has to be used to obtain the value of the RCS
radar_cal = (Pt)*(Arx)/(4*pi*Omega_t*rR0*rR0*rT0*rT0*Tx_beam*Rx_beam);
% radar calibration in W m-2
f_reference=ftx(signal_ref);        %FFT reference signal

convolution=zeros(1,n_pulse);       % initialise this vector

% A complete synthetic aperture is required to achieve the desired RCS
% the system is able to focus correctly n_pulse - m pulses. The grid
size
% defined by the vector yn has to be shorter than the value
% (n_pulse-m)*dyimpulse

k=1;                                % counter that will be used in the
focussing
% the index k allows to perform correctly the convolution

for j=n_pulse_ref:n_pulse  % loop over the pulses
f_signal=ftx(signal(k:k+m-1));% FFT of the no-noise signal
F_convolution=(f_signal).*conj(f_reference)/n_pulse_ref;
convolution(k:k+m-1)=convolution(k:k+m-1)+iftx(F_convolution);
k=k+1;           % additional counter that is not included in the for
end
```

```
convolution=convolution/(n_pulse-n_pulse_ref);
%%%%%%%%%%%%%%%%%%%%%%%%%%%%%%%%%%%%%%%%%%%%%%%%
%       end  SAR focussing
%%%%%%%%%%%%%%%%%%%%%%%%%%%%%%%%%%%%%%%%%%%%%%%%
```

8. draw_plots.m

This Matlab program generates the required plots. This routine has to be called within the code *simulator.m*.

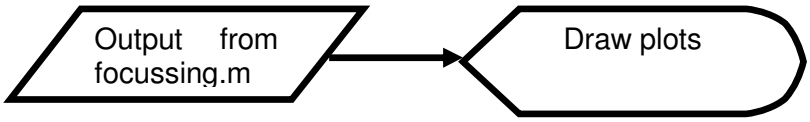


```
%%%%%%%%%%%%%%%%%%%%%%%%%%%%%%%%%%%%%%%%%%%%%%%%
%       START  plots
%%%%%%%%%%%%%%%%%%%%%%%%%%%%%%%%%%%%%%%%%%%%%%%%

figure(1)
%rcs=(real(convolution).^2+imag(convolution).^2);
rcs=abs(convolution);
plot(rcs/radar_cal)
title('Focused SAR image')
xlabel('Synthetic Aperture (samples)')
grid
hold on

figure(2)
%rcs=(real(convolution).^2+imag(convolution).^2);
plot(10*log10((rcs/radar_cal)/max(rcs/radar_cal)))
axis ([0.1068,-20.0])
xlabel('Synthetic Aperture (samples)')
ylabel ('Magnitude (dB)')
grid
hold on
```

9. slant_range.m

This Matlab function estimated the scalar product between two vectors.This function is called in the *simulation.m* subroutine to estimate the distance between satellites and scatterers.

```
function SR=slant_range(a,b)
    dx = a(1) - b(1);
    dy = a(2) - b(2);
    dz = a(3) - b(3);
```

```
SR = (dx*dx+dy*dy+dz*dz)^0
```

10. Impulse_response.m

Program impulse_response
10/3/2004 - Davide Bruno

Description

This program evaluates, in the space domain, the system transfer function related to a single scatterer located at the point x,r,teta. This code requires in input all the parameters that characterise the SAR evaluated.

To verify the correct implementation of this code its results have been compared with the outputs present in Franceschetti and Lanari (1999).

```
%I have considered some ERS-1 parameters in order to set all the
parameters
%to some realistic values.
clear
tau=             3.712e-05 ;          %pulse duration
chirp_slope=     4.17788e+11;    %chirp slope
DF= 15E6;                        %chirp bandwidth
rng_samp_rate=  1.89625 x 10+07;       %range sampling frequency
lambda=0.056666;                       %lambda
c=3E8;                                 %velocity of light
f=c/lambda;

near_range=829924.365777     %distance to first range bin Rnear
earth_radius=6371746.4379    %earth radius 1/2 way into image
SC_height=787955.52          %spacecraft height 1/2 way into image
SC_vel= 7125.0330            %ground-track velocity V
PRF =1679.902394             %pulse repetition frequency
D=10 ; %10 m antenna length

dx=1/PRF*SC_vel; %distance in azimuth between different samples

%distance in range between different samples
dr=c/(2*DF)
fcr=1/(2*dr);                 %critical frequency in range direction
fcx=1/(2*dx);                 %critical frequency across-track

R0=near_range+2808*dr;  %range at mid-swadth

X=(lambda/D)*R0; %width of the antenna footprint


  %dx=X/1500 %The footprint has been divided in 1000 points
```

```
%dr=c*tau/1567;   % 1000 samples in range direction

% a and b introduced to simplify calculation
b=c*tau/(2*X);
a=pi*X/(D/2);
t=-tau/2:tau/5617:tau/2;

for k=1:1000
    x_primo=-dx*500+dx*(k-1);
    x_primo=x_primo/(X); %adimensional with respect to the antenna
footprint

for m=1:5616

          DR=((R0+dr*(m-2808))^2+(x_primo*X)^2)^0.5-(R0+dr*(m-2808));

%DR derives from the approximation r= R0+DR
            DR=DR/X; %adimensional

        R   _primo=dr*(m-1)-(dr*(5616/2));
% r_primo is the distance (range direction) from the target to the
antenna
         r_primo=r_primo/(c*tau/2); %adimensional

         %analytical expression for the STF
G(k,m)=rect*exp(i*pi*(DF/tau)*(r_primo*tau-(DR*X*2/c))^2)*exp(-
j*a*2*D*DR/lambda);

end
end
imagesc (real(G)) %plot the real value of the function G.
```

11. Cdf2idl.pro

This routine in IDL has been made by S. Rupert in 1998 and is available on the internet at http://www-c4.ucsd.edu/~cids/software/cdf2idl.html. This code has been used to import in IDL ionospheric *spectre* dataset that are provided in netcdf format.

```
;;;;;;;;;;;;;;;;;;;;;;;;;;;;;;;;;;;;;;;;;;;;;;;;;;;;;;;;;;;;;;;;;;;;;;;
;;;;;;;
;
; cdf2idl.pro - This file contains IDL functions to read netCDF data
files
;               into IDL variables.
;
;  This file contains the following functions and procedures:
;     functions:
```

```
;        getFile - strips the directory and optionally) any suffixes
from
;                  the path+file
;        getDir - returns the directory from the full path+file
;        validateName - validates the name that will be used as a
netCDF
;                       variable
;     procedures:
;        cdf2idl - reads netCDF varaibles into IDL
;
;  History:
;  Date       Name          Action
;  ---------  ------------  ----------------------------------------
----
;  06 Jun 97  S. Rupert     Created.
;  09 Jun 97  S. Rupert     Fully tested.
;  10 Jun 97  S. Rupert     Modified keyword usage.
;  03 Feb 98  S. Rupert     Added additional error checking, and
warning to
;                           output script.
;  17 Feb 98  S. Rupert     Corrected validation routine to handle
instance
;                           of name strating with a number and
containing a
;                           dash.
;
;;;;;;;;;;;;;;;;;;;;;;;;;;;;;;;;;;;;;;;;;;;;;;;;;;;;;;;;;;;;;;;;;;;;;;;
;;;;;;;


function getFile, fullpath, suffix=suffix
; func_description
; This function returns the filename name from the full path.
; Inputs:    fullpath - full directory+file path
; Keyword:   /suffix:   include inptu suffix in output file name
; Outputs:   file - filename
; Example Call: file = getFile(fullpath)

; Retrieve the postion at which the first '/' character occurs from
; the end of the string.
dirlen = rstrpos(fullpath, '/')

; Retrieve the full length of the original string.
len = strlen(fullpath)

; Retrieve the filename.
fullfile = strmid(fullpath, dirlen+1, len)

; Retrieve the position at which the first '.' character occurs from
; the end of the string.
len = -1
if not(keyword_set(suffix)) then len = rstrpos(fullfile, '.')
```

```
if (len EQ -1) then len = strlen(fullfile)

; Retrieve the file.
file = strmid(fullfile, 0, len)

; Return the file name.
return, file

; End function.
end


function getDir, fullpath
; func_description
; This function returns the directory name from the full path.
; Inputs:   fullpath - full directory+file path
; Outputs:  dir - directory path
; Example Call: dir = getDir(fullpath)

; Retrieve the postion at which the first '/' character occurs from
; the end of the string.
len = rstrpos(fullpath, '/')

; Retrieve the filename.
if (len EQ -1) then dir = "./" $
else dir = strmid(fullpath, 0, len+1)

; Return the file name.
return, dir

; End function.
end


function validateName, varname
; func_description
; This routine ensures that the given name does not start with a
number,
; nor contain a dash.  IDL cannot accept a variable starting with a
; number or containing a dash.  If the name starts with a number, an
; underscore is prepended to the name, and if it contains a dash, the
; dash is replaced with an underscore.

; Initialize the name.
name = varname

; If the name starts with a number, prepend it with an underscore.
if (strpos(varname, '0') EQ 0) then name = strcompress("_"+varname)
if (strpos(varname, '1') EQ 0) then name = strcompress("_"+varname)
if (strpos(varname, '2') EQ 0) then name = strcompress("_"+varname)
if (strpos(varname, '3') EQ 0) then name = strcompress("_"+varname)
if (strpos(varname, '4') EQ 0) then name = strcompress("_"+varname)
```

```
if (strpos(varname, '5') EQ 0) then name = strcompress("_"+varname)
if (strpos(varname, '6') EQ 0) then name = strcompress("_"+varname)
if (strpos(varname, '7') EQ 0) then name = strcompress("_"+varname)
if (strpos(varname, '8') EQ 0) then name = strcompress("_"+varname)
if (strpos(varname, '9') EQ 0) then name = strcompress("_"+varname)

; If the name contains a dash replace it with an underscore.
if (strpos(name, '-') NE -1) then begin
   pieces = str_sep(name, '-')
   n_pieces = n_elements(pieces)
   name = pieces(0)
   for i=1,n_pieces-1 do begin
      name = strcompress(name+"_"+pieces(i))
   endfor
endif

; Return the file name.
return, name

; End function.
end

pro cdf2idl, infile, outfile=outfile, verbose=verbose
; pro_description, infile, outfile=outfile
; This procedure creates a script to read the data in a given netCDF
; file into IDL.  The default output file is the name of the netCDF
; file with idl replacing any existing suffix.  The default output is
; variable data only.
; Inputs:           infile  - full path to netCDF file of interest
; Optional Inputs:  outfile - name of script file for data input to
IDL
;                   verbose - includes extractions of all input file
;                             attributes in idl script
; Outputs:          outfile - idl script to read netCDF data into IDL
; Example:  cdf2idl, '/vol1/cids/netCDF.file', 'netCDF.idl'

; Establish that the correct data have been input.
if n_params() LT 1 then begin
   print, "Usage:  cdf2idl, 'inputfile', outfile='outputfile', "+$
          "/verbose"+string(10B)+$
          string(9B)+"inputfile  - full path to netCDF file of
interest"+string(10B)+$
          string(9B)+"outputfile - desired name of resultant idl
script"+string(10B)+$
          string(9B)+"/verbose:    keyword indicating inclusion of
netCDF attributes"
   return
endif

if (keyword_set(outfile)) then script = outfile $
else script = strcompress(getFile(infile)+".idl", /remove_all)
```

```
; Ensure that the netCDF format is supported on the current platform.
if not(ncdf_exists()) then begin
   print, "The Network Common Data Format is not supported on this
platform."
   return
endif

; Open the netcdf file for reading.
ncid = NCDF_OPEN(strcompress(infile, /remove_all))
if (ncid EQ -1) then begin
   print, "The file "+infile+" could not be opened, please check the
path."
   return
endif

; Open the output script file for writing.
openw, unit, script, /GET_LUN, ERROR=err
if (err NE 0) then begin
   print, !err_string
   return
endif

; Retrieve general information about this netCDF file.
ncidinfo = NCDF_INQUIRE(ncid)

; Write the file header.
dir = getDir(infile)
if (dir EQ './') then dir = 'the current directory'
file = getFile(infile,/suffix)
warning = "'Warning:  If you have moved "+file+" from
"+dir+"'+string(10B)+$"+string(10B)+$
          string(9B)+"string(9B)+'idl will not be able to open the
file unless you modify'+$"+$
          string(10B)+string(9B)+"string(10B)+string(9B)+'the
NCDF_OPEN line in this script to "+$
          "reflect the new path.'"
printf, unit,
";************************************************************"
printf, unit, "; IDL script for reading NetCDF file:
printf, unit,
";************************************************************"
printf, unit, ""
printf, unit, "print, "+warning
printf, unit, ""
printf, unit, "ncid = NCDF_OPEN('"+infile+"')            ; Open The
NetCDF file"
printf, unit, ""

; Place the desired variables in local arrays.
for i=0, ncidinfo.Nvars-1 do begin
   vardata = NCDF_VARINQ(ncid, i)
   varname = validateName(vardata.Name)
```

```
   printf, unit, "NCDF_VARGET, ncid, "+strcompress(string(i))+",
"+varname+$
                 "      ; Read in variable '"+vardata.Name+"'
   if (keyword_set(verbose)) then begin
      for j=0, vardata.Natts-1 do begin
         att = NCDF_ATTNAME(ncid, i, j)
         attname =
strcompress(varname+"_"+strcompress(att,/REMOVE_ALL))
         printf, unit, "   NCDF_ATTGET, ncid,
"+strcompress(string(i))+$
                       ", '"+att+"', "+attname
         printf, unit, "   "+attname+" = STRING("+attname+")"
      endfor
   endif
   printf, unit, ""
endfor

if (keyword_set(verbose)) then begin
  printf, unit, "; Read in the Global Attributes."
  for i=0, ncidinfo.Ngatts-1 do begin
     name = NCDF_ATTNAME(ncid, /GLOBAL, i)
     attname = validateName(name)
     printf, unit, "NCDF_ATTGET, ncid, /GLOBAL, '"+name+"', "+attname
     printf, unit, attname+" = STRING("+attname+")"
  endfor
  printf, unit, ""
endif

printf, unit, "NCDF_CLOSE, ncid      ; Close the NetCDF file"

; Close the open script file.
free_lun, unit

; Tell the user how to use the result.
print, 'You may now type @'+script+' at the IDL prompt to input '+$
       'data from '+infile+'.'

; Return to the caller.
return

; End procedure.
end
```

Appendix C – SAR simulators

1. SAR processing oriented simulators

Figure C-1 illustrates the relationship between SAR processors and SAR simulators. A simulator converts the reflectivity map into a simulated raw data set. A SAR processor has the aim of generating the reflectivity function from the raw signal while the simulator has to reconstruct the raw signal starting from the reflectivity map (Figure C-2Figure).

The intermediate step between input and output is the SAR System Transfer Function (STF). It can be considered as a SAR image simulator.

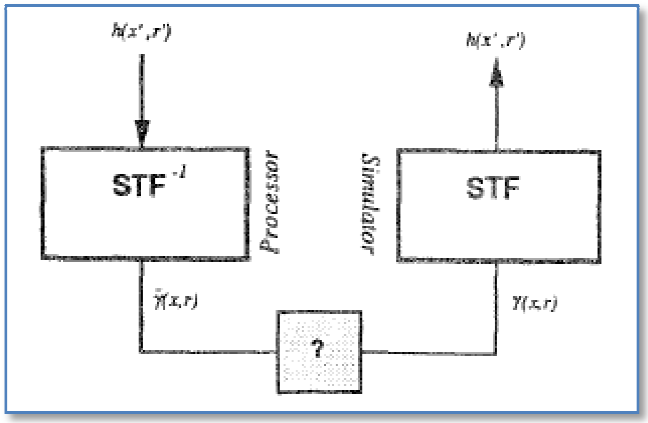

Figure C-1. SAR processing oriented simulator (right hand side) and dual SAR processing procedure (left hand side). The bidden box is the generally unknown relation between the actual reflectivity $\gamma(x,r)$ and the estimated reflectivity $\hat{\gamma}(x,r)$ (Franceschetti *et al.*, 1995).

2. SAR simulator scheme

The SAR simulation process that has been implemented is presented in the flow chart in Figure C-2. The rationale of the processing is the same presented by Franceschetti *et al.* (1995) as a "*SAR processing oriented simulator*" (Figure C-3). There are a few main steps, which have to be worked out.

- Assume a certain scenario with given RCS and geometry.

- Simulate raw data relative to the scenario imaged.
- Process the raw data produced in order to obtain the final SAR image.

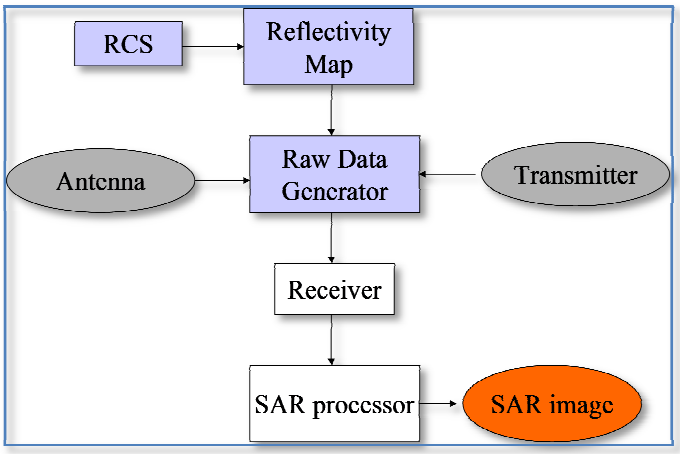

Figure C-2. SAR processing oriented simulator scheme.

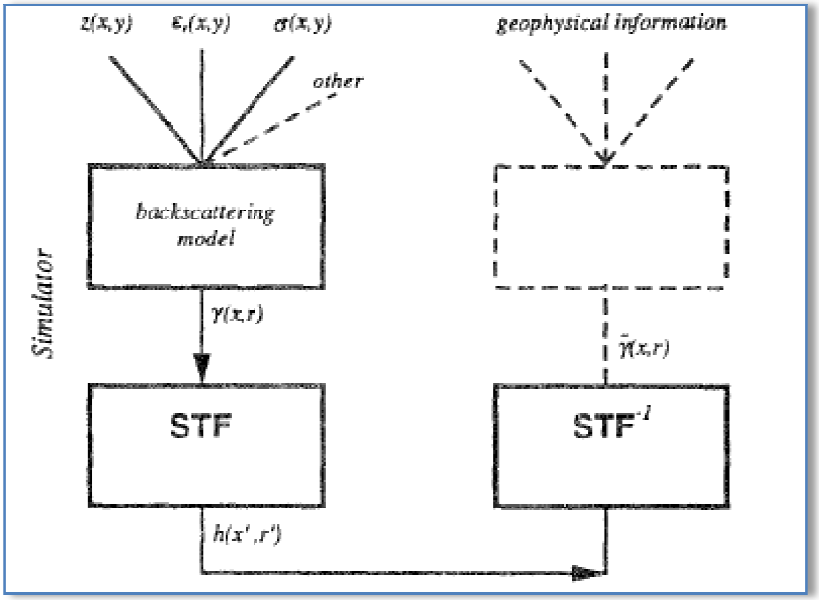

Figure C-3. SAR-oriented simulator processing scheme. (Franceschetti *et al.* 1995).

3. Defining the scenario

Input data are both mission data and scene characteristic data (Franceschetti *et al.* 1992). Mission data are:

- spacecraft height;
- velocity
- nominal look angle;
- antenna parameters and polarization;
- carrier frequency;
- pulse repetition rate;
- chirp bandwidth.

4. Define mission data

All the orbit parameters of the satellite carrying the SAR have to be taken into account. At first it could be useful to consider a case simpler than the geosynchronous orbit by using the system parameters (wavelength, orbit) of an existing LEO satellite (ERS-1).

5. Define the backscattering coefficient map

The first step in simulating a set of raw data is determining the grid upon which the backscattering coefficient has to be defined. The two directions of the coordinate systems are across-track and along-track (coordinates *x, r*).

The function we need to work out is the matrix with all the values $\gamma(x,r)$ (x is the along-track coordinate while r is the slant range from the antenna centre).

Scene characteristic data involve the terrain imaged. Hartl *et al.* (1986) specify the main parameters that are necessary to characterise the radar backscatter of a given terrain.

A description of physical parameters of the scene:

- geometry;
- moisture;
- canopy (volume, correlation roughness, orientation).

EM parameters of the target:

- complex scattering matrix;
- extinction coefficients;
- albedo.

The backscattering coefficient can be assigned as a function of electromagnetic parameters or it can be simply assigned by the user.

Franceschetti and Lanari (1999) describe the reflectivity $\gamma(x, r)$ caused by the scattering from rough surfaces. According to this simplified model, returns from different areas of the model sum up incoherently. Three different effects have modified the reflectivity coefficient phase term:

- the distance from the target to the radar;
- an additional term $\Lambda(x, r)$ accounting for terrain roughness;
- a second additional term $\delta(x, r)$ which takes into account the macroscopic properties of the surface. "It is noted that both δ and Λ are random variables but on two different large (δ) and small (Λ) scales" (Franceschetti and Lanari, 1999).

$$\gamma(x,r) = \left|\gamma(x,r)\right| \exp\left[j\delta(x,r) - j\frac{4\pi}{\lambda}\Lambda(x,r) - j\frac{4\pi}{\lambda}r \right] \quad \text{Equation C-1}$$

In Equation C-1, r is the slant range coordinate;
x is the along-track azimuth coordinate.

6. SAR raw data generation

Assuming that the radar transmits a linear chirp, the pulse has the following expression:

$$f_1(t - t_n) = \exp\left[i\omega(t - t_n) - \frac{j\alpha(t - t_n)^2}{2} \right] rect\left[\frac{t - t_n}{\tau} \right] \quad \text{Equation C-2}$$

In Equation C-2, α is the chirp bandwidth;
τ is the pulse duration;
t_n is a discrete variable;
ω is the angular frequency.

The antenna pattern is considered squared because a monostatic radar is assumed.

Considering an elementary the signal backscattered and received onboard is given by (assuming that the radar transmits a linear chirp at times t_n-$\tau/2$) Equation C-3.

$$f\left(x_n - x, t - t_n, r\right) = \exp\left[-j\omega\frac{2R}{c}\right]\exp\left[j\frac{\alpha}{2}\left(t - t_n - \frac{2R}{c}\right)^2\right] rect\left[\frac{t - t_n - \frac{2R}{c}}{\tau}\right] w^2\left[x_n - x, r\right]$$

Equation C-3

In Equation C-3, x_n is the coordinate of the antenna centre;
R is the slant range $R = \sqrt{r^2 + \left(x_n - x\right)^2} \approx r + \Delta R$;

According to Franceschetti and Lanari (1999), the received signal can be normalised in three steps:

- the time coordinate has been changed to range coordinates $r' = \frac{ct'}{2}$;
- the range coordinate has been normalised to half the pulse spatial extension ($c\tau/2$);
- the across-track coordinate has been normalised to the mid-swath azimuth illumination footprint X/2.

The raw signal *h(x', r')* can be obtained by superimposing all the elementary returns from the illuminated surface, hence:

$$h\left(x', r'\right) = \iint dx dr \gamma\left(x, r\right)\exp\left[-j2\pi\frac{c\tau}{\lambda}r\right]\exp\left[-j4\pi\frac{X}{\lambda}\Delta R\right] w^2\left[x_n - x, r\right]$$

$$\exp\left[-j\omega\tau r + j\frac{\alpha}{2}\left(r - r' - \frac{2X}{c\tau}\Delta R\right)\right] rect\left[r - r' - \frac{2X}{c\tau}\Delta R\right]$$

Equation C-4

Franceschetti and Schirinzi (1990) provide this functional expression for the SAR raw data.

$$h\left(x' = vt_n, r' = \frac{ct'}{2}\right) = \iint_A \gamma\left(x, r\right) g\left(x' - x, r' - r; x, r\right) dx dr$$

Equation C-5

In Equation C-5, x is the azimuth coordinate;
r is the slant range coordinate;
x' and r' refer to the output coordinates;
$\gamma(x,r)$ is the equivalent backscattering coefficient;
$g()$ is the System Transfer Function (STF);
v is the spacecraft velocity;
t_n is the centre instant of the transmitted pulse.

The reflectivity pattern *γ(x,r)* takes into account the phase variation connected to the slant range coordinate:

$$\gamma(x,r) \rightarrow \gamma(x,r)\exp\left[-j2\pi\frac{c\tau}{\lambda}r\right] \qquad \text{Equation C-6}$$

The STF is the impulse response of the radar system. In the time domain (Figure C-4), it can be expressed as:

$$g(x'-x,r'-r,r) = \exp\left[-ja\frac{2L}{\lambda}\Delta R\right]w^2\left[x'-x,r\right] \qquad \text{Equation C-7}$$

$$\exp\left[-j\omega\tau r + j\frac{\alpha}{2}\left(r-r'-\frac{2X}{c\tau}\Delta R\right)\right]rect\left[r-r'-\frac{2X}{c\tau}\Delta R\right]$$

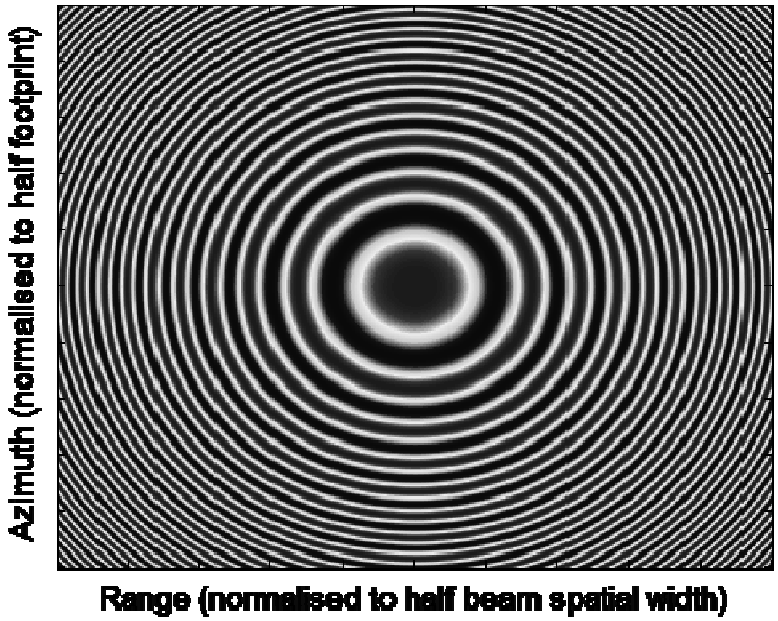

Figure C-4. Impulse response of the system to a unitary point target. The range span is between $-c\tau/2$ and $+c\tau/2$; the azimuth span is between –X/8 and X/8 where X is the nominal footprint. The plot has been obtained implementing Equation C-7 in Matlab (code *impulse_response.m* in Appendix B).

Franceschetti and Schirinzi (1990) and Franceschetti *et al.* (1992) compute expression Equation C-5 in the frequency domain using FFT. They assume that the function Equation C-7 is linear thus, they compute the raw data integral as a convolution.

The result is:

$$H(\xi,\eta)=\Gamma(\xi,\eta)G(\xi,\eta) \qquad \text{Equation C-8}$$

In Equation C-8, (ξ,η) are the Fourier mates of *x* and *r*, the along track and slant range coordinate;
$H(\xi,\eta)$ is the bi-dimensional Fourier Transform of the raw data;
$\Gamma(\xi,\eta)$ is the bi-dimensional Fourier Transform of the equivalent backscattering $\gamma(x,r)$;
$G(\xi,\eta)$ is the bi-dimensional Fourier Transform of the STF.

Franceschetti and Lanari (1999), provide an analytic expression for the FT of the STF *g(x,r).*

$$G(\xi,\eta,r)\approx\frac{\pi}{\sqrt{a(R_0/r)b}}rect\left[\frac{\eta}{2b}\right]w^2\left[-\frac{\xi}{2a}\right]\exp\left[-j\Psi(\xi,\eta,r)\right]$$

Equation C-9

The function Ψ In Equation C-9 is given in Equation C-10.

$$\Psi=\frac{\eta^2}{4b}-2a\left(\frac{L}{\lambda}\right)^2\left(1+\varepsilon\frac{\eta}{2b}\right)\frac{r}{R_0}+\frac{L}{\lambda}\frac{r}{R_0}\sqrt{\left(2a\frac{L}{\lambda}\right)^2\left(1+\varepsilon\frac{\eta}{2b}\right)^2-\xi^2} \qquad \text{Equation C-10}$$

The parameters included in Equation C-10 are specified in the following equations.

$$a=\frac{2\pi X^2}{\lambda R_0} \qquad \text{Equation C-11}$$

$$b=\frac{\alpha\tau^2}{2} \qquad \text{Equation C-12}$$

$$\varepsilon=\frac{\Delta f}{f} \qquad \text{Equation C-13}$$

Some considerations on the STF in Equation C-9 are useful to a better understanding of the problem. If the illumination over the ground is uniform (along azimuth direction) the *G()* function is band-limited both along ξ and along η.

In normalised units the ξ bandwidth is:

$$-a \le \xi \le +a \qquad \text{Equation C-14}$$

De-normalisation is accomplished by the use of the multiplicative factor *1/X*. The frequency bandwidth corresponding to the azimuth spatial frequency $2a/2\pi$ is:

$$\frac{2a}{2\pi} \to \frac{2v}{L} \qquad \text{Equation C-15}$$

In Equation C-15, *v* is the spacecraft velocity (transformation from a wave number to frequency domain);

The second term in Equation C-15 is usually interpreted as Doppler bandwidth (Franceschetti and Lanari, 1999).

Neglecting the r dependence of the amplitude term, the *r* dependence in Equation C-9 is related only to the term in Equation C-10. This equation is linearly dependent on range *r*. It is useful to neglect the *r*-invariant component. Equation C-10 can be expressed as in Equation C-16 and in the following ones(Franceschetti and Lanari, 1999).

$$\Psi(\xi,\eta,r) = \Psi_0(\xi,\eta,R_0) + (r - R_0) K(\xi,\eta) \qquad \text{Equation C-16}$$

$$K(\xi,\eta) \approx \mu(\xi) + \nu(\xi)\eta + \zeta(\xi)\eta^2 \qquad \text{Equation C-17}$$

$$\mu(\xi) = -\frac{2a}{R_0}\left(\frac{L}{\lambda}\right)^2 + \sqrt{\left(2a\frac{L}{\lambda}\right)^2 - \xi^2} \qquad \text{Equation C-18}$$

$$\nu(\xi) = -2a\left(\frac{L}{\lambda}\right)^2 \frac{\varepsilon}{2bR_0} + \frac{\frac{L}{\lambda}\left(2a\frac{L}{\lambda}\right)^2 \frac{\varepsilon}{2bR_0}}{\sqrt{\left(2a\frac{L}{\lambda}\right)^2 - \xi^2}} \qquad \text{Equation C-19}$$

$$\zeta(\xi) = -\frac{\frac{L}{\lambda}\left(2a\frac{L}{\lambda}\right)^2 \varepsilon^2 \left(\frac{\varepsilon}{2b}\right)^2}{2R_0\sqrt{\left[\left(2a\frac{L}{\lambda}\right)^2 - \xi^2\right]^3}} \qquad \text{Equation C-20}$$

7. Narrow focus approximation

The first step in generating raw data sets is to neglect completely the *r* dependence in the SAR TF. This simplification is usually quite coarse as it does not take into account the range migration problem but it is useful to obtain a first approximation solution.
According to this approximation, the raw data FT is expressed as:

$$H(\xi,\eta) = \Gamma(\xi,\eta) G_0(\xi,\eta) \qquad \text{Equation C-21}$$

$$G_0(\xi,\eta) = G(\xi,\eta,R_0) \qquad \text{Equation C-22}$$

The name *narrow focus approximation* derives from the fact that, if the same approximation was used in SAR data processing, only the line corresponding to mid-swath would be correctly focused.

8. Wide focus approximation

Neglecting the *r* dependence is usually unacceptable. The right expression for the STF is:

$$G(\xi,\eta,r) = G_0(\xi,\eta)\exp\left[-j(r-R_0)K(\xi,\eta)\right] \qquad \text{Equation C-23}$$

This implies that the raw data FT is:

$$H(\xi,\eta) = G_0(\xi,\eta)\Gamma\left[\xi,\eta+K(\xi,\eta)\right] \qquad \text{Equation C-24}$$

In Equation C-24 the new reflectivity map is obtained interpolating the existing and known function $\Gamma(\xi,\eta)$ on the new grid [ξ, η+K(ξ,η)].
Equation C-8 applies if the dependence of the system transfer function from the range coordinate *r* can be neglected.
For a precise simulation it is desirable to retain the r dependence in Equation C-9. This is equivalent of considering the correct focus depth in the simulation. Equation C-9 can be expressed as (Franceschetti *et al.*, 1992):

$$G(\xi,\eta,r) \approx G_0(\xi,\eta)\sqrt{1+\beta r}\exp\left[-j\beta\frac{\xi^2}{4a^2}r\right] \qquad \text{Equation C-25}$$

$G_0(\xi,\eta)$ is the value of $G(\xi,\eta)$ when β=0 thus neglecting the *r* dependence in Equation C-9.

Applying Equation C-25 the transfer function of the raw data function is:

$$H(\xi,\eta) = \Gamma'(\xi',\eta')\,G_0(\xi,\eta) \qquad \text{Equation C-26}$$

In Equation C-26, $\Gamma'(\xi',\eta')$ is the FT of the modified reflection coefficient $\gamma(x,r)\sqrt{1+\beta r}$.

The wide focus approximation is a category that includes all the commonly used SAR processing procedures (Range Doppler algorithm and ω–K procedure).

Appendix D – Earth tide

1. Solid Earth Tide

Milbert (2002) provides a code that estimates solid Earth Tidal motion for a given date and a given site on the Earth surface.

Data are sampled every 60 seconds. The solid earth tide components are north, east, Up in the local geodetic (ellipsoidal) horizon system.

The following section describes the output of the solid.exe executable.

"*Program* solid *is based on an edited version of the* dehanttideinelMJD.f *source code provided by Professor V. Dehant. This code is an implementation of the solid earth tide computation found in section 7.1.2 of the IERS Conventions (2003) , IERS Technical Note No. 32*" (Milbert, 2002)

2. Solid.exe output

```
 year,month,day=  2007  1  1
lat, east lon.=    50.000000000   50.000000000
     0.0  0.003275 -0.055918 -0.050749
    60.0  0.003426 -0.055735 -0.051767
   120.0  0.003575 -0.055550 -0.052782
   180.0  0.003723 -0.055363 -0.053792
   240.0  0.003869 -0.055174 -0.054799
   300.0  0.004014 -0.054984 -0.055803
   360.0  0.004158 -0.054792 -0.056802
   420.0  0.004300 -0.054598 -0.057797
   480.0  0.004440 -0.054402 -0.058789
   540.0  0.004579 -0.054204 -0.059777
   600.0  0.004716 -0.054005 -0.060760
   660.0  0.004852 -0.053804 -0.061740
   720.0  0.004986 -0.053601 -0.062716
   780.0  0.005119 -0.053396 -0.063687
   840.0  0.005250 -0.053190 -0.064655
   900.0  0.005380 -0.052982 -0.065618
   960.0  0.005508 -0.052772 -0.066577
  1020.0  0.005634 -0.052561 -0.067532
  1080.0  0.005759 -0.052348 -0.068483
  1140.0  0.005882 -0.052133 -0.069430
  1200.0  0.006004 -0.051917 -0.070372
```

```
  1260.0  0.006124 -0.051700 -0.071310
  1320.0  0.006242 -0.051480 -0.072244
  1380.0  0.006359 -0.051260 -0.073173
  1440.0  0.006474 -0.051037 -0.074098
  1500.0  0.006587 -0.050813 -0.075018
  1560.0  0.006699 -0.050588 -0.075934
  1620.0  0.006809 -0.050361 -0.076846
  1680.0  0.006918 -0.050133 -0.077753
  1740.0  0.007025 -0.049903 -0.078656
  1800.0  0.007130 -0.049672 -0.079553
  1860.0  0.007233 -0.049440 -0.080447
  1920.0  0.007335 -0.049206 -0.081336
  1980.0  0.007435 -0.048971 -0.082220
  2040.0  0.007534 -0.048734 -0.083099
  2100.0  0.007631 -0.048496 -0.083974
  2160.0  0.007726 -0.048257 -0.084844
  2220.0  0.007819 -0.048016 -0.085710
  2280.0  0.007911 -0.047774 -0.086570
  2340.0  0.008001 -0.047531 -0.087426
  2400.0  0.008089 -0.047287 -0.088277
  2460.0  0.008176 -0.047041 -0.089123
  2520.0  0.008260 -0.046795 -0.089965
  2580.0  0.008344 -0.046547 -0.090801
  2640.0  0.008425 -0.046298 -0.091633
  2700.0  0.008505 -0.046047 -0.092459
  2760.0  0.008582 -0.045796 -0.093281
  2820.0  0.008659 -0.045543 -0.094098
  2880.0  0.008733 -0.045290 -0.094910
```

3. Ocean loading displacement

This is the output of a code that simulates ocean loading displacement (Scherneck, 2006).

```
$$ Ocean loading displacement
$$
$$ Calculated on Ore using olfg/olmpp of H.-G. Scherneck $$ $$ COLUMN ORDER:
M2  S2  N2  K2  K1  O1  P1  Q1  MF  MM SSA $$ $$ ROW ORDER:
$$ AMPLITUDES (m)
$$   RADIAL
$$   TANGENTL    EW
$$   TANGENTL    NS
$$ PHASES (degrees)
$$   RADIAL
$$   TANGENTL    EW
$$   TANGENTL    NS
$$
$$ Displacement is defined positive in upwards, south and west direction.
$$ The phase lag is relative to Greenwich and lags positive. The $$ Gutenberg-
Bullen Green's function is used. In the ocean tide model the $$ deficit of
```

```
tidal water mass has been corrected by subtracting a uniform $$ layer of water
with a certain phase lag globally.
$$
$$ Complete <model name> : No interpolation of ocean model was necessary
$$ <model name>_PP       : Ocean model has been interpolated near the station
$$                         (PP = Post-Processing)
$$
$$ Ocean tide model: GOT00.2, long period tides from FES99 $$ $$ END HEADER $$
  ONSALA
$$ GOT00.2_PP ID: Dec  26, 2006  9:20
$$ Computed by OLMPP by H G Scherneck, GEODAC, Porto Observatory, 2006
$$ Onsala                                  RADI   TANG   lon/lat:        11.9264
57.3958
  .00366 .00124 .00089 .00032 .00223 .00115 .00071 .00009 .00082 .00044 .00037
  .00149 .00035 .00040 .00009 .00046 .00043 .00015 .00009 .00012 .00006 .00006
  .00069 .00027 .00020 .00004 .00029 .00014 .00009 .00004 .00004 .00002 .00001
   -62.1  -51.3  -94.5  -39.7  -57.7 -110.8  -60.3 -165.4    8.4    5.2    2.1
    87.1  114.1   57.3  126.4  102.3   35.3   96.9   -7.0 -167.4 -170.0 -177.7
   109.9  152.4   86.4  149.1   50.7  -59.4   47.7  173.6  -14.5    2.3    5.1
$$ END TABLE
```